Technische Universität München

Max-Planck-Institut für Physik
(Werner-Heisenberg-Institut)

Phenomenology of Supersymmetric Particle Production Processes at the LHC

Maike Kristina Trenkel

Abstract

We study the hadronic production of strongly interacting SUSY particles in the framework of the MSSM. In particular, we consider top-squark pair, gluino–squark pair, and same sign squark-squark pair production processes. Aiming at precise theoretical predictions, we calculate the cross section contributions of electroweak origin up to the one-loop level. We find sizable effects both from tree-level electroweak subprocesses and next-to-leading order electroweak corrections, reaching the 20% level in kinematical distributions.

In a second part of this thesis, we investigate the phenomenology of $\mathcal{R}$-parity violating B_3 SUSY models with the lightest stau ($\tilde{\tau}_1$) being the LSP. We analyze the possible $\tilde{\tau}_1$ decay modes, taking into account the dynamical generation of non-zero $\mathcal{R}$-parity violating couplings at lower scales. As an application of our studies which is interesting for experiments at particle accelators, we discuss single slepton production at the LHC and give numerical results for single smuon production.

Zusammenfassung

Wir beschäftigen uns mit der hadronischen Paarerzeugung stark wechselwirkender SUSY-Teilchen im Rahmen des MSSM und betrachten insbesondere die Produktion von Top-Squark Paaren, Gluino–Squark Paaren und gleichgeladenen Squark–Squark Paaren. Um möglichst präzise theoretische Vorhersagen zu erreichen, berechnen wir die elektroschwachen Beiträge zu den Produktionswirkungsquerschnitten. Dabei ziehen wir sowohl elektroschwach-induzierte Prozesse auf Born-Niveau als auch elektroschwache Quantenkorrekturen nächstführender Ordnung in Betracht. Die größte Bedeutung erreichen diese Beiträge in kinematischen Verteilungen, wo sie bis auf 20% anwachsen können.

In einem zweiten Teil der Arbeit untersuchen wir die Phänomenologie $\mathcal{R}$-Parität-verletzender B_3 supersymmetrischer Modelle, in denen das leichteste Stau ($\tilde{\tau}_1$) das leichteste SUSY Teilchen ist. Wir analysieren die möglichen $\tilde{\tau}_1$-Zerfallsmoden und berücksichtigen dabei auch weitere, dynamisch erzeugte $\mathcal{R}$-parität-verletzende Kopplungen. Als eine für Experimente an Teilchenbeschleunigern interessante Anwendung unserer Studien diskutieren wir die Resonanzproduktion von Sleptonen am LHC und werten die Ergebnisse für die Resonanzproduktion von Smyonen numerisch aus.

Contents

vi

Chapter 1
Introduction

The Standard Model of elementary particle physics (SM) [1–4] has been proven to successfully describe all observed particles and their electroweak and strong interactions. Despite the excellent agreement between the theoretical predictions and experimental data [5], there remain unresolved issues such as the hierarchy problem, the non-unification of gauge couplings or the unknown source of dark matter in the universe, which point to new physics beyond the weak scale. It is thus widely believed that the SM is an effective theory, valid only in the low-energy limit of a more fundamental theory describing physics at arbitrarily high energies.

Numerous candidate theories of physics beyond the SM have been elaborated in the past. In this thesis we delve into the possibility of extending the SM in a supersymmetric way. Imposing a symmetry between fermionic and bosonic states, supersymmetry (SUSY) [6,7] predicts new partner particles to every known particle that only differ in spin by half a unit. If SUSY was an exact symmetry, SM particles and their SUSY partners would be degenerate in mass. But no SUSY particle has been observed so far. In order to comply with present data, the possibly new particles have to be massive in comparison to their SM counterparts and supersymmetry has to be broken at low energies.

Supersymmetry, and in particular if it is realized around the weak scale, is very attractive from the phenomenological point of view. Owing to the existence of new particles obeying opposite spin statistics, it allows for a stabilization of the large hierarchy between the Planck scale and the electroweak scale [8] and for a consistent unification of SM gauge couplings at high energies [9]. In addition, if the lightest SUSY particle is stable, SUSY provides a dark matter candidate and can account for the observed cold dark matter relic density [10,11].

The search for SUSY particles is one of the major topics in the experimental program of particle physics. In the low-energy region, electroweak and B-physics precision observables provide a powerful tool for testing the consistency of SM predictions with data. Since new particles would enter the theoretical evaluations via virtual quantum effects, it is also possible to discriminate between the SM and alternative theories. The comparison of measurements with computational results of a given model allows to set indirect limits on the

masses and couplings of the postulated particles, even if they are too heavy to be produced directly. The minimal supersymmetric extension of the Standard Model (MSSM) [12–14] has extensively been investigated in the past. The mass of the SM W boson, m_W, and the effective leptonic weak mixing angle, $\sin^2 \theta_{\text{eff.}}$, as measured at LEP, SLC, and at the Tevatron are among the most relevant electroweak precision observables in this respect. While strong bounds on the SUSY parameters have been derived, a certain preference for relatively light SUSY particles has been found (see e. g. Refs. [15,16] or Ref. [17] for a review). There are also low-energy observables, such as the anomalous magnetic moment of the muon, $(g - 2)_\mu / 2$, where SUSY yields a better fit to data than the SM [18].

However a decisive answer to the existence of SUSY can only be given by the direct detection of SUSY particles produced at high-energy particle accelerators. With the imminent startup of the Large Hadron Collider (LHC) at CERN, it will soon be possible to probe SUSY and its predictions at energies which were not accessible at colliders so far. If SUSY is realized around the TeV scale, some of the SUSY particles have to be discovered at the LHC.

A good understanding of the theory and reliable theoretical predictions are essential ingredients for a successful analysis of LHC data. To further investigate the phenomenology of SUSY particle production processes at hadron colliders, the main intent of this thesis is twofold. On the one hand we perform precise cross section calculations by taking into account quantum effects. On the other hand we are interested in how to measure SUSY particles in accelerator experiments and examine distinctive SUSY signatures in detectors.

Among the potential SUSY discovery channels, certainly the direct production of colored SUSY particles, squarks and gluinos, will play a key role. Since these can be produced via the strong interaction, high production rates are expected at hadron colliders. First theoretical cross section predictions for squark and gluino production processes based on leading order (LO) calculations were made already many years ago [19]. Later calculations of next-to-leading order (NLO) in perturbative QCD [20,21] could reduce theoretical uncertainties considerably and revealed corrections of typically 20%-30%. Considering higher-order corrections to the cross sections, the corrections due to strongly interacting particles (QCD corrections) cause the largest effects. Electroweak (EW) contributions, in comparison, are typically suppressed from the weak coupling by at least one order of magnitude and are often neglected. However the spectrum of weakly interacting particles in the MSSM is broad and the interplay of EW corrections can be involved, in particular if not only QCD-mediated but also EW-mediated production channels exist at tree-level. And including electroweak effects in the parton evolution, a non-zero photon density is dynamically generated inside protons which opens up further photon-induced production mechanisms. The above statement on the smallness of EW contributions thus needs not necessarily to be true. Owing to the large amount of data that will be provided by the LHC experiments, it seems indispensable to extend the theoretical calculations beyond one-loop in QCD in or-

der to compete with statistical uncertainties. Both higher-order QCD [22,23], and one-loop EW corrections [24–27] to squark and gluino production processes are subjects of current research. In this work, we study the production of top-squark pairs, gluino–squark pairs, and same-sign squark–squark pairs and calculate the tree-level and one-loop cross section contributions of electroweak origin up to $\mathcal{O}(\alpha_s^2\alpha)$ in the strong and electroweak couplings.

Within the SM, given the SM particle content and gauge invariance of the theory, lepton and baryon number are accidentally conserved. This however is not guaranteed a priori by a supersymmetric extension of the SM. Assuming a supersymmetric SM with minimal particle content, renormalizable lepton- and baryon-number violating operators are allowed [28,29]. If couplings of both types are present, rapid proton decay can take place [30,31]. Since this clearly contradicts experimental observations [32], an additional symmetry is needed to stabilize the proton. Most commonly, $\mathcal{R}$-parity conservation is postulated [33], leading to the MSSM. An alternative approach is provided by $\mathcal{R}$-parity violating but baryon-number conserving B_3 supersymmetric models [34–37]. Only the final discovery of SUSY particles will allow to draw conclusions if or how SUSY is realized in nature. It is thus crucial to understand and distinguish between possible SUSY signatures of different SUSY models. In a second part of this thesis, we focus on B_3 models predicting the lightest stau $\tilde{\tau}_1$ as lightest supersymmetric particle and study characteristic signatures at the example of slepton production at the LHC.

The outline of this report is as follows.

In Chapter 2 we introduce the conceptual framework of our studies. To begin with we briefly review the Standard Model and discuss some of its open questions to motivate the search for new physics. We then concentrate on supersymmetry, illustrate its basic ideas and provide the necessary theoretical background to construct a SUSY Lagrangian. On this basis, a phenomenologically viable and testable SUSY model can be built, the MSSM. We discuss the concept of $\mathcal{R}$-parity, and present in detail the field content and physical particle spectrum of the MSSM.

The main focus of this thesis is on the calculation of EW contributions to the production of colored SUSY particles at the LHC. In Chapter 3, we give an introductory overview of the topic with the intention to provide a solid basis for the forthcoming process-specific investigations. We start by reviewing the current status of experimental searches and comment on the prospects for the LHC. Next, being a crucial ingredient in the theoretical approach of how to calculate cross sections at hadron colliders, we introduce the parton model and the idea of factorization. We then turn to squark and gluino production within the MSSM and classify the possible final states. We discuss the dominant production channels and list the contributions of QCD and EW origin up to the one-loop level.

The technical setup required for NLO calculations is explained in Chapter 4. Two types of singularities arise in cross section computations beyond tree-level and have to be addressed.

The momentum integrations can diverge for high internal loop momenta (UV singularities) and if low-energetic or collinear massless particles are attached to the external particles in loop and real radiation diagrams (IR singularities). Whereas UV singularities require a redefinition of the free parameters of the theory (renormalization), IR singularities cancel in sufficiently inclusive defined observables. In this chapter, we describe the general treatment of both types of singularities. We introduce different regularization and renormalization schemes and give methods at hand for the integration over IR singular phase-space regions.

In Chapters 5, 6, and 7 we then explicitly discuss the EW contributions up to $\mathcal{O}(\alpha_s^2\alpha)$ to stop–anti-stop $(\tilde{t}_a\tilde{t}_a^*)$, gluino–squark $(\tilde{g}\tilde{q}_a)$, and diagonal squark–squark $(\tilde{q}_a\tilde{q}_a)$ pair production processes at the LHC. The three chapters are organized in a parallel way. We first give analytical results for the LO cross sections of $\mathcal{O}(\alpha_s^2)$. Second, we investigate the various EW contributions, including both tree-level EW-induced subprocesses of $\mathcal{O}(\alpha^2)$ and $\mathcal{O}(\alpha_s\alpha)$ and NLO EW corrections of $\mathcal{O}(\alpha_s^2\alpha)$, and give details on the handling of UV and IR singularities. In a third section, we perform numerical studies within specific (mSUGRA) SUSY scenarios. In order to determine the impact of the EW-induced effects on the LO results, we investigate integrated hadronic cross sections and differential distributions with respect to kinematical variables.

Chapter 8 is devoted to the second, independent project on the phenomenology of $\mathcal{R}$-parity violating B_3 SUSY models. If SUSY particles exist, they are typically much heavier than their SM partners and at colliders will mostly decay rapidly. This leads to cascade decay chains in the detector ending up with the lightest supersymmetric particle (LSP). The nature of the LSP and its possible decay modes is an essential feature for all SUSY signatures. As a consequence of $\mathcal{R}$-parity violation, the LSP is not restricted from cosmological constraints to be electrically neutral [10] and regions in the SUSY parameter space predicting charged LSPs are reopened. We consider B_3 SUSY models with a $\tilde{\tau}_1$ LSP and classify the possible $\tilde{\tau}_1$ decays and collider signatures. Assuming a single non-zero B_3 coupling λ' at the GUT scale, we take into account that the renormalization group equations of B_3 couplings are coupled and that further B_3 couplings can be dynamically generated at lower scales. The results are then applied to the example of single slepton production at the LHC and a numerical study of single smuon production is given, focussing on signatures with like-sign dimuons and three and four muons in the final state.

Finally we summarize in Chapter 9. In the appendices, we provide a reference of definitions and numerical inputs used throughout the work. In Appendix A, we briefly summarize our conventions of spinorial calculus. More details on the definition of low-energy input parameters for the numerical studies in Chapters 5–7 are given in Appendix B. Referring to the B_3 mSUGRA parameter sets A and B defined in Chapter 8, we list in Appendix C explicit results for cross sections and branching ratios that are relevant in single slepton production and decay processes.

Chapter 2
Theoretical framework

2.1 The Standard Model

The Standard Model of particle physics (SM) [1–4] is among the best tested theories in physics [5]. It successfully describes all elementary particles which have been found in experiments so far and their strong, weak, and electromagnetic interactions.

The SM is a renormalizable quantum-field theory, based on a non-Abelian gauge group of the inner direct product $SU(3)_C \times SU(2)_L \times U(1)_Y$ and an outer symmetry of the Poincaré group of space-time transformations.

$SU(3)_C$ is the color gauge group of strong interactions based on the theory of QCD. The unified electroweak group $SU(2)_L \times U(1)_Y$ specifies the weak and electromagnetic interaction. Within each group, the generators are hermitian matrices that obey the commutation relations of a Lie algebra. Denoting the generators of the groups $SU(3)_C$, $SU(2)_L$, and $U(1)_Y$ by T^a ($a = 1, \ldots, 8$), I^i ($i = 1, \ldots, 3$), and Y, respectively, the algebraic properties of the generators are given by

$$[T^a, T^b] = i f^{abc} T^c, \qquad [I^i, I^j] = i \epsilon^{ijk} I^k, \qquad [Y, Y] = 0, \tag{2.1}$$

where the real, totally antisymmetric tensors ϵ^{ijk}, f^{abc} are the structure constants of the gauge groups. The quantum numbers corresponding to T^a define the color charge of a particle, those of I^i the weak isospin and Y refers to the weak hypercharge. The latter are defined such that the correct electric charge Q of a particle is recovered by the Gell-Mann–Nishijima relation, $Q = I^3 + Y/2$.

We classify the particles of the SM, which are described by relativistic quantum fields, as matter, gauge, and Higgs boson fields. The constituents of matter are spin-1/2 particles (fermions) which divide into quarks and leptons according to their transformation properties under $SU(3)_C$. While quarks are color-charged $SU(3)_C$ triplets, leptons are color-neutral $SU(3)_C$ singlets and do not interact strongly. We know from experiments that there are six types of leptons and six flavors of quarks which can be grouped into three generations of left-handed and right-handed chiral quarks and leptons. The left-handed fermions transform

as weak isospin doublets, whereas the right-handed ones behave as singlets under $SU(2)_L$ gauge transformations. The complete list of matter fields is[1],

$$\begin{pmatrix} \nu_e \\ e \end{pmatrix}_L, \begin{pmatrix} \nu_\mu \\ \mu \end{pmatrix}_L, \begin{pmatrix} \nu_\tau \\ \tau \end{pmatrix}_L, e_R, \mu_R, \tau_R, \\ \begin{pmatrix} u \\ d \end{pmatrix}_L, \begin{pmatrix} c \\ s \end{pmatrix}_L, \begin{pmatrix} t \\ b \end{pmatrix}_L, u_R, d_R, c_R, s_R, t_R, b_R. \tag{2.2}$$

The gauge boson fields correspond to the generators of the gauge groups. They describe the spin-one bosons that mediate the interactions among the SM particles. Gauge bosons transform under the adjoint representation of the respective gauge group. As a consequence, there exist eight gluons for the $SU(3)_C$ mediating the strong interaction, while in the electroweak sector, there are three gauge bosons for $SU(2)_L$, called W bosons, and one for $U(1)_Y$, the B boson.

The Higgs boson field is required to give masses to the gauge bosons and fermions. If the SM was an exact gauge theory, all gauge bosons would be massless. However this contradicts experimental observations: whereas in the strong sector the gluons do not carry masses, there are massive gauge bosons in the electroweak sector. Explicit mass terms for both bosons and fermions cannot be introduced into the theory without a manifest breakdown of the invariance of the Lagrangian under local $SU(2)_L \times U(1)_Y$ transformations. A solution to the problem is provided by the Higgs mechanism [40], where the masses are generated in a gauge invariant way and where thus the renormalizability of the theory is not spoiled. The idea is to break the $SU(2)_L \times U(1)_Y$ symmetry *spontaneously*, by inserting additional terms into the Lagrangian in such a way that the Lagrangian is kept invariant under $SU(2)_L \times U(1)_Y$ gauge transformations while the ground state is not.

This is achieved by postulating an additional complex scalar field $\Phi = (\phi^+, \phi^0)^T$ which transforms as a $SU(2)_L$ doublet with hypercharge $Y = +1$. From the scalar potential, $V(\Phi) = \mu^2 \Phi^\dagger \Phi + \lambda(\Phi^\dagger \Phi)^2$, the doublet field develops a non-vanishing vacuum expectation value (VEV) for $\mu^2 < 0$, $\langle 0|\Phi|0\rangle = \sqrt{-\mu^2/(2\lambda)} \equiv v/\sqrt{2}$. Expanding Φ around its VEV and inserting it to the Lagrangian, one can see that three of the four degrees of freedom (d.o.f.) of Φ are absorbed by the gauge bosons to form their longitudinal polarizations. As a result, the latter acquire masses. The remaining d.o.f. corresponds to a new scalar particle, the Higgs boson H. Defining the field Φ such that only the lower, electrical neutral component gets a VEV, the $SU(2)_L \times U(1)_Y$ symmetry of the ground state is spontaneously broken but

---

[1]Right-handed neutrinos are usually not included in the SM (but can easily be accommodated) and neutrinos are assumed to be massless. Nowadays there is experimental evidence for non-vanishing neutrino masses from the observation of neutrino oscillations. For reviews on the phenomenology of massive neutrinos and neutrino oscillations, see e.g. [38]. However, finite-mass effects are negligible for the phenomenology at large colliders [39] and neutrino masses are neglected throughout this thesis. Furthermore we assume that neutrinos appear only with their left-handed components, and consequently only left-handed sneutrinos are considered in the SUSY sector.

a $U(1)_Q$ symmetry related to the electrical charge $Q = I^3 + Y/2$ is preserved. The $U(1)_Q$ gauge boson stays massless and can be identified with the photon A_μ. After electroweak symmetry breaking, the $SU(2)_L$ and $U(1)_Y$ gauge bosons do not form mass eigenstates of the theory any longer. The mass eigenstates are linear combinations of the gauge fields W_μ^i and B_μ and obtained by rotations,

$$\begin{pmatrix} Z_\mu \\ A_\mu \end{pmatrix} = \begin{pmatrix} \cos\theta_W & -\sin\theta_W \\ \sin\theta_W & \cos\theta_W \end{pmatrix} \begin{pmatrix} W_\mu^3 \\ B_\mu \end{pmatrix}, \quad W_\mu^\pm = \frac{1}{\sqrt{2}}\left(W_\mu^1 \mp iW_\mu^2\right), \quad (2.3)$$

where θ_W is the weak mixing angle, defined in terms of the $SU(2)_L$ and $U(1)_Y$ gauge couplings g and g', respectively, by $\cos\theta_W = g/\sqrt{g^2 + g'^2}$. The masses of the gauge bosons are proportional to the Higgs VEV v. The charged $W^\pm$ bosons gain masses $m_W = vg/2$ and the mass of the neutral Z boson is $m_Z = (v/2)\sqrt{g^2 + g'^2}$. Expressed by the gauge boson masses, the weak mixing angle reads $\cos\theta_W = m_W/m_Z$.

In analogy to the generation of masses in the gauge sector, the mechanism of spontaneous symmetry breaking also provides the possibility to implement fermion masses in the Lagrangian in a gauge invariant way. Introducing $SU(2)_L \times U(1)_Y$ invariant Yukawa interaction terms that couple the fermions to the Higgs boson (or its charged conjugate of hypercharge $Y = -1$), the fermions gain masses due to the non-zero Higgs VEV. Again, the mass eigenstates are obtained by a rotation of the weak eigenstates. Since we neglect neutrino masses, the mass and gauge eigenstates coincide in the leptonic sector. In the quark sector, the rotation is described by the Cabibbo-Kobayashi-Maskawa (CKM) matrix [41]. Only couplings to charged W bosons are affected by the CKM rotation, interactions mediated by neutral currents do not depend on the quark mixing.

The Higgs boson is the only SM particle which has not been found in experiment so far. Its mass ($m_H = 2\lambda v^2 = -2\mu^2$) is not predicted within the SM and remains as a free parameter of the theory. However there exist theoretical constraints on the Higgs boson mass from the requirement of perturbativity of the SM and positivity and finiteness of the Higgs boson self-coupling λ. A positive coupling λ is needed to ensure that the scalar Higgs potential is bounded from below. Depending on a cutoff scale Λ_C up to which the SM is assumed to be valid, this "stability bound" gives an lower bound on the Higgs boson mass. In order to avoid the Landau pole and to remain with a finite Higgs boson self-coupling, upper bounds on the Higgs boson mass can be derived in turn. As a result, the Higgs boson mass is allowed to be in the following ranges [42],

$$\begin{aligned} 50 \text{ GeV} \lesssim m_H \lesssim 800 \text{ GeV} \qquad &\text{for } \Lambda_C \sim 10^3 \text{ TeV,} \\ 130 \text{ GeV} \lesssim m_H \lesssim 180 \text{ GeV} \qquad &\text{for } \Lambda_C \equiv \Lambda_{\text{GUT}} \sim 10^{16} \text{ TeV,} \end{aligned} \qquad (2.4)$$

yielding a rather strong constraint on the Higgs boson mass if the SM is required to be valid up to the Grand Unification (GUT) scale Λ_{GUT}. Experimentally, direct searches of

the LEP collaborations have set a lower limit on the Higgs mass from the non-observation of the Higgs boson, $m_H > 114.4$ GeV (at the 95% confidence level) [43]. For an extensive review on both theoretical and experimental constraints on the Higgs boson mass we refer the reader to e. g. [44] and references therein.

The SM as a gauge theory involves in general unphysical d.o.f. allowed by gauge invariance. The quantization of the theory requires a fixing of the gauge in order to avoid equivalent field configurations. In the unitary gauge the gauge fixing is such that only physical fields remain in the Lagrangian. This is an appropriate choice to understand the Higgs mechanism (absorption of the would-be Goldstone bosons into the gauge bosons that acquire masses), however it is a non-renormalizable gauge. Higher-order calculations are, therefore, often performed in a gauge of the 't Hooft type (R_ξ gauges). The gauge fixing then yields a cancellation of all bilinear terms in the Lagrangian that involve two different fields. As a consequence, the gauge-boson propagators behave as $\propto 1/k^2$ for large internal loop momenta k and the theory is renormalizable according to power counting [45]. In the path-integral formalism the integral measure is changed by the Fadeev–Popov determinant, which can be expressed in terms of scalar, anticommuting fields. These "Fadeev–Popov ghost fields" compensate the unphysical d.o.f. introduced by the gauge fixing. In the 't Hooft–Feynman gauge ($\xi = 1$), the Goldstone bosons and ghosts have equal masses to those of the corresponding physical gauge bosons.

We conclude that the SM is a consistent quantum-field theory. It is renormalizable and free of anomalies [46][2]. Therefore, it allows to calculate unique quantum corrections. With a given finite set of input parameters, measurable quantities can be predicted order by order in perturbation theory.

Open questions of the Standard Model

A comparison of the theoretical predictions with experimental data confirms the validity of the SM in a convincing way: All observed particles and interactions can be described at a very high accuracy [5], with small deviations which might be considered as normal [48]. Also quantum effects as predicted from the perturbative expansion of the SM are well established.

Despite of its success, the SM suffers from a list of conceptual problems which point towards some new physics beyond the SM. It is widely believed that the SM is an effective theory, valid only in the low-energy limit of a more fundamental theory that describes physics at arbitrarily high energies.

One of the strongest arguments against the SM as the ultimate theory is the fact that

---

[2]In principle, there are chiral or Adler-Bardeen-Jackiw anomalies [47] in the SM, which originate from triangular fermionic loops involving axial-vector current couplings and which thus spoil its renormalizability. However, these anomalies cancel as the sum of the (hyper-)charges of all fermions within one generation is zero.

it does not include gravitational interactions. The latter become important at energies comparable to the Planck scale $\Lambda_{\text{Planck}} \sim 10^{18}$ GeV, and if the SM was valid up to Λ_{Planck} it had to incorporate gravity in some way. In turn, if physics up to such high scales can be described within the SM, the hierarchy problem has to be addressed. It refers to the astonishing smallness of the electroweak scale compared to the Planck scale, $m_W/\Lambda_{\text{Planck}} \sim 10^{-16}$, which cannot be explained satisfactorily in the SM.

A related problem arises when taking into account radiative corrections to the Higgs boson mass. From the electroweak symmetry breaking, we naturally expect the Higgs boson mass to be of the order of the weak scale (cf. Eq. (2.4)). However fermions, massive gauge bosons, and the Higgs boson itself give direct and indirect loop contributions to the Higgs boson self-energy and the (bare) Higgs boson mass squared gets huge corrections, $m_H^2 = (m_H^0)^2 + \Delta m_H^2$. The corrections Δm_H^2 can be regularized by introducing an UV momentum cutoff Λ_{UV} (see Section 4.1 for details about regularization and renormalization), yielding

$$\Delta m_H^2 = \Lambda_{UV}^2 \sum_{n=0}^{\infty} c_n \log^n \left(\frac{\Lambda_{UV}}{\mu_R} \right), \tag{2.5}$$

where μ_R is the renormalization scale. The coefficients c_n are functions of the masses of the particles running in the loops and of their couplings to the Higgs boson[3]. In contrast to the logarithmically divergent self-energy contributions to fermions and gauge bosons, the Higgs boson mass corrections depend quadratically on the cutoff scale Λ_{UV}. This scale can be identified as the scale up to which the SM is valid and where new physics enters. Naively, one would expect from Eq. (2.5) a Higgs boson mass of the order of the cutoff scale Λ_{UV}. If Λ_{UV} is very large, for instance of the order of the GUT or the Planck scale, one needs a very fine arrangement between the bare Higgs boson mass m_H^0 and the corrections Δm_H at each order in perturbation theory to obtain a physical Higgs boson mass m_H around the EW scale. A small Higgs boson mass thus seems to be unnatural. It is because of this situation, that this problem is often referred to as fine-tuning or naturalness problem.

The behavior of the SM gauge couplings gives another hint to the limited validity of the model. Being based on the direct product of $SU(3)_C \times SU(2)_L \times U(1)_Y$, the three gauge couplings are different and the electroweak and strong interactions are not truly unified within the SM. Therefore, one might postulate the existence of a more fundamental theory (a Grand Unified Theory, GUT) in which the SM gauge group is a subgroup of a simple gauge group such as e. g. $SU(5)$ [49] or $SO(10)$ [50], with just one coupling constant. The scale-dependent evolution of the SM gauge couplings is determined by the renormalization group equations. In order to embed the SM into a GUT, it is necessary that the running

---

[3]The leading coefficient c_0, neglecting all fermion masses except for the top-quark mass m_t, reads $(16\pi^2)c_0 = 3/(2v^2) \times (m_H^2 + 2m_W^2 + m_Z^2 - 4m_t^2)^2$. Higher-order coefficients c_n are suppressed by factors of $1/(16\pi^2)$ and can be evaluated from the requirement that the renormalized Higgs boson mass does not depend on μ_R [44].

of the gauge couplings is such that the couplings meet at a common point, the GUT scale. However this is not the case with the given particle content of the SM. Assuming new physics entering at some intermediate scale, the renormalization group equations are altered and a unification of the gauge couplings can become possible at a high scale.

A further argument in favor of physics beyond the SM is given by cosmological observations. Measurements of the rotation velocities of galaxies and precision measurements of the cosmic microwave background [11] revealed that our universe consists to a large extent of "dark matter", i.e. of non-baryonic, non-luminous and only weakly interacting matter. The only particles provided in the SM which fulfill these requirements are the neutrinos. However current upper limits on their masses [5] imply that they only make a small contribution to the required density of dark matter. Moreover, since neutrinos move with relativistic velocities ("hot dark matter"), they cannot explain structure formation on small scales. And in its strict version, the SM does not even include non-zero neutrino masses.

Lastly, the large number of free parameters which have to be taken from experiments can also be seen as a weakness of the SM. An underlying theory with a reduced number of free parameters seems to be desirable. The problem of unpredicted parameters relates to open questions about the origin of particle masses, about the hierarchical structure of fermion masses, and about the origin of CP violation.

A large variety of models has been proposed to solve the described problems. In this thesis, we focus on supersymmetric theories which are often considered the most attractive extension of the SM. It is the aim of the next chapter to introduce the concept of supersymmetry and to discuss how some of the previously mentioned open issues are addressed.

2.2 Supersymmetry

In this section we briefly review some fundamental concepts of supersymmetry, based on Refs. [51,52]. We start in Section 2.2.1 with an introduction of the basic ideas and the motivation for a phenomenologically viable supersymmetric model. More formal aspects of the theory are discussed in Section 2.2.2; in particular we define a Lagrangian which is invariant under supersymmetric transformations.

2.2.1 Basic ideas and motivation

The original intention for supersymmetry was to build a nontrivial extension of the SM.

The SM provides internal symmetries based on the $SU(3)_C \times SU(2)_L \times U(1)_Y$ gauge group (see last section) and it is invariant under space-time symmetries described by the Poincaré group, i.e. Lorentz boost and rotations and space-time translations in Minkowski space. The group generators of the Poincaré and the internal symmetries commute with each other. Accordingly, a particle state is defined by the eigenvalues of a maximal set of

commuting space-time observables (mass, spin, momentum) and internal quantum numbers (color, weak isospin, hypercharge, ...). Indeed it has been shown that any group combining an internal symmetry group with the Poincaré group can only be a direct product with commuting operators [53].

In four dimensions, the only way to circumvent this *no-go theorem* and to extend the Poincaré group in a nontrivial way is to abandon the idea that the group generators of the additional symmetry obey the commutator structure of an internal symmetry (cf. Eq. (2.1)), and to postulate anticommutation relations instead [54]. The group generators of such a *supersymmetry* (SUSY) thus have to be fermionic operators [6,7]. The resulting supersymmetric Poincaré algebra for a SUSY generator Q_α and its conjugate $\overline{Q}_{\dot\beta}$ is given by

$$
\begin{aligned}
\{Q_\alpha, Q_\beta\} &= \{\overline{Q}_{\dot\alpha}, \overline{Q}_{\dot\beta}\} = 0, \\
\{Q_\alpha, \overline{Q}_{\dot\beta}\} &= 2(\sigma^\mu)_{\alpha\dot\beta}\, P_\mu,
\end{aligned}
\tag{2.6a}
$$

together with

$$
\begin{aligned}
[Q_\alpha, P_\mu] &= [\overline{Q}_{\dot\alpha}, P_\mu] = 0, \\
[Q_\alpha, M_{\mu\nu}] &= -\frac{1}{2}(\sigma_{\mu\nu})_\alpha^{\ \beta}\, Q_\beta, \\
[\overline{Q}_{\dot\alpha}, M_{\mu\nu}] &= -\frac{1}{2}(\overline{\sigma}_{\mu\nu})_{\dot\alpha}^{\ \dot\beta}\, \overline{Q}_{\dot\beta},
\end{aligned}
\tag{2.6b}
$$

while Q_α and $\overline{Q}_{\dot\alpha}$ commute with the generators of the gauge group $SU(3)_C \times SU(2)_L \times U(1)_Y$.

The SUSY generators are two-component Weyl spinors with distinct indices $\alpha, \beta = 1, 2$, and $\dot\alpha, \dot\beta = 1, 2$ (see Appendix A.3 for the notations). The elements of the Pauli matrices act as structure functions in terms of the quantities σ^μ and $\sigma^{\mu\nu}$, defined in Eq. (A.19) and Eq. (A.20). P_μ and $M_{\mu\nu}$ are the generators for space-time translations and Lorentz transformations, respectively.

The second line of Eq. (2.6a) illustrates the entanglement of SUSY and space-time symmetry, a (global) SUSY transformation inducing a (constant) translation in Minkowski space. This equation thus gives a hint on how to embed gravitational interactions into the theory. Since general relativity is invariant under local Poincaré transformations, a *local* SUSY can, in general, include general relativity and therefore gravity [55]. In this work however, we restrict the discussion to global SUSY transformations, only.

In the application of supersymmetry to particle physics, the main effect of a SUSY transformation is to relate bosonic and fermionic fields. Since a SUSY operator Q_α is an fermionic object, it changes the spin of a particle and transforms bosons into fermions and vice-versa,

$$
Q_\alpha|\text{boson}\rangle = |\text{fermion}\rangle, \quad Q_\alpha|\text{fermion}\rangle = |\text{boson}\rangle.
\tag{2.7}
$$

Fields related by Eq. (2.7) form a supermultiplet. It is important to notice that a SUSY transformation only affects the spin, whereas all internal quantum numbers of the particles in the same supermultiplet remain unchanged. Within the SM, there are no such particles which are identical except for their spin. The postulation of a supersymmetry Eq. (2.7) is thus directly related to the assumption of new particles.

In principle, it is possible to consider a system of N supersymmetries generated by N distinct SUSY operators Q_α^N. However the introduction of $N > 1$ operators leads to conceptional problems: in a four-dimensional field theory, extended supersymmetries cannot allow for chiral fermions and parity violation to the observed amount [56].

As one can easily derive from the first line of Eq. (2.6b), particles and their SUSY partners would be mass degenerate if supersymmetry was an exact theory[4]. However, no SUSY particle has been observed so far thus supersymmetry needs to be broken at low energies if it is realized in nature.

In this work, we focus on phenomenologically viable SUSY models, i. e. on models that are based on a minimal $N = 1$ SUSY algebra and that include the breaking of SUSY at some lower scale. The SUSY generator Q_α assigns exactly one bosonic state to a fermionic one, both having the same gauge quantum numbers. As a consequence, the particle content of the SM is basically doubled. However, since left- and right-handed SM fermions behave differently under gauge transformations, two distinct bosonic states are introduced as SUSY partners. Furthermore, as we will see later, a second Higgs boson doublet needs to be defined. We will give more details on the physical fields of the minimal supersymmetric extension of the SM (MSSM) in Section 2.3.

The energy scale at which SUSY is broken is not constrained by the theory and the SUSY particles might get high masses. However a relatively low SUSY breaking scale is very attractive from the phenomenological point of view, in particular if new particles around the TeV scale are predicted.

As we discussed in the previous section, the lightness of the Higgs boson compared to scales like Λ_{GUT} or $\Lambda_{\mathrm{Planck}}$ seems unnatural within the SM and requires extreme finetuning of parameters. Radiative corrections to the Higgs boson mass are quadratically divergent and induce contributions of the order of a upper cutoff scale squared, which is typically understood as the scale up to which the SM is valid. In supersymmetric theories, however, the Higgs boson mass is prevented from acquiring large radiative corrections. Since fermion and boson loops appear with opposite signs, the quadratic divergencies ($\propto \Lambda_{UV}^2$) cancel in the sum of SM and SUSY contributions [8]. An exact cancellation is obtained in unbroken supersymmetries only, where the particles within one supermultiplet have equal masses ($m_F = m_B$) and where the fermionic and bosonic dimensionless couplings to the Higgs boson, λ_F and λ_B, respectively, are related. If the mass degeneracy of SM and SUSY

---

[4]The mass degeneracy of a fermion f of mass m and its bosonic partner b follows from Eq. (2.6b) and the on-shell relation for f, $P^2|f\rangle = m^2|f\rangle$, yielding $P^2|b\rangle = P^2Q|f\rangle = QP^2|f\rangle = Qm^2|f\rangle = m^2|b\rangle$.

partners is lifted by SUSY breaking, logarithmic divergent terms ($\propto (m_F^2 - m_B^2) \log \Lambda_{UV}$) proportional to the mass difference $m_F^2 - m_B^2$ remain. In order to provide a solution to the fine-tuning problem and to keep the Higgs boson mass in the range of the electroweak symmetry breaking scale, we have to assume that the SUSY particle masses are not too heavy ($\sim \mathcal{O}(1 \text{ TeV})$) since otherwise the large logarithmic corrections would reintroduce the problem in the theory[5].

Another argument in favor of supersymmetry at an energy scale reachable by today and future collider experiments, is the unification of the three gauge couplings which is not possible within the SM. The new SUSY particle spectrum contributes to the renormalization group evolution of the gauge coupling constants. Assuming the SUSY particles to enter around the TeV scale, the running of the couplings is changed in such a way the couplings meet at a high scale (Λ_{GUT}) [9].

In addition, low-energy supersymmetric models with $\mathcal{R}$-parity conservation provide a suitable candidate for the dark matter in our universe (see Section 2.3.2).

2.2.2 Theoretical concepts of supersymmetry

In order to properly describe SUSY transformations and to build a Lagrangian which is invariant under SUSY transformations, it is convenient to first introduce the concept of superspace and superfields.

This section is meant to be rather independent on the physical application of super-symmetry to the SM, and therefore the implementation of the minimal supersymmetric extension of the SM is postponed to Section 2.3.

Superspace and superfields

The superspace extends the four-dimensional space-time by two Grassmann dimensions θ^α, $\overline{\theta}_{\dot{\alpha}}$. Grassmann numbers are anticommuting fermionic objects, i.e. (see Appendix A.5)

$$\{\theta_\alpha, \theta_\beta\} = \{\overline{\theta}_{\dot{\alpha}}, \overline{\theta}_{\dot{\beta}}\} = \{\theta_\alpha, \overline{\theta}_{\dot{\beta}}\} = 0. \tag{2.8}$$

Every physical point in the superspace has the same number of bosonic and fermionic degrees of freedom and is defined by a supercoordinate $X = (x^\mu, \theta^\alpha, \overline{\theta}_{\dot{\alpha}})$, where x^μ is a (bosonic) Minkowski coordinate.

Superfields are single objects containing the fermionic and bosonic fields of a supermultiplet and thus allow for a convenient formulation of the Lagrangian. A superfield Φ is

---

[5]A further constraint on the SUSY breaking can be derived from the motivation that SUSY cures the hierarchy problem: The quadratic divergencies enter proportional to the difference ($|\lambda_F|^2 - \lambda_B$). Only if the dimensionless couplings ($|\lambda_F|^2 = \lambda_B$) are unaffected by the SUSY breaking, the dangerous Λ_{UV}^2-divergencies do cancel. One therefore considers *soft* SUSY breaking, where SUSY breaking terms with positive mass dimension only are added by hand to the effective Lagrangian, thus leaving the original Lagrangian, providing the gauge and Yukawa interactions, invariant under SUSY transformations.

defined on the superspace, $\Phi = \Phi(x, \theta, \overline{\theta})$. Owing to the anticommuting nature of Grassmann numbers, products of more than two Grassmann numbers vanish and a superfield can be expanded as a finite power series in $\theta, \overline{\theta}$. The most general form of a superfield in terms of its component fields reads

$$
\begin{aligned}
\Phi(x, \theta, \overline{\theta}) = {} & \phi(x) + \theta \psi(x) + \overline{\theta} \overline{\chi}(x) + \theta\theta F(x) + \overline{\theta}\,\overline{\theta} H(x) \\
& + \theta \sigma^\mu \overline{\theta} A_\mu(x) + (\theta\theta) \overline{\theta}\,\overline{\lambda}(x) + (\overline{\theta}\,\overline{\theta})\,\theta \xi(x) + (\theta\theta)(\overline{\theta}\,\overline{\theta}) D(x),
\end{aligned}
\tag{2.9}
$$

where ϕ, F, H, D are complex scalar fields, A_μ is a complex vector field, and $\psi, \overline{\chi}, \overline{\lambda}, \xi$ are two-component Weyl spinor fields. Counting the d.o.f., there are 16 bosonic and 16 fermionic d.o.f. for a general superfield, which are too many for a SUSY with particles with spin ≤ 1. Irreducible representations are obtained by imposing covariant (i. e. SUSY invariant) constraints on a general superfield to remove the redundant component fields.

To find the covariant derivative, we make use of the fact that the (fermionic) Grassmann numbers allow to define the SUSY algebra Eq. (2.6) in terms of commutators only,

$$
\begin{aligned}
[\theta Q, \theta Q] = [\overline{\theta}\,\overline{Q}, \overline{\theta}\,\overline{Q}] &= 0, \\
[\theta Q, \overline{\theta}\,\overline{Q}] &= 2\theta\sigma^\mu \overline{\theta} P_\mu, \\
[\theta Q, P_\mu] = [\overline{\theta}\,\overline{Q}, P_\mu] &= 0.
\end{aligned}
\tag{2.10}
$$

A general finite SUSY transformation can then be parameterized in analogy to a non-Abelian gauge transformation based on a Lie algebra with anticommuting generators. We thus define the group element of a global SUSY transformation as

$$
S(y_\mu, \xi^\alpha, \overline{\xi}_{\dot\alpha}) = e^{-i(\xi^\alpha Q_\alpha + \overline{\xi}_{\dot\alpha} \overline{Q}^{\dot\alpha} + y_\mu P^\mu)},
\tag{2.11}
$$

where $\xi, \overline{\xi}$ are again Grassmann variables. This yields the following transformation rule for a superfield $\Phi(x, \theta, \overline{\theta})$ if $S(y_\mu, \xi, \overline{\xi})$ is applied[6],

$$
S(y_\mu, \xi, \overline{\xi})\, \Phi(x_\mu, \theta, \overline{\theta}) = \Phi(x_\mu + y_\mu + i\xi\sigma\overline{\theta} - i\theta\sigma\overline{\xi},\ \xi + \theta,\ \overline{\xi} + \overline{\theta}),
\tag{2.12}
$$

where repeated spinor indices have been dropped (according to Eqs. (A.17) and (A.18)). Taylor expanding the above result, we find that an infinitesimal SUSY transformation $\delta_S(\xi, \overline{\xi})$ acts on a superfield as

$$
\begin{aligned}
\delta_S(\xi, \overline{\xi})\, \Phi(x, \theta, \overline{\theta}) &= -i \left[\xi Q + \overline{\xi}\,\overline{Q} \right]\, \Phi(x, \theta, \overline{\theta}) \\
&= \left[\xi^\alpha \frac{\partial}{\partial \theta^\alpha} + \overline{\xi}_{\dot\alpha} \frac{\partial}{\partial \overline{\theta}_{\dot\alpha}} + i(\xi \sigma_\mu \overline{\theta} - \theta \sigma_\mu \overline{\xi}) \frac{\partial}{\partial x_\mu} \right] \Phi(x, \theta, \overline{\theta}),
\end{aligned}
\tag{2.13}
$$

---

[6]following from the evaluation of two successive SUSY transformations with the help of the Baker-Campbell-Hausdorff formula $e^A e^B = e^{A+B+\frac{1}{2}[A,B]}$ for $[A,[A,B]] = 0$ and the commutator relations Eq. (2.10).

so that a linear representation of the SUSY generators is given by

$$
\begin{aligned}
Q_\alpha &= i\partial_\alpha - (\sigma^\mu\overline{\theta})_\alpha\,\partial_\mu, \\
\overline{Q}_{\dot\alpha} &= -i\overline{\partial}_{\dot\alpha} + (\theta\sigma^\mu)_{\dot\alpha}\,\partial_\mu, \\
P_\mu &= i\partial_\mu,
\end{aligned}
\tag{2.14a}
$$

with the abbreviations $\partial_\alpha = \partial/\partial\theta^\alpha$, $\overline{\partial}_{\dot\alpha} = \partial/\partial\overline{\theta}^{\dot\alpha} = -\epsilon_{\dot\alpha\dot\beta}\,\partial/\partial\overline{\theta}_{\dot\beta}$, $\partial_\mu = \partial/\partial x^\mu$. In analogy to the covariant derivative in gauge theories we can now define covariant derivatives $D_\alpha, \overline{D}_{\dot\alpha}$ with respect to the SUSY generators $Q_\alpha, \overline{Q}_{\dot\alpha}$. The SUSY covariant derivatives have to be invariant under SUSY transformations δ_S, i. e. $[\xi Q + \overline{\xi}\,\overline{Q}, D_\alpha] = 0$, which is equivalent to imposing the following anticommutator relations,

$$
\{D_\alpha, Q_\beta\} = \{D_\alpha, \overline{Q}_{\dot\beta}\} = \{\overline{D}_{\dot\alpha}, Q_\beta\} = \{\overline{D}_{\dot\alpha}, \overline{Q}_{\dot\beta}\} = 0.
\tag{2.15}
$$

One finds for the SUSY covariant derivatives $D_\alpha, \overline{D}_{\dot\alpha}$,

$$
\begin{aligned}
D_\alpha &= i\partial_\alpha + (\sigma^\mu\overline{\theta})_\alpha\,\partial_\mu, \\
\overline{D}_{\dot\alpha} &= -i\overline{\partial}_{\dot\alpha} - (\theta\sigma^\mu)_{\dot\alpha}\,\partial_\mu,
\end{aligned}
\tag{2.16}
$$

obeying the nontrivial commutator relation $\{D_\alpha, \overline{D}_{\dot\beta}\} = -2(\sigma^\mu)_{\alpha\dot\beta}\,P_\mu$.

With the help of the SUSY covariant derivatives Eq. (2.16) it is now possible to find irreducible representations of a general superfield Φ. One defines

$$
\overline{D}_{\dot\alpha}\Phi = 0 \qquad \Rightarrow \quad \text{(left-handed) chiral superfield,} \tag{2.17a}
$$

$$
D_\alpha\Phi = 0 \qquad \Rightarrow \quad \text{(right-handed) anti-chiral superfield,} \tag{2.17b}
$$

$$
\Phi = \Phi^\dagger \qquad \Rightarrow \quad \text{vector superfield.} \tag{2.17c}
$$

It is interesting to notice that the product of two chiral fields is still a chiral field, whereas the combination of a chiral field and its conjugate is a vector superfield.

Imposing the condition Eq. (2.17a) on the general superfield Φ, cf. Eq. (2.9), a left-handed chiral superfield Φ_L expands to its component fields as follows,

$$
\begin{aligned}
\Phi_L(x,\theta,\overline{\theta}) = {} & \phi(x) + \sqrt{2}\theta\,\psi(x) + \theta\theta\,F(x) \\
& + i\theta\sigma^\mu\overline{\theta}\,\partial_\mu\phi(x) - i\frac{1}{\sqrt{2}}\,(\theta\theta)\left(\partial_\mu\psi(x)\,\sigma^\mu\overline{\theta}\right) - \frac{1}{4}(\theta\theta)(\overline{\theta}\,\overline{\theta})\,\partial^\mu\partial_\mu\phi(x),
\end{aligned}
\tag{2.18}
$$

where the $\overline{\theta}$-component fields do not enter. $\psi(x)$ is a two-component complex Weyl spinor (4 d.o.f. in general), $\phi(x)$ is a complex scalar field (2 d.o.f.). They describe a left-handed chiral fermion and its scalar SUSY partner within one supermultiplet. The equality of fermionic and bosonic d.o.f. is guaranteed by the complex scalar field $F(x)$ (2 d.o.f.). F is

an auxiliary field which is needed to close the SUSY algebra off-shell. For on-shell fields, the d.o.f. of the spinor field ψ reduce by two. Correspondingly, the auxiliary field F has trivial equations of motion ($F = F^* = 0$) and can be eliminated by going on-shell. The representation of a right-handed field Φ_R is obtained in complete analogy by imposing $\Phi_R = \overline{\Phi_L} = (\Phi_L)^\dagger$. The behavior of the component fields under an infinitesimal SUSY transformation $\delta_S(\xi, \overline{\xi})$, Eq. (2.13), is given by

$$
\begin{aligned}
\delta_S(\xi, \overline{\xi})\ \phi(x) &= \sqrt{2}\xi\,\psi(x), \\
\delta_S(\xi, \overline{\xi})\ \psi_\alpha(x) &= \sqrt{2}F(x)\,\xi_\alpha - \sqrt{2}\left(\sigma^\mu \overline{\xi}\right)_\alpha \partial_\mu \phi(x), \\
\delta_S(\xi, \overline{\xi})\ F(x) &= \partial_\mu\left(i\sqrt{2}\,\psi(x)\,\sigma^\mu \overline{\xi}\right).
\end{aligned}
\tag{2.19}
$$

Eq. (2.19) shows explicitly that under a SUSY transformation a bosonic state is transformed into a fermionic one and vice-versa, whereas the change induced in the auxiliary function is a total derivative. Under a non-Abelian SUSY gauge transformation (with generators T^a and coupling g), a chiral superfield and its conjugate transform as

$$
\Phi_L \to e^{-i2g\Lambda}\Phi_L, \quad \text{and} \quad \overline{\Phi_L} \to \overline{\Phi_L}e^{i2g\Lambda},
\tag{2.20}
$$

where $\Lambda(x, \theta, \overline{\theta})$ is a chiral superfield and $\Lambda = \Lambda^a T^a$.

A vector superfield $V(x, \theta, \overline{\theta})$ can be constructed from Eq. (2.9) by imposing $V = V^\dagger$, cf. Eq. (2.17c). In terms of real scalar fields C, M, N, D, two complex Weyl spinors χ, λ and a real spin-one vector field A_μ, it is

$$
\begin{aligned}
V(x, \theta, \overline{\theta}) = {}& C(x) + i\theta\chi(x) - i\overline{\theta}\,\overline{\chi}(x) + \theta\sigma^\mu\overline{\theta}\,A_\mu(x) \\
& + \frac{i}{2}\theta\theta\big[M(x) + iN(x)\big] - \frac{i}{2}(\overline{\theta}\,\overline{\theta})\big[M(x) - iN(x)\big] \\
& + i(\theta\theta)\overline{\theta}\left[\overline{\lambda}(x) + \frac{i}{2}\overline{\sigma}^\mu\partial_\mu\chi(x)\right] - i(\overline{\theta}\,\overline{\theta})\theta\left[\lambda(x) + \frac{i}{2}\sigma^\mu\partial_\mu\overline{\chi}(x)\right] \\
& + \frac{1}{2}(\theta\theta)(\overline{\theta}\,\overline{\theta})\left[D(x) - \frac{1}{2}\partial^\mu\partial_\mu C(x)\right].
\end{aligned}
\tag{2.21}
$$

A general vector superfield has 8 bosonic and 8 fermionic d.o.f.. Unphysical components can be removed by choosing an appropriate gauge. Under a non-Abelian SUSY gauge transformation, the vector superfield transforms as

$$
e^{2gV} \to e^{-i2g\overline{\Lambda}}\,e^{2gV}\,e^{i2g\Lambda},
\tag{2.22}
$$

where $V = V^a T^a$. In the Abelian case, Eq. (2.22) simplifies to

$$
V \to V + i(\Lambda - \overline{\Lambda}).
\tag{2.23}
$$

Accordingly, one can choose the Wess-Zumino gauge [7] where $C = M = N = 0$ and $\chi = 0$. The remaining component fields of the vector superfield are the gauge field A_μ, its fermionic superpartner λ (called *gaugino*), and also a bosonic auxiliary field D. In complete analogy to the case of chiral superfields, the auxiliary field is needed in order for SUSY to be consistent off-shell and can be eliminated on-shell using its equation of motion. Furthermore, it transforms under SUSY transformations into a total derivative,

$$\delta_S(\xi, \overline{\xi}) \, D = \partial_\mu\Big(-\xi\sigma^\mu\overline{\lambda} + \lambda\,\sigma^\mu\overline{\xi}\Big). \tag{2.24}$$

One can also easily show that the vector field A^μ and the spinor λ_α are related by a SUSY transformation,

$$\delta_S(\xi, \overline{\xi}) \, A^\mu = i\big(\xi\sigma^\mu\overline{\lambda} - \lambda\,\sigma^\mu\overline{\xi}\big) - \partial^\mu\big(\xi\chi + \overline{\xi}\,\overline{\chi}\big),$$
$$\delta_S(\xi, \overline{\xi}) \, \lambda_\alpha = -iD\xi_\alpha - \frac{1}{2}\,(\sigma^\mu\overline{\sigma}^\nu)_\alpha^{\ \beta}\,\xi_\beta\,(\partial_\mu A_\nu - \partial_\nu A_\mu). \tag{2.25}$$

The SUSY Lagrangian

The aim of this section is to construct a Lagrangian density $\mathcal{L}$ which is invariant under SUSY and gauge transformations, referred to as SUSY Lagrangian in the following.

$\mathcal{L}$ is obtained from the requirement that the action $\int d^4x\,\mathcal{L}(x)$ needs to be invariant under SUSY transformations,

$$\delta_S \int d^4x\,\mathcal{L}(x) = 0. \tag{2.26}$$

To ensure the invariance of the action, it is sufficient to impose that $\mathcal{L}$ changes by a total space-time derivative. As we know from the previous section, the F-terms of chiral superfields and D-terms of vector superfields both transform into a total derivative under a SUSY transformation and are thus appropriate objects to define the SUSY Lagrangian. One schematically writes

$$\mathcal{L}(x) \equiv \mathcal{L}_F + \mathcal{L}_D = \int d^2\theta\mathcal{L}_f + \int d^2\theta\,d^2\overline{\theta}\,\mathcal{L}_d + h.c., \tag{2.27}$$

where $h.c.$ refers to the hermitian conjugated terms.

Let $\mathcal{L}_f$ be an analytic function of chiral superfields (remember that the product of two chiral superfields is a chiral superfield, whereas a product of a superfield and its conjugate yields a vector superfield). Owing to the behavior of Grassmann numbers under integration, cf. Appendix A.5, $\mathcal{L}_F$ only contains the F-component fields. In order to not spoil the renormalizability of the theory, only terms up to mass dimension four are allowed in $\mathcal{L}_f$.

By convention, $\mathcal{L}_f$ is given in terms of the (gauge invariant) superpotential $\mathcal{W}$,

$$\mathcal{W}(\{\Phi_i\}) = \sum_i a_i \Phi_i + \frac{1}{2} \sum_{ij} m_{ij} \, \Phi_i \Phi_j + \frac{1}{3!} \sum_{ijk} \lambda_{ijk} \, \Phi_i \Phi_j \Phi_k, \qquad (2.28)$$

where all Φ_i are left-chiral superfields, and the couplings m_{ij}, λ_{ijk} are totally symmetric matrices under the interchange of i, j, k. In component fields ϕ_i, ψ_i and F_i, the F-component of the superpotential $\mathcal{W}$ reads

$$
\begin{aligned}
\int d^2\theta \, \mathcal{W}(\{\Phi_i\}) &= \sum_i a_i F_i + \sum_{ij} m_{ij} \Big(\phi_i F_j - \frac{1}{2} \psi_i \psi_j \Big) + \sum_{ijk} \frac{\lambda_{ijk}}{2} \Big(\phi_i \phi_j F_k - \phi_i \psi_j \psi_k \Big) \\
&= \sum_j \frac{\partial \mathcal{W}(\phi)}{\partial \phi_j} F_j - \frac{1}{2} \sum_{jk} \frac{\partial^2 \mathcal{W}(\phi)}{\partial \phi_j \partial \phi_k} \, \psi_j \psi_k,
\end{aligned}
$$
$$(2.29)$$

where in the last line the superpotential is understood to be a function of scalar fields ϕ_i, $\mathcal{W} \equiv \mathcal{W}(\phi)$. Eq. (2.29) provides fermion mass terms and Yukawa-type interactions for the scalars and fermions in the theory.

Kinetic terms for scalars and fermions ($\propto \overline{\Phi}\Phi$) can only be given by the D-term contributions from vector superfields. The gauge invariance of the SUSY Lagrangian with respect to a non-Abelian gauge group with generators T^a, is guaranteed by defining

$$\mathcal{L}_d = \overline{\Phi} e^{2gV} \Phi, \qquad (2.30)$$

cf. Eq. (2.20) and Eq. (2.22), and by replacing the usual derivative ∂_μ by the gauge covariant derivative D_μ,

$$\partial_\mu \rightarrow D_\mu = \partial_\mu + ig A_\mu^a T^a, \qquad (2.31)$$

where A_μ is the vector component in the general vector superfield Eq. (2.21). The $\mathcal{L}_D$-part of the Lagrangian then also generates interaction terms of the scalars and fermions with the gauge boson fields and "SUSY-gauge interactions" involving gauginos. In component fields, it reads

$$
\begin{aligned}
\mathcal{L}_D &= \sum_i \int d^2\theta \, d^2\overline{\theta} \; \overline{\Phi}_i e^{2gV} \Phi_i \\
&= \sum_i \Big[D_\mu \phi_i \, D^\mu \phi_i^* + i \overline{\psi}_i \overline{\sigma}^\mu D_\mu \psi_i - \sqrt{2} g \Big(\overline{\psi}_i \overline{\lambda} \phi_i + \phi_i^* \lambda \psi_i \Big) + g \phi_i^* D \phi_i + F_i^* F_i \Big].
\end{aligned}
$$
$$(2.32)$$

Both $\mathcal{L}_D$ and the superpotential, however, do not provide kinetic terms for either gauge bosons or gauginos. Also, gauge-boson–gaugino-couplings are allowed by gauge invariance

and not described yet. We include these terms by inserting an additional contribution $\mathcal{L}_{\text{kin}}$ in the Lagrangian,

$$\mathcal{L}_{\text{kin}} = \frac{1}{16g^2} \text{Tr}(W_\alpha W^\alpha), \tag{2.33}$$

with W_α being field strength tensors,

$$W_\alpha = \frac{1}{4} \overline{D}\,\overline{D}\, e^{-2gV} D_\alpha\, e^{2gV}, \tag{2.34}$$

in terms of the SUSY covariant derivatives D_α and $\overline{D}_{\dot\alpha}$ given in Eq. (2.16). For Abelian gauge groups, Eq. (2.34) reduces to

$$W_\alpha = \frac{g}{2} \overline{D}\,\overline{D}\, D_\alpha\, V. \tag{2.35}$$

Since W_α is chiral (i.e. $\overline{D}_{\dot\beta} W_\alpha = 0$), also $W_\alpha W^\alpha$ is chiral. It is easy to show that $W_\alpha W^\alpha$ is also gauge invariant. The $\theta\theta$-components of $\mathcal{L}_{\text{kin}}$ then transform as a total derivative under SUSY transformations and can be used for the F-term of the SUSY Lagrangian,

$$\frac{1}{16g^2} \int d^2\theta \left[\text{Tr}(W_\alpha W^\alpha) + h.c. \right] = -\frac{1}{4} F^a_{\mu\nu} F^{\mu\nu a} + i \overline{\lambda}^a \overline{\sigma}^\mu (D_\mu \lambda)^a + \frac{1}{2} D^a D^a, \tag{2.36}$$

with the field-strength tensors

$$F^a_{\mu\nu} = \partial_\mu A^a_\nu - \partial_\nu A^a_\mu + f^{abc} A^b_\mu A^c_\nu, \tag{2.37}$$

and f^{abc} are the group structure constants.

To summarize, the final F-term reads

$$\begin{aligned}
\mathcal{L}_F &= \int d^2\theta\, \mathcal{L}_f + h.c. \\
&= \int d^2\theta \left[\mathcal{W} + \overline{\mathcal{W}} \right] + \frac{1}{16g^2} \int d^2\theta \left[\text{Tr}(W_\alpha W^\alpha) + h.c. \right],
\end{aligned} \tag{2.38}$$

and the complete SUSY Lagrangian is given by $\mathcal{L}(x) = \mathcal{L}_F + \mathcal{L}_D$, with $\mathcal{L}_F$ of Eq. (2.38) and $\mathcal{L}_D$ referring to Eq. (2.32).

By expanding the SUSY Lagrangian in component fields, one finds that, as anticipated above, the auxiliary fields $F(x)$ and $D(x)$ do not obtain a kinetic energy term. Instead, one can combine them into the scalar potential $\mathcal{V}$ (having $\mathcal{L} = \mathcal{T} - \mathcal{V}$ in mind), defined as

$$\mathcal{V} = \sum_i \left(-F_i^* F_i - \frac{\partial \mathcal{W}(\phi)}{\partial \phi_i} F_i - \frac{\partial \overline{\mathcal{W}}(\phi^*)}{\partial \phi_i^*} F_i^* \right) + \frac{1}{2} \sum_a D^a D^a, \tag{2.39}$$

where F_i is the F-component of the superfield Φ_i and D^a is the D-component of the vector superfield $V = V^a T^a$. Since the Euler-Lagrange equations for the auxiliary fields yield

$$\frac{\partial \mathcal{L}(x)}{\partial F(x)} = \frac{\partial \mathcal{L}(x)}{\partial D(x)} = 0, \tag{2.40}$$

it is possible to eliminate F and D from the Lagrangian. The scalar potential $\mathcal{V}$ is thus

$$\mathcal{V} = \sum_i F_i^* F_i + \frac{1}{2} \sum_a (D^a)^2 = \sum_i \frac{\partial \mathcal{W}(\phi)}{\partial \phi_i} \frac{\partial \overline{\mathcal{W}}(\phi^*)}{\partial \phi_i^*} + \frac{1}{2} \sum_l g_l^2 \sum_a \left(\sum_i \phi_i^* T_l^a \phi_i \right)^2, \tag{2.41}$$

where g_l and T_l with $l = 1, 2, 3$ are the gauge couplings and generators for $U(1)_Y$, $SU(2)_L$, and $SU(3)_C$, respectively. We see that $\mathcal{V}$ is a sum of squares and is hence non-negative for every field configuration.

Supersymmetry breaking

A realistic phenomenological SUSY model has to include SUSY breaking and to provide extra mass terms for the new SUSY partners. In analogy to the electroweak symmetry breaking one can consider a spontaneous breaking of supersymmetry. This implies that the Lagrangian remains invariant under SUSY transformations whereas the vacuum state does not. As we have seen, the spectrum is bounded from below in a SUSY theory, i. e. the scalar potential $\mathcal{V}$ is always positive or equal to zero. The case $\mathcal{V} = 0$ corresponds to the SUSY invariant case. A non-vanishing vacuum state can only be achieved if some field develops a non-zero VEV, then the minimum of $\mathcal{V}$ will be a positive constant. The two possibilities are $\langle 0|F|0 \rangle \neq 0$ (F-term breaking [57]) and $\langle 0|D^a|0 \rangle \neq 0$ (D-term breaking [58]). However both mechanisms cause problems in the phenomenological realization of the model, requiring either the postulation of an additional gauge singlet field or the breaking of charge or color symmetry by non-zero VEVs.

One therefore adapts the approach of indirect or radiative SUSY breaking and adds explicit symmetry breaking terms by hand, at any given SUSY breaking scale. In this sense, SUSY is hidden at lower scales. The SUSY breaking couplings have to respect SM gauge and Poincaré invariance and they should be *soft* to not alter the dimensionless couplings, i. e. they are of positive mass dimension only (see also the footnote 5 on p. 13).

The possible soft-breaking terms are classified in [59] as mass terms for gauginos and scalars, trilinear couplings for scalar fields, and, if the theory provides gauge singlets, also linear (tadpole) contributions. Chiral fermions do not gain masses from the SUSY breaking. The masses for all known SM particles must arise via spontaneous breaking of the electroweak symmetry in order not to spoil explicitly the gauge invariance with respect to the electroweak symmetry.

Still, the origin of the explicit SUSY-breaking terms is spontaneous supersymmetry

breaking, but the breaking is now shifted into a hidden sector. The SUSY breaking is communicated to the visible sector of ordinary matter via an interaction shared by both sectors. Fields in the hidden sector do not have direct renormalizable couplings to the fields in the visible sector, hence possible interactions are loop-suppressed or induced by non-renormalizable operators. As a consequence, the SUSY-breaking terms arise radiatively, rather than through tree-level couplings to SUSY-breaking VEVs. The particle physics phenomenology depends mainly on the communicating mechanism for the SUSY breaking and only little on the SUSY-breaking mechanism itself.

There are different suggestions how the SUSY breaking is mediated to the visible sector. Among the most popular theories are supergravity models (SUGRA) [60,61] that assume the SUSY breaking being communicated by gravitational-strength interactions, gauge mediated models (GMSB) [62,63], and models of anomaly mediation (AMSB) [64]. Within the MSSM (see below), the most widely studied constrained model is minimal supergravity (mSUGRA) [61], assuming universality relations among the couplings in the effective Lagrangian at the GUT scale and we itemize the corresponding soft-breaking terms in the next section.[7] For phenomenological reviews on mSUGRA, GMSB and AMSB models, we refer the reader to e. g. [51,65,66].

2.3 The minimal supersymmetric extension of the Standard Model (MSSM)

We now turn to the application of supersymmetry to particle physics. The most economic realization of SUSY is given by the *minimal supersymmetric extension of the Standard Model* (MSSM) [12–14], based on the following principles:

- the SM is extended by a minimal $N = 1$ supersymmetry,

- the MSSM Lagrangian is invariant under the $SU(3)_C \times SU(2)_L \times U(1)_Y$ gauge group,

- at low energies, supersymmetry is softly broken,

- only $\mathcal{R}$-parity conserving interactions are allowed.

The following discussion is based on the contents of the last chapter, where we learned how to build a Lagrangian which is invariant under SUSY and gauge transformations. First, we present the field content of the MSSM in Section 2.3.1. The concept of $\mathcal{R}$-parity is introduced in Section 2.3.2. It is then straight-forward to build the MSSM Lagrangian including the soft SUSY-breaking terms, which is done in Section 2.3.3. We conclude the section with a detailed list of the physical particle states of the MSSM in Section 2.3.4.

---

[7]Note that most of the presented work is independent on the assumption of a specific SUSY breaking scenario. In particular, the calculation of EW contributions to colored SUSY particle production processes holds within the MSSM in general. Only for the numerical evaluation of our results and in the rather independent Chapter 8 we refer to mSUGRA and B_3 mSUGRA models, respectively.

2.3.1 Field content of the MSSM

In a minimal $N = 1$ SUSY model, the single SUSY generator Q_α assigns exactly one bosonic state to a fermionic one. Each single-particle state falls into an irreducible representation of the SUSY algebra, a "supermultiplet". The supermultiplets contain both a bosonic and a fermionic state with equal number of d.o.f., these are called superpartners to each other. Since the SUSY generator Q_α commutes with the generators of the internal symmetries $SU(3)_C \times SU(2)_L \times U(1)_Y$, the particles within one supermultiplet have to be in the same representation of the gauge group. As a consequence, all of the superpartners of the SM particles have to be new particles not being part of the SM particle zoo.

The simplest irreducible representation of the SUSY algebra is a chiral supermultiplet, containing a two-component Weyl fermion and a complex scalar field. All SM fermions occur in chiral supermultiplets and thus get scalar partners, called sfermions (squarks, sleptons). Since the left- and right-handed fermions are separate Weyl spinors with different gauge transformation properties, each of them gets its own scalar SUSY partner. We denote the latter by left-/right-handed sfermions $\tilde{f}_{L/R}$, where the name and the subscript refer to the helicity state of the corresponding SM fermion.

Second, a massless spin-one boson and a Weyl fermion can be incorporated into a vector supermultiplet. The SM gauge bosons, which are all massless before electroweak symmetry breaking, are absorbed into a vector supermultiplet and thus get fermionic partners, the gauginos. The electrically neutral gauginos (eight gluinos, neutral wino, bino) are Majorana fermions, the SUSY partners of charged gauge bosons (charged winos) are Dirac fermions (see Appendices A.3 and A.4).

The SM Higgs boson is a spin-0 particle and hence resides in a chiral supermultiplet, yielding a fermionic superpartner. More precisely, as mentioned already, a second supermultiplet is needed in the Higgs sector: The generation of masses for charged leptons and both up- and down-type quarks in a gauge invariant way would require both the Higgs boson field and its conjugate. In a SUSY theory, the corresponding Yukawa couplings arise from the superpotential. However, the superpotential is an analytic function of (left-handed) chiral fields only and conjugated (right-handed) fields would spoil the gauge invariance. Thus two Higgs boson doublets of opposite hypercharge are introduced to give masses to the SM fermions. In addition, the second Higgs boson doublet is necessary to keep the MSSM free of gauge anomalies. The cancellation of those is given if the trace running over the weak hypercharges of all Weyl fermions in the theory vanishes, which is guaranteed in the SM by each generation of quarks and leptons (see footnote 2 on p. 8). Postulating a single fermionic superpartner to the Higgs boson of a given non-zero hypercharge, the anomaly cancellation is spoiled. In contrast a second Higgs boson doublet of opposite hypercharge provides a second fermionic partner to the Higgs boson and the total contribution to the anomaly traces is zero again.

The field content of the MSSM is summarized in Tab. 2.1.

	superfield	boson field	fermion field	$\left(SU(3)_C, SU(2)_L, U(1)_Y\right)$	name
chiral superfields	Q	$\tilde{q}_L = (\tilde{u}_L, \tilde{d}_L)^T$	$q_L = (u_L, d_L)^T$	$(3, 2, +\frac{1}{3})$	
	$\overline{U}$	$\tilde{u}_R^*$	$u_R^\dagger$	$(\bar{3}, 1, -\frac{4}{3})$	(s)quark
	$\overline{D}$	$\tilde{d}_R^*$	$d_R^\dagger$	$(\bar{3}, 1, +\frac{2}{3})$	
	L	$\tilde{\ell}_L = (\tilde{\nu}, \tilde{e}_L)^T$	$\ell_L = (\nu, e_L)^T$	$(1, 2, -1)$	
	$\overline{E}$	$\tilde{e}_R^*$	$e_R^\dagger$	$(\bar{1}, 1, +2)$	(s)lepton
	H_u	$h_u = (h_u^+, h_u^0)^T$	$\tilde{h}_u = (\tilde{h}_u^+, \tilde{h}_u^0)^T$	$(1, 2, +1)$	
	H_d	$h_d = (h_d^0, h_d^-)^T$	$\tilde{h}_d = (\tilde{h}_d^0, \tilde{h}_d^-)^T$	$(1, 2, -1)$	Higgs(ino)
vector superfields	G^a	g	$\tilde{g}$	$(8, 1, 0)$	gluon(-ino)
	W^i	$W^\pm, W^0$	$\tilde{W}^\pm, \tilde{W}^0$	$(1, 3, 0)$	W(-ino)
	B	B	$\tilde{B}$	$(1, 1, 0)$	B(-ino)

Table 2.1.: Classification of the chiral and vector superfields within the MSSM. The superfields, denoted by capital letters, have bosonic and fermionic component fields. The SUSY partners of the SM particles carry a tilde, and the subscript L, R of the scalar SUSY particles refers to the helicity state of the corresponding fermionic partner. The behavior under gauge transformations is the same for fields belonging to the same supermultiplet (indicated in column 5). In the last column, the names of the SM (SUSY) particles are given. To avoid clutter, family and color indices are suppressed in the notation of the chiral superfields, i. e. the first generation representatives are used to label the fields introduced for each generation. For the vector fields, the indices $a = 1 \ldots 8$ and $i = 1 \ldots 3$ denote the $SU(3)_C$ and $SU(2)_L$ quantum numbers, respectively.

2.3.2 $\mathcal{R}$-parity

Interactions among scalars and fermions in a SUSY theory are given by the superpotential $\mathcal{W}$, Eq. (2.28). As argued above, the superpotential needs to respect supersymmetry and gauge invariance under $SU(3)_C \times SU(2)_L \times U(1)_Y$ transformations. With the given minimal field content of Table 2.1, the most general renormalizable superpotential is [28,29]

$$\mathcal{W} = \mathcal{W}_{\mathcal{R}} + \mathcal{W}_{\cancel{\mathcal{R}}} \,, \tag{2.42}$$

with the two parts, written in terms of the superfields introduced in Table 2.1,

$$\mathcal{W}_{\mathcal{R}} = \epsilon_{ab} \left[(\mathbf{Y}_U)_{ij} Q_i^{ax} H_u^b \overline{U}_{jx} - (\mathbf{Y}_E)_{ij} L_i^a H_d^b \overline{E}_j - (\mathbf{Y}_D)_{ij} Q_i^{ax} H_d^b \overline{D}_{jx} + \mu H_d^a H_u^b \right], \tag{2.43a}$$

$$\mathcal{W}_{\cancel{\mathcal{R}}} = \epsilon_{ab} \left[\frac{1}{2} \lambda_{ijk} L_i^a L_j^b \overline{E}_k + \lambda'_{ijk} L_i^a Q_j^{bx} \overline{D}_{kx} \right] + \epsilon_{ab} \kappa^i L_i^a H_u^b + \frac{1}{2} \epsilon_{xyz} \lambda''_{ijk} \overline{U}_i^x \overline{D}_j^y \overline{D}_k^z, \tag{2.43b}$$

where i, j, k denote the generations of matter fields, a, b are $SU(2)_L$ indices, and x, y, z are $SU(3)$ color indices. The signs are chosen for later convenience. Due to the absence of a gauge singlet field in the MSSM, no linear term arises in Eq. (2.43), but only bi- and trilinear couplings of chiral matter supermultiplets.

The first term, $\mathcal{W}_{\mathcal{R}}$, contains the Yukawa interactions of Higgs boson, quark, and lepton superfields which give masses to the up- and down-type quarks and charged leptons after electroweak symmetry breaking. The Yukawa couplings are 3×3 matrices in family space, denoted by $\mathbf{Y}_U$, $\mathbf{Y}_D$, $\mathbf{Y}_E$, respectively. To fully establish the two-doublet Higgs sector, also a coupling μ mixing the two different Higgs boson fields is provided.

In the second part, $\mathcal{W}_{\mathcal{R}}$, the couplings λ_{ijk}, λ'_{ijk}, and κ_i lead to lepton number L violating processes, whereas λ''_{ijk} induces baryon number B violation. Gauge invariance enforces that λ_{ijk} (λ''_{ijk}) is antisymmetric under the interchange of the first (last) two indices. Following the usual convention, corresponding factors of $1/2$ are introduced in $\mathcal{W}_{\mathcal{R}}$ to avoid double counting in scattering amplitudes.

The combination of non-zero lepton and baryon number violating couplings $(\lambda'\lambda'')$ can lead to rapid proton decay [30,31], e. g. via the process $p \rightarrow \pi^0 e^+$ mediated by an s-channel down-type squark, which is clearly excluded by experimental observations [32]. Whereas in the SM lepton and baryon number are conserved accidentally at tree-level, its minimal supersymmetric extension requires an additional symmetry to stabilize the proton. There are only three discrete symmetries which are consistent with an underlying anomaly-free $U(1)$ gauge theory and thus do not experience violation by quantum gravity effects [34,35]: $\mathcal{R}$-parity, proton-hexality, and baryon-triality.

The most widely assumed symmetry is $\mathcal{R}$-parity [33] (or equivalently matter parity). To each particle, a multiplicative discrete quantum number $P_{\mathcal{R}}$ is assigned to,

$$P_{\mathcal{R}} = (-1)^{3(B-L)+2s}, \tag{2.44}$$

where s denotes the particle's spin. The definition Eq. (2.44) yields a positive quantum number $P_{\mathcal{R}} = +1$ for all SM and Higgs particles, whereas all SUSY particles carry $P_{\mathcal{R}} = -1$. The postulation of $\mathcal{R}$-parity conservation implies that only those terms are allowed in the superpotential Eq. (2.42) which give rise to interaction vertices of SM and SUSY particles with a positive product of all $P_{\mathcal{R}}$ eigenvalues. As a consequence, the part $\mathcal{W}_{\mathcal{R}}$ is prohibited from the superpotential.

Although the dimension-four terms in $\mathcal{W}_{\mathcal{R}}$ are the most dangerous for proton decay, they are not the only ones that must be suppressed in general. Higher-dimension terms may also lead to proton decay. They are suppressed by inverse powers of a high mass scale at which the new baryon and lepton-number violating processes occur. In a compactified string theory this scale may be the compactification scale (of the order of the Planck scale) or a lower scale associated with the breaking of a GUT left unbroken after compactification. Even if one assumes the scale as high as the Planck scale, some of the dimension-five

operators will generate proton decay at an unacceptably high rate. $\mathcal{R}$-parity still allows for the dangerous dimension-five operators such as $QQQL$ [67]. A preferred solution is thus to assume conservation of proton-hexality, P_6 [34], which has the same effect on the renormalizable interactions as $\mathcal{R}$-parity, but forbids, in addition, the dangerous dimension-five operators.

The third possibility is baryon-triality, B_3 [34–37]. B_3 is a discrete $\boldsymbol{Z}_3$-symmetry which prohibits in Eq. (2.43b) only the $\overline{U}\,\overline{D}\,\overline{D}$ operators (i. e. $\lambda'' = 0$) but also the dangerous dimension-five operators. Since proton decay proceeds via both B and L violating couplings, it can be avoided if one of the two sets of couplings vanishes. This is the approach of the $\mathcal{R}$-parity violating B_3 models, where B is conserved but not the combination of B and L as required by Eq. (2.44).

In the framework of the MSSM, one considers $\mathcal{R}$-parity as the underlying symmetry. From the phenomenological point of view, $\mathcal{R}$-parity conservation has important implications. First of all, the $P_{\mathcal{R}}$-odd SUSY particles can only be produced and annihilated in pairs. As a consequence, the lightest SUSY particle (LSP) has to be stable. This being massive and stable would be a good candidate particle to constitute the non-baryonic dark matter in our universe. In general, every SUSY particle can be the LSP [68]. However for stable LSPs, only scenarios where it is electrically neutral and only weakly interacting provide a viable solution to the cosmological constraints. In the MSSM with conserved $\mathcal{R}$-parity, one therefore excludes regions from the SUSY parameter space leading to a charged LSP [10] and mostly considers the lightest of the neutralinos (see next section) to be the LSP. Considering the phenomenology at particle accelerators, one finds that any produced heavy SUSY particle will decay into lighter SUSY particles, yielding a possibly long decay chain ending up with the LSP. The signatures of SUSY particle production processes will thus depend crucially on the nature of the LSP. If $\mathcal{R}$-parity is conserved, the LSP cannot further decay into SM particles. As it is neutral, the LSPs escape detection and a typical SUSY signal involves a high amount of missing transverse energy and multiple jets from the hadronic decays of the heavy SUSY particles.

In this thesis, we consider both SUSY models with and without $\mathcal{R}$-parity conservation. The calculation of the production of colored SUSY particles at the LHC is performed in the framework of the MSSM, i. e. assuming $\mathcal{R}$-parity conservation, and we refer to pair production of colored SUSY particles, only. In the last chapter of this report, Chapter 8, we further exploit the phenomenology of B_3 SUSY models, focussing on scenarios where the (unstable) LSP is charged. We thus postpone any further discussion of $\mathcal{R}$-parity violating couplings and the related phenomenology to Chapter 8.

2.3.3 The MSSM Lagrangian

We have now all ingredients to write down the $\mathcal{R}$-parity conserving MSSM Lagrangian $\mathcal{L}_{\text{MSSM}}$, based on the MSSM field content (given in Table 2.1), which is invariant under

transformations of the SM non-Abelian gauge group and includes at most soft SUSY-breaking terms. Following the discussion Section 2.2.2, we write

$$\mathcal{L}_{\text{MSSM}} = \mathcal{L}_{\text{SUSY}} + \mathcal{L}_{\text{soft}}, \tag{2.45}$$

where $\mathcal{L}_{\text{SUSY}}$ is a SUSY-invariant Lagrangian and $\mathcal{L}_{\text{soft}}$ parameterizes the soft SUSY-breaking[8].

The supersymmetric part of the Lagrangian itself can be decomposed into three parts, two F-type contributions (from the superpotential and the kinetic terms for the gauge bosons and gauginos, Eq. (2.38)) and a D-term, cf. Eq. (2.30), with kinetic terms for scalars and fermions.

The superpotential of the MSSM is given by the $\mathcal{R}$-parity conserving part of Eq. (2.42), $\mathcal{W}_{\text{MSSM}} \equiv \mathcal{W}_{\mathcal{R}}$, yielding the contribution

$$\mathcal{L}_{F,1} = \int d^2\theta \left[\mathcal{W}_{\text{MSSM}} + \overline{\mathcal{W}}_{\text{MSSM}} \right]. \tag{2.46}$$

The kinetic terms for the gauge bosons $\mathcal{L}_{F,2}$ are given in terms of field strength tensors defined in analogy to Eqs. (2.34) and (2.35). For the three gauge groups $SU(3)_C$, $SU(2)_L$, $U(1)_Y$ with gauge couplings g_s, g, and g', respectively, they are

$$
\begin{aligned}
(W_G)_\alpha^a &= \frac{1}{4}\overline{D}\,\overline{D}\,e^{-2g_s G} D_\alpha\, e^{2g_s G}, \\
(W_W)_\alpha^i &= \frac{1}{4}\overline{D}\,\overline{D}\,e^{-2g W} D_\alpha\, e^{2g W}, \\
(W_B)_\alpha &= \frac{g'}{4}\overline{D}\,\overline{D}\, D_\alpha\, B',
\end{aligned}
\tag{2.47}
$$

with

$$G = T^a G^a, \qquad W = I^i W^i, \qquad B' = Y B, \tag{2.48}$$

where T^a, I^i, Y are the generators of the three gauge groups, respectively, and G^a, W^i, B are the superfields as introduced in Table 2.1. The corresponding part in the Lagrangian reads

$$\mathcal{L}_{F,2} = \frac{1}{16} \int d^2\theta \left\{ \frac{1}{g_s^2}\text{Tr}[(W_G)_\alpha^a (W_G)_a^\alpha] + \frac{1}{g^2}\text{Tr}[(W_W)_\alpha^i (W_W)_i^\alpha] + \frac{1}{g'^2}(W_B)_\alpha (W_B)^\alpha \right\} + h.c.. \tag{2.49}$$

---

[8]Furthermore, as in the SM, a consistent quantization of the MSSM Lagrangian requires gauge fixing and the introduction of Fadeev-Popov ghosts to cancel the additional unphysical d.o.f.. The ghost fields and gauge-fixing terms for the MSSM gauge bosons (gluons, photon, W's, Z) and Goldstone bosons are chosen in complete analogy to the SM. Explicit expressions can be found in e. g. [69,70]. The calculations presented in this work have been performed in the 't Hooft–Feynman gauge.

Third, using the same notation, the D-term contribution is of the form

$$
\mathcal{L}_D = \int d^2\theta \, d^2\overline{\theta} \bigg\{ \overline{L}e^{2(g'B+gW)}L + \overline{E}e^{2(g'B+gW)}E
$$
$$
+ \overline{Q}e^{2(g'B+gW+g_sG)}Q + \overline{U}e^{2(g'B+gW+g_sG)}U + \overline{D}e^{2(g'B+gW+g_sG)}D \quad (2.50)
$$
$$
+ \overline{H}_u \, e^{2(g'B+gW)}H_u + \overline{H}_d \, e^{2(g'B+gW)}H_d \bigg\}.
$$

To complete the MSSM Lagrangian we need to specify the soft-breaking terms. With the requirement of gauge invariance and $\mathcal{R}$-parity conservation, the soft-breaking part of the Lagrangian is[9]

$$
\begin{aligned}
\mathcal{L}_{\text{soft}} = - & \frac{1}{2}(M_1 \, \tilde{B}\tilde{B} + M_2 \, \tilde{W}\tilde{W} + M_3 \, \tilde{g}\tilde{g}) \, + \, h.c. \\
& - \tilde{q}_L^\dagger \, \mathbf{m}_{\tilde{Q}}^2 \, \tilde{q}_L - \tilde{u}_R^* \, \mathbf{m}_{\tilde{U}}^2 \, \tilde{u}_R - \tilde{d}_R^* \, \mathbf{m}_{\tilde{D}}^2 \, \tilde{d}_R - \tilde{\ell}_L^\dagger \, \mathbf{m}_{\tilde{L}}^2 \, \tilde{\ell}_L - \tilde{e}_R^* \, \mathbf{m}_{\tilde{E}}^2 \, \tilde{e}_R \\
& - m_{h_u}^2 \, h_u^\dagger h_u - m_{h_d}^2 \, h_d^\dagger h_d - (b \, h_u h_d + h.c.) \\
& - \Big(\mathbf{a}_U \, \tilde{q}_L \, h_u \, \tilde{u}_R^* - \mathbf{a}_D \, \tilde{q}_L \, h_d \, \tilde{d}_R^* - \mathbf{a}_E \, \tilde{\ell}_L \, h_d \, \tilde{e}_R^*\Big) \, + \, h.c. \, .
\end{aligned} \quad (2.51)
$$

As already anticipated above, the allowed soft-breaking terms are gaugino mass terms (first line) squark and slepton mass terms (second line), Higgs boson mass and bilinear terms (third line), and trilinear Higgs-sfermion-sfermion interaction terms (fourth line) [59]. Linear terms are absent in the MSSM, due to the non-existence of a gauge singlet. In the notation above, in contrast to Eq. (2.42), $SU(2)_L$ indices are suppressed and e.g. $\tilde{q}_L^\dagger \tilde{q}_L = \tilde{u}_L^* \tilde{u}_L + \tilde{d}_L^* \tilde{d}_L$ and $h_u \tilde{q}_L = \epsilon_{ab} h_u^a \, \tilde{q}_L^b$. Furthermore, generation indices are understood implicitly: The soft-breaking mass parameters $\mathbf{m}$ are hermitian 3×3 matrices in family space, which in general can be complex. The same is true for the couplings $\mathbf{a}$ which are usually be expressed in terms of trilinear couplings $\mathbf{A}$ and Yukawa couplings $\mathbf{Y}$

$$
\mathbf{a}_{\{U,D,E\}} \equiv \mathbf{A}_{\{u,d,e\}} \mathbf{Y}_{\{U,D,E\}}. \quad (2.52)
$$

The gaugino mass parameters M_1, M_2, M_3 and the bilinear Higgs boson coupling b are complex numbers, the Higgs boson mass parameters m_{h_u}, m_{h_d} have to be real.

In order to obtain the Feynman rules, one needs to expand the MSSM Lagrangian in component fields. Complete expressions both for the on-shell Lagrangian (where the auxiliary fields are eliminated) and the off-shell Lagrangian can be found in the literature, see e.g. [69,71]. For the Feynman rules we refer to [13,70,72,73].

---

[9]Allowing for $\mathcal{R}$-parity violating interactions, additional soft-breaking terms have to be considered, see Eq. (C.2).

Free parameters and constrained SUSY models

While the kinetic and gauge parts of the MSSM Lagrangian only depend on SM parameters, the superpotential in Eq. (2.46) and the soft-breaking part Eq. (2.51) introduces 105 new parameters (couplings, masses, complex phases) into the theory. Most of them however are rather strongly restricted by experimental (non-)observations of flavor-changing neutral-currents (FCNC) or CP violation [5,74]. In general, the 3×3 mass matrices in $\mathcal{L}_{\text{soft}}$ induce mixing in the sfermion sector among the generations. Under the assumption of minimal flavor violation, the SM Higgs-Yukawa matrices (i.e. the CKM matrix) are the only possible sources of CP violation and the mass matrices and trilinear couplings are diagonal in family space so that FCNCs are absent at tree level,

$$
\begin{aligned}
\mathbf{m}_{\tilde{F}}^2 &= \text{diag}(m_{\tilde{F}_1}^2, m_{\tilde{F}_2}^2, m_{\tilde{F}_3}^2), \qquad \text{for} \quad \tilde{F} = \{\tilde{Q}, \tilde{U}, \tilde{D}, \tilde{L}, \tilde{E}\}, \\
\mathbf{A}_f &= \text{diag}(A_{f_1}, A_{f_2}, A_{f_3}), \qquad \text{for} \quad f = \{u, d, e\},
\end{aligned}
\tag{2.53}
$$

where the index $i = 1, 2, 3$ denotes the three generations. Moreover, we will consider the MSSM with real parameters only, i.e. no new phases are introduced.

Further restrictions on the soft-breaking parameters arise in constrained SUSY models, when specific assumptions are made on how the SUSY breaking is mediated from the hidden to the visible sector. Here, we focus on mSUGRA models where the SUSY breaking sector communicates with the visible sector only via gravitational interactions as specified by supergravity. In the minimal version of these models (mSUGRA) the supergravity interactions are flavor-blind and the soft-breaking parameters are universal. Besides the unification of the three gauge couplings, a unification of the scalar and gaugino masses and trilinear soft-breaking parameters is required at some high scale, the GUT scale ($\Lambda_{\text{GUT}} \sim 2 \times 10^{16}$ GeV, fixed by the unification of the gauge couplings). In terms of a universal scalar mass M_0, a universal gaugino mass $M_{1/2}$ and a universal trilinear scalar coupling A_0 this implies the following relations to hold at Λ_{GUT},

$$
\begin{aligned}
\mathbf{m_Q^2} = \mathbf{m_L^2} = \mathbf{m_U^2} = \mathbf{m_D^2} = \mathbf{m_E^2} &= M_0^2 \, \mathbb{1}_3 \\
m_{h_u}^2 = m_{h_d}^2 &= M_0^2 \\
M_1 = M_2 = M_3 &= M_{1/2} \\
\mathbf{a}_U = A_0 \mathbf{Y}_U \quad \mathbf{a}_D = A_0 \mathbf{Y}_D, \quad \mathbf{a}_E &= A_0 \mathbf{Y}_E.
\end{aligned}
\tag{2.54}
$$

These equations act as GUT-scale boundary conditions for the soft-breaking parameters. By renormalization group techniques all masses and couplings can then be extrapolated to low scales. Two further independent parameters enter in the Higgs sector, the mass parameter μ and bilinear coupling b. However, one has to require that electroweak symmetry breaking takes place at some low energy scale. This results in two necessary minimization conditions of the scalar Higgs potential which allow to equivalently choose the ratio of the

VEVs of the Higgs bosons $\tan\beta$ and the sign of μ as free parameters (see next section for details and definitions). In summary, only five parameters are needed in mSUGRA models to determine the low-energy spectrum:

$$M_0, \ M_{1/2}, \ A_0, \ \tan\beta, \ \text{sgn}(\mu). \tag{2.55}$$

We stress that our general results for colored SUSY particle production processes do not rely on a specific SUSY softbreaking mechanism. Only the numerical studies are performed within the mSUGRA framework. For the actual calculation of the spectrum and the evaluation of the renormalization group equations at lower scales we make use of publically available programs [75] (see also Appendix B). Furthermore in Chapter 8, where we study the phenomenological consequences of non-zero $\mathcal{R}$-parity violating couplings, we also assume the SUSY breaking to be mediated via gravitational interactions.

2.3.4 The particle spectrum of the MSSM

Like in the SM, in the MSSM the $SU(2)_L \times U(1)_Y$ symmetry is spontaneously broken down to the electromagnetic $U(1)_Q$ symmetry in order to yield masses for the gauge bosons and SM fermions [76]. The Higgs mechanism in the MSSM proceeds in a similar way as in the SM.

The two MSSM Higgs boson fields have eight real scalar d.o.f.. After electroweak symmetry breaking (EWSB), three of them can be identified as unphysical Goldstone bosons which are subsequently absorbed by the gauge bosons to acquire masses. The remaining five d.o.f. form the physical Higgs bosons. Furthermore, after EWSB, all particles with the same quantum numbers of the unbroken $SU(3)_C \times U(1)_Q$ group (color, electric charge) can mix. Therefore, we have mixing among the gauge eigenstates in the sfermion sector and among the electrically neutral and charged higgsinos and gauginos, respectively. These mass eigenstates are called neutralinos and charginos. It is the purpose of this section, to introduce in more detail the physical fields of the MSSM at tree-level.

Higgs bosons and SM gauge bosons

The scalar potential for the Higgs boson scalar fields in the MSSM is

$$\begin{aligned}
\mathcal{V}_{\text{Higgs}} = &\left(|\mu|^2 + m_{h_d}^2\right) h_d^\dagger h_d + \left(|\mu|^2 + m_{h_u}^2\right) h_u^\dagger h_u + (b\, h_u h_d + h.c.) \\
&+ \frac{g'^2 + g^2}{8} (h_d^\dagger h_d - h_u^\dagger h_u)^2 + \frac{g^2}{2} |h_u h_d^\dagger|^2,
\end{aligned} \tag{2.56}$$

where the terms proportional to μ and the gauge couplings g, g' arise from the F- and D-field terms of the scalar potential and terms proportional to $m_{h_d}^2, m_{h_u}^2, b$ are contributions from the soft-breaking part of the MSSM Lagrangian, cf. Eq. (2.51).

The neutral components of the Higgs boson fields are assigned to a non-vanishing, positive VEV v_d, v_u. In terms of the real scalar fields $\phi_{d,u}^{0,\pm}$, $\zeta_{d,u}^0$ of vanishing VEV, the Higgs boson fields can be decomposed as follows,

$$
\begin{aligned}
h_d &= \begin{pmatrix} h_d^0 \\ h_d^- \end{pmatrix} = \begin{pmatrix} v_d + (\phi_d^0 + i\zeta_d^0)/\sqrt{2} \\ -\phi_d^- \end{pmatrix}, \\
h_u &= \begin{pmatrix} h_u^+ \\ h_u^0 \end{pmatrix} = \begin{pmatrix} \phi_u^+ \\ v_u + (\phi_u^0 + i\zeta_u^0)/\sqrt{2} \end{pmatrix},
\end{aligned}
\tag{2.57}
$$

yielding non-zero, $U(1)_Q$-invariant VEVs for the Higgs boson fields,

$$
\langle h_d \rangle = \begin{pmatrix} v_d \\ 0 \end{pmatrix}, \qquad \langle h_u \rangle = \begin{pmatrix} 0 \\ v_u \end{pmatrix}.
\tag{2.58}
$$

In order to provide a solution to EWSB, the potential needs to be bounded from below while the origin is a saddle point. This is the case if

$$
(|\mu|^2 + m_{h_d}^2) + (|\mu|^2 + m_{h_u}^2) > 2b, \qquad (|\mu|^2 + m_{h_d}^2)\,(|\mu|^2 + m_{h_u}^2) < b^2.
\tag{2.59}
$$

These relations directly link EWSB and SUSY breaking, since $m_{h_u}^2 \neq m_{h_d}^2$ is required. In an unbroken SUSY however, the soft-breaking Higgs boson mass terms are absent and thus equal zero. If the above conditions are fulfilled, the values of the two VEVs are obtained from the scalar potential by minimization with respect to h_d^0 and h_u^0,

$$
\begin{aligned}
(|\mu|^2 + m_{h_d}^2) &= b\frac{v_u}{v_d} - \frac{g^2 + g'^2}{4}\frac{v_d^2 - v_u^2}{v_d}, \\
(|\mu|^2 + m_{h_u}^2) &= b\frac{v_d}{v_u} - \frac{g^2 + g'^2}{4}\frac{v_u^2 - v_d^2}{v_d}.
\end{aligned}
\tag{2.60}
$$

It is interesting to notice that only the combination $g^2 + g'^2$ of the gauge couplings enters the potential, whereas in the SM the arbitrary Higgs boson coupling λ enters. There are only two independent parameters in the MSSM Higgs sector at Born level, the ratio of the Higgs VEVs, referred to as $\tan\beta$,

$$
\tan\beta = v_u/v_d,
\tag{2.61}
$$

and the soft-breaking parameter b. By convention, one replaces b by the mass of the CP-odd Higgs boson A^0, (see below),

$$
m_{A^0}^2 = m_{h_d}^2 + m_{h_u}^2 + 2|\mu|^2 = b\,(\tan\beta + \cot\beta).
\tag{2.62}
$$

The Higgs mixing parameter μ is a dependent quantity and constrained by Eq. (2.60).

To find the mass eigenstates of the theory, we insert Eq. (2.57) into the Lagrangian and diagonalize the mass matrices by a unitary transformation.

First of all, the mixing of the gauge bosons eigenstates proceeds as in the SM. The photon, Z boson, and W boson mass eigenstates are given by

$$\begin{pmatrix} Z_\mu \\ A_\mu \end{pmatrix} = \begin{pmatrix} \cos\theta_W & -\sin\theta_W \\ \sin\theta_W & \cos\theta_W \end{pmatrix} \begin{pmatrix} W_\mu^3 \\ B_\mu \end{pmatrix}, \quad W_\mu^\pm = \frac{1}{\sqrt{2}}\left(W_\mu^1 \mp iW_\mu^2\right), \tag{2.63}$$

in terms of the weak mixing angle θ_W, which is related to the gauge couplings via $\tan\theta_W = g'/g$. The masses of the W and Z bosons are, in complete analogy to the SM, related to the gauge couplings and the Higgs VEVs

$$m_W^2 = \frac{g^2}{2}(v_d^2 + v_u^2), \qquad m_Z^2 = \frac{g^2 + g'^2}{2}(v_d^2 + v_u^2), \tag{2.64}$$

while the photon A_μ remains massless. The electric charge, the gauge coupling of the photon, can be expressed in terms of g and g',

$$e = g\sin\theta_W = g'\cos\theta_W. \tag{2.65}$$

With Eqs. (2.64) and (2.65) and the definition of $\tan\beta$, Eq. (2.61), the Higgs VEVs are

$$v_d = \frac{\sqrt{2}m_W\sin\theta_W}{e}\cos\beta, \qquad v_u = \frac{\sqrt{2}m_W\sin\theta_W}{e}\sin\beta. \tag{2.66}$$

The terms bilinear in the scalar fields ϕ and ζ in the Higgs potential yield the Higgs boson mass terms,

$$\mathcal{V}_{\text{Higgs, mass}} = \frac{1}{2}(\phi_d^0,\ \phi_u^0)\,\mathcal{M}_{\phi^0}^2\begin{pmatrix}\phi_d^0\\\phi_u^0\end{pmatrix} + \frac{1}{2}(\zeta_d^0,\ \zeta_u^0)\,\mathcal{M}_{\zeta^0}^2\begin{pmatrix}\zeta_d^0\\\zeta_u^0\end{pmatrix} + \frac{1}{2}(\phi_d^+,\ \phi_u^+)\,\mathcal{M}_{\phi^\pm}^2\begin{pmatrix}\phi_d^-\\\phi_u^-\end{pmatrix}, \tag{2.67}$$

where the squared mass matrix $\mathcal{M}_{\phi^0}^2$ for the neutral CP-even Higgs boson fields is

$$\mathcal{M}_{\phi^0}^2 = \begin{pmatrix} |\mu|^2 + m_{h_d}^2 + \bar{g}^2\,(3v_d^2 - v_u^2)/4 & -b - \bar{g}^2\,v_dv_u/2 \\ -b - \bar{g}^2\,v_dv_u/2 & |\mu|^2 + m_{h_u}^2 + \bar{g}^2\,(3v_u^2 - v_d^2)/4 \end{pmatrix}, \tag{2.68}$$

the squared mass matrix $\mathcal{M}_{\zeta^0}^2$ for the neutral CP-odd Higgs boson fields reads

$$\mathcal{M}_{\zeta^0}^2 = \begin{pmatrix} |\mu|^2 + m_{h_d}^2 + \bar{g}^2\,(v_d^2 - v_u^2)/4 & -b \\ -b & |\mu|^2 + m_{h_u}^2 + \bar{g}^2\,(v_u^2 - v_d^2)/4 \end{pmatrix}, \tag{2.69}$$

and $\mathcal{M}^2_{\phi\pm}$ denotes the squared mass matrix of the charged Higgs boson fields,

$$\mathcal{M}^2_{\phi\pm} = \begin{pmatrix} |\mu|^2 + m^2_{h_d} + (\bar{g}^2 v^2_d + \bar{\bar{g}}^2 v^2_u)/4 & -b - g^2\, v_d v_u/2 \\ -b - g^2\, v_d v_u/2 & |\mu|^2 + m^2_{h_u} + (\bar{g}^2 v^2_d + \bar{\bar{g}}^2 v^2_u)/4 \end{pmatrix}, \tag{2.70}$$

where the abbreviations $\bar{g}^2 = g^2 + g'^2$ and $\bar{\bar{g}}^2 = g^2 - g'^2$ have been used. The Higgs boson mass eigenstates are obtained by rotation and can be classified as follows,

$$\text{2 neutral, CP-even } h^0, H^0 \text{ bosons:} \qquad \begin{pmatrix} H^0 \\ h^0 \end{pmatrix} = U_{\phi^0}(\alpha) \begin{pmatrix} \phi^0_d \\ \phi^0_u \end{pmatrix},$$

$$\text{2 neutral, CP-odd } A^0, G^0 \text{ bosons:} \qquad \begin{pmatrix} G^0 \\ A^0 \end{pmatrix} = U_{\zeta^0}(\beta) \begin{pmatrix} \zeta^0_d \\ \zeta^0_u \end{pmatrix}, \tag{2.71}$$

$$\text{4 charged } H^\pm, G^\pm \text{ bosons:} \qquad \begin{pmatrix} G^\pm \\ H^\pm \end{pmatrix} = U_{\phi^\pm}(\beta) \begin{pmatrix} \phi^\pm_d \\ \phi^\pm_u \end{pmatrix},$$

with a generic unitary matrix U,

$$U(\alpha) = \begin{pmatrix} \cos\alpha & \sin\alpha \\ -\sin\alpha & \cos\alpha \end{pmatrix}. \tag{2.72}$$

The tree-level masses of the five physical Higgs boson fields $h^0, H^0, A^0, H^\pm$ and of the three Goldstone bosons $G^0, G^\pm$ are given by the diagonalized (squared) mass matrices,

$$\begin{aligned} \mathcal{D}^2_{\phi^0} &= U_{\phi^0}\, \mathcal{M}^2_{\phi^0}\, U^\dagger_{\phi^0} &&= \text{diag}(m^2_{H^0}, m^2_{h^0}), \\ \mathcal{D}^2_{\zeta^0} &= U_{\zeta^0}\, \mathcal{M}^2_{\zeta^0}\, U^\dagger_{\zeta^0} &&= \text{diag}(0, m^2_{A^0}), \\ \mathcal{D}^2_{\phi^\pm} &= U_{\phi^\pm}\, \mathcal{M}^2_{\phi^\pm}\, U^\dagger_{\phi^\pm} &&= \text{diag}(0, m^2_{H^\pm}), \end{aligned} \tag{2.73}$$

where $m^2_{A^0}$ has already been introduced in Eq. (2.62) and

$$\begin{aligned} m^2_{h^0/H^0} &= \frac{1}{2}(m^2_{A^0} + m^2_Z) \mp \frac{1}{2}\sqrt{(m^2_{A^0} + m^2_Z)^2 - 4\, m^2_{A^0} m^2_Z \cos^2 2\beta}, \\ m^2_{H^\pm} &= m^2_{A^0} + m^2_Z. \end{aligned} \tag{2.74}$$

In these terms, the mixing angle α can be expressed as

$$\tan 2\alpha = \tan 2\beta\, \frac{m^2_{A^0} + m^2_Z}{m^2_{A^0} - m^2_Z}, \tag{2.75}$$

and the scalar Higgs potential in the mass eigenstate basis is

$$\mathcal{V}_{\text{Higgs, mass}} = \frac{1}{2}\,(h^0,\ H^0)\,\mathcal{D}_{\phi^0}^2 \begin{pmatrix} h^0 \\ H^0 \end{pmatrix} + \frac{1}{2}\,(A^0,\ G^0)\,\mathcal{D}_{\zeta^0}^2 \begin{pmatrix} A^0 \\ G^0 \end{pmatrix} + \frac{1}{2}\,(H^+,\ G^+)\,\mathcal{D}_{\phi^\pm}^2 \begin{pmatrix} H^- \\ G^- \end{pmatrix}. \tag{2.76}$$

Let us note that Eq. (2.74) imposes an upper bound on the mass of the lightest Higgs boson mass, $m_{h^0} \le m_Z$. This bound arises in the MSSM due to the above mentioned fact that the Higgs boson self-couplings are given by the electroweak gauge couplings, whereas in the SM the coupling is unconstrained and no comparable bound can be derived.

Even though $m_{h^0} \le m_Z$ is in contradiction with experimental observations from LEP [43, 77] and Tevatron [78], the MSSM is not ruled out: The inclusion of higher-order corrections raises the tree-level mass considerably (see e. g. [79] and references therein). One-loop and dominant two-loop corrections shift the upper bound of the lightest Higgs boson mass to $m_{h^0} \lesssim 140$ GeV [80]. Within this work, the computation of Higgs boson masses is done by the program `FeynHiggs` [81] (or using a two-loop approximation [82] included now in [83]).

Standard Model fermions

As in the SM, fermions obtain masses by Yukawa interaction terms. The first three terms of the superpotential $\mathcal{W}_{\text{MSSM}}$ Eq. (2.43a) provide the necessary couplings,

$$\mathcal{L}_{\text{yukawa}} = \epsilon_{ab} \left[(\mathbf{Y}_E)_{ij}\,\ell_{Li}^a\,h_d^b\,\bar{e}_{Rj} + (\mathbf{Y}_D)_{ij}\,q_{Li}^a\,h_d^b\,\bar{d}_{Rj} - (\mathbf{Y}_U)_{ij}\,q_{Li}^a\,h_u^b\,\bar{u}_{Rj} \right]\ + h.c., \tag{2.77}$$

where i, j are generation indices and the color indices of the quark fields are suppressed. The fermions yield masses if the Higgs fields get their VEVs,

$$\mathcal{L}_{\text{fermions, mass}} = -(\mathbf{Y}_E)_{ij}\,e_{Li}\,v_d\,\bar{e}_{Rj} - (\mathbf{Y}_D)_{ij}\,d_{Li}\,v_d\,\bar{d}_{Rj} - (\mathbf{Y}_U)_{ij}\,u_{Li}\,v_u\,\bar{u}_{Rj} + h.c., \tag{2.78}$$

which turns out explicitly when the two-component Weyl spinors are combined into four-component Dirac spinors,

$$e_i = \begin{pmatrix} e_{Li} \\ \bar{e}_{Ri} \end{pmatrix}, \qquad d_i = \begin{pmatrix} d_{Li} \\ \bar{d}_{Ri} \end{pmatrix}, \qquad u_i = \begin{pmatrix} u_{Li} \\ \bar{u}_{Ri} \end{pmatrix}. \tag{2.79}$$

Rewriting Eq. (2.78),

$$\mathcal{L}_{\text{fermion, mass}} = -(\mathbf{Y}_E)_{ij}\,e_i\,v_d\,\bar{e}_j - (\mathbf{Y}_D)_{ij}\,d_i\,v_d\,\bar{d}_j - (\mathbf{Y}_U)_{ij}\,u_i\,v_u\,\bar{u}_j, \tag{2.80}$$

the fermion mass matrices are

$$\mathbf{m_e} = \mathbf{Y}_E \times v_d, \qquad \mathbf{m_d} = \mathbf{Y}_D \times v_d, \qquad \mathbf{m_u} = \mathbf{Y}_U \times v_u, \tag{2.81}$$

with v_d and v_u given in Eq. (2.66). As mentioned earlier, we do not include right-handed neutrinos and no neutrino masses are introduced.

So far, all parameters are given in the weak-current eigenstate basis. However, in general, the Yukawa and mass matrices are not diagonal and we need to rotate the (charged) lepton and quark fields from the weak into the mass eigenstate basis,

$$f_{L,R}^{\text{mass}} = \mathbf{V_{f\,L,R}}\, f_{L,R}^{\text{weak}}, \tag{2.82}$$

with $f_{L,R}$ denoting the left- and right-handed fermion fields, respectively and $\mathbf{V_{f\,L,R}}$ denoting the corresponding rotation matrices. The mass matrices in the mass eigenstate basis are then given by

$$\begin{aligned}
\mathbf{V_{e\,L}}\, \mathbf{m_e}\, \mathbf{V_{e\,R}^\dagger} &= \operatorname{diag}(m_e, m_\mu, m_\tau), \\
\mathbf{V_{d\,L}}\, \mathbf{m_d}\, \mathbf{V_{d\,R}^\dagger} &= \operatorname{diag}(m_d, m_s, m_b), \\
\mathbf{V_{u\,L}}\, \mathbf{m_u}\, \mathbf{V_{u\,R}^\dagger} &= \operatorname{diag}(m_u, m_c, m_t),
\end{aligned} \tag{2.83}$$

defined at the weak scale m_Z. The rotation matrices $\mathbf{V_{f\,L,R}}$ are not directly experimentally accessible but only the CKM matrix $\mathbf{V}_{\text{CKM}}$,

$$\mathbf{V}_{\text{CKM}} = \mathbf{V_{u\,L}}\mathbf{V_{d\,L}^\dagger}. \tag{2.84}$$

In general, the rotation matrices for the left-handed fields differ from the those for the right-handed fields. In the following, however, for simplicity and definiteness, we assume real and symmetric Yukawa coupling matrices, thus $\mathbf{V_{f\,L}} = \mathbf{V_{f\,R}}$. Furthermore, since we neglect neutrino masses, $\mathbf{Y}_E$ is diagonal in the weak-current basis. Correspondingly, $\mathbf{V_{e\,L,R}} = \mathbb{1}_3$.

It is instructive to further constrain the quark Yukawa couplings by considering three extreme cases of quark mixing.

- **no mixing:** In the discussion of squark and gluino production we neglect the quark mixing completely and assume the CKM matrix to be unity. This implies

$$\mathbf{V_{u\,L,R}} = \mathbb{1}_3, \qquad \mathbf{V_{d\,L,R}} = \mathbb{1}_3, \tag{2.85}$$

and diagonal Yukawa matrices

$$\begin{aligned}
\mathbf{Y}_U \times v_u &= \operatorname{diag}(m_u, m_c, m_t), \\
\mathbf{Y}_D \times v_d &= \operatorname{diag}(m_d, m_s, m_b).
\end{aligned} \tag{2.86}$$

- **up-type mixing:** In Chapter 8 we refer to up-type mixing, i. e. the quark mixing

takes place completely in the up-quark sector, and

$$\mathbf{V_{u\,L,R}} = \mathbf{V}_{\mathrm{CKM}}, \qquad \mathbf{V_{d\,L,R}} = \mathbb{1}_3. \qquad (2.87)$$

Therefore, in up-type mixing scenarios, the Yukawa matrices are at the weak scale

$$\begin{aligned} \mathbf{Y}_U(m_Z) \times v_u &= \mathbf{V}_{\mathrm{CKM}}^\dagger \cdot \mathrm{diag}(m_u, m_c, m_t) \cdot \mathbf{V}_{\mathrm{CKM}}, \\ \mathbf{Y}_D(m_Z) \times v_d &= \mathrm{diag}(m_d, m_s, m_b). \end{aligned} \qquad (2.88)$$

- **down-type mixing:** We also consider down-type mixing scenarios in Chapter 8, where the quark mixing takes place completely in the down-quark sector, i.e.

$$\mathbf{V_{u\,L,R}} = \mathbb{1}_3, \qquad \mathbf{V_{d\,L,R}} = \mathbf{V}_{\mathrm{CKM}}^\dagger \qquad (2.89)$$

at the weak scale. The Yukawa matrices are then given by

$$\begin{aligned} \mathbf{Y}_U(m_Z) \times v_u &= \mathrm{diag}(m_u, m_c, m_t), \\ \mathbf{Y}_D(m_Z) \times v_d &= \mathbf{V}_{\mathrm{CKM}} \cdot \mathrm{diag}(m_d, m_s, m_b) \cdot \mathbf{V}_{\mathrm{CKM}}^\dagger. \end{aligned} \qquad (2.90)$$

Sfermions

The mass terms of the sfermions arise from all three types of contributions to the scalar potential, F- and D-terms and soft-breaking terms. With the restrictions Eq. (2.53), mixing in the sfermion sector takes place only among the particles within one generation and the sfermion mass matrices can be cast into a 2×2 form. In summary, the sfermion mass terms of the Lagrangian can be written as

$$\mathcal{L}_{\mathrm{sfermions,\ mass}} = -\left(\tilde{f}_{Li}^*,\ \tilde{f}_{Ri}^*\right) \mathcal{M}_{\tilde{f}_i}^2 \begin{pmatrix} \tilde{f}_{Li} \\ \tilde{f}_{Ri} \end{pmatrix} - \tilde{\nu}_i^* \, m_{\tilde{\nu}_i}^2 \, \tilde{\nu}_i, \qquad (2.91)$$

where again $i = 1, 2, 3$ denotes the three generations and $\tilde{f} = \tilde{u}, \tilde{d}, \tilde{e}$. The mass matrix for sfermion $\tilde{f}_i$ being the superpartner of the SM fermion f_i with mass m_{f_i}, has the entries

$$\mathcal{M}_{\tilde{f}_i}^2 = \begin{pmatrix} m_{f_i}^2 + A_i^{LL} & m_{f_i} B_i^{LR} \\ m_{f_i} B_i^{LR} & m_{f_i}^2 + C_i^{RR} \end{pmatrix}, \qquad (2.92)$$

with, assuming real parameters,

$$\begin{aligned} A_i^{LL} &= m_{\tilde{F}_{Li}}^2 - (I_{f_i}^3 - e_{f_i} \sin^2 \theta_W) \, m_Z^2 \cos 2\beta, \\ B_i^{LR} &= A_{f_i} - \mu\kappa, \\ C_i^{RR} &= m_{\tilde{F}_{Ri}}^2 + e_{f_i} \sin^2 \theta_W \, m_Z^2 \cos 2\beta. \end{aligned} \qquad (2.93)$$

Here, $m_{\tilde{F}_{Li}}^2 = m_{\tilde{Q}_i}^2, m_{\tilde{L}_i}^2$ are the left-handed soft-breaking parameters for squarks and sleptons of generation i, respectively, and $m_{\tilde{F}_{Ri}}^2 = m_{\tilde{U}_i}^2, m_{\tilde{D}_i}^2, m_{\tilde{E}_i}^2$ are the corresponding right-handed soft-breaking parameters. A_{f_i} are the trilinear couplings, Eq. (2.53). $I_{f_i}^3$ denotes the eigenvalue of the third component of the weak isospin of sfermion $\tilde{f}_i$ and e_{f_i} its electrical charge. $\kappa = \cot\beta$ for up-type squarks and charged sleptons, while for right-handed squarks it is $\kappa = \tan\beta$. The sneutrino mass matrix $m_{\tilde{\nu}_i}^2$ is one-dimensional (for a given generation i) and has only the purely left-handed entry A^{LL} of Eq. (2.92),

$$m_{\tilde{\nu}_i}^2 = m_{\tilde{L}_i}^2 + \frac{1}{2}\, m_Z^2 \cos 2\beta. \tag{2.94}$$

The sfermion mass matrices can be diagonalized by a unitary 2×2 matrix $U_{\tilde{f}_i}$,

$$\mathcal{D}_{\tilde{f}_i}^2 = U_{\tilde{f}_i} \mathcal{M}_{\tilde{f}_i}^2 U_{\tilde{f}_i}^\dagger = \begin{pmatrix} m_{\tilde{f}_{1i}}^2 & 0 \\ 0 & m_{\tilde{f}_{2i}}^2 \end{pmatrix}, \qquad U_{\tilde{f}_i} = \begin{pmatrix} U_{11}^{\tilde{f}_i} & U_{12}^{\tilde{f}_i} \\ U_{21}^{\tilde{f}_i} & U_{22}^{\tilde{f}_i} \end{pmatrix} = \begin{pmatrix} \cos\theta_{\tilde{f}_i} & \sin\theta_{\tilde{f}_i} \\ -\sin\theta_{\tilde{f}_i} & \cos\theta_{\tilde{f}_i} \end{pmatrix}, \tag{2.95}$$

with the (squared) mass eigenvalues $m_{\tilde{f}_{1i}}^2, m_{\tilde{f}_{2i}}^2$,

$$m_{\tilde{f}_{1i,2i}}^2 = m_{f_i}^2 + \frac{1}{2}\left[(A_i^{LL} + C_i^{RR}) \mp \sqrt{(A_i^{LL} - C_i^{RR})^2 + 4 m_{f_i}^2 (B_i^{LR})^2} \right], \tag{2.96}$$

of the mass eigenstates $\tilde{f}_{1i,2i}$,

$$\begin{pmatrix} \tilde{f}_{1i} \\ \tilde{f}_{2i} \end{pmatrix} = U_{\tilde{f}_i} \begin{pmatrix} \tilde{f}_{Li} \\ \tilde{f}_{Ri} \end{pmatrix}. \tag{2.97}$$

Per convention, the mixing matrix $U_{\tilde{f}_i}$ is chosen such that $\tilde{f}_{1i}$ is the lighter of the two sfermions. In the mass eigenstate basis, the sfermion mass terms of the Lagrangian Eq. (2.91) are given by

$$\mathcal{L}_{\text{sfermions, mass}} = -\left(\tilde{f}_{1i}^*,\ \tilde{f}_{2i}^* \right) \mathcal{D}_{\tilde{f}_i}^2 \begin{pmatrix} \tilde{f}_{1i} \\ \tilde{f}_{2i} \end{pmatrix} - \tilde{\nu}_i^* m_{\tilde{\nu}_i}^2 \tilde{\nu}_i. \tag{2.98}$$

Imposing Eq. (2.95) to hold defines the mixing angle $\theta_{\tilde{f}_i}$ in terms of the soft-breaking parameters. As the off-diagonal elements of $U\mathcal{M}^2 U^\dagger$ have to vanish, one finds

$$B_i^{LR} m_{f_i} \cos 2\theta_{\tilde{f}_i} - \frac{A_i^{LL} - C_i^{RR}}{2} \sin 2\theta_{\tilde{f}_i} = 0 \qquad \Rightarrow \qquad \tan 2\theta_{\tilde{f}_i} = \frac{2 m_{f_i} B_i^{LR}}{A_i^{LL} - C_i^{RR}}. \tag{2.99}$$

It is often useful to reparameterize the mass matrix as a function of the mixing angle

and the mass eigenstates,

$$\mathcal{M}_{\tilde{f}_i}^2 = \begin{pmatrix} \cos^2\theta_{\tilde{f}_i} m_{\tilde{f}_{1i}}^2 + \sin^2\theta_{\tilde{f}_i} m_{\tilde{f}_{2i}}^2 & \sin\theta_{\tilde{f}_i}\cos\theta_{\tilde{f}_i}\left(m_{\tilde{f}_{1i}}^2 - m_{\tilde{f}_{2i}}^2\right) \\ \sin\theta_{\tilde{f}_i}\cos\theta_{\tilde{f}_i}\left(m_{\tilde{f}_{1i}}^2 - m_{\tilde{f}_{2i}}^2\right) & \sin^2\theta_{\tilde{f}_i} m_{\tilde{f}_{1i}}^2 + \cos^2\theta_{\tilde{f}_i} m_{\tilde{f}_{2i}}^2 \end{pmatrix}. \tag{2.100}$$

Together with Eq. (2.92), a second parameterization of the mixing angle can be derived,

$$\sin 2\theta_{\tilde{f}_i} = \frac{2 m_{f_i} B_i^{LR}}{m_{\tilde{f}_{1i}}^2 - m_{\tilde{f}_{2i}}^2} = \frac{2 m_{f_i}(A_{f_i} - \mu\kappa)}{m_{\tilde{f}_{1i}}^2 - m_{\tilde{f}_{2i}}^2}. \tag{2.101}$$

If the mass eigenstates are known, Eq. (2.101) gives a direct relation among the mixing angle and the trilinear coupling.

Focussing on the squark sector, it is important to note that due to the $SU(2)_L$ invariance, the left-handed soft-breaking parameter $m_{\tilde{Q}_i}^2$ is identical in the mass matrices for up-type and down-type squarks. The masses of up- and down-type squarks within one generation i are thus related,

$$\left(U_{11}^{\tilde{d}_i}\right)^2 m_{\tilde{d}_{1i}}^2 + \left(U_{12}^{\tilde{d}_i}\right)^2 m_{\tilde{d}_{2i}}^2 = \left(U_{11}^{\tilde{u}_i}\right)^2 m_{\tilde{u}_{1i}}^2 + \left(U_{12}^{\tilde{u}_i}\right)^2 m_{\tilde{u}_{2i}}^2 + m_{d_i}^2 - m_{u_i}^2 - m_W^2 \cos 2\beta. \tag{2.102}$$

Counting the number of free parameters for one generation of squarks, we find five independent parameters,

$$m_{\tilde{Q}_i}^2, \ m_{\tilde{U}_i}^2, \ m_{\tilde{D}_i}^2, \ A_{u_i}, \ A_{d_i}, \tag{2.103}$$

(plus the SM quark and gauge boson masses), since μ and $\tan\beta$ are usually considered to belong to the higgsino and Higgs sectors. The soft-breaking parameters are directly related to the mass eigenstates (see also Appendix B.2, Eqs. (B.8) and (B.9)) and can be replaced accordingly. Also, Eq. (2.101) relates the trilinear couplings and mixing angles (cf. Eq. (B.10)). Hence, a set of independent parameters equivalent to Eq. (2.103) is given by[10]

$$m_{\tilde{u}_{1i}}^2, \ m_{\tilde{u}_{2i}}^2, \ m_{\tilde{d}_{1i}}^2, \ \theta_{\tilde{u}_i}, \ A_{d_i}, \qquad \text{or} \qquad m_{\tilde{u}_{1i}}^2, \ m_{\tilde{u}_{2i}}^2, \ m_{\tilde{d}_{1i}}^2, \ \theta_{\tilde{u}_i}, \ \theta_{\tilde{d}_i}. \tag{2.104}$$

We will come back to this point later (Section 4.1.2), when we have to fix sets of independent input parameters for a consistent treatment of the squark sector at one-loop level.

To conclude, we recall that the mixing of the sfermion gauge eigenstates (L–R mixing) is proportional to the mass of the SM partner fermion, Eq. (2.101). Neglecting the light quark and lepton masses, the off-diagonal elements of Eq. (2.92) vanish for the sfermions

---

[10]only if $U_{12}^{\tilde{d}_i} \neq 0$, i.e. the dependent squark $\tilde{d}_{i2}$ needs to have a non-zero left-handed component. If $\tilde{d}_{i2} = \tilde{d}_{iR}$, its mass replaces the mass of the heavier squark $m_{\tilde{d}_{i1}}$ in the given set of input parameters.

of the first two generations. This results in trivial mixing matrices U and coinciding gauge and mass eigenstates[11].

Charginos and neutralinos

After EWSB, also the superpartners of the Higgs bosons and of the gauge bosons mix with each other. The charged higgsinos ($\tilde{h}_u^+, \tilde{h}_d^-$) and charged gauginos (winos, $\tilde{W}^\pm$) mix and form two mass eigenstates called charginos ($\tilde{\chi}_{1,2}^\pm$). The neutral higgsinos ($\tilde{h}_d^0, \tilde{h}_u^0$) and gauginos ($\tilde{B}, \tilde{W}^0$) combine to form the four neutralinos ($\tilde{\chi}_{1-4}^0$).

The mass terms for charginos and neutralinos arise from the soft-breaking Lagrangian (terms proportional to the gaugino masses M_1, M_2), from the supersymmetric D-term contribution (Higgs-higgsino-gaugino couplings proportional to g, g'), and from the higgsino mass terms in the superpotential (proportional to μ).

The chargino mass terms in the MSSM Lagrangian are, in the gauge-eigenstate basis,

$$\mathcal{L}_{\text{char., mass}} = -\frac{1}{2}(\Psi^{+T}, \ \Psi^{-T}) \begin{pmatrix} 0 & \mathcal{M}_{\tilde{\chi}^\pm}^T \\ \mathcal{M}_{\tilde{\chi}^\pm} & 0 \end{pmatrix} \begin{pmatrix} \Psi^+ \\ \Psi^- \end{pmatrix} + h.c., \qquad (2.105)$$

$$\text{with} \qquad \Psi^+ = \begin{pmatrix} \tilde{W}^+ \\ h_u^+ \end{pmatrix}, \qquad \Psi^- = \begin{pmatrix} \tilde{W}^- \\ h_d^- \end{pmatrix}.$$

The mass matrix $\mathcal{M}_{\tilde{\chi}^\pm}$ has the following entries,

$$\mathcal{M}_{\tilde{\chi}^\pm} = \begin{pmatrix} M_2 & g v_u \\ g v_d & \mu \end{pmatrix} = \begin{pmatrix} M_2 & \sqrt{2}\sin\beta\,m_W \\ \sqrt{2}\cos\beta\,m_W & \mu \end{pmatrix}, \qquad (2.106)$$

where Eq. (2.66) has been applied in the second step. The mass eigenstates are related to the gauge eigenstates by two unitary 2×2 matrices $U_{\tilde{\chi}^\pm}$ and $V_{\tilde{\chi}^\pm}$,

$$\chi_L^- = U_{\tilde{\chi}^\pm}\,\Psi^-, \qquad \chi_L^+ = V_{\tilde{\chi}^\pm}\,\Psi^+, \qquad \text{with} \qquad \chi_L^\pm = \begin{pmatrix} \chi_{L1}^\pm \\ \chi_{L2}^\pm \end{pmatrix}. \qquad (2.107)$$

One usually combines the left-handed Weyl spinors into four-component Dirac spinors,

$$\tilde{\chi}_i^+ = \begin{pmatrix} \chi_{Li}^+ \\ \overline{\chi}_{Li}^- \end{pmatrix}, \qquad \tilde{\chi}_i^- = \begin{pmatrix} \chi_{Li}^- \\ \overline{\chi}_{Li}^+ \end{pmatrix}, \qquad i = 1, 2. \qquad (2.108)$$

Note that we impose a different mixing Eq. (2.107) for the positively and negatively charged particles, respectively. The mixing matrices have to chosen such that they diagonalize the

---

[11]One might think of scenarios with extreme fine-tuning among the entries of the mass matrix such that $2m_{f_i}B_i^{LR} - (A_i^{LL} - C_i^{RR}) \approx 0$. This results in a non-negligible mixing angle even for small fermion masses, cf. Eq. (2.99), [84]. In the scenarios considered here, however, the mixing angle for light-flavor sfermions can safely be neglected.

mass matrix,

$$U^*_{\tilde{\chi}^\pm} \, \mathcal{M}_{\tilde{\chi}^\pm} \, V^\dagger_{\tilde{\chi}^\pm} = \mathcal{D}_{\tilde{\chi}^\pm} = \text{diag}(m_{\tilde{\chi}_1^\pm}, m_{\tilde{\chi}_2^\pm}), \tag{2.109}$$

where $\mathcal{D}_{\tilde{\chi}^\pm}$ has only real, non-negative entries $m_{\tilde{\chi}_1^\pm}$, $m_{\tilde{\chi}_2^\pm}$. Assuming real parameters only, the chargino masses are given by

$$m^2_{\tilde{\chi}_{1,2}^\pm} = \frac{1}{2}(M_2^2 + \mu^2 + 2m_W^2) \mp \frac{1}{2}\sqrt{(M_2^2 + \mu^2 + 2m_W^2)^2 - 4(\mu M_2 - m_W^2 \sin 2\beta)^2}. \tag{2.110}$$

The neutralino mass terms in the Lagrangian are the following,

$$\mathcal{L}_{\text{neut., mass}} = -\frac{1}{2}\left(\Psi^0\right)^T \mathcal{M}_{\tilde{\chi}^0} \, \Psi^0 + h.\,c. \qquad \text{with} \qquad \left(\Psi^0\right) = \left(\tilde{B}^0, \ \tilde{W}^0, \ \tilde{h}_d^0, \ \tilde{h}_u^0\right)^T, \tag{2.111}$$

where the mass matrix reads

$$\mathcal{M}_{\tilde{\chi}^0} = \begin{pmatrix} M_1 & 0 & -m_Z \sin\theta_W \cos\beta & m_Z \sin\theta_W \sin\beta \\ 0 & M_2 & m_Z \cos\theta_W \cos\beta & -m_Z \cos\theta_W \sin\beta \\ -m_Z \sin\theta_W \cos\beta & m_Z \cos\theta_W \cos\beta & 0 & -\mu \\ m_Z \sin\theta_W \sin\beta & -m_Z \cos\theta_W \sin\beta & -\mu & 0 \end{pmatrix}. \tag{2.112}$$

In order to find the mass eigenstates and to diagonalize the mass matrix $\mathcal{M}_{\tilde{\chi}^0}$, a unitary 4×4 matrix $N_{\tilde{\chi}^0}$ is introduced with properties

$$N^*_{\tilde{\chi}^0} \, \mathcal{M}_{\tilde{\chi}^0} \, N^\dagger_{\tilde{\chi}^0} = \mathcal{D}_{\tilde{\chi}^0} = \text{diag}(m_{\tilde{\chi}_1^0}, m_{\tilde{\chi}_2^0}, m_{\tilde{\chi}_3^0}, m_{\tilde{\chi}_4^0}), \tag{2.113}$$

yielding the neutralino mass eigenstates

$$\chi_L^0 = N_{\tilde{\chi}^0} \, \Psi^0, \qquad (\chi_L^0) = (\chi_{L1}^0, \ \chi_{L2}^0, \ \chi_{L3}^0, \ \chi_{L4}^0)^T. \tag{2.114}$$

Neutralinos are Majorana fermions and we introduce the four Majorana spinors

$$\tilde{\chi}_i^0 = \begin{pmatrix} \chi_{Li}^0 \\ \overline{\chi}_{Li}^0 \end{pmatrix}, \qquad i = 1, \ldots, 4. \tag{2.115}$$

Again, the mixing matrix $N_{\tilde{\chi}^0}$ can be chosen in a way that $\mathcal{D}_{\tilde{\chi}^0}$ has only real, non-negative entries obeying the ordering $m_{\tilde{\chi}_1^0} \leq m_{\tilde{\chi}_2^0} \leq m_{\tilde{\chi}_3^0} \leq m_{\tilde{\chi}_4^0}$.

In general, the neutralino masses are functions of M_1, M_2, μ, $\tan\beta$, obtained by solving quartic equations. In practice, this will be done numerically. The dimension of the parameter space can be reduced by one under the assumption that the gaugino masses unify at

the GUT scale Λ_{GUT}. This assumption is motivated by the (approximate) unification of the gauge couplings if one starts from their experimentally determined values at the weak scale m_Z and runs them up by the renormalization group equations. The gaugino masses run in the same way as the corresponding squared gauge couplings and one finds

$$M_1(\Lambda_{\text{GUT}}) = M_2(\Lambda_{\text{GUT}}) \quad \Rightarrow \quad M_1(m_Z) = \frac{5}{3}\tan^2\theta_W\, M_2(m_Z) \approx \frac{1}{2}M_2(m_Z). \quad (2.116)$$

Furthermore, in many mSUGRA scenarios, EWSB effects can be seen as a small perturbation on the neutralino mass matrix. If $m_Z \ll |\mu \pm M_1|, |\mu \pm M_2|$, the lightest neutralino is bino-like, $\tilde{\chi}_1^0 \approx \tilde{B}$; the second lightest neutralino is wino-like, $\tilde{\chi}_2^0 \approx \tilde{W}$; and the heavier ones are higgsino-like $\tilde{\chi}_{3,4}^0 \approx (\tilde{h}_u^0 \pm \tilde{h}_d^0)/\sqrt{2}$. The approximate masses are then[12]

$$m_{\tilde{\chi}_1^0} = M_1, \quad m_{\tilde{\chi}_2^0} = M_2, \quad m_{\tilde{\chi}_{3,4}^0} = |\mu|. \quad (2.117)$$

The lightest of the neutralino, $\tilde{\chi}_1^0$, is the lightest supersymmetric particle (LSP) in a wide range of the mSUGRA parameter space. Being neutral, massive, weakly interacting and stable (in the $\mathcal{R}$-parity conserving MSSM) it is an attractive candidate particle to form the dark matter in the universe.

Gluinos

Gluinos $\tilde{g}^x$ are the only color octet fermions ($x = 1, \ldots, 8$) and cannot mix with other particles in the MSSM. The mass term is provided by the soft-breaking part of the Lagrangian,

$$\mathcal{L}_{\text{gluino}} = \frac{1}{2}(M_3\,\tilde{g}^x\tilde{g}^x + M_3\,\overline{\tilde{g}}^x\overline{\tilde{g}}^x), \quad (2.118)$$

and the gluino mass is entirely determined by the soft-breaking parameter M_3 (which is in general complex), $m_{\tilde{g}} = |M_3|$. Being Majorana fermions, gluinos are usually described by four-component Majorana spinors $\Psi_{\tilde{g}}$,

$$\Psi_{\tilde{g}} = \begin{pmatrix} \tilde{g} \\ \overline{\tilde{g}} \end{pmatrix}, \quad (2.119)$$

build from the left-handed Weyl spinors $\tilde{g}$ only.

The definition of the MSSM particle spectrum completes our introduction of the framework of our calculations and we will now turn to the discussion of SUSY particle production processes.

---

[12]The given mass ordering assumes $M_1 < M_2 \ll |\mu|$, otherwise the subscript labels have to be rearranged accordingly.

Chapter 3

Production of colored SUSY particles
at hadron colliders

Having introduced the theoretical concept of supersymmetry in the last chapter, we now concentrate on the phenomenological implications of the MSSM. In particular, we are interested in particle physics at colliders. No evidence for supersymmetric particles has been found so far. However with the imminent startup of the LHC at CERN, the TeV scale becomes reachable and thus possibly new SUSY particles of TeV-scale masses should become detectable.

If SUSY is realized, the colored SUSY particles, squarks and gluinos, will be produced at hadron colliders via the strong interaction and high cross sections are expected. The most sensitive direct searches for SUSY particles thus often include gluino and squark production processes, based on promising "jets plus missing transverse energy $(\not{E}_T)$" signatures. Studies for the LHC see the possibility of an early SUSY discovery with 1 fb^{-1} for inclusive multijet plus $\not{E}_T$ final states [85], provided that squark and gluino masses are not too heavy (i.e. below 2 TeV). A good understanding of the theory and reliable theoretical predictions for the production cross sections of the colored SUSY particles gluinos and squarks are vital to the successful analysis of LHC data.

In the following, we will distinguish between squarks of the first two generations ("light-flavor squarks") and third generation squarks (sbottoms, stops). Whereas the light-flavor squarks are often considered to be degenerated in mass, this assumption does not hold for stops and sbottoms, for reasons related to the large third-generation Yukawa couplings. First of all, the latter have to be taken into account in the evolution of the soft-breaking parameters when running down from a high scale to lower scales. Considering the mSUGRA model and assuming a universal scalar mass at the GUT scale, one thus finds at the weak scale lower values for the masses of stops and sbottoms than for those of the squarks of the first generations [86]. Second, the L–R mixing among the gauge eigenstates is proportional to the Yukawa couplings and leads to a substantial splitting between the mass eigenstates of the third-generation squarks, cf. Eqs. (2.92) and (2.99). As a result, the lighter of the top-

squarks, $\tilde{t}_1$, is a candidate for the lightest colored SUSY particle in many SUSY models [87]. In the following, we denote the light-flavor squarks by a common label $\tilde{q}_a = \tilde{q}_L, \tilde{q}_R$, while we refer to the sbottom and stop mass eigenstates with $\tilde{b}_a = \tilde{b}_1, \tilde{b}_2$ and $\tilde{t}_a = \tilde{t}_1, \tilde{t}_2$.

The purpose of this chapter is to give a general overview of the production of colored SUSY particles at hadron colliders, including the results from experimental searches and the basic steps in the theoretical approach. The framework of our studies is the MSSM with $\mathcal{R}$-parity conservation. In these models, (colored) SUSY particles can be produced in pairs only. Hence, possible final states are gluino pairs, squark pairs, as well as mixed gluino–squark pairs.

The outline of this chapter is as follows. We first review the status of experimental direct searches for colored SUSY particles in Section 3.1. In Section 3.2, we discuss how to calculate cross sections at hadron colliders and introduce the parton model and the idea of factorization. The various production channels for colored SUSY particles are presented in Section 3.3, where we also give a short review of the presently available higher-order calculations. At higher orders in perturbation theory, singularities of IR and UV origin arise. The technical treatment of IR singularities and the procedure of regularization and renormalization necessary to obtain a UV-finite result is postponed to Chapter 4.

3.1 Experimental searches

Many experimental direct searches for colored SUSY particles have been performed (and are ongoing) at particle accelerators. So far, no disagreement has been found between data and SM expectations. But the comparison of theoretical predictions for SUSY processes and the experimental results allows to restrict the SUSY parameter space and to set (lower) bounds on the masses of the predicted particles [5]. Usually bounds are defined at 95% confidence level (C.L.), including statistical and systematic uncertainties as well as uncertainties from the theoretical cross sections into the analysis.

Considering the $\mathcal{R}$-parity conserving MSSM, the SUSY particles are produced in pairs and decay subsequently via possibly long decay chains into lighter SUSY particles, ending up with the LSP which is assumed to be the lightest of the neutralinos $\tilde{\chi}_1^0$. The LSP is stable and escapes detection, leading to significant missing transverse energy $\not{E}_T$ in the detectors. A characteristic signal for squark or gluino production is thus $\not{E}_T$ and several jets, the latter arising from the hadronic decays of the colored SUSY particles (for a given mass configuration e.g. $\tilde{g} \to \tilde{q}q$, $\tilde{q} \to \tilde{\chi}^0 q$). Alternative analyses are based on inclusive final states including one or several muons or two like-sign muons, together with high-transverse momentum jets and large $\not{E}_T$. The additional requirement of leptons, in particular of like-sign leptons, reduces the SM background considerably whereas at the same time most of the SUSY signal can be retained [88,89].[13]

---

[13]Also complementary approaches that avoid signatures involving $\not{E}_T$ have been proposed, e.g. [90].
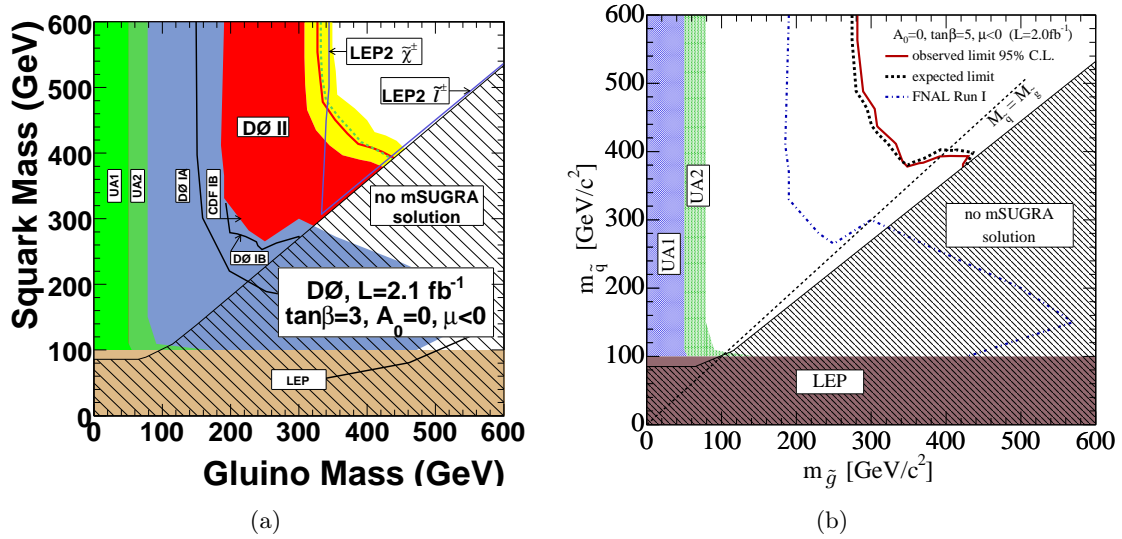
Figure 3.1.: 95% C.L. exclusion regions in the mSUGRA framework, from direct searches by the (a) DØ and (b) CDF collaborations. The solid red (dotted) lines are the limit of the observed (expected) excluded region obtained from the QCD NLO cross section prediction at central scales. The hatched areas indicate the region in the plane with no mSUGRA solution.
(a) Squark and gluino mass plane for $\tan\beta = 3$, $A_0 = 0$ GeV, $\mu < 0$ [91]. The yellow band illustrates the effect of the PDF choice and estimates the factorization and renormalization scale dependence.
(b) Squark and gluino mass plane for $\tan\beta = 5$, $A_0 = 0$ GeV, $\mu < 0$ [92]. The dashed-dotted line recalls the results from Run I at the Tevatron.

3.1.1 Light-flavor squarks and gluinos

Current limits for (light-flavor) squarks and gluinos at hadron colliders include searches performed at Tevatron Run II by the CDF and DØ collaborations, reported e. g. in [91–93]. Fig. 3.1(a) [91] gives an overview of the exclusion bounds obtained from various collider experiments, investigating the squark and gluino mass plane in the mSUGRA framework for $\tan\beta = 3$, $A_0 = 0$ GeV, and $\mu < 0$.

Depending on the relative masses of the squarks and gluinos, analyses based on different signatures are performed. If squarks are heavier than gluinos, gluino pair production is the dominant process. The produced gluinos decay typically via a three-body decay mode into a quark–anti-quark pair and a neutralino ($\tilde{g} \to q\bar{q}\tilde{\chi}_1^0$), leading to four (or more) jets in the final state. In contrast if squarks are lighter, squark–anti-squark pair production is the leading production mechanism, with the subsequent decay of the squarks into a quark and the LSP ($\tilde{q} \to q\tilde{\chi}_1^0$). Final states with only two jets are dominating. Also the missing energy is supposed to be larger than in the first case. Third, in scenarios where squarks and gluinos have similar masses, an event topology with at least three jets is expected from

43

the production of gluino–squark pairs. In this region, the most stringent bounds can be obtained, see Fig. 3.1(a). In [91], 2.1 fb^{-1} of Tevatron data have been analyzed by the DØ collaboration, leading to lower limits of $m_{\tilde{g}} > 308$ GeV and $m_{\tilde{q}} > 379$ GeV for the gluino and (degenerated) squark mass in the considered scenario. Uncertainties from the choice of the PDFs and of the factorization and renormalization scales are estimated and taken into account. Similar results were obtained by the CDF collaboration in an analysis of 2.0 fb^{-1} of data [92], see Fig. 3.1(b). For the considered mSUGRA scenarios ($\tan \beta = 5$, $A_0 = 0$ GeV, $\mu < 0$), all squark masses are excluded for $m_{\tilde{g}} < 290$ GeV, while for equal squark and gluino masses the lower limit $m_{\tilde{g}} = m_{\tilde{q}} > 392$ GeV has been set.

Model independent bounds on squark and gluino masses are difficult to obtain and much weaker so far. In [94], gluino mass limits could be derived from an analysis of event shape data from ALEPH and OPAL. The analysis is based on the fact that new colored SUSY particles would affect the running of α_s and thus the distribution of the event-shape variable thrust. Modifying the SM by adding Δn_f new flavors of mass m at a threshold scale $\mu_{\mathrm{th}} = m$, they compare the thrust distribution with the data for each m and Δn_f. The assumption of a gluino can be described by $\Delta n_f = 3$ (the leading n_f dependence). For this value, the limit $m_{\tilde{g}} > 51$ GeV has been obtained, with theoretical uncertainties included.

3.1.2 Top-squarks (stops)

Experimentally, squarks of the third generation can be distinguished from the squarks of the first and second generations for several reasons. First of all because of their masses, which are in general not degenerated with the light-flavor squarks due to the large quark-Yukawa couplings. Second, the large L–R mixing of the gauge eigenstates cannot be neglected and has to be taken into account in the couplings that enter in the production and decay channels. Third, if the decays are kinematically accessible, stops and sbottoms provide distinct decay signatures involving top and bottom quarks so that b-tagging methods can be used in analyses.

Owing to their potential small mass, the lighter of the top-squarks $\tilde{t}_1$ are of special interest for SUSY searches at particle accelerators. Furthermore, the only SUSY parameter entering the production cross section at LO is the mass of the produced stop, $m_{\tilde{t}_1}$. All other SUSY parameters (as the gluino mass or the stop mixing angle) enter only at higher orders in perturbation theory. As a result, the stop mass can directly be extracted from the cross section measurement in case of discovery. This is different for the production of light-flavor squarks and gluinos, see also the discussion of the various LO processes in Section 3.3.

Most results from top-squark searches depend strongly on the considered SUSY scenario, where specific assumptions on the stop decay signatures can be made from the mass hierarchy among the SUSY particles. The fact that the SM partner of the stops, the top quark,
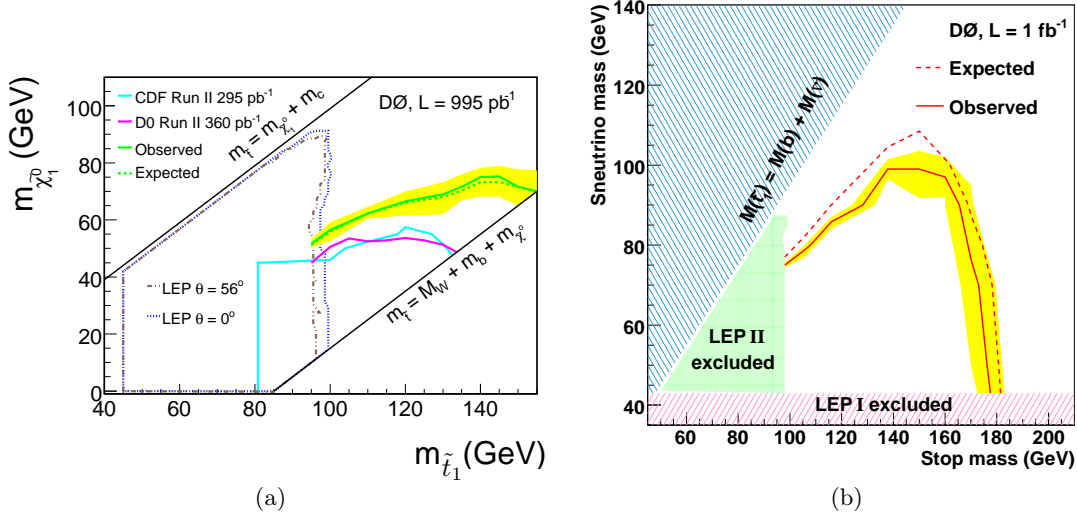
Figure 3.2.: 95% C.L. exclusion regions in the mSUGRA framework, from direct searches for top-squarks by the experiments as labeled. The solid (dotted) lines represent the limit of the observed (expected) excluded region obtained from the QCD NLO cross section prediction at central scales. The yellow band illustrates the effect of the PDF choice and estimates the factorization and renormalization scale dependence.
(a) Neutralino and top-squark mass plane assuming BR($\tilde{t}_1 \to c\tilde{\chi}_1^0$) = 100% [99],
(b) Sneutrino and top-squark mass plane assuming BR($\tilde{t}_1 \to b\ell\tilde{\nu}$) = 100% [100].

is heavy, leads to distinct phenomenological features for stop decays. All possible two- and three-body decay modes of stops have been investigated e.g. in [95].

While for light-flavor squarks the decay into (nearly) massless quarks and the LSP is always kinematically accessible, the decay channels $\tilde{t}_a \to t\tilde{\chi}_1^0$ require the mass relation $m_{\tilde{t}_a} \geq m_t + m_{\tilde{\chi}_1^0}$ and are closed otherwise. Also the decay $\tilde{t}_a \to t\tilde{g}$ is then forbidden as the gluino is obviously heavier than the LSP. Moreover, if the stop is also lighter then the lightest chargino together with a bottom quark, the decay modes $\tilde{t}_a \to b\tilde{\chi}_1^\pm$ are not accessible. In this region of the SUSY parameter space, the flavor-changing loop-induced decay $\tilde{t}_a \to c\tilde{\chi}_1^0$ is the dominating stop decay. Further possible modes include four-body decay channels into a bottom quark, the LSP, and two massless fermions ($\tilde{t}_a \to bff'\tilde{\chi}_1^0$) and three-body decays into a bottom quark, the LSP, and a W boson ($\tilde{t}_a \to bW\tilde{\chi}_1^0$).

Top-squarks searches include analyses from LEP [96], see e.g. [97] for a short review. Also in ep collision at HERA, experimental searches for stops have been performed [98]. Note however that in ep collisions the dominant process is the production of a single stop as a resonance, which is only possible in $\mathcal{R}$-parity violating SUSY models.

Nowadays, the most stringent bounds are provided by the DØ and CDF collaborations based on the Tevatron Run II data [99–101], see also e.g. [102] for more general reviews. Many experimental analyses focused on scenarios where the $\tilde{t}_1$ is the next-to-lightest SUSY

particle (the $\tilde{\chi}_1^0$ being the LSP) and where it is lighter than its SM partner. The considered parameter space is further restricted by assuming $m_{\tilde{t}_1} > m_c + m_{\tilde{\chi}_1^0}$ and $m_{\tilde{t}_1} < m_W + m_b + m_{\tilde{\chi}_1^0}$ so that the $\tilde{t}_1 \rightarrow c\tilde{\chi}_1^0$ is the dominating stop decay. Fig. 3.2(a) shows the according results from a DØ analysis [99], that can be summarized as $m_{\tilde{t}_1} > 150$ GeV for a neutralino mass $m_{\tilde{\chi}_1^0} = 65$ GeV. In Fig. 3.2(b), we also present results from an alternative DØ analysis based on the assumption $\mathrm{BR}(\tilde{t}_1 \rightarrow b\ell\tilde{\nu}) = 100\%$ [100], concentrating on final states with an electron and a muon or with two electrons. The largest stop mass excluded is $m_{\tilde{t}_1} = 175$ GeV for a sneutrino mass $m_{\tilde{\nu}} = 45$ GeV.

If the light stops are considerably heavier, they are probably beyond the kinematical reach of the Tevatron. However, they are well testable at the LHC [88,89]. In this region of the SUSY parameter space, the decay channels into a top-quark and a neutralino is open ($\tilde{t}_1 \rightarrow t\tilde{\chi}^0$). The neutralino can be either the LSP or a heavier neutralino which in turn decays into a LSP. If kinematically allowed, the decay modes into higgsino-like neutralinos are the dominant ones, leading to final states with at least one top-quark and large $\not{E}_T$, possibly with additional lepton pairs and hence provide promising signatures.

3.1.3 Prospects for LHC

Using Markov-chain Monte Carlo methods, the authors of [16] did a probabilistic analysis of the presently available experimental and cosmological constraints to find the most preferred region of the mSUGRA parameter space. Lower bounds on the masses of possibly new SUSY particles can be imposed from direct searches for SUSY particles [5] and also indirectly from Higgs boson searches performed at LEP [43]. Further constraints on SUSY parameters arise from EW precision observables and B-physics (see e.g. [15] and references in [16]), where most observables agree with SM predictions. But there are also observational constraints which allow for an interpretation in favor of the existence of SUSY and which allow to set upper limits on SUSY particle masses: the experimental measurements of the density of cold dark matter [11] that cannot be explained by the SM alone, and of the anomalous magnetic moment of the muon where a derivation of more than three sigma from the best SM calculation has been found [18]. The results of the analysis, taking all these constraints into account, are shown in Fig. 3.3. A comparison with SUSY particle discovery contours as published by the ATLAS and CMS collaborations [88,89] reveals that the 95% C.L. area in the $(M_0, M_{1/2})$ plane lies largely within the region that can be explored within 1 fb^{-1} of good-quality data at a center-of-mass energy of 14 TeV. Thus indeed, the prospects are good that if SUSY exists and is realized around the TeV scale we will detect first SUSY signals at the LHC. We hope that already in the early stage of the LHC we will be able to determine "the fate of many speculations about the relevance of low-energy SUSY to particle physics" [16].
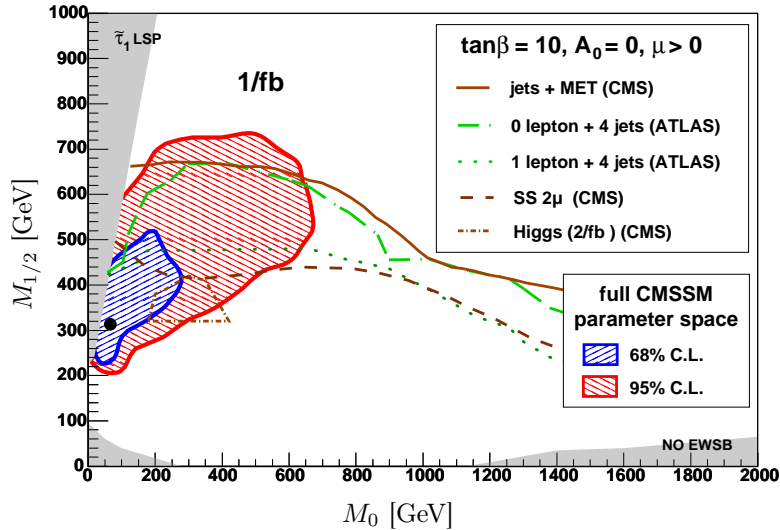
Figure 3.3.: Probabilistic analysis of the mSUGRA parameter space [16]. Shown are the best fit point, the 68%, and the 95% confidence level area in the $(M_0, M_{1/2})$ plane for $\tan\beta$ and A_0 scanned over. For a specific scenario with $\tan\beta = 10$ and $A_0 = 0$ GeV, ATLAS and CMS 5σ discovery contours for 1 fb^{-1} of good-quality data at $\sqrt{S} = 14$ TeV (for 2 fb^{-1} for the Higgs boson discovery in SUSY particle decays) are overlaid. Dark shaded regions are excluded (charged $\tilde{\tau}$ LSP, no EW symmetry breaking, LEP searches).

3.2 Hadronic cross sections

Before we can introduce the various production channels and contributions for a theoretical prediction of the cross sections, we have to discuss how to define cross sections at hadron colliders. In general, we consider the perturbative approach to calculate cross sections for scattering process among the elementary particles of a theory at a given accuracy. It is based on the smallness of the gauge couplings which are used as ordering parameters. If the couplings are large, however, perturbation theory breaks down. This has to be considered when dealing with quarks and gluons, described by QCD. At low scales, the confinement of QCD comes into play, the strong coupling of $SU(3)_C$ increases, and the interacting particles get bound into hadrons. In hadronic collisions, the quarks and gluons are thus not directly accessible and the description of the bound states cannot be performed perturbatively but has to be extracted from experiment. A connection between the short-distance, parton-level interactions and the observable hadronic collisions is delivered by the *parton model* [103] (see also textbooks as e. g. [104]).

In the framework of the parton model, we consider a hadron to consist of point-like constituents, called partons. It has been shown that the partons can be identified as quarks and gluons. A proton is described by three valence quarks (two up-quarks and a down-quark) which determine its quantum numbers, and an infinite sea of virtual gluons

and light-flavor quark–anti-quark pairs. The basic assumption of the parton model is that the interactions of hadrons are due to the interactions of the partons, with the hadron's momentum being distributed among the partons. The most simple approach is to apply the infinite momentum frame, where the momentum of the hadron is considered to be very high and where thus the masses of the hadron and partons can be neglected. Furthermore, one assumes that the partons are moving parallel with the hadron. During the hard scattering process, the partons do not interact among themselves and carry a specified fraction x, $0 < x < 1$, of the hadron's momentum. There is no overlap of the partons of different hadrons before the hard scattering and only one parton is involved in the hard process. In this prescription, we can consider the partons which are involved in the hard scattering as free particles. The process of hadronization only happens after the interaction, on time scales much larger than the interaction itself. As a result, we can evaluate partonic cross sections perturbatively, based on the Feynman diagrammatic approach with partons used as incoming particles.

On the other hand, the non-perturbative hadron structure is described in terms of parton distribution functions (PDFs) or parton densities, which have to be extracted from experiments. These depend solely on the hadron's constitution and are independent of the nature of the hard process. The universal distribution functions can thus be used for the calculation of any hadronic cross section.

Considering a collision of hadrons A and B to produce a generic final state F, the hadronic cross section $d\sigma_{AB \to F}$ is then obtained by a convolution of the partonic cross section $d\hat{\sigma}_{ab \to F}$ with the PDFs of the involved partons a, b and a summation over all possible initial states (factorization, [105]),

$$d\sigma_{AB \to F}(S) = \sum_{a,b} \int_0^1 dx_a \, f_{a/A}(x_a, \mu_F) \int_0^1 dx_b \, f_{b/B}(x_b, \mu_F) \, d\hat{\sigma}_{ab \to F}(x_a x_b S, \mu_F), \quad (3.1)$$

where the PDFs $f_{a/A}(x_a, \mu_F)$ $[f_{b/B}(x_b, \mu_F)]$ give the probability of finding a parton a $[b]$ in the hadron A $[B]$ carrying a fraction x_a $[x_b]$ of the hadron's momentum at a given scale μ_F. At the LHC, both A and B are protons P.

Here, we introduced an arbitrary parameter μ_F, called factorization scale. It separates the long-distance effects entering the non-perturbative hadronic structure and the short-distance region of the hard-scattering process. The scale has to be in the order of a process-typical scale, however its precise value is a-priori unknown. Whereas the PDFs depend on μ_F already at lowest order, the explicit factorization scale dependence of the partonic cross section only arises at NLO and beyond. As the scale is artificial, the factorization scale dependence of the hadronic cross section is expected to decrease when going to higher orders in perturbation theory.

Usually, the parton densities are extracted from measurements of hadronic structure func-

tions in deep inelastic scattering (DIS) and thus obtained at specific reference points, only. For the theoretical computation of hadronic cross sections, we need the PDFs at any given factorization scale however. Combining perturbative QCD and the parton model, the scale dependence of the PDFs can be described by the integro-differential Dokshitzer-Gribov-Lipatov-Altarelli-Parisi (DGLAP) evolution equations [106], including a finite number of higher-order corrections.

For the hard-scattering process, the available center-of-mass (c. m.) squared energy $\hat{s} = x_a x_b S$ is less than the overall hadronic c. m. energy S by a factor of $\tau = x_a x_b$, since the partons i only carry a fraction x_i of their parent's momenta. It is convenient to quantify this by parameterizing the cross section as a product of a parton luminosity factor for the relevant partons and the subprocess cross section for the partonic collision,

$$d\sigma_{AB \to F}(S) = \sum_{a,b} \int_{\tau_0}^1 d\tau \, \frac{d\mathcal{L}_{AB}^{ab}}{d\tau} \, d\hat{\sigma}_{ab \to F}(\tau S) \,, \qquad (3.2)$$

where the differential parton luminosities $d\mathcal{L}_{AB}^{ab}/d\tau$ are defined as follows,

$$\frac{d\mathcal{L}_{AB}^{ab}}{d\tau} = \frac{1}{1 + \delta_{ab}} \int_\tau^1 \frac{dx}{x} \left[f_{a/A}(x, \mu_F) \, f_{b/B}\left(\frac{\tau}{x}, \mu_F\right) + f_{b/A}\left(\frac{\tau}{x}, \mu_F\right) f_{a/B}(x, \mu_F) \right]. \quad (3.3)$$

With the prefactor $1/(1 + \delta_{ab})$ we avoid double counting in case of identical partons. The minimum energy squared at which the partonic process can occur, $\tau_0 S$, provides an lower cutoff on the x-range of the participating partons.

The parton distributions are an essential ingredient in the calculation of hadronic cross sections. For a consistent treatment, the PDFs and the partonic results have to be defined in the same factorization scheme (see Section 4.2.1) and to be determined with a comparable accuracy. In the context of perturbative QCD, next-to-next-to-leading order corrections are currently available. Just from a naive power counting, we can expect electroweak effects of $\mathcal{O}(\alpha)$ to be numerically important at the same level. The inclusion of $\mathcal{O}(\alpha)$ QED corrections into the evolution of the PDFs has two important physical consequences. First of all, the quark and gluon PDFs get altered by additional photon radiation off the partons. Even though this effect is small, it necessarily leads to isospin violation since up- and down-quarks evolve differently when the non-flavorblind photonic effects are included. Second, a non-zero photon density is dynamically generated inside hadrons. This allows to include additional, photon-induced production channels in the calculation of hadronic cross sections.

Currently, the MRST 2004 QED set [107] is the only set of PDFs on the market where $\mathcal{O}(\alpha)$ effects are properly taken into account. The photon density is parameterized as one-photon emission off the valence quarks in the leading-logarithm approximation. As an
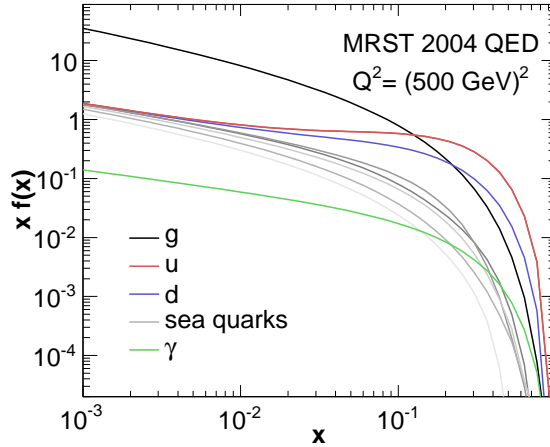
Figure 3.4.: Parton distributions in the proton at $Q^2 = (500 \text{ GeV})^2$, obtained from the $\mathcal{O}(\alpha_s^2)$ QCD and $\mathcal{O}(\alpha)$ QED global fit, according to MRST 2004 QED [107]. The curves for the sea quarks correspond to $\bar{u}$, $\bar{d}$, s, c, and b quark densities.

example for the resulting PDF, we compare in Fig. 3.4 the various parton distributions in the proton at a scale $Q^2 = (500 \text{ GeV})^2$, including $\mathcal{O}(\alpha_s^2)$ QCD and $\mathcal{O}(\alpha)$ QED contributions. Whereas the photon density is smaller by more then one order in magnitude for small fractions x of the proton's momentum, it ranges at the same level as the sea quark densities for higher values $x \gtrsim 0.1$.

3.3 Classification of processes

In the MSSM, colored SUSY particles are produced in pairs at hadron colliders. In this section, we classify the various production mechanisms and final states, starting with the leading order (LO) processes. In the second paragraph, we discuss the next-to-leading order (NLO) corrections of QCD origin. Also EW effects can alter the cross sections considerably and we present the contributing channels in the third paragraph.

3.3.1 Squark and gluino production at LO

Owing to the large interest in squarks and gluinos, theoretical predictions of the LO production cross sections were already published in the 1980's [19]. At hadron colliders, pair production of squarks and gluinos proceeds at lowest order QCD $\mathcal{O}(\alpha_s^2)$ via the following partonic processes [19]. Example Feynman diagrams are given in Fig. 3.5.

- Gluino pairs are produced by gg and $q\bar{q}$ initial states, see Fig. 3.5(a).

- Gluino–squark final states require gluon–quark initial states, the quark and the produced squark being of the same flavor. In the following, we restrict the discussion of

gluino–squark production to left- and right-handed (anti-)squarks of the first two generations. The Feynman diagrams for $\tilde{g}\tilde{q}_a$ production are shown in Fig. 3.5(b). Note that $\tilde{g}\tilde{t}$ final states cannot be produced at LO owing to the vanishing top-quark PDF. Similarly, $\tilde{g}\tilde{b}$ production is suppressed by the bottom-quark PDF. Furthermore, third-generation squarks are experimentally distinguishable from the light-flavor squarks by their decay products (see previous section).

- Squark–squark production at LO QCD proceed only via qq initiated t-channel diagrams. Again we restrict the discussion to light-flavor squarks, which can be produced in any combination of left- and right-handed squarks or anti-squarks ($\tilde{q}_a\tilde{q}_b$, $\tilde{q}_a\tilde{q}'_b$, $\tilde{q}_a^*\tilde{q}_b^*$, $\tilde{q}_a^*\tilde{q}_b'^*$, $a,b = L,R$). As an example, the Feynman diagram for diagonal $\tilde{q}_a\tilde{q}_a$ production is shown in Fig. 3.5(c). The diagram with crossed final states also contributes and is not shown, explicitly.

- Squark–anti-squark pairs are produced via gg fusion and $q\bar{q}$ annihilation, as shown in Fig. 3.5(d) and (e) for diagonal $\tilde{q}_a\tilde{q}_a^*$ production. The $q\bar{q}$ initiated processes can be either gluon-mediated s-channel diagrams with quarks of any flavor in the initial state, cf. the last diagram of Fig. 3.5(d), or gluino-mediated t-channel diagrams, cf. Fig. 3.5(e) (referring also to the diagram with crossed final states). Only the diagram Fig. 3.5(e) also allows for the production of non-diagonal ($\tilde{q}_a\tilde{q}_b^*$) and mixed-flavor ($\tilde{q}_a\tilde{q}_b'^*$) squark pairs.

- Stop–anti-stop (and sbottom–anti-sbottom) pair production has to be discussed separately from $\tilde{q}\tilde{q}^*$ production since, excluded by the PDF, it does not proceed via $q\bar{q}$ initiated t-channel diagrams. Moreover, the L–R mixing of the mass eigenstates has to be taken into account. Due to the absence of the t-channel diagram, stops (and sbottoms) can only be produced diagonally at LO QCD (i.e. $\tilde{t}_a\tilde{t}_a^*$, $a = 1,2$) since the involved $g\tilde{t}\tilde{t}^*$ and $gg\tilde{t}\tilde{t}^*$ couplings conserve the chirality and mass eigenstate.

At lowest order QCD, mixed-flavor $\tilde{t}\tilde{b}^*$ and $\tilde{t}^*\tilde{b}$ pairs cannot be produced. The dominant contributions to mixed $\tilde{t}\tilde{b}^*$ production are of $\mathcal{O}(\alpha^2)$, induced by the weak $W\tilde{t}\tilde{b}$ vertex. These processes have been studied in in [108] and in [109], where additionally real quark radiation via the semi-weak $Wg\tilde{t}\tilde{b}$ vertex has been included. Also, the production of non-diagonal stop–anti-stop pairs is loop suppressed at hadron colliders and occurs at $\mathcal{O}(\alpha_s^4)$ [21]. The only tree-level mechanism proceeds by Z-boson exchange in $q\bar{q}$-annihilation channel, yielding contributions at $\mathcal{O}(\alpha^2)$ [108]. In the following, we however restrict the discussion to the production of diagonal stop–anti-stop pairs.

Which of the processes is the dominant one? The answer to this question depends of course crucially on the masses of the produced particles. Furthermore, the interplay of the various parton-level production channels is specific for a given hadronic c. m. energy and is different for PP or $P\bar{P}$ colliders. We refer to SUSY particle production at the LHC and
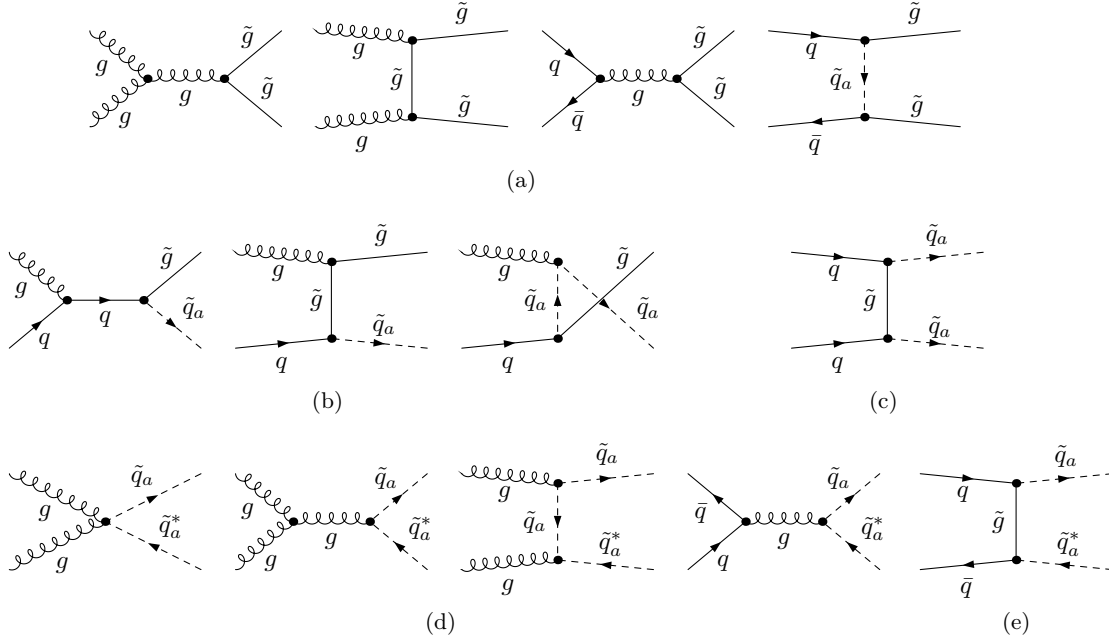
Figure 3.5.: Parton-level Feynman diagrams at LO for the following processes: (a) $\tilde{g}\tilde{g}$ production, (b) $\tilde{g}\tilde{q}_a$ production, (c) $\tilde{q}_a\tilde{q}_a$ production, (d) $\tilde{q}_a\tilde{q}_a^*$, $\tilde{b}_a\tilde{b}_a^*$ or $\tilde{t}_a\tilde{t}_a^*$ production, (e) additional t-channel diagram for $\tilde{q}_a\tilde{q}_a^*$ production. Diagrams with cross final states are not shown explicitly.

cite in Fig. 3.6 the relative weights of $\tilde{g}\tilde{g}$, $\tilde{g}\tilde{q}$, $\tilde{q}\tilde{q}$, and $\tilde{q}\tilde{q}^*$ final states in PP collisions at a c. m. energy of $\sqrt{S} = 14$ TeV as presented in [20]. As a typical mass ratio of (degenerated) light-flavor squark masses and the gluino mass, the values 0.8 and 1.6 have been chosen. If squarks are lighter than gluinos, cf. Fig. 3.6(a), then $\tilde{g}\tilde{q}$ final states dominate in the range of intermediate masses. In the high-mass range, $m_{\tilde{q}}$, $m_{\tilde{g}} > 1$ TeV, predominantly $\tilde{q}\tilde{q}$ pairs are produced. These proceed from qq-induced initial states and profit from the high valence-quark density in the large-x region. In contrast, if the gluino is lighter than squarks, cf. Fig. 3.6(b), the $\tilde{g}\tilde{g}$ pairs contribute with more than 50% to the inclusive cross section. $\tilde{q}\tilde{q}$ and $\tilde{q}\tilde{q}^*$ final states are suppressed considerably, while $\tilde{g}\tilde{q}$ production is important for masses around the TeV scale.

A reliable prediction of the cross sections however needs to include contributions beyond LO QCD, both of QCD and EW origin. They not only give important corrections to the total cross section results, but also provide a higher stability of the cross section against a variation of the factorization and renormalization scale.
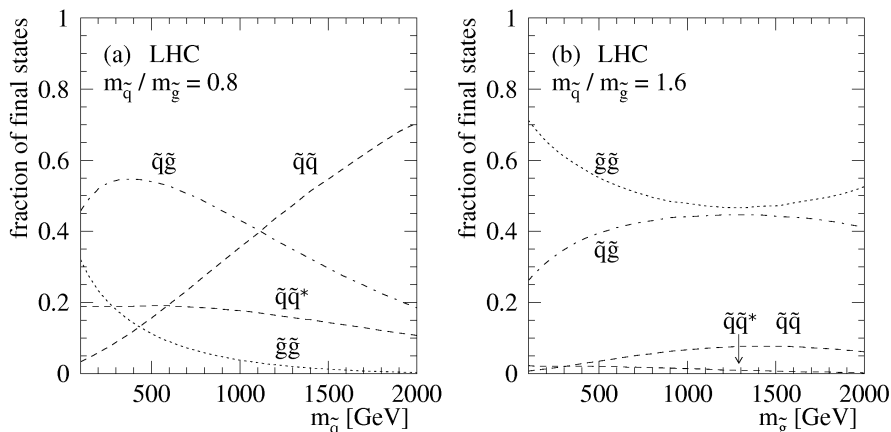
Figure 3.6.: The relative yields at LO of $\tilde{g}\tilde{g}$, $\tilde{g}\tilde{q}$, $\tilde{q}\tilde{q}$, and $\tilde{q}\tilde{q}^*$ final states in squark and gluino pair production processes at the LHC [20]. The ratio of light-flavor squark masses and the gluino mass is set to (a) $m_{\tilde{q}}/m_{\tilde{g}} = 0.8$ and (b) $m_{\tilde{q}}/m_{\tilde{g}} = 1.6$.
In Ref. [20], the PDF set GRV 94 [110] and central factorization and renormalization scales ($\mu = m_{\tilde{q}}$ for squark pairs, $\mu = m_{\tilde{g}}$ for gluino pairs, and $\mu = (m_{\tilde{g}} + m_{\tilde{q}})/2$ for gluino–squark pairs in the final state) are chosen.

3.3.2 Higher-order QCD corrections

The NLO QCD corrections of $\mathcal{O}(\alpha_s^3)$ have been calculated in [20] for gluino and squark pair production, with the restriction to final-state squarks of the first two generations, and in [21] for the production of stop–anti-stop pairs. The results can be included in analyses via the public program `Prospino` [111]. Depending on the considered SUSY scenario, the NLO QCD typically alter the cross section for squark and gluino production at the LHC by 20–30%. Even higher corrections can be obtained in case of stop–anti-stop pair production. Also, the cross sections are stabilized considerably against the uncertainty from the proper choice of factorization and renormalization scale.

Only recently, first results beyond the one-loop level in QCD have become available. The NLO QCD corrections get important contributions from the energy region near the partonic production threshold ($\tau_H = 4m^2/\hat{s}$, m being the average mass of one produced particle). In this region, the c. m. velocity of the produced particles is small and the corrections are dominated by Coulomb corrections (the exchange of gluons) and soft gluon corrections (initial and final state emission of low-energy gluons) [20].

In [22], the soft gluon corrections have been resummed at next-to-leading logarithmic (NLL) accuracy, for squark–anti-squark and gluino pair production processes. Matching consistently the NLL resummed and full NLO cross sections, the cross section predictions are altered by 8% (for $\tilde{g}\tilde{g}$ production with $m_{\tilde{g}} = 1$ TeV, $m_{\tilde{q}} = 833$ TeV) and 2% (for $\tilde{q}\tilde{q}^*$ production with $m_{\tilde{g}} = 2$ TeV, $m_{\tilde{q}} = 1$ TeV). In particular, the scale dependence was shown to be reduced significantly in case of $\tilde{g}\tilde{g}$ production, where the soft gluon corrections
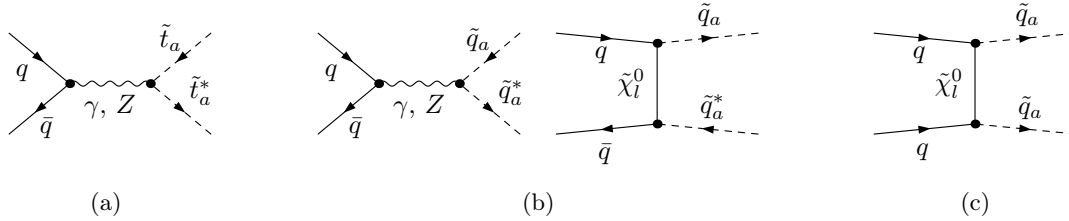
Figure 3.7.: Tree-level EW Feynman diagrams for (a) $\tilde{t}_a\tilde{t}_a^*$ production, (b) $\tilde{q}_a\tilde{q}_a^*$ production, (c) $\tilde{q}_a\tilde{q}_a$ production.

are especially important due to the dominance of the gg-induced channel.

Starting from the available NLO QCD results for squark–anti-squark production at the LHC [20,111], the authors of [23] present approximate next-to-next-to-leading order (NNLO) QCD predictions that include soft gluon resummation to next-to-next-to-leading logarithmic (NNLL) accuracy as well as the complete two-loop Coulomb corrections. As a result, the $\tilde{q}\tilde{q}^*$ production cross section is increased by 9% at (approx.) NNLO compared to NLO QCD ($m_{\tilde{g}} = 500$ GeV, $m_{\tilde{q}} = 400$ GeV) and the uncertainty due to a variation of (common) renormalization and factorization scales could be reduced to 3%.

3.3.3 Electroweak contributions

As we know from SM processes (see e. g. [112]), also electroweak corrections can give sizeable effects to production cross sections of colored particles. The full EW contribution includes both tree-level EW production processes and higher-order corrections of EW origin.

Tree-level EW production mechanisms

The above described tree-level production mechanisms of $\mathcal{O}(\alpha_s^2)$ are the dominant ones for squark and gluino production at hadron colliders. But diagonal and non-diagonal squark pairs can also be produced by $q\bar{q}$ induced tree-level EW processes [113,114].

For stops and sbottoms, only s-channel diagrams with photon or Z boson exchange are present at $\mathcal{O}(\alpha^2)$, shown in 3.7(a). These contributions are suppressed by the coupling and, as we will see later, give negligible contributions only. However the production of squark–anti-squark pairs of the first generations has a richer kinematic structure. Additional t-channel diagrams mediated by a neutralino (or chargino, if an up-type–down-type squark pair is produced) are present, cf. Fig. 3.7(b). As a consequence, also non-zero interferences of $\mathcal{O}(\alpha_s\alpha)$ between the $q\bar{q}$-initiated QCD-mediated and EW-mediated diagrams arise. In case of squark–squark production, only gaugino-mediated t-channel diagrams are allowed from the fermion flow, shown in Fig. 3.7(c). For diagonal and same-flavor $\tilde{q}_a\tilde{q}_a$ production (and $\tilde{q}_L\tilde{q}'_L$ production where q and q' denote $SU(2)_L$ partners of the same generation) also diagrams with crossed final states are present, both of QCD- and EW origin. In this case,
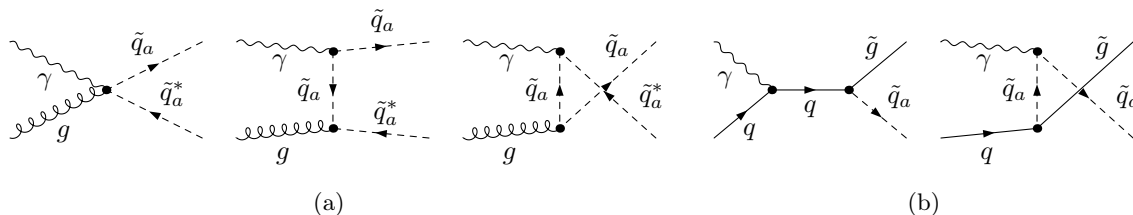
Figure 3.8.: Feynman diagrams for photon-induced (a) $\tilde{q}_a \tilde{q}_a^*$ (and $\tilde{t}_a \tilde{t}_a^*$) production and (b) $\tilde{g}\tilde{q}_a$ production at tree-level.

the EW diagrams can interfere with the QCD-mediated diagrams and form an important part of the full EW contribution.

As an independent production mechanism, photon-induced processes give further tree-level contributions to the production of colored SUSY particles. At the hadronic level, these processes vanish at leading order owing to the non-existence of a photon distribution inside the proton. At NLO in QED, however, a non-zero photon density arises in the proton as a direct consequence of including higher-order QED effects into the evolution of PDFs, leading thus to non-zero photon-induced hadronic contributions (see the discussion in Section 3.2).

Largest cross sections are obtained from photon-induced $2 \to 2$ processes, contributing to (top-)squark pair production (via photon–gluon fusion, cf. Fig. 3.8(a)) and to gluino–squark production (via photon–quark fusion, cf. Fig. 3.8(b)). Although these channels are in general suppressed by the photon distribution, they can become sizable. In particular, as we will see later, photon-induced stop–anti-stop production turns out to be important and needs to be included in analyses.

Higher-order EW corrections

Finally, also higher-order EW corrections alter the predictions for squark and gluino production process at hadron colliders. We concentrate on the NLO EW corrections of $\mathcal{O}(\alpha_s^2 \alpha)$. From naive power counting, we expect contributions of comparable size to NNLO QCD corrections.

The structure of NLO EW corrections can be rather complex.

First of all, contributions of $\mathcal{O}(\alpha_s^2 \alpha)$ arise from the interference of tree-level QCD amplitudes and one-loop diagrams with EW insertions, see the example diagrams in Fig. 3.9 (a). The supersymmetric final states do not allow to separate the SM-like corrections from the superpartner contributions which are necessary for the cancellation of ultraviolet singularities that arise in the loop diagrams. As the photino is not a mass eigenstate of the theory, it is also not possible to split the EW corrections into a QED and a weak part, which is often the case in SM processes (see e. g. [112]). In order to obtain a finite result, one has to deal with the complete set of virtual EW corrections including photonic contributions.

(a)

(b)

(c)

Figure 3.9.: Example Feynman diagrams for virtual NLO EW corrections to squark–anti-squark production. At $\mathcal{O}(\alpha_s^2 \alpha)$, there are interference contributions from
(a) QCD-mediated Born diagrams and one-loop diagrams with EW insertions,
(b) EW-mediated s-channel Born diagrams and one-loop box diagrams with QCD insertions,
(c) EW-mediated t-channel (and resp. u-channel) Born diagrams and full pure-QCD one-loop amplitude.

Second, as discussed above, also tree-level EW diagrams are present for squark and top-squark pair production. The interference terms of tree-level EW diagrams with pure-QCD one-loop diagrams give additional contributions at $\mathcal{O}(\alpha_s^2 \alpha)$ and need to be included. In case of stop–anti-stop production, the only non-zero interference terms arise from the EW s-channel diagrams combined with QCD boxes (see Fig. 3.9 (b)). For light-flavor squarks however, the additional gaugino-mediated t-channel diagrams give rise to interference contributions with the full QCD one-loop amplitude, cf. Fig. 3.9 (c).

The virtual corrections comprise loop diagrams where the external particles exchange a massless photon or gluon. These contributions cause infrared singularities in the limit of vanishing momentum transfer. In order to cure the singularities, real photon and gluon radiation processes have to be taken into account and constitute the third part of $\mathcal{O}(\alpha_s^2 \alpha)$ corrections. Lastly, also real quark and real anti-quark bremsstrahlung contributes at $\mathcal{O}(\alpha_s^2 \alpha)$ through the interference of EW-mediated and QCD- mediated diagrams.

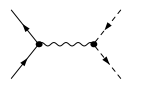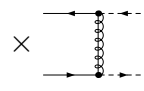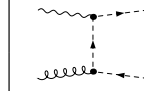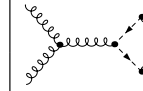|	$\mathcal{O}(\alpha_s^2)$	$\mathcal{O}(\alpha_s^3)$	$\mathcal{O}(\alpha^2)$	$\mathcal{O}(\alpha_s\alpha)$	$\mathcal{O}(\alpha_s\alpha)$	$\mathcal{O}(\alpha_s^2\alpha)$
$\tilde{g}\tilde{g}$	+	+	−	−	−	+
$\tilde{g}\tilde{q}$	+	+	−	−	+	+
$\tilde{q}\tilde{q}$	+	+	+	+	−	+
$\tilde{q}\tilde{q}^*$	+	+	+	+	+	+
$\tilde{t}\tilde{t}^*$	+	+	+	−	+	+

Table 3.1.: Overview of contributions up to the one-loop level to squark and gluino pair production processes. The processes divide into five classes, $\tilde{g}\tilde{g}$, $\tilde{g}\tilde{q}$, $\tilde{q}\tilde{q}$, $\tilde{q}\tilde{q}^*$, and $\tilde{t}\tilde{t}^*$ production. The LO processes are of $\mathcal{O}(\alpha_s^2)$, NLO QCD corrections of $\mathcal{O}(\alpha_s^3)$, contributing to all processes, as indicated by the + symbol in the table.
The EW contributions consist of tree-level $\mathcal{O}(\alpha^2)$ diagrams ($\tilde{q}\tilde{q}$, $\tilde{q}\tilde{q}^*$, $\tilde{t}\tilde{t}^*$ only) and EW-QCD interference terms of $\mathcal{O}(\alpha_s\alpha)$ (light-flavor $\tilde{q}\tilde{q}$, $\tilde{q}\tilde{q}^*$ only), photon-induced processes of $\mathcal{O}(\alpha_s\alpha)$ ($\tilde{g}\tilde{q}$, $\tilde{q}\tilde{q}^*$, $\tilde{t}\tilde{t}^*$ only), and NLO EW contributions of $\mathcal{O}(\alpha_s^2\alpha)$ (to all processes).
For each contribution of a specified order of perturbation theory, an example Feynman graph is depicted in the last row.

The focus of this thesis is on the calculation of the EW contribution to gluino–squark [25], stop–anti-stop [24], and squark–squark production [115], including the tree-level EW diagrams of $\mathcal{O}(\alpha^2(+\alpha_s\alpha))$, photon-induced processes of $\mathcal{O}(\alpha_s\alpha)$, and NLO EW corrections of $\mathcal{O}(\alpha_s^2\alpha)$. Gluino–gluino and squark–anti-squark final states have been further investigated in [26,27] and will not be discussed in more detail, here.

The calculation of NLO EW corrections is nontrivial, in particular the proper treatment of ultraviolet and infrared singularities needs care. It is the purpose of the next chapter to present all details that are required in order to obtain a finite cross section at $\mathcal{O}(\alpha_s^2\alpha)$.

To conclude this section, we summarize the five dominant classes of production processes for colored SUSY particles in Tab. 3.1 and indicate the QCD and EW contributions up to the one-loop level. For each contribution of a specified order of perturbation theory, an example Feynman graph is depicted in the last row.

Chapter 4
How to obtain a finite result at $\mathcal{O}(\alpha_s^2\alpha)$

In a calculation of cross sections at higher orders in perturbation theory one typically has to deal with several kinds of singularities. Ultraviolet (UV) singularities arise from infinite momenta in the evaluation of self-energy and vertex diagrams and require a proper regularization and renormalization of the theory. Moreover, infrared (IR) singularities are caused by loop integrals and real radiation diagrams where massless particles are attached to external on-shell particles. At $\mathcal{O}(\alpha_s^2\alpha)$, both photons and gluons enter the diagrams and a careful treatment of singularities is needed to obtain an IR-finite result.

In this chapter, we first refer to UV singularities and discuss the procedure of regularization and renormalization in Section 4.1. Second, the treatment of IR singularities is described in Section 4.2.

4.1   Handling ultraviolet singularities

In general, the Lagrangian of a given model involves free parameters which are not fixed by the theory but have to be determined experimentally. At tree level, these parameters can be chosen in such a way that they directly correspond to physical observables like masses or couplings. If higher-order contributions are taken into account, however, this direct correspondence is destroyed and modified relations have to be established. The scheme which defines the parameters via their relations to measurable quantities is called a renormalization scheme. Moreover, the higher-order corrections involve loop diagrams which diverge for arbitrarily high energies. The parameters of the original Lagrangian, the bare parameters, thus differ from the corresponding physical quantities by UV-divergent contributions. For a consistent mathematical treatment, the divergences have to be regularized to render the integrals finite. As a result, the bare parameters do not have any physical meaning and have to be replaced by renormalized quantities. By choosing a suitable renormalization scheme, the renormalized parameters absorb our ignorance of physics entering beyond the UV cutoff scale and allow to make theoretical predictions for observable quantities in terms of the parameters determined by experiments, independent on the regularization procedure.

Only in renormalizable theories, all UV divergences can be removed by an appropriate re-definition of the fields and parameters in the Lagrangian, and finite results are obtained in each order of perturbation theory. It was proven by 't Hooft [45] that the SM as a non-Abelian gauge theory with spontaneous symmetry breaking is renormalizable. The renormalizability of supersymmetric extension of the SM, the MSSM, was shown in [116].

We first discuss briefly the general ideas of regularization and renormalization methods in Sections 4.1.2 and 4.1.2, respectively. We then focus on the processes considered in this report, where we need to renormalize the quark and squark sector and also the strong sector. The renormalization of these sectors is worked out in detail in Section 4.1.3.

4.1.1 Regularization

Higher-order loop diagrams give rise to UV singularities from the integration over internal loop momenta in the region where the integration momenta become infinite. The divergences can be extracted by introducing a regulator Λ, such that the integrals are finite but dependent on Λ. As anticipated above, the problem of the treatment of divergent integrals thus results in the problem how to obtain theoretical predictions that do not depend on the unphysical regularization parameter Λ and renormalization (see below) is required.

The choice of a mathematically consistent regularization is not unique and different procedures have been worked out. The most intuitive method is provided by the *Pauli-Villars regularization* [117]: One simply introduces an upper cutoff parameter on the momentum integration to prevent the integral from reaching the UV-divergent limit. As a drawback, results obtained in the Pauli-Villars prescription are in general not gauge-invariant.

Alternative approaches are based on a dimensional analysis. In four dimensions, the integrals are UV divergent. However, if the number of dimensions is reduced by an infinitesimal value ϵ to a new dimension $D = 4 - \epsilon$, the integrals converge. The UV singularities then appear as poles in ϵ. In order to keep integrals and couplings dimensionless and independent of the dimensions D of space-time, the integrals have to be multiplied with the factor $(2\pi\mu)^{4-D}$, where the additional parameter μ has the dimension of a mass.

The described procedure is called *dimensional regularization* [118,119], and is commonly used for SM calculations. As a consequence of the extension to D dimensions, also the Dirac matrices γ_μ need to be defined as D-dimensional objects (satisfying the usual anti-commutation relations and hermiticity conditions, see Eq. (A.6)). The generalization of γ_5 to D dimensions is more involved and different treatments are possible [119–121]. We adopt the approach of [121] and consider anticommuting relations of γ_5 and γ_μ in D dimensions together with the non-zero trace $\text{Tr}(\gamma_5\gamma_\mu\gamma_\nu\gamma_\rho\gamma_\sigma) = 4i\epsilon_{\mu\nu\rho\sigma}$ (see App. A.2).

Using the space-time as an regulator, dimensional regularization preserves Lorentz and gauge invariance and is appropriate for higher-order calculations. However, considering a supersymmetric theory in D dimensions leads to a mismatch between the $(D-2)$ number

of d.o.f. for gauge bosons and the 2 gauginos d.o.f.. This $\mathcal{O}(\epsilon)$ mismatch results in finite, non-zero contributions and thus SUSY is explicitly broken at higher orders.

An elegant way to avoid the symmetry violation is provided by the *dimensional reduction* scheme [122]. The idea is to only continue the number of space-time dimensions to D, while keeping the number of components of the fields fixed. Early problems of the scheme [123] could be solved [124]. For a mathematical consistent formulation, the four-dimensional space is realized as quasi-four-dimensional space, where gauge fields and in particular Dirac matrices remain four-dimensional objects but Fierz identities do not hold.

4.1.2 Renormalization

The regularization procedure of higher-order contributions introduces unphysical parameters into the theory. Different to the situation in tree-level considerations, the bare parameters of the original Lagrangian do not have a physical meaning anymore and may be replaced. Renormalization of the theory allows to cure the dependence on the regularization parameter and to replace the UV-divergent bare parameters by finite renormalized quantities and divergent renormalization constants (counterterms) such that the parameters of the theory can be related again to physical observables.

Within the common approach of multiplicative renormalization, we write for a generic bare parameter g_0 of the Lagrangian

$$
\begin{aligned}
g_0 \;\longrightarrow\; Z_g g &= \left(1 + \delta Z_g^{(1)} + \delta Z_g^{(2)} + \dots\right) g \\
&\equiv g + \delta g^{(1)} + \delta g^{(2)} + \dots,
\end{aligned}
\tag{4.1}
$$

where g is the UV-finite renormalized parameter. All singularities are absorbed into the the renormalization constant Z_g. In Eq. (4.1), a perturbative expansion of Z_g in the regularization parameter up to order i makes the counterterms $\delta g^{(i)}$ explicit. In the following, we are only interested in one-loop corrections and second order terms will be neglected. i.e. $g_0 \;\longrightarrow\; g + \delta g$, where the superscript $i = 1$ is suppressed.

Renormalization of the parameters is sufficient to obtain finite S-matrix elements, but it leaves Green functions divergent. This is due to the fact that radiative corrections change the normalization of the fields by an infinite amount. In order to get finite propagators and vertex functions, also the fields need to be renormalized. We proceed analogously and replace the bare fields ψ_0 in the Lagrangian by normalized fields ψ and field renormalization constants Z_ψ. Again, the renormalization constant can be written as an perturbative expansion, $Z_\psi = 1 + \delta Z_\psi^{(1)} + \delta Z_\psi^{(2)} + \dots$, yielding at one loop the replacement rule

$$
\psi_0 \;\longrightarrow\; \sqrt{Z_\psi}\,\psi = \left(1 + \frac{1}{2}\delta Z_\psi\right)\psi.
\tag{4.2}
$$

In general, radiative corrections provide non-diagonal corrections to mass matrices and the bare fields are no longer mass eigenstates. In this case, one has to introduce matrix valued field renormalization constants in order to re-diagonalize the mass matrices. These allow to define the renormalized fields in such a way that they are the correct physical mass eigenstates in all orders of perturbation theory.

With the above definitions of the renormalized parameters and fields, one can split the bare Lagrangian $\mathcal{L}_0$ as follows,

$$\mathcal{L}_0(g_0, \psi_0) = \mathcal{L}(g, \psi) + \delta\mathcal{L}(g, \delta g, \psi, \delta Z_\psi \psi), \tag{4.3}$$

where the Lagrangian $\mathcal{L}$ has the same form has $\mathcal{L}_0$ but depends on renormalized parameters and fields instead of unrenormalized ones. All counterterms are contained in $\delta\mathcal{L}$. They give rise to additional Feynman diagrams which have to be added to the loop graphs. In the sum of both, loop corrections and counterterms, all UV-divergent parts cancel and finite quantities are obtained.

Renormalization schemes

The choice of the renormalization constants is arbitrary to a great extent, only their divergent parts have to match the divergent parts of the relevant loop integrals. The finite parts are fixed by renormalization conditions which establish a relation between the independent parameters of the theory and physical observables. Different renormalization schemes can be based on distinct sets of physical input variables and can lead to differences among the finite parts of the renormalization constants. In an exact calculation to all orders in perturbation theory, the final result does not depend on the renormalization scheme. But at finite orders, differences among results obtained in distinct schemes remain. These can be understood as an estimate of the theoretical uncertainty induced by missing higher-order corrections. In the following, we will distinguish between three schemes.

- $\overline{MS}$ *scheme:*
  In the minimal subtraction (MS) scheme [45] only the UV-divergent parts are absorbed into the counterterms of the Lagrangian, but no finite contributions. The evaluation of loop diagrams is based on dimensional regularization and the UV-divergent parts are thus proportional to $\propto 1/\epsilon$. A convenient generalization of the MS scheme is provided by the modified minimal subtraction ($\overline{MS}$) scheme [125,126] where not only the pure ϵ-poles are absorbed, but also finite remnants of the regularization procedure. At one-loop order, the divergent terms are proportional to Δ,

$$\Delta = \frac{2}{\epsilon} - \gamma_E + \ln 4\pi, \tag{4.4}$$

  where γ_E is the Euler-Mascheroni constant. The scale at which the counterterms

are absorbed is the renormalization scale μ_R. Absorbing also constants into the counterterms according to Eq. (4.4), the renormalization scale in the $\overline{\text{MS}}$ scheme is related to the scale parameter μ introduced by the regularization procedure via

$$\ln(\mu_R^2) = -\gamma_E + \ln 4\pi + \ln \mu^2. \qquad (4.5)$$

Results obtained in the $\overline{\text{MS}}$ prescription depend on the choice of the renormalization scale. Again, this scale dependence reflects the theoretical uncertainty of a fixed order calculation and has to cancel if contributions from all orders are taken into account.

- $\overline{DR}$ *scheme:*

  This scheme follows the same approach as the $\overline{\text{MS}}$ scheme except for the fact that the divergent integrals are regularized by dimensional reduction. The renormalization scale is defined according to Eq. (4.5). At the one-loop level, the counterterms within both schemes are identical. Only at higher orders different finite contributions from the two regularization schemes induce a disagreement.

- *OS scheme:*

  In the on-shell (OS) scheme [127] one imposes direct relations between the renormalized parameters in the Lagrangian and physical observables at all orders in perturbation theory. The renormalized mass parameter of a particle is required to equal its physical mass, i.e. it corresponds to the real part of the pole of its propagator. In case of mass matrices, these conditions have to be fulfilled by the corresponding eigenvalues. The resulting expressions can be simplified by requiring simultaneously on-shell conditions for the field renormalization matrices. These state that the renormalized fields are properly normalized, i.e. that the renormalized propagators have unity residues and that the renormalized one-particle irreducible (1PI) two-point functions (the inverse of the renormalized propagators) are diagonal for on-shell external particles. As a consequence, the renormalization conditions for the mass parameters involve only diagonal self energies.

  Also couplings can be renormalized "on-shell", by defining the coupling counterterm to absorb all loop-induced corrections. By construction, if all quantities arising in a calculation are determined to be on-shell, the final result does not depend on the mass scale introduced by regularization.

  The complete OS renormalization conditions have been worked out for the SM in [127, 128] and were generalized to the MSSM in [69].

4.1.3 Renormalization for squark and gluino pair production at $\mathcal{O}(\alpha_s^2 \alpha)$

The strategy of our calculations is as follows. As described above, we replace the bare parameters in the Lagrangian with renormalized quantities and renormalization constants. A

perturbative expansion of the renormalization constants allows to split the bare Lagrangian $\mathcal{L}_0$ in an original-like part $\mathcal{L}$ and a counterterm part $\delta\mathcal{L}$. The latter gives rise to additional interactions and Feynman diagrams (counterterm diagrams), in terms of the renormalization constants. The counterterm diagrams have to match the singular parts of the virtual corrections. Obviously, one needs counterterm and loop diagrams in the same order of perturbation theory in order to obtain a finite result. Due to the involved structure of the $\mathcal{O}(\alpha_s^2 \alpha)$ corrections involving both EW-mediated and QCD-mediated Born-level diagrams, care has to be taken to evaluate the renormalization constants at the right order when the renormalization conditions are applied.

In case of $\tilde{t}\tilde{t}^*$ and $\tilde{g}\tilde{q}$ production, UV singularities only arise from loop diagrams with weak insertions to QCD-mediated tree-level graphs. Correspondingly, only the quark and the squark sector of the MSSM need to be renormalized and the renormalization constants have to be evaluated at $\mathcal{O}(\alpha)$. This is different for $\tilde{q}\tilde{q}$ production, where pure-QCD one-loop diagrams cause UV singularities. In this case, also the strong sector has to be renormalized and we need renormalization constants of $\mathcal{O}(\alpha_s)$. We will come back to this in more detail in the respective chapters. At this point, we want to give a general description of the renormalization procedure in those sectors of the MSSM that are relevant for our calculations. We introduce renormalization constants for masses and fields and impose on-shell conditions to fix the counterterms. This scheme is appropriate for cross section calculations as the OS renormalization of external particles guarantees that the pole masses recover the correct kinematical thresholds. In the strong sector, as usual, the QCD coupling constant is defined in the $\overline{\text{MS}}$ scheme. The Feynman rules for the arising counterterm diagrams are collected in Tables 4.1 and 4.2.

Renormalization of the quark sector

The bilinear part of the (Fourier transformed) Lagrangian for SM quarks is

$$\mathcal{L}_{\text{quarks}} = \overline{\psi}_q \left(\not{p} - m_q \right) \psi_q, \tag{4.6}$$

where ψ_q denotes the four-component Dirac spinor of a quark $q = u, d, c, s, b, t$. The renormalized quark masses and fields are obtained by the following replacements,

$$
\begin{aligned}
m_q &\longrightarrow m_q + \delta m_q, \\
P_L \psi_q &\longrightarrow \left(1 + \frac{1}{2} \delta Z_L^q \right) P_L \psi_q, \\
P_R \psi_q &\longrightarrow \left(1 + \frac{1}{2} \delta Z_R^q \right) P_R \psi_q,
\end{aligned}
\tag{4.7}
$$

where $P_{L/R}$ are the projection operators $P_{L/R} = (1 \mp \gamma_5)/2$. Here, we neglect CKM effects and thus quarks of different generations do not mix. δZ_L^q and δZ_R^q are the renormaliza-

tion constants of the left- and right-handed quark field, respectively. δm_q is the mass counterterm.

Inserting Eq. (4.7) into Eq. (4.6) yields the counterterm Lagrangian,

$$\delta\mathcal{L} = \overline{\psi}_q \, \not{p} \left[\delta Z_L^q \, P_L + \delta Z_R^q \, P_R\right]\psi_q - \left[\frac{m_q}{2}\left(\delta Z_L^q + \delta Z_R^q\right) + \delta m_q\right]\overline{\psi}_q\psi_q. \tag{4.8}$$

In order to impose the renormalization conditions, we need the renormalized self-energy $\hat{\Sigma}^q(p)$ entering the renormalized 1PI two-point function $i\hat{\Gamma}^q(p) = i(\not{p} - m_q) + i\hat{\Sigma}^q(p)$. In general, it is equal to the unrenormalized self-energy $\Sigma^q(p)$ plus the corresponding counterterms $\delta\Sigma^q(p)$, which are the derivatives of the counterterm Lagrangian $\delta\mathcal{L}$ with respect to the fields $\overline{\psi}_q$ and ψ_q,

$$\hat{\Sigma}^q(p) = \Sigma^q(p) + \frac{\partial}{\partial\overline{\psi}_q}\frac{\partial}{\partial\psi_q}\,\delta\mathcal{L} \;\equiv \Sigma^q(p) + \delta\Sigma^q(p), \tag{4.9}$$

With the decomposition of the self-energy into scalar coefficients,

$$\Sigma^q(p) = \not{p}\,P_L\,\Sigma_L^q(p^2) + \not{p}\,P_R\,\Sigma_R^q(p^2) + m_q\,\Sigma_S^q(p^2), \tag{4.10}$$

we find for the scalar coefficients of the analogously decomposed renormalized self-energy,

$$
\begin{aligned}
\hat{\Sigma}_a^q(p^2) &= \Sigma_a^q(p^2) + \delta Z_a^q, && (a = L, R)\\
\hat{\Sigma}_S^q(p^2) &= \Sigma_S^q(p^2) - \frac{1}{2}\left(\delta Z_L^q + \delta Z_R^q\right) - \frac{\delta m_q}{m_q}.
\end{aligned} \tag{4.11}
$$

The on-shell conditions require that the renormalized fermion masses are the poles of the real parts of the propagators and that the renormalized propagators have unity residues. This results in[14]

$$\mathrm{Re}\,\hat{\Sigma}^q(\not{p} = m_q) = 0 \qquad\text{and}\qquad \lim_{p^2\to m_q^2}\frac{\not{p} + m_q}{p^2 - m_q^2}\,\mathrm{Re}\,\hat{\Sigma}^q(p)\,\Psi^q(p) = 0, \tag{4.12}$$

where $\Psi^q(p)$ is the spinor of the external quark field. In terms of the above introduced coefficients of the self-energies, the renormalization constants are then given by

$$
\begin{aligned}
\delta m_q &= \frac{m_q}{2}\,\mathrm{Re}\left[\Sigma_L^q(m_q^2) + \Sigma_R^q(m_q^2) + 2\Sigma_S^q(m_q^2)\right],\\
\delta Z_a^q &= -\mathrm{Re}\,\Sigma_a^q(m_q^2) - m_q^2\,\mathrm{Re}\left[\frac{\partial}{\partial p^2}\Sigma_L^q(p^2) + \frac{\partial}{\partial p^2}\Sigma_R^q(p^2) + 2\frac{\partial}{\partial p^2}\Sigma_S^q(p^2)\right]\bigg|_{p^2 = m_q^2}.
\end{aligned} \tag{4.13}
$$

---

[14]to be precise, the renormalization conditions have to formulated in terms of the operator $\widetilde{\mathrm{Re}}(X)$ which selects the real part in each loop integral L_i of expression $X = \sum c_i L_i$, i.e. $\widetilde{\mathrm{Re}}\sum c_i L_i = \sum c_i\,\mathrm{Re}(L_i)$. We suppress the tilde on the Re operator in the following.

Note that in our actual calculations, only the field renormalization constants of light-flavor quarks enter. There are no external top-quark lines and for the light-flavor quarks, we generally neglect the masses. (However the quark masses have to be kept as regulators in the quark field renormalization constants.)

Renormalization of the squark sector

The kinetic and mass terms of the squark Lagrangian are, for a given squark $\tilde{q}$,

$$\mathcal{L}_{\text{squarks}} = \begin{pmatrix} \tilde{q}_L^*, & \tilde{q}_R^* \end{pmatrix} (p^2 - \mathcal{M}_{\tilde{q}}^2) \begin{pmatrix} \tilde{q}_L \\ \tilde{q}_R \end{pmatrix}. \tag{4.14}$$

To simplify the notation, we suppress generation indices here. At the one-loop level, the squark sector is renormalized by introducing counterterms for the squark mass matrix $\mathcal{M}_{\tilde{q}}$,

$$\mathcal{M}_{\tilde{q}}^2 \longrightarrow \mathcal{M}_{\tilde{q}}^2 + \delta\mathcal{M}_{\tilde{q}}^2, \tag{4.15}$$

where the elements of the matrix $\delta\mathcal{M}_{\tilde{q}}^2$ are the counterterms of the elements of $\mathcal{M}_{\tilde{q}}^2$ in the prescription of Eq. (2.95) or equivalently of Eq. (2.100) (see Eq. (4.19) below). In order to get finite Green functions, the fields are renormalized according to

$$\begin{pmatrix} \tilde{q}_L \\ \tilde{q}_R \end{pmatrix} \longrightarrow U_{\tilde{q}}^\dagger \left(\mathbb{1} + \frac{1}{2}\delta\mathcal{Z}_{\tilde{q}} \right) \begin{pmatrix} \tilde{q}_1 \\ \tilde{q}_2 \end{pmatrix}, \qquad \delta\mathcal{Z}_{\tilde{q}} = \begin{pmatrix} \delta Z_{11}^{\tilde{q}} & \delta Z_{12}^{\tilde{q}} \\ \delta Z_{21}^{\tilde{q}} & \delta Z_{22}^{\tilde{q}} \end{pmatrix}, \tag{4.16}$$

where we included a rotation of the L–R eigenstates for a convenient definition of the counterterms in the mass eigenstate basis. The counterterm Lagrangian then reads

$$\begin{aligned} \delta\mathcal{L} = &\begin{pmatrix} \tilde{q}_1^*, & \tilde{q}_2^* \end{pmatrix} \frac{p^2}{2} \big(\delta\mathcal{Z}_{\tilde{q}}^\dagger + \delta\mathcal{Z}_{\tilde{q}} \big) \begin{pmatrix} \tilde{q}_1 \\ \tilde{q}_2 \end{pmatrix} \\ &- \begin{pmatrix} \tilde{q}_1^*, & \tilde{q}_2^* \end{pmatrix} \left[\frac{1}{2}\delta\mathcal{Z}_{\tilde{q}}^\dagger \mathcal{D}_{\tilde{q}}^2 + \frac{1}{2}\mathcal{D}_{\tilde{q}}^2 \delta\mathcal{Z}_{\tilde{q}} + U_{\tilde{q}} \delta\mathcal{M}_{\tilde{q}}^2 U_{\tilde{q}}^\dagger \right] \begin{pmatrix} \tilde{q}_1 \\ \tilde{q}_2 \end{pmatrix}, \end{aligned} \tag{4.17}$$

in terms of the diagonalized mass matrix $\mathcal{D}_{\tilde{q}}^2 = U_{\tilde{q}}\mathcal{M}_{\tilde{q}}^2 U_{\tilde{q}}^\dagger$. From Eq. (4.17), we directly read off the matrix-valued renormalized self-energy $\hat{\Sigma}_{ab}^{\tilde{q}}(p^2)$,

$$\hat{\Sigma}_{ab}^{\tilde{q}}(p^2) = \Sigma_{ab}^{\tilde{q}}(p^2) + \frac{p^2}{2}\left(\delta\mathcal{Z}_{\tilde{q}}^\dagger + \delta\mathcal{Z}_{\tilde{q}} \right)_{ab} - \frac{1}{2}\left(\delta\mathcal{Z}_{\tilde{q}}^\dagger \mathcal{D}_{\tilde{q}}^2 + \mathcal{D}_{\tilde{q}}^2 \delta\mathcal{Z}_{\tilde{q}} \right)_{ab} - \left(U_{\tilde{q}} \delta\mathcal{M}_{\tilde{q}}^2 U_{\tilde{q}}^\dagger \right)_{ab}. \tag{4.18}$$

The appropriate set of on-shell renormalization conditions depends on which set of input parameters is chosen. As discussed in Section 2.3.4, the squark sector is described by five independent parameters (per generation), thus five renormalization conditions are needed. All other parameters and their counterterms are dependent quantities and can be derived

from the expressions of the independent counterterms. Since we include field renormalization Eq. (4.16), also the corresponding on-shell conditions for the field renormalization constants have to be imposed.

The perhaps most intuitive choice is to start from the masses and mixing angles as input parameters, $m_{\tilde{u}_1}^2$, $m_{\tilde{u}_2}^2$, $m_{\tilde{d}_1}^2$, $\theta_{\tilde{u}}$, $\theta_{\tilde{d}}$ (cf. Eq. (2.104), generation indices suppressed) [129]. The corresponding counterterms are parameterized in the counterterm matrix $\delta\mathcal{M}_{\tilde{q}}^2$, which follows from Eq. (2.100) by differentiation,

$$
\begin{aligned}
(\delta\mathcal{M}_{\tilde{q}}^2)_{11} &= \cos^2\theta_{\tilde{q}}\,\delta m_{\tilde{q}_1}^2 + \sin^2\theta_{\tilde{q}}\,\delta m_{\tilde{q}_2}^2 - 2\sin\theta_{\tilde{q}}\,\cos\theta_{\tilde{q}}\,(m_{\tilde{q}_1}^2 - m_{\tilde{q}_2}^2)\,\delta\theta_{\tilde{q}}, \\
(\delta\mathcal{M}_{\tilde{q}}^2)_{12} &= \sin\theta_{\tilde{q}}\,\cos\theta_{\tilde{q}}\,(\delta m_{\tilde{q}_1}^2 - \delta m_{\tilde{q}_2}^2) + \cos(2\theta_{\tilde{q}})\,(m_{\tilde{q}_1}^2 - m_{\tilde{q}_2}^2)\,\delta\theta_{\tilde{q}}, \\
(\delta\mathcal{M}_{\tilde{q}}^2)_{21} &= (\delta\mathcal{M}_{\tilde{q}}^2)_{12}, \\
(\delta\mathcal{M}_{\tilde{q}}^2)_{22} &= \sin^2\theta_{\tilde{q}}\,\delta m_{\tilde{q}_1}^2 + \cos^2\theta_{\tilde{q}}\,\delta m_{\tilde{q}_2}^2 + 2\sin\theta_{\tilde{q}}\,\cos\theta_{\tilde{q}}\,(m_{\tilde{q}_1}^2 - m_{\tilde{q}_2}^2)\,\delta\theta_{\tilde{q}}.
\end{aligned}
\tag{4.19}
$$

This corresponds to the following relations between the counterterms and the entries of the rotated counterterm matrix $U_{\tilde{q}}\,\delta\mathcal{M}_{\tilde{q}}^2\,U_{\tilde{q}}^\dagger$,

$$
\delta m_{\tilde{q}_a}^2 = \left(U_{\tilde{q}}\,\delta\mathcal{M}_{\tilde{q}}^2\,U_{\tilde{q}}^\dagger\right)_{aa}, \qquad a = 1, 2.
\tag{4.20a}
$$

$$
\delta\theta_{\tilde{q}} = \frac{\left(U_{\tilde{q}}\,\delta\mathcal{M}_{\tilde{q}}^2\,U_{\tilde{q}}^\dagger\right)_{12}}{m_{\tilde{q}_1}^2 - m_{\tilde{q}_2}^2}.
\tag{4.20b}
$$

The three independent mass counterterms are fixed by the on-shell requirement of vanishing real parts of the diagonal entries of the renormalized self-energies Eq. (4.18), i. e.

$$
\operatorname{Re}\hat{\Sigma}_{aa}^{\tilde{q}}(m_{\tilde{q}_a}^2) = 0, \qquad a = 1, 2.
\tag{4.21}
$$

Together with Eq. (4.20a), this leads to

$$
\delta m_{\tilde{u}_1}^2 = \operatorname{Re}\Sigma_{11}^{\tilde{u}}(m_{\tilde{u}_1}^2), \quad \delta m_{\tilde{u}_2}^2 = \operatorname{Re}\Sigma_{22}^{\tilde{u}}(m_{\tilde{u}_2}^2), \quad \delta m_{\tilde{d}_1}^2 = \operatorname{Re}\Sigma_{11}^{\tilde{d}}(m_{\tilde{d}_1}^2).
\tag{4.22}
$$

The diagonal elements of the field renormalization matrix $\delta\mathcal{Z}_{\tilde{q}}$ directly follow from the condition that the residues of the renormalized squark propagators are unity, $(a = 1, 2)$,

$$
\operatorname{Re}\frac{\partial}{\partial p^2}\hat{\Sigma}_{aa}^{\tilde{q}}(p^2)\Big|_{p^2 = m_{\tilde{q}_a^2}} = 0 \qquad \Rightarrow \qquad \delta Z_{aa}^{\tilde{q}} = -\operatorname{Re}\frac{\partial}{\partial p^2}\Sigma_{aa}^{\tilde{q}}(p^2)\Big|_{p^2 = m_{\tilde{q}_a^2}}.
\tag{4.23}
$$

The mixing angles are defined on-shell if they do not receive loop corrections. This imposes that the sum of the non-diagonal elements of the renormalized self-energies evaluated at both mass eigenvalues vanishes,

$$
\operatorname{Re}\hat{\Sigma}_{12}^{\tilde{q}}(m_{\tilde{q}_1}^2) + \operatorname{Re}\hat{\Sigma}_{12}^{\tilde{q}}(m_{\tilde{q}_2}^2) = 0.
\tag{4.24}
$$

Inserting Eqs. (4.18) and (4.20b) into the condition Eq. (4.24), the counterterms for the mixing angles follow,

$$\delta\theta_{\tilde{q}} = \frac{\mathrm{Re}\,\Sigma_{12}^{\tilde{q}}(m_{\tilde{q}_1}^2) + \mathrm{Re}\,\Sigma_{12}^{\tilde{q}}(m_{\tilde{q}_2}^2)}{2(m_{\tilde{q}_1}^2 - m_{\tilde{q}_2}^2)}, \tag{4.25}$$

where the convenient choice $\delta Z_{12}^{\tilde{q}} = \delta Z_{21}^{\tilde{q}}$ has been applied.

To fix the remaining non-diagonal entries of the field renormalization matrix $\delta\mathcal{Z}_{\tilde{q}}$, we furthermore require to have zero mixing on each squark mass-shell, i.e. $\mathrm{Re}\hat{\Sigma}_{12}^{\tilde{q}}(m_{\tilde{q}_2}^2) = 0$. With the definition Eq. (4.18) and the above conditions this finally results in

$$\delta Z_{12}^{\tilde{q}} = \delta Z_{21}^{\tilde{q}} = -\frac{\mathrm{Re}\Sigma_{12}^{\tilde{q}}(m_{\tilde{q}_1}^2) - \mathrm{Re}\Sigma_{12}^{\tilde{q}}(m_{\tilde{q}_2}^2)}{m_{\tilde{q}_1}^2 - m_{\tilde{q}_2}^2}. \tag{4.26}$$

Owing to the introduction of an explicit counterterm for the mixing angle, one relies on a specific parameterization of the squark mixing matrix $U_{\tilde{q}}$, Eq. (2.95), entering in Eq. (4.19). It is straightforward to derive more general formulas which also allow for different definitions of the squark masses and mixing angles. We introduce the counterterm $\delta Y_{\tilde{q}}^2$,

$$\delta Y_{\tilde{q}}^2 \equiv \left(U_{\tilde{q}}\,\delta\mathcal{M}_{\tilde{q}}^2\,U_{\tilde{q}}^\dagger\right)_{12}, \tag{4.27}$$

which is in the explicit parameterization of Eq. (2.95), cf. Eq. (4.20b),

$$\delta Y_{\tilde{q}}^2 = (m_{\tilde{q}_1}^2 - m_{\tilde{q}_2}^2)\,\delta\theta_{\tilde{q}}. \tag{4.28}$$

The renormalization condition for $\delta Y_{\tilde{q}}^2$ replaces then that of $\delta\theta_{\tilde{q}}$ in Eq. (4.25),

$$\delta Y_{\tilde{q}}^2 = \frac{1}{2}\left(\mathrm{Re}\,\Sigma_{12}^{\tilde{q}}(m_{\tilde{q}_1}^2) + \mathrm{Re}\,\Sigma_{12}^{\tilde{q}}(m_{\tilde{q}_2}^2)\right). \tag{4.29}$$

All independent quantities are now defined. By differentiation of Eq. (2.102), we find the counterterm for the dependent mass $m_{\tilde{d}_2}^2$. Written in a way independent on the explicit parameterization of the squark mixing matrix, it is

$$\delta m_{\tilde{d}_2}^2 = \frac{1}{\left(U_{12}^{\tilde{d}}\right)^2}\Bigg[-\left(U_{11}^{\tilde{d}}\right)^2\delta m_{\tilde{d}_1}^2 - \left(U_{11}^{\tilde{u}}\right)^2\delta m_{\tilde{u}_1}^2 - \left(U_{12}^{\tilde{u}}\right)^2\delta m_{\tilde{u}_2}^2 + 2U_{12}^{\tilde{d}}U_{22}^{\tilde{d}}\,\delta Y_{\tilde{d}}^2 - 2U_{12}^{\tilde{u}}U_{22}^{\tilde{u}}\,\delta Y_{\tilde{u}}^2$$

$$+ 2m_d\,\delta m_d - 2m_u\,\delta m_u - \cos 2\beta\,\delta m_W^2 + 4m_W^2\frac{\tan\beta\,\delta\tan\beta}{(1+\tan^2\beta)^2}\Bigg]. \tag{4.30}$$

In the second line of Eq. (4.30) counterterms from other sectors enter. The quark mass counterterms are defined OS according to Eq. (4.13). δm_W^2 is the W mass counterterm,

which in the OS scheme is given by the transverse part of the W boson self-energy,

$$\delta m_W^2 = \text{Re}\Sigma_W^T(m_W^2).\tag{4.31}$$

The counterterm $\delta\tan\beta$ is introduced according to $\tan\beta \to \tan\beta + \delta\tan\beta$. Following [130, 131], a vanishing $A^0 - Z$ mixing for an on-shell A^0 boson can be used as a renormalization condition for $\tan\beta$ (DCPR scheme),

$$\text{Re}\,\hat{\Sigma}^{A^0 Z}(m_{A^0}^2) = \text{Re}\,\Sigma^{A^0 Z}(m_{A^0}^2) - m_Z\sin 2\beta\frac{\delta\tan\beta}{\tan\beta} = 0\tag{4.32}$$

in terms of the renormalized self-energy $\hat{\Sigma}^{A^0 Z}$ (derived from the vertex function $\Gamma_\mu^{A^0 Z}(k, -k)$ $= k_\mu\Sigma^{A^0 Z}(k^2)$, where k is the incoming A^0 momentum). Here, we apply a $\overline{\text{DR}}$ renormalization condition instead [69,132],

$$\delta\tan\beta = \frac{1}{2m_Z\cos^2\beta}\text{Re}\,\Sigma^{A^0 Z}(m_{A^0}^2)\Big|_{\text{UV div.}},\tag{4.33}$$

where the subscript $_{\text{UV div.}}$ indicates that only the UV-divergent part of the $A^0 - Z$ self-energy has to be taken. As pointed out in [133], this definition is process independent and gauge invariant at the one-loop level.

So far, we treated up- and down-type squarks in the same way. However for third generation squarks, this scheme can lead to numerical instabilities [79]. There are important differences between the top and the bottom sector. First, we have implicitly chosen the SM quark masses as input parameters for the definition of the squark mass counterterms. Whereas the mass of the top-quark can experimentally be measured, the precise determination of the on-shell bottom quark mass is difficult due to non-perturbative effects. Potential problems with the bottom pole mass can be avoided by adopting a renormalization scheme with a running bottom-quark mass. In the context of the MSSM it is appropriate to renormalize the bottom quark mass in the $\overline{\text{DR}}$ scheme and to include the SUSY contributions into the running. The bottom mass counterterm is then given by Eq. (4.13) but now the self-energies are regularized within dimensional reduction and only the UV-divergent contributions have to be kept.

Furthermore, the $\tan\beta$-dependence in the top- and bottom-squark mass matrices is different. In the above described scheme, the trilinear couplings A_f are dependent quantities and their counterterm δA_f is obtained by differentiating Eq. (2.101) and inserting the above defined counterterms for the (s)quark masses and mixing angles[15]. In the bottom sector,

---

[15]To fully determine the counterterm δA_b at $\mathcal{O}(\alpha)$, also the counterterm $\delta\mu$ of the gaugino sector is needed. It can be defined via the neutralino self-energies and is given in e. g. [134].

the $\tan\beta$-dependence of the counterterm is

$$\delta A_b = \frac{1}{m_b}[-\delta m_b \left(A_b - \mu \tan\beta\right) + \dots], \qquad (4.34)$$

which can cause large corrections to A_b in parameter regions where $\mu \tan\beta \gg A_b$. It seems thus appropriate to use A_b as an input parameter directly.

To summarize, we replace the input set $\{(m_b)^{\text{OS}}, (m_{\tilde{b}_1}^2)^{\text{OS}}, (\theta_{\tilde{b}})^{\text{OS}}\}$ and choose a modified renormalization scheme for the bottom-sbottom sector according to [79] based on the inputs $\{(m_b)^{\overline{\text{DR}}}, (m_{\tilde{b}_1}^2)^{\text{OS}}, (A_b)^{\overline{\text{DR}}}\}$. In this scheme, the counterterm for the mixing angle $\delta\theta_b$ is a dependent quantity. The explicit formulas for δA_b and $\delta\theta_b$ are given in [79,135].

In the discussion of squarks of the first two generations, $\tilde{q} = \tilde{u}, \tilde{d}, \tilde{c}, \tilde{s}$, we neglect light quark masses. Thus, the mixing angle does not enter and the above formulas simplify considerably. In particular, the two renormalization schemes yield the same result.

Neglecting the mixing also at the one-loop level, the mass matrix, the field renormalization matrix, and the squark self-energies are diagonal. We introduce field and mass renormalization as follows,

$$\begin{aligned}
\tilde{q}_{L/R} &\longrightarrow \left(1 + \frac{1}{2}\delta Z^{\tilde{q}}_{LL/RR}\right) \tilde{q}_{L/R}, \\
m^2_{\tilde{q}_{L/R}} &\longrightarrow m^2_{\tilde{q}_{L/R}} + \delta m^2_{\tilde{q}_{L/R}}.
\end{aligned} \qquad (4.35)$$

In these terms, the renormalized self-energy reads

$$\hat{\Sigma}^{\tilde{q}}_{L/R}(p^2) = \Sigma^{\tilde{q}}_{L/R}(p^2) + \left(p^2 - m^2_{\tilde{q}_{L/R}}\right) \delta Z^{\tilde{q}}_{LL/RR} - \delta m^2_{\tilde{q}_{L/R}}, \qquad (4.36)$$

yielding for the three independent mass counterterms

$$\delta m^2_{\tilde{u}_R} = \text{Re}\,\Sigma^{\tilde{u}}_R(m^2_{\tilde{u}_R}), \quad \delta m^2_{\tilde{u}_L} = \text{Re}\,\Sigma^{\tilde{u}}_L(m^2_{\tilde{u}_L}), \quad \delta m^2_{\tilde{d}_R} = \text{Re}\,\Sigma^{\tilde{d}}_R(m^2_{\tilde{d}_R}). \qquad (4.37)$$

The mass of the left-handed down-squark is constrained by the $SU(2)_L$ invariance and its counterterm follows from Eq. (4.30),

$$\delta m^2_{\tilde{d}_L} = \delta m^2_{\tilde{u}_L} - \cos 2\beta \, \delta m^2_W + 4m^2_W \frac{\tan\beta \, \delta\tan\beta}{(1 + \tan^2\beta)^2}, \qquad (4.38)$$

with $\delta m_u = \delta m_d = 0$. The field renormalization constants are determined by Eq. (4.23),

$$\delta Z^{\tilde{q}}_{LL/RR} = -\text{Re}\frac{\partial}{\partial p^2}\Sigma^{\tilde{q}}_{L/R}(p^2)\Big|_{p^2=m^2_{\tilde{q}_{L/R}}}. \qquad (4.39)$$

The definition of the counterterm Lagrangian yields new Feynman diagrams that have to be taken into account in the calculation of loop amplitudes. Having introduced the renor-

malization constants in the quark and in the squark sector, we can define the counterterms for self-energies, vertex, and quartic interactions necessary for $\tilde{t}_a \tilde{t}_a^*$ and $\tilde{g}\tilde{q}$ production, as listed in Table 4.1. Note that counterterms involving the non-diagonal elements of the stop field renormalization constant are not given explicitly as they do not enter the calculation since only chirality-conserving vertices appear in the diagrams for $\tilde{t}_a \tilde{t}_a^*$ production at LO (see also Section 5.2.2).

Renormalization of the gluino

If required, we also renormalize the gluino and impose OS conditions. The renormalization proceeds similar as in the quark sector, however gluinos are Majorana fermions. The relevant part of the Fourier transformed Lagrange density is

$$\mathcal{L}_{\text{gluino}} = \overline{\Psi}_{\tilde{g}} \left(\not{p} - m_{\tilde{g}} \right) \Psi_{\tilde{g}}, \qquad \text{with} \quad \Psi_{\tilde{g}} = \begin{pmatrix} \tilde{g} \\ \overline{\tilde{g}} \end{pmatrix}, \tag{4.40}$$

where $\Psi_{\tilde{g}}$ is a Majorana spinor build from the left-handed Weyl spinors $\tilde{g}$ only. The renormalization constants for the gluino mass $m_{\tilde{g}}$ and the gluino field are introduced by the replacement

$$\begin{aligned} m_{\tilde{g}} &\longrightarrow m_{\tilde{g}} + \delta m_{\tilde{g}}, \\ \tilde{g} &\longrightarrow \left(1 + \frac{1}{2} \delta Z_{\tilde{g}} \right) \tilde{g}. \end{aligned} \tag{4.41}$$

Due to the Majorana nature of gluinos, there is no difference between left- and right-handed renormalization constants. The counterterm Lagrangian results for real entries $\delta Z_{\tilde{g}}$ in

$$\delta\mathcal{L} = \overline{\Psi}_{\tilde{g}} \; \not{p} \, \delta Z_{\tilde{g}} \, \Psi_{\tilde{g}} - \left(m_{\tilde{g}} \, \delta Z_{\tilde{g}} + \delta m_{\tilde{g}} \right) \overline{\Psi}_{\tilde{g}} \Psi_{\tilde{g}}. \tag{4.42}$$

The scalar coefficients of the gluino self-energy are defined as follows,

$$\Sigma^{\tilde{g}}(p^2) = \not{p} \Sigma_L^{\tilde{g}}(p^2) + m_{\tilde{g}} \Sigma_S^{\tilde{g}}(p^2), \tag{4.43}$$

such that we find for the coefficients of the renormalized gluino self-energy from Eq. (4.42),

$$\hat{\Sigma}_L^{\tilde{g}}(p^2) = \Sigma_L^{\tilde{g}} + \delta Z_{\tilde{g}}, \qquad \hat{\Sigma}_S^{\tilde{g}}(p^2) = \Sigma_S^{\tilde{g}} - \delta Z_{\tilde{g}} - \frac{\delta m_{\tilde{g}}}{m_{\tilde{g}}}. \tag{4.44}$$

The counterterms are given by the on-shell conditions that the renormalized mass is equal to the physical mass and that the renormalized propagators have unity residue, cf. Eq. (4.12),
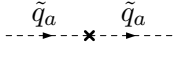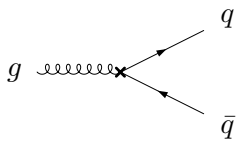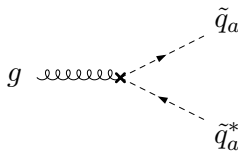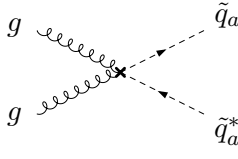
$$
\tilde{q}_a \quad \tilde{q}_a \qquad = \qquad i\left[(p^2 - m_{\tilde{q}_a}^2)\,\delta Z_{aa}^{\tilde{q}} - \delta m_{\tilde{q}_a}^2\right]
$$

$$
g,\ q,\ \bar{q} \qquad = \qquad -ig_s T^c \left(\delta Z_L^{\tilde{q}}\,\gamma_\mu P_L + \delta Z_R^{\tilde{q}}\,\gamma_\mu P_R\right)
$$

$$
g,\ \tilde{q}_a,\ \tilde{q}_a^* \qquad = \qquad -ig_s T^c\,\delta Z_{aa}^{\tilde{q}}\,(k + k')_\mu
$$
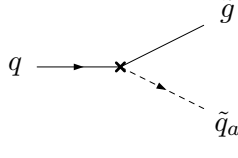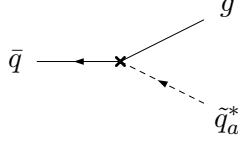
$$
g,\ g,\ \tilde{q}_a,\ \tilde{q}_a^* \qquad = \qquad ig_s^2 \left(T^{c_1} T^{c_2} + T^{c_2} T^{c_1}\right) \delta Z_{aa}^{\tilde{q}}\, g_{\mu\nu}
$$

$$
q,\ \tilde{g},\ \tilde{q}_a \qquad = \qquad \mp ig_s \frac{1}{\sqrt{2}}\, T^c \left(\delta Z_{aa}^{\tilde{q}} + \delta Z_a^q\right) P_{L/R}, \qquad a = L, R
$$

$$
\bar{q},\ \tilde{g},\ \tilde{q}_a^* \qquad = \qquad \pm ig_s \frac{1}{\sqrt{2}}\, T^c \left(\delta Z_{aa}^{\tilde{q}} + \delta Z_a^q\right) P_{R/L}, \qquad a = L, R
$$

Table 4.1.: List of counterterms relevant for $\tilde{t}_a \tilde{t}_a^*$ and $\tilde{g}\tilde{q}$ production at $\mathcal{O}(\alpha_s^2\alpha)$; all renormalization constants have to be evaluated at $\mathcal{O}(\alpha)$. In the upper four diagrams, the label $\tilde{q}_a$ refers both to light-flavor squarks ($a = L, R$) and stops ($a = 1, 2$). Color indices for quarks and squarks are suppressed, while c and c_i are gluonic color indices and T^c, T^{c_i} denote the $SU(3)_C$ color matrices. In the diagrams involving Majorana particles, the fermion flow is fixed according to the arrow depicted on the quark line [73].

yielding

$$
\delta m_{\tilde{g}} = m_{\tilde{g}} \left(\Sigma_L^{\tilde{g}} + \Sigma_S^{\tilde{g}} \right),
$$

$$
\delta Z_{\tilde{g}} = -\mathrm{Re}\,\Sigma_L^{\tilde{g}} - 2 m_{\tilde{g}} \mathrm{Re} \left[\frac{\partial}{\partial p^2} \Sigma_L^{\tilde{g}}(p^2) + \frac{\partial}{\partial p^2} \Sigma_S^{\tilde{g}}(p^2) \right]\Bigg|_{p^2 = m_{\tilde{g}}^2}.
\tag{4.45}
$$

Renormalization of strong couplings

Finally, we also need to renormalize the strong coupling g_s and the strong $\tilde{q}\tilde{g}q$ Yukawa coupling $\hat{g}_s$. Supersymmetry requires both couplings to be identical. We introduce the renormalization constants by the replacement of the bare couplings as follows,

$$
\begin{aligned}
g_s &\longrightarrow (1 + \delta Z_{g_s})\, g_s, \\
\hat{g}_s &\longrightarrow (1 + \delta Z_{\hat{g}_s})\, \hat{g}_s,
\end{aligned}
\tag{4.46}
$$

Care has to be taken to define the strong coupling in the loop computations in accordance with the coupling used in the extraction of the PDFs. Therefore, we define g_s in the $\overline{\mathrm{MS}}$ scheme, in terms of the gluonic self-energy and the triple gluon vertex,

$$
\delta Z_{g_s} = -\frac{\alpha_s}{4\pi}\,\Delta\frac{\beta_0}{2},
\tag{4.47}
$$

where β_0 is the one-loop coefficient of the running coupling $\alpha_s(\mu) = g_s^2(\mu)/4\pi$. In high-energy collisions the typical scales at which to evaluate the coupling are comparable or above the weak scale. At such high scales, the contribution β_0^H of heavy particles as the gluino, squarks and the top quark has to be considered in the definition of the running coupling. Including the light-quark and gluonic contributions β_0^L as well as those from gluinos, squarks, and top quarks, the β_0-coefficient is

$$
\beta_0 \equiv \beta_0^L + \beta_0^H = \left(\frac{11}{3}N - \frac{2}{3}n_f \right) + \left(-\frac{2}{3}N - \frac{1}{3}(n_f + 1) - \frac{2}{3} \right) = 3,
\tag{4.48}
$$

with $N = 3$ and $n_f = 5$ light quark flavors. However the PDFs are obtained using a running $\overline{\mathrm{MS}}$ coupling determined by light particles only (i.e. $\beta_0 \equiv \beta_0^L$). At a high scale $\mu > m_t$, the two couplings are related by explicit decoupling of the gluino, squark, and top-quark contributions. We compensate this shift by a redefinition of the counterterm of the strong coupling in the zero momentum subtraction scheme [136,137]

$$
\delta Z_{g_s} = -\frac{\alpha_s}{4\pi} \left[\frac{3}{2}\Delta + \ln\left(\frac{m_{\tilde{g}}^2}{\mu^2} \right) + \sum_{\tilde{q}_a} \frac{1}{12} \ln\left(\frac{m_{\tilde{q}_a}^2}{\mu^2} \right) + \frac{1}{3} \ln\left(\frac{m_t^2}{\mu^2} \right) \right],
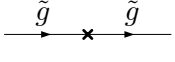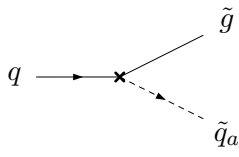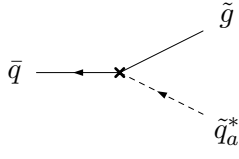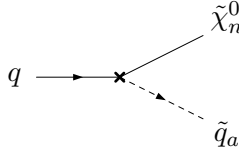\tag{4.49}
$$

$$\tilde{g} \qquad \tilde{g} \qquad\qquad = \qquad i\left[(\not{p} - m_{\tilde{g}})\,\delta Z_{\tilde{g}} - \delta m_{\tilde{g}}\right]$$
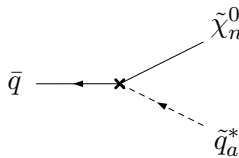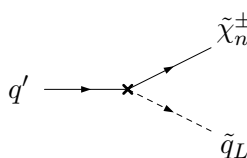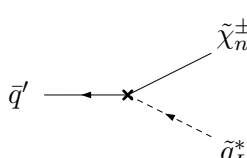
$$\begin{array}{c} q \\ \tilde{g} \\ \tilde{q}_a \end{array} \qquad = \qquad \mp i g_s \frac{1}{\sqrt{2}}\, T^c \left(\delta Z_{aa}^{\tilde{q}} + \delta Z_a^q + \delta Z_g + 2\delta Z_{\hat{g}_s}\right) P_{L/R}, \quad a = L, R$$

$$\begin{array}{c} \bar{q} \\ \tilde{g} \\ \tilde{q}_a^* \end{array} \qquad = \qquad \pm i g_s \frac{1}{\sqrt{2}}\, T^c \left(\delta Z_{aa}^{\tilde{q}} + \delta Z_a^q + \delta Z_g + 2\delta Z_{\hat{g}_s}\right) P_{R/L}, \quad a = L, R$$

$$\begin{array}{c} q \\ \tilde{\chi}_n^0 \\ \tilde{q}_a \end{array} \qquad = \qquad -ie\frac{1}{\sqrt{2}}\,\kappa_{L/R}^0(q)\left(\delta Z_{aa}^{\tilde{q}} + \delta Z_a^q\right) P_{L/R}, \qquad\qquad a = L, R$$

$$\begin{array}{c} \bar{q} \\ \tilde{\chi}_n^0 \\ \tilde{q}_a^* \end{array} \qquad = \qquad -ie\frac{1}{\sqrt{2}}\,\left[\kappa_{L/R}^0(q)\right]^*\left(\delta Z_{aa}^{\tilde{q}} + \delta Z_a^q\right) P_{R/L}, \qquad\qquad a = L, R$$

$$\begin{array}{c} q' \\ \tilde{\chi}_n^\pm \\ \tilde{q}_L \end{array} \qquad = \qquad -ie\frac{1}{2}\,\kappa_L^\pm(q')\left(\delta Z_{aa}^{\tilde{q}} + \delta Z_a^{q'}\right) P_L,$$

$$\begin{array}{c} \bar{q}' \\ \tilde{\chi}_n^\pm \\ \tilde{q}_L^* \end{array} \qquad = \qquad -ie\frac{1}{2}\,\left[\kappa_L^\pm(q')\right]^*\left(\delta Z_{aa}^{\tilde{q}} + \delta Z_a^{q'}\right) P_R,$$

Table 4.2.: List of counterterms relevant for $\tilde{q}\tilde{q}$ production at $\mathcal{O}(\alpha_s^2\alpha)$. The renormalization constants have to be evaluated at $\mathcal{O}(\alpha)$ or $\mathcal{O}(\alpha)$ as specified below in Figures 7.2, 7.3, and 7.4. The notation refers to Fig. 4.1, with q' denoting the $SU(2)_L$ partner of q, and n labels the neutralino ($n = 1\ldots 4$) and chargino ($n = 1, 2$) mass eigenstates. The $\tilde{\chi}^0 q\tilde{q}$ couplings are $\kappa_L^0(q) = N_{n1}^*(e_q - I_q^3)/\cos\theta_W + N_{n2}^* I_q^3/\sin\theta_W$ and $\kappa_R^0(q) = -N_{n1} e_q$, where $N \equiv N_{\tilde{\chi}^0}$ is the neutralino mixing matrix defined in Eq. (2.113); the $\tilde{\chi}^\pm q'\tilde{q}$ couplings are $\kappa_L^\pm(q' = u_i) = U_{n1}^*/\sin\theta_W$ and $\kappa_L^\pm(q' = d_i) = V_{n1}^*/\sin\theta_W$, in terms of the chargino mixing matrices $U \equiv U_{\tilde{\chi}^\pm}$, $V \equiv V_{\tilde{\chi}^\pm}$, defined in Eq. (2.109), [72].

where the divergences associated with the heavy-particle loops are subtracted at zero momentum. Here, the sum runs over all twelve squark mass eigenstates $\tilde{q}_a$.

Furthermore, since we define the strong coupling in the $\overline{\text{MS}}$ scheme, a mismatch between g_s and the Yukawa coupling $\hat{g}_s$ is introduced at the one-loop level owing to the treatment of UV divergences by means of dimensional regularization. In order to restore supersymmetry in physical amplitudes, one has to shift the renormalization constant for $\delta Z_{\hat{g}_s}$ by a finite amount to be different from δZ_{g_s}. At the one-loop level, it is [136]

$$\delta Z_{\hat{g}_s} = \delta Z_{g_s} + \frac{\alpha_s}{3\pi}. \tag{4.50}$$

As a result, supersymmetry is preserved and the definition of the strong coupling corresponds to the usual SM measurements.

For a complete renormalization of the strong sector, also the gluon field renormalization constant needs to be introduced and fixed by renormalization conditions. However, in the processes considered here ($\tilde{q}\tilde{q}$ production at $\mathcal{O}(\alpha_s^2 \alpha)$), the gluon enters only at one-loop and needs not to be renormalized at this order of perturbation theory.

The resulting counterterms that are relevant for $\tilde{q}\tilde{q}$ production are given in Table 4.2.

4.2   Handling infrared singularities

As shown by Kinoshita [138], IR singularities result from two configurations: Soft singularities appear if two external on-shell particles exchange a massless particle, and collinear singularities arise if an external massless particle splits into two internal massless particles. Also both conditions can be fulfilled in a single diagram, then the singularities overlap. The IR singularities are of logarithmic nature. If the involved particles have a small, but non-vanishing mass, the singularities appear as logarithms $\propto \left\{ \ln(m^2/\mu^2), \ln^2(m^2/\mu^2) \right\}$ of the mass parameter m and a high scale μ.[16]

The IR singularities of virtual corrections are intrinsically connected to those of real corrections. Real radiation cross sections become singular from the phase-space integration if a massless particle is emitted off an external particle either in the soft limit (vanishing momentum) or in the collinear region (small angle between the radiated and the massless emitting particle).

However if sufficiently inclusive observables are considered (i.e. their actual values do not depend on the precise number of collinear or soft particles in the final state), the cancellation of IR singularities is guaranteed by factorization theorems [104]. The Kinoshita–Lee–Nauenberg (KLN) theorem [138,140] states that all soft singularities and also the singularities due to collinear final state particles cancel in the sum of virtual and real cor-

---

[16]A list of all IR-singular three-point functions and their analytic expressions in the soft and/or collinear limit has been worked out in [139].

rections, even though defined on different phase spaces. Remaining collinear singularities related to initial state partons are process independent and can, therefore, be absorbed by universal collinear 'counterterms' generated by redefining the parton distribution functions of the incoming hadrons. As a result, the physical higher-order cross section is IR finite and free of the fictious mass regulator, as required from experiment.

Considering squark and gluino production at $\mathcal{O}(\alpha_s^2\alpha)$, one has to deal with the following IR singularities in real radiation processes.[17]

- *Soft photon singularities* arise in diagrams where the external particles exchange a photon, as e. g. in the first two loop diagrams in Fig. 3.9 (a). We regularize the amplitude by a non-zero photon mass λ. This is allowed because the renormalizability of QED is not violated by an explicit mass term for the gauge boson. The singularities cancel against their counterparts from real photon bremsstrahlung contributions.

  Soft photon singularities appear in all production channels for $\tilde{g}\tilde{g}$, $\tilde{g}\tilde{q}$, $\tilde{q}\tilde{q}$, $\tilde{q}\tilde{q}^*$, and $\tilde{t}\tilde{t}^*$ production.

- Production channels with light-flavor quarks in the initial state suffer from *singularities due to collinearly radiated photons*. An example diagram is given by the first loop diagram in Fig. 3.9 (a). The singularities occur for massless quarks only, if they radiate off a photon under a small angle, and can be regularized by a non-zero quark mass m_q. In the loop diagrams, collinear and soft singularities overlap and both single and double logarithmic contributions of the quark mass arise. The double logarithms cancel in the sum of virtual and real photon corrections. The remaining single logarithms are process independent and can be absorbed into the PDFs by an appropriate redefinition with respect to collinear photon radiation at $\mathcal{O}(\alpha)$.

  Singularities related to collinear photons have to be considered for the full set of $\tilde{g}\tilde{g}$, $\tilde{g}\tilde{q}$, $\tilde{q}\tilde{q}$, $\tilde{q}\tilde{q}^*$, and $\tilde{t}\tilde{t}^*$ production processes, connected to the quarks and anti-quarks in the initial states.

- If EW tree-level diagrams are present, also loop diagrams with virtual gluons contribute at $\mathcal{O}(\alpha_s^2\alpha)$, cf. e. g. the first box diagram in Fig. 3.9 (a) and Fig. 3.9 (b), respectively, and induce IR singularities. We can regularize the *soft gluon singularities* analogously to the photonic ones by giving a mass to the gluon, since the gluons behave Abelian-like in the respective diagrams. The non-Abelian ggg vertex does not enter at this order of perturbation theory. To cancel the soft gluon singularities, we need to include soft gluon bremsstrahlung at the right order, as resulting from interference contributions of QCD- and EW-mediated diagrams.

---

[17]For a detailed description of generic IR singularities in virtual and real photonic corrections and explicit discussions on their cancellation we refer to textbooks, e. g. [141], see also [69]. Here, we will restrict ourselves to a general classification of the IR singularities that we actually have to deal with and the calculation of the real corrections.

Soft gluon singularities are present for $\tilde{q}\tilde{q}$ production and in the $q\bar{q}$-annihilation channels in $\tilde{q}\tilde{q}^*$ and $\tilde{t}\tilde{t}^*$ production.

- Only for $\tilde{q}\tilde{q}$ and $\tilde{q}\tilde{q}^*$ production, where the full QCD one-loop amplitude enters, also singularities due to collinearly radiated gluons off initial state quarks contribute. As an example see the first loop diagram in Fig. 3.9 (c). To absorb also the universal *gluonic collinear singularities*, the redefinition of the PDFs has to be done accordingly including $\mathcal{O}(\alpha_s)$ effects.

- For completeness, we mention that at $\mathcal{O}(\alpha_s^2\alpha)$, squarks and gluinos can also be produced in association with a real quark or anti-quark. For $\tilde{q}\tilde{q}^*$ and $\tilde{q}\tilde{q}$ production the real (anti-)quark radiation proceeds from qg $(\bar{q}g)$ initial states. These processes exhibit singularities if the *gluon splits collinearly into a quark–anti-quark pair*. Again, this requires an appropriate redefinition of the (anti-)quark PDF at $\mathcal{O}(\alpha_s)$.

  Singularities due to collinearly radiated quarks only occur in the qg-fusion channel for $\tilde{q}\tilde{q}^*$ and $\tilde{q}\tilde{q}$ production. Due to color and charge conservation, they are absent for $\tilde{t}\tilde{t}^*$ production as well as for $\tilde{g}\tilde{q}$ production.

The calculation of the real corrections is nontrivial owing to the IR singularities that arise in the integration of phase space of the emitted particle. In case of real gluons, the calculation is even more involved since the color structure of the diagrams has to be taken into account properly. We first describe the treatment of real photon corrections in Section 4.2.1. Details for real gluon radiation and the treatment of the color correlation are given in Section 4.2.2. We briefly comment on real quark radiation in Section 4.2.3.

4.2.1 Real photon bremsstrahlung

To cancel the photonic IR singularities from the virtual corrections, we need to include real photon bremsstrahlung at the right order. In our case, these are $\mathcal{O}(\alpha_s^2\alpha)$ contributions from lowest-order $2 \to 3$ processes. We consider the generic partonic process

$$a(p_a)\ b(p_b) \to c(p_c)\ d(p_d)\ \gamma(k), \tag{4.51}$$

where a and b are here massless partons $(a, b = q, \bar{q}, g)$ and c and d are massive SUSY particles $(c, d = \tilde{g}, \tilde{q}, \tilde{q}^*)$. The masses and momenta of the partons and SUSY particles are denoted with m_i, p_i $(i = a, b, c, d)$, respectively, and the photon carries momentum k. The photon can be emitted by any of the involved (anti-)quarks and (anti-)squarks. As a notation and convenient bookkeeping device for later, we introduce the labels $d\hat{\sigma}_X^{m,n}$ for a cross section of the partonic process X at a given order $\mathcal{O}(\alpha_s^m\alpha^n)$ in the strong and electroweak coupling constants. Matrix elements are denoted analogously.[18]

---

[18]In the following we refer to cross sections at $\mathcal{O}(\alpha_s^2\alpha)$ only, however the discussion of real photon bremsstrahlung is rather general and the presented methods can be applied to tree-level processes

At the partonic level, the cross section reads

$$\int d\hat{\sigma}^{2,1}_{ab\to cd\gamma} = \frac{1}{2\hat{s}} \int d\mathrm{PS}_3 \, \overline{\sum} |\mathcal{M}^{1,\,1/2}_{ab\to cd\gamma}|^2, \tag{4.52}$$

$$\text{with} \quad d\mathrm{PS}_3 = \int \frac{d^3 p_c}{(2\pi)^3} \frac{1}{2E_c} \int \frac{d^3 p_d}{(2\pi)^3} \frac{1}{2E_d} \int \frac{d^3 k}{(2\pi)^3} \frac{1}{2E_\gamma} (2\pi)^4 \, \delta^{(4)}(p_a + p_b - p_c - p_d - k),$$

in terms of the c. m. energy squared $\hat{s}$, the three-particle phase-space element $d\mathrm{PS}_3$, and the (spin- and polarization-summed and squared) amplitude $\mathcal{M}^{1,\,1/2}_{ab\to cd\gamma}$. For photon emission off the i-th particle, the amplitude is obtained from that of the $2 \to 2$ process $ab \to cd$ without photon radiation by inserting an additional particle propagator with momentum q (and an additional interaction vertex) and we write schematically

$$\mathcal{M}^{1,\,1/2}_{ab\to cd\gamma} \propto \frac{1}{q^2 - m_i^2}, \tag{4.53}$$

where the momentum transfer is $q = p_i - k$ for initial state photon radiation and $q = p_i + k$ for final state radiation. As the external particles are on-shell, the propagator simplifies to

$$\frac{1}{q^2 - m_i^2} = \frac{1}{\pm 2p_i k} = \frac{1}{\pm 2E_i E_\gamma \left(1 - \sqrt{1 - \frac{m_i^2}{E_i^2}} \cos\theta_{i\gamma}\right)}, \tag{4.54}$$

with $\theta_{i\gamma}$ being the angle between the emitter i and the photon.

From Eq. (4.54) we see that the integration over the photon phase space Eq. (4.52) can become problematic in two regions: In the soft region, where the photon is produced with vanishing energy $E_\gamma \approx 0$ and, if the emitter is massless ($m_i = 0$), in the collinear region, where the angle between the photon and the emitting particle is small and $\cos\theta_{i\gamma} \approx 1$. In the singular regions, we therefore insert a non-zero photon mass λ (i. e. $q^2 = \pm 2p_i k + \lambda^2$) and keep non-zero quark masses m_q as regulators. Note that for the SUSY processes considered here, Eq. (4.51), collinear singularities only appear from initial state radiation, since the final (SUSY) particles are massive.

Several methods have been worked out to perform the phase-space integration Eq. (4.52) in the soft and collinear regions.

The idea of the phase-space slicing approach [128,142] is to separate the singular from the finite regions in the phase-space integration. By introducing a cutoff parameter ΔE, we divide the photon bremsstrahlung contribution into a soft part, where the photon energy is below the cutoff $E_\gamma \leq \Delta E$, and in a hard part, where the photon is emitted with $E_\gamma > \Delta E$. Whereas the soft photon part is IR singular, the hard photon contributions are well defined and IR finite and can safely be integrated numerically.

---

of other orders in perturbation theory in complete analogy.

It has been shown that the soft photon part factorizes into the underlying $2 \to 2$ lowest order process and a soft correction factor which contains the singularities. In the approximation of small photon energies it can be calculated analytically. For the cross section for real photon emission we write generically

$$
\begin{aligned}
\int d\hat{\sigma}^{2,1}_{ab \to cd\gamma} &= \int_{E_\gamma \leq \Delta E} d\hat{\sigma}^{2,1}_{ab \to cd\gamma} \;+\; \int_{E_\gamma > \Delta E} d\hat{\sigma}^{2,1}_{ab \to cd\gamma} \\
&= \int d\hat{\sigma}^{2,1}_{ab \to cd\gamma}(\Delta E)\Big|_{\text{soft}} + \int d\hat{\sigma}^{2,1}_{ab \to cd\gamma}(\Delta E)\Big|_{\text{hard}}.
\end{aligned}
\tag{4.55}
$$

The dependence on the cutoff parameter cancels after summing soft and hard contributions. The precise value of the cutoff is therefore arbitrary, however it should be small compared to typical energy scales Q of the process since the results from the soft photon approximation are correct up to $\mathcal{O}(\Delta E/Q)$ only.

In bremsstrahlung contributions from quark-induced channels, also collinear singularities have to be taken in to account properly. Therefore a second cutoff $\Delta\theta$ is introduced, on the angle $\theta_{i\gamma}$ between the emitter i and the photon. As a result the hard photon part is split into a (hard) collinear and a (hard) non-collinear contribution,

$$
d\hat{\sigma}^{2,1}_{ab \to cd\gamma}(\Delta E)\Big|_{\text{hard}} = d\hat{\sigma}^{2,1}_{ab \to cd\gamma}(\Delta E, \Delta\theta)\Big|_{\text{coll.}} + d\hat{\sigma}^{2,1}_{ab \to cd\gamma}(\Delta E, \Delta\theta)\Big|_{\text{non-coll.}}.
\tag{4.56}
$$

Similar to the soft photon case, the cross section in the collinear region is related to the lowest order result and can be approximated analytically. Again, the angle cutoff is a priori arbitrary and cancels in the sum of collinear and non-collinear contributions. But for reliable approximations it it necessary to choose a cutoff which justifies the assumption that the direction of flight of the emitting particle is unaffected by the photon radiation (collinear limit).

The analytical expressions for the cross sections in the soft and collinear region will be discussed in the next subsection.

The biggest advantage of the phase-space slicing approach is clearly its intuitivity. However the proper choice of the cutoffs needs some care. If the cutoffs are chosen too large, the analytical approximations are not valid anymore. If chosen too small, the numerical integration becomes unstable in the regions "too close" to the singularities and large integration errors are obtained.

An alternative approach is provided by the dipole subtraction method which avoids singular numerical integrations, as originally presented for massless QCD in [143] and later extended to massive particles in QED and QCD in [144–146]. Here, a simple auxiliary function is subtracted from and added to the singular integrand. The auxiliary function has to be constructed under two conditions. First of all it is supposed to cancel all IR singularities contained in the real photon contributions. As a result, the integration of the

subtracted amplitude can be performed numerically over the full phase space. On the other hand, it has to be so simple that it can be integrated analytically when it is added again. Schematically, the real correction cross section can be expressed as follows

$$d\hat{\sigma}^{2,1}_{ab\to cd\gamma} = \frac{1}{2\hat{s}} \int d\mathrm{PS}_3 \left(\overline{\sum} \left| \mathcal{M}^{1,\,1/2}_{ab\to cd\gamma} \right|^2 - \left| \mathcal{M}^{1,\,1/2}_{\mathrm{aux.}} \right|^2 \right) + \frac{1}{2\hat{s}} \int d\mathrm{PS}_3 \left| \mathcal{M}^{1,\,1/2}_{\mathrm{aux.}} \right|^2, \quad (4.57)$$

where $\mathcal{M}_{\mathrm{aux.}}$ is the appropriately chosen auxiliary function. In the sum of real and virtual corrections, the IR singularities from the virtual corrections cancel their counterparts from the integrated auxiliary function and the result is IR finite.

As shown in [145], results derived by application of the dipole subtraction methods typically have integration errors reduced by an order of magnitude compared to results obtained from phase-space slicing (if the same statistics is used). By construction, no cutoff parameters need to be introduced. However the actual implementation of the formalism is less intuitive than for phase-space slicing and becomes complicated for massive particles, if cuts are applied, and in particular if non-inclusive quantities are considered.

In the following, we will refer to the phase-space slicing method only.

Soft photon bremsstrahlung

In the soft region, the energy of the emitted photon is small by definition. Hence the real radiation matrix element can be approximated under the assumption that the momenta of the other final state particles are unaffected by the emission. As a consequence, the amplitude for the $2 \to 3$ processes factorizes from the original $2 \to 2$ amplitude (with unchanged momenta). For a photon emission off particle i with fractional electrical charge e_{q_i} it is, in the limit $k \to 0$ (eikonal approximation),

$$\mathcal{M}^{1,\,1/2}_{ab\to cd\gamma,i}\Big|_{\mathrm{soft}} = -e\, e_{q_i}\, \frac{\epsilon p_i}{\pm k p_i}\, \mathcal{M}^{1,0}_{ab\to cd}, \quad (4.58)$$

ϵ being the polarization vector of the photon. The sign in the nominator depends on the charge flow, the plus sign refers to initial state radiation, the minus sign to final state radiation. In Eq. (4.58), all terms proportional to the photon momentum k in the denominator have been neglected. The soft singularity is fully contained in the nominator $\propto k p_i$. One can easily show (see e.g. [128]), that Eq. (4.58) holds generally for external fermion, boson and scalar lines (with the respective charge factors). Diagrams with photons radiated off internal lines or quartic vertices do not induce IR singularities and can be neglected in the soft approximation. Thus, the full soft photon matrix element results from summation over all external charged particles i,

$$\mathcal{M}^{1,\,1/2}_{ab\to cd\gamma}\Big|_{\mathrm{soft}} = \sum_i \mathcal{M}^{1,\,1/2}_{ab\to cd\gamma,i}\Big|_{\mathrm{soft}} = -e\, \mathcal{M}^{1,0}_{ab\to cd} \sum_i e_{q_i}\, \frac{\epsilon p_i}{\pm k p_i}. \quad (4.59)$$

The term $J^\mu(k) = \sum_i e_{q_i} p_i^\mu/(\pm k p_i)$ is the *eikonal current* for the emission of the soft photon with momentum k.

Under the approximation that the remaining momenta are unchanged by the photon emission, also the three-particle phase space factorizes from the original two-particle phase space. This yields for the differential cross section

$$
\begin{aligned}
d\hat{\sigma}^{2,1}_{ab\to cd\gamma}(\Delta E)\Big|_{\text{soft}} &= -d\hat{\sigma}^{2,0}_{ab\to cd} \times \frac{\alpha}{2\pi^2} \int_{|\vec{k}|\leq\Delta E} \frac{d^3|\vec{k}|}{2E_\gamma} \sum_{i,j} \frac{\pm e_{q_i} e_{q_j} p_i p_j}{(kp_i)(kp_j)}, \\
&\equiv -d\hat{\sigma}^{2,0}_{ab\to cd} \times \frac{\alpha}{\pi} \sum_{i,j} \pm e_{q_i} e_{q_j} \mathcal{I}_{ij}
\end{aligned}
\tag{4.60}
$$

where now the sign refers to the relative sign of emitter i and j. Note that we use here a photon mass λ as regulator, i.e. $E_\gamma = \sqrt{|\vec{k}|^2 + \lambda^2}$. General analytic expressions for the process independent phase-space integrals $\mathcal{I}_{ij}$ are given in [128,147],

$$
\begin{aligned}
\mathcal{I}_{ij} = \frac{r p_i p_j}{(r p_i)^2 - p_j^2} &\left\{ \frac{1}{2} \log \frac{(r p_i)^2}{p_j^2} \log \frac{4(\Delta E)^2}{\lambda^2} \right. \\
&\left. + \left[\frac{1}{4} \log^2 \frac{u_0 - |\vec{u}|}{u_0 + |\vec{u}|} + \text{Li}_2\left(1 - \frac{u_0 + |\vec{u}|}{v}\right) + \text{Li}_2\left(1 - \frac{u_0 - |\vec{u}|}{v}\right) \right]_{u=p_j}^{u=r p_i} \right\},
\end{aligned}
\tag{4.61}
$$

where $\text{Li}_2(z) = \int_z^0 dt/t \, \ln(1-t)$ is the dilogarithm and r and v are defined through

$$
r^2 p_i^2 - 2r p_i p_j + p_j^2 = 0, \qquad \frac{r E_i - E_j}{E_j} > 0; \qquad v = \frac{(r p_i)^2 - p_j^2}{2(r E_i - E_j)}.
\tag{4.62}
$$

More explicit formulas can be worked out in the limit of small quark masses and for the specific process under consideration, depending on the type and charge of the external particles. For $\tilde{t}\tilde{t}^*$, $\tilde{g}\tilde{q}$, and $\tilde{q}\tilde{q}$ production the formulas are given in the respective chapters.

Collinear photon bremsstrahlung

For the processes considered here, collinear singularities only arise from initial state radiation off a quark or anti-quark. Keeping the incoming parton momentum fixed, the momentum entering the hard scattering process depends on the momentum fraction carried away by the emitted particle. In cross section calculations, we cannot treat the fermion–photon pair inclusively. I.e. not only the summed momenta of the fermion and the photon, but both their values are important for cross sections and, in particular, for distributions.

The situation is different for *collinear-safe* observables [148]. As a typical example, let us consider collinear photon radiation off final electrons. In an experiment, both the collinear
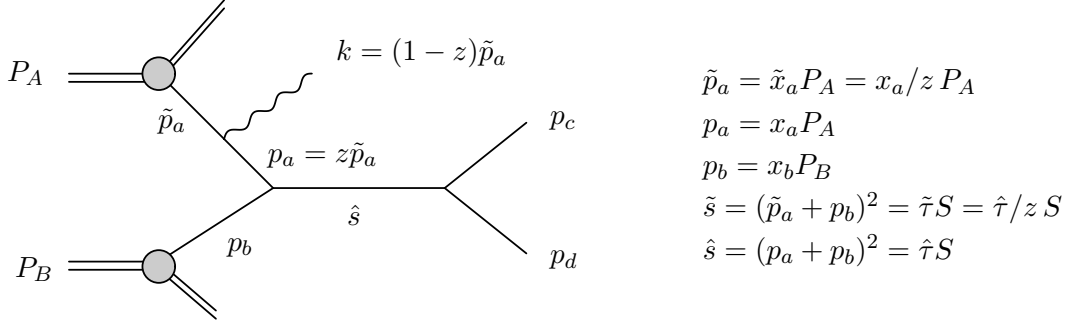
Figure 4.1.: Generic Feynman diagram for initial state photon radiation. Particle a with momentum $\tilde{p}_a$ emits a photon with momentum $k = (1 - z)\tilde{p}_a$. The squared energy of the hard scattering process is $\hat{s} = (p_a + p_b)^2 = (z\tilde{p}_a + p_b)^2 = (p_c + p_d)^2$. The colliding hadrons carry momentum P_A and P_B, respectively, yielding the hadronic squared energy $S = (P_A + P_B)^2$, the gray blobs refer to the PDFs.

electron and photon would hit the same cell in the calorimeter and only their summed energy could be measured. In this case one would treat the electron and the photon inclusively as one quasi-particle. For the calculation of collinear-safe observables, the precise energy fraction $z = E_i/(E_i + E_\gamma)$ of the electron after collinear photon emission is not relevant and can be integrated out analytically. If collinear singularities arise from final state radiation only, and if the photon is considered sufficiently inclusively, all IR singularities cancel in the sum of virtual and real corrections as guaranteed by the KLN theorem.

The extraction of the collinear singularities from the bremsstrahlung cross section has been done in e. g. in [149,150]. We only refer to initial state radiation and use the notation as introduced in Fig. 4.1. The collinear region is defined by an upper cutoff on the angle $\theta_{i\gamma}$ between the emitter and the photon or, equivalently, requiring $\cos\theta_{i\gamma} > 1 - \delta_\theta$. In this region, the phase-space element for the total process $\tilde{p}_a + p_b \to p_c + p_d + k$ (expressed in terms of the involved momenta) factorizes into the two particle phase-space element for the hard process $p_a + p_b \to p_c + p_d$ and a collinear part referring to the photon phase space. Also, the squared matrix element factorizes into the leading order matrix element and a collinear factor. As a result, the cross section in the collinear region for photon radiation off all initial state charged particles i of energy $E_i = \sqrt{\hat{s}}/2$ can be expressed as

$$d\hat{\sigma}^{2,1}_{ab\to cd\gamma}(\Delta E, \delta_\theta)\Big|_{\text{coll.}} = \frac{\alpha}{\pi} \sum_i e_{q_i}^2 \int_{z_0}^{1-\Delta E/E_i} dz \; \kappa_{\text{coll.}}(z, \hat{s}) \; d\hat{\sigma}^{2,0}_{ab\to cd}(\hat{s}), \qquad (4.63)$$

where the collinear factor $\kappa_{\text{coll.}}$ depends on the IR regulator m_q and reads

$$\kappa_{\text{coll.}}(z, \hat{s}) = \frac{1}{2}P_{q\leftarrow q}(z)\left[\ln\left(\frac{\hat{s}}{zm_q^2}\frac{\delta_\theta}{2}\right) - 1\right] + \frac{1}{2}(1 - z), \qquad (4.64)$$

and $P_{q \leftarrow q}(z)$ being the LO splitting function of a photon from a quark or anti-quark [106],

$$P_{q \leftarrow q}(z) = \frac{1 + z^2}{1 - z}. \tag{4.65}$$

Note that the leading order cross section depends on the energy $\hat{s} = (p_a + p_b)^2$ of the hard scattering process, while the relevant energy for the collinear factor is the full energy $\hat{s}/z = (\tilde{p}_a + p_b)^2$. The lower integration limit of the z-integration is restricted from the production threshold, $z_0 = (m_c + m_d)^2/\hat{s}$. The upper limit has to be chosen such that an overlap with the soft region is avoided and is thus reduced from $z = 1$ to $z = 1 - \Delta E/E_i$, where ΔE is the upper cutoff on the energy a photon may have to be considered as soft.

Factorization of initial state singularities

The quark mass logarithm in the collinear factor of Eq. (4.64) is not canceled in the sum of virtual and real corrections. It can be understood as contribution from collinear photon emission at very low momentum transfers. In this region, perturbation theory is not applicable anymore. Instead, these collinearly emitted photons have to be seen as a long-distance effect, as processes which occur *before* the emitting parton enters the hard-scattering process and which are thus already included in the extraction of the PDFs. In the calculation of hadronic cross sections at NLO, care has to be taken to not overcount these effects. IR-finite results are obtained by absorbing the collinear mass logarithms from the real radiation contribution into redefined PDFs.

The redefinition of the PDF for parton i $(i = q, \bar{q})$ in hadron A including photon radiation at $\mathcal{O}(\alpha)$ is performed at the factorization scale μ_F as follows [149,151],

$$f_{i/A}(x, \mu_F) \rightarrow f_{i/A}(x, \mu_F) \left(1 + \frac{\alpha}{\pi} e_{q_i}^2 \, \kappa_{\text{soft}}^{\text{PDF}}\right) + \frac{\alpha}{\pi} e_{q_i}^2 \int_x^{1-\delta_s} \frac{dz}{z} \, f_{i/A}\left(\frac{x}{z}, \mu_F\right) \kappa_{\text{coll.}}^{\text{PDF}}(z), \tag{4.66}$$

with the soft photon cutoff parameter $\delta_s = 2\Delta E/\sqrt{\hat{s}}$ and

$$\kappa_{\text{soft}}^{\text{PDF}} = -1 + \ln \delta_s + \ln^2 \delta_s - \ln\left(\frac{\mu_F^2}{m_q^2}\right) \left[\frac{3}{4} + \ln \delta_s\right] + \frac{\lambda_{sc}}{4} \left[9 + \frac{2\pi^2}{3} + 3 \ln \delta_s - 2 \ln^2 \delta_s\right],$$

$$\kappa_{\text{coll.}}^{\text{PDF}}(z) = \frac{1}{2} P_{qq}(z) \left[\ln\left(\frac{m_q^2 (1-z)^2}{\mu_F^2}\right) + 1\right] - \frac{\lambda_{sc}}{2} \left[P_{qq}(z) \ln \frac{1-z}{z} - \frac{3}{2} \frac{1}{1-z} + 2z + 3\right]. \tag{4.67}$$

The lower integration limit $z_0 = x$ guarantees that the parton momentum fraction in the PDF (x/z) is smaller than unity.

There is some freedom in the redefinition of the PDFs. In addition to the IR-singular

terms, also finite terms can be absorbed. For a consistent treatment, a factorization scheme has to be defined and to be used both in the extraction of the PDFs from experiment and in the theoretical calculation. In Eq. (4.66), the results for different choices of factorization schemes are parameterized by the parameter λ_{sc}. In the $\overline{\text{MS}}$ scheme, only the singular terms are subtracted and it is $\lambda_{sc} = 0$. In contrast it is $\lambda_{sc} = 1$ in the *DIS* scheme, where the PDFs are defined to absorb the quantum corrections to the structure function F_2 in all orders of perturbation theory. Obviously, the absorption of collinear singularities due to photons into the quark PDFs requires the consistent inclusion of $\mathcal{O}(\alpha)$ effects both in the theoretical evolution and in the extraction of the distributions from experiment. At present, there is only one set of PDFs available where the $\mathcal{O}(\alpha)$ are taken properly into account: MRST 2004 QED [107], using the *DIS* factorization scheme (i.e. $\lambda_{sc} = 1$).

The actual effect of using the redefined PDFs is that for the total hadronic cross section at $\mathcal{O}(\alpha_s^2 \alpha)$, new contributions arise from the interference of the $\mathcal{O}(\alpha)$ terms in Eq. (4.66) with the $\mathcal{O}(\alpha_s^2)$ LO cross sections, sometimes referred to as collinear counterterms. Summing over all initial state emitters i among the partons a, b (where j denotes the respective second parton), it is at $\mathcal{O}(\alpha_s^2 \alpha)$

$$
\begin{aligned}
d\sigma_{AB \to cd\gamma}^{\text{coll.CT}}(\Delta E) = {} & \frac{\alpha}{\pi} \sum_i e_{q_i}^2 \int d\tau \int dx_i \int dx_j \; \kappa_{\text{soft}}^{\text{PDF}} \; d\hat{\sigma}_{ab \to cd}^{2,0}(\hat{s}) \, \delta(\tau - x_i x_j) \\
& \times \frac{1}{1 + \delta_{ij}} \left[f_{i/A}(x_i, \mu_F) f_{j/B}(x_j, \mu_F) + f_{j/A}(x_j, \mu_F) f_{i/B}(x_i, \mu_F) \right] \\
& + \frac{\alpha}{\pi} \sum_i e_{q_i}^2 \int d\tilde{\tau} \int d\tilde{x}_i \int dx_j \int dz \; \kappa_{\text{coll.}}^{\text{PDF}}(z) \; d\hat{\sigma}_{ab \to cd}^{2,0}(\hat{s}) \, \delta(\tilde{\tau} - \tilde{x}_i x_j) \\
& \times \frac{1}{1 + \delta_{ij}} \left[f_{i/A}(\tilde{x}_i, \mu_F) f_{j/B}(x_j, \mu_F) + f_{j/A}(x_j, \mu_F) f_{i/B}(\tilde{x}_i, \mu_F) \right],
\end{aligned}
\tag{4.68}
$$

in terms of the inclusive variables $\tilde{x}_i = \frac{x_i}{z}$ and $\tilde{\tau} = \frac{\tau}{z}$ and the hard energy squared $\hat{s} = (p_1 + p_2)^2 = x_1 x_2 S$ (see Fig. 4.1 for the notation). We perform a transformation of $\tilde{x}_i$, $\tilde{\tau}$ to the hard variables x_i, τ and use the δ-functions to cancel the x_j integrations. This leads to

$$
\begin{aligned}
d\sigma_{AB \to cd\gamma}^{\text{coll.CT}}(\Delta E) = {} & \frac{\alpha}{\pi} \sum_i e_{q_i}^2 \int d\tau \, \frac{d\mathcal{L}_{AB}^{ij}}{d\tau} \, \kappa_{\text{soft}}^{\text{PDF}} \; d\hat{\sigma}_{ab \to cd}^{2,0}(\hat{s}) \tag{4.69} \\
& + \frac{\alpha}{\pi} \sum_i e_{q_i}^2 \int d\tau \int \frac{dx_i}{x_i} \int_{x_i}^{1 - \Delta E / E_i} \frac{dz}{z} \, \kappa_{\text{coll.}}^{\text{PDF}}(z) \; d\hat{\sigma}_{ab \to cd}^{2,0}(\hat{s}) \\
& \times \frac{1}{1 + \delta_{ij}} \left[f_{i/A}\!\left(\frac{x_i}{z}, \mu_F\right) f_{j/B}\!\left(\frac{\tau}{x_i}, \mu_F\right) + f_{j/A}\!\left(\frac{\tau}{x_i}, \mu_F\right) f_{i/B}\!\left(\frac{x_i}{z}, \mu_F\right) \right],
\end{aligned}
$$

expressed in terms of the parton luminosity $d\mathcal{L}/d\tau$ defined in Eq. (3.3).

In the sum of all contributions, the mass singularities from the collinear factor $\kappa_{\text{coll.}}(z)$ in Eq. (4.63) cancel those from $\kappa_{\text{coll.}}^{\text{PDF}}(z)$ in Eq. (4.69). The first summand of Eq. (4.69), proportional to $\kappa_{\text{soft}}^{\text{PDF}}$, cancels singularities that remain in the sum of virtual and soft photon corrections. The resulting cross section is finite with respect to photon singularities, i. e. it is independent of the IR regulators λ, m_q and, in a wide range, of the cutoff parameters ΔE, δ_θ introduced by the phase-space slicing[19].

4.2.2 Real gluon bremsstrahlung

Processes that also provide EW tree-level production channels give rise to gluonic IR singularities in the virtual corrections at $\mathcal{O}(\alpha_s^2\alpha)$. The soft and collinear singularities cancel if the corresponding real gluon bremsstrahlung contributions are taken into account.

The treatment of singularities proceeds in close analogy to that of photonic singularities described above, as the emitted gluons behave Abelian-like in the occurring diagrams. At the considered order of perturbation theory, gluons are only emitted off external (anti-)quarks and (anti-)squarks and the non-Abelian gluon self-interaction vertex does not appear. This implies that we can regularize the gluonic IR singularities by giving a mass to the gluon. Furthermore we keep non-zero quark masses where necessary. The calculation of the real gluon bremsstrahlung has also been done in the phase-space slicing approach. To simplify matters we use the same mass regulator λ and cutoff parameters ΔE, δ_θ in the notation as for the photonic singularities, even though in the actual calculation they are to be considered as independent parameters.

However two difficulties arise since the gluon couples via the strong interaction and carries color charge in contrast to the photon. First, by counting orders, we find that gluon emission can only contribute at the appropriate order $\mathcal{O}(\alpha_s^2\alpha)$ in the interference of an EW-mediated diagram with gluon emission and a QCD-mediated diagram with a real gluon attached. Separately taken, the diagrams would give contributions of $\mathcal{O}(\alpha_s\alpha^2)$ and $\mathcal{O}(\alpha_s^3)$, respectively. Secondly, the emission of a gluon changes the color structure of an diagram. This has to be taken into account in the soft approximation where it leads to color correlations in the eikonal current. As a result, the soft and collinear parts of the differential cross sections do factorize analogously to the photonic case into soft/collinear factors and contributions from diagrams without real emission. But the latter are $\mathcal{O}(\alpha_s\alpha)$ interference contributions and in the soft gluon part a rearrangement of the color structure has to be performed.

Soft gluon bremsstrahlung

The approximation of real gluon bremsstrahlung in the soft region has been done in [143] and we closely follow the prescription introduced there. In analogy to Eq. (4.59), we can

---

[19]As an example, see the numerical studies on the cutoff dependence of the results in Figs. 5.10 and 7.8.

write a $2 \to 3$ matrix element in the soft limit as factorized from the corresponding $2 \to 2$ matrix element without gluon emission,

$$\left.\left| \mathcal{M}_{ab \to cdg} \right\rangle \right|_{\text{soft}} = -g_s \, \epsilon_\mu(k) J^\mu(k) \left| \mathcal{M}_{ab \to cd} \right\rangle. \tag{4.70}$$

Here, g_s is the strong coupling and ϵ_μ denotes the gluon polarization vector. The eikonal current $J^\mu(k)$ for the emission of a soft gluon of momentum k is

$$J^\mu(k) = \sum_i \mathbf{T}_i \frac{p_i^\mu}{kp_i}, \tag{4.71}$$

where now the sum over i runs over all colored external particles. For the emission of a gluon with color index c off particle i with color index β, the matrix-valued color charge operator $\mathbf{T}_i$ is

$$\mathbf{T}_i \;\to\; (T_i)_{\alpha\beta}^c = \begin{cases} t_{\alpha\beta}^c & \text{if } i = \text{ ingoing quark or outgoing anti-(s)quark} \\ -t_{\beta\alpha}^c & \text{if } i = \text{ ingoing anti-quark or outgoing (s)quark} \end{cases} . \tag{4.72}$$

The operator $\mathbf{T}_i$ is defined on the color space. The matrix elements in Eq. (4.70) have to be identified as abstract vectors in this space for a proper definition. For more details we refer to [143], here we keep the sloppy notation of Eq. (4.70). The color charge algebra is

$$\mathbf{T}_i \cdot \mathbf{T}_j = \mathbf{T}_j \cdot \mathbf{T}_i \quad \text{if } i \neq j; \qquad \mathbf{T}_i^2 = C_i, \tag{4.73}$$

where C_i is the Casimir operator, i. e. $C_i = C_F = 4/3$ for emitting (anti-)(s)quarks.

The differential cross section for soft gluon radiation at $\mathcal{O}(\alpha_s^2 \alpha)$ can then be expressed in an similar way to the one for soft photon radiation in Eq. (4.60),

$$\left. d\hat{\sigma}_{ab \to cdg}^{2,1}(\Delta E) \right|_{\text{soft}} =$$
$$-\frac{1}{2\hat{s}} \, d\text{PS}_2 \, \frac{\alpha_s}{2\pi^2} \int_{|\vec{k}| \leq \Delta E} \frac{d^3|\vec{k}|}{2E_g} \; \overline{\sum} \, 2\text{Re}\left\{ \left\langle \mathcal{M}_{ab \to cd}^{0,1} \right| [J^\mu(k)]^\dagger J_\mu(k) \left| \mathcal{M}_{ab \to cd}^{1,0} \right\rangle \right\}, \tag{4.74}$$

with

$$[J^\mu(k)]^\dagger J_\mu(k) = \sum_i \mathbf{T}_i^2 \frac{p_i^2}{(kp_i)^2} + 2 \sum_{i<j} \mathbf{T}_i \cdot \mathbf{T}_j \frac{p_i p_j}{(kp_i)(kp_j)}, \tag{4.75}$$

and the two-particle phase-space element $d\text{PS}_2$

$$d\text{PS}_2 = \int \frac{d^3 p_c}{(2\pi)^3} \frac{1}{2E_c} \int \frac{d^3 p_d}{(2\pi)^3} \frac{1}{2E_d} (2\pi)^4 \, \delta^{(4)}(p_a + p_b - p_c - p_d). \tag{4.76}$$

The summation over final state colors and helicities and average of initial state colors is included on the right hand side of Eq. (4.74) as indicated by the symbol $\overline{\sum}$. Note that the cross section results from an interference contribution of an EW-mediated Born amplitude $\mathcal{M}^{0,1}_{ab \to cd}$ and a QCD-mediated Born amplitude $\mathcal{M}^{1,0}_{ab \to cd}$.

The explicit result of Eq. (4.74) depends of course on the process under consideration. In our calculations, soft gluon radiation enters in diagrams with two (anti-)quarks in the initial state and two (anti-)squarks in the final state. All four particles can emit a gluon, i.e. the sums in Eq. (4.75) run over $i, j = 1, \ldots, 4$. To further evaluate Eq. (4.74), we use the definition of the color charge operators, Eq. (4.73),

$$\mathbf{T}_i^2 \left| \mathcal{M}_{ab \to cd} \right\rangle = \frac{4}{3} \left| \mathcal{M}_{ab \to cd} \right\rangle, \qquad \mathbf{T}_i \sum_{j=1}^{4} \mathbf{T}_j \left| \mathcal{M}_{ab \to cd} \right\rangle = 0, \tag{4.77}$$

where the second equation follows from color charge conservation. Eq. (4.77) allows to express the six symmetric charge operators $\mathbf{T}_i \cdot \mathbf{T}_j$ ($i \neq j$) in terms of only two independent operators, e.g. $\mathbf{T}_1 \cdot \mathbf{T}_2$ and $\mathbf{T}_1 \cdot \mathbf{T}_3$ (see Appendix A of [143] for explicit formulas). The squared matrix element of Eq. (4.74) thus splits into three summands only. For our case of four (s)quarks or anti-(s)quarks interacting, one finds

$$\left\langle \mathcal{M}^{0,1}_{ab \to cd} \right| [J^\mu(k)]^\dagger J_\mu(k) \left| \mathcal{M}^{1,0}_{ab \to cd} \right\rangle =$$
$$\frac{4}{3} \left\langle \mathcal{M}^{0,1}_{ab \to cd} \middle| \mathcal{M}^{1,0}_{ab \to cd} \right\rangle \left(\sum_{i=1}^{4} \mathcal{P}_{ii} - 2\mathcal{P}_{23} - 2\mathcal{P}_{14} \right)$$
$$+ 2 \left\langle \mathcal{M}^{0,1}_{ab \to cd} \middle| \mathbf{T}_1 \cdot \mathbf{T}_2 \middle| \mathcal{M}^{1,0}_{ab \to cd} \right\rangle (\mathcal{P}_{12} + \mathcal{P}_{34} - \mathcal{P}_{23} - \mathcal{P}_{14})$$
$$+ 2 \left\langle \mathcal{M}^{0,1}_{ab \to cd} \middle| \mathbf{T}_1 \cdot \mathbf{T}_3 \middle| \mathcal{M}^{1,0}_{ab \to cd} \right\rangle (\mathcal{P}_{13} + \mathcal{P}_{24} - \mathcal{P}_{23} - \mathcal{P}_{14}), \tag{4.78}$$

with $\mathcal{P}_{ij} = (p_i p_j)/[(kp_i)(kp_j)]$. The first term on the r.h.s. of Eq. (4.78) is proportional to the color-unchanged interference contribution of the EW-mediated and QCD-mediated diagrams. With explicit color indices for the external particles denoted by α_i, $i = 1, \ldots, 4$, we write

$$\left\langle \mathcal{M}^{0,1}_{ab \to cd} \middle| \mathcal{M}^{1,0}_{ab \to cd} \right\rangle = \left(\mathcal{M}^{0,1\,[\alpha_1,\alpha_2,\alpha_3,\alpha_4]}_{ab \to cd} \right)^* \mathcal{M}^{1,0\,[\alpha_1,\alpha_2,\alpha_3,\alpha_4]}_{ab \to cd}. \tag{4.79}$$

The second and third terms on the r.h.s. of Eq. (4.78) are connected to color-modified interference contributions, defined as

$$\left\langle \mathcal{M}^{0,1}_{ab \to cd} \middle| \mathbf{T}_1 \cdot \mathbf{T}_2 \middle| \mathcal{M}^{1,0}_{ab \to cd} \right\rangle = \left(\mathcal{M}^{0,1\,[\beta_1,\beta_2,\alpha_3,\alpha_4]}_{ab \to cd} \right)^* T^c_{\beta_1 \alpha_1} T^c_{\beta_2 \alpha_2} \mathcal{M}^{1,0\,[\alpha_1,\alpha_2,\alpha_3,\alpha_4]}_{ab \to cd}, \tag{4.80}$$

$$\left\langle \mathcal{M}^{0,1}_{ab \to cd} \middle| \mathbf{T}_1 \cdot \mathbf{T}_3 \middle| \mathcal{M}^{1,0}_{ab \to cd} \right\rangle = \left(\mathcal{M}^{0,1\,[\beta_1,\alpha_2,\beta_3,\alpha_4]}_{ab \to cd} \right)^* T^c_{\beta_1 \alpha_1} T^c_{\beta_3 \alpha_3} \mathcal{M}^{1,0\,[\alpha_1,\alpha_2,\alpha_3,\alpha_4]}_{ab \to cd}, \tag{4.81}$$

where the particle-specific color matrices $T_{\alpha_i \beta_i}^c = (T_i)_{\alpha\beta}^c$ refer to Eq. (4.72).

In Eq. (4.78), only the factors $\mathcal{P}_{ij}$ depend on the integration momentum k. Inserting Eq. (4.78) into Eq. (4.74), the differential cross section for soft gluon radiation thus factorizes from the color modified tree-level cross sections. The integrated factors $\mathcal{P}_{ij}$ are nothing else then the universal phase-space factors $\mathcal{I}_{ij}$ defined in Eq. (4.61),

$$\mathcal{I}_{ij} = \frac{1}{4\pi} \int_{|\vec{k}| \leq \Delta E} \frac{d^3 |\vec{k}|}{2E_g} \; \frac{2 p_i p_j}{(k p_i)(k p_j)} = \frac{1}{2\pi} \int_{|\vec{k}| \leq \Delta E} \frac{d^3 |\vec{k}|}{2E_g} \; \mathcal{P}_{ij}. \tag{4.82}$$

We express the differential cross section as follows,

$$
\begin{aligned}
d\hat{\sigma}_{ab \to cdg}^{2,1}(\Delta E)\Big|_{\text{soft}} = -\frac{\alpha_s}{\pi} \Bigg\{ &\frac{4}{3} \left(\sum_{i=1}^{4} \mathcal{I}_{ii} - 2\mathcal{I}_{23} - 2\mathcal{I}_{14} \right) \times d\hat{\sigma}_{ab \to cd}^{1,1}(\hat{s}) \\
&+ 2 \left(\mathcal{I}_{12} + \mathcal{I}_{34} - \mathcal{I}_{23} - \mathcal{I}_{14} \right) \times \left[d\tilde{\sigma}_{ab \to cd}^{1,1}(\hat{s}) \right]_{12} \\
&+ 2 \left(\mathcal{I}_{13} + \mathcal{I}_{24} - \mathcal{I}_{23} - \mathcal{I}_{14} \right) \times \left[d\tilde{\sigma}_{ab \to cd}^{1,1}(\hat{s}) \right]_{13} \Bigg\},
\end{aligned}
\tag{4.83}
$$

in terms of the interference contribution from the tree-level EW and tree-level QCD amplitudes,

$$d\hat{\sigma}_{ab \to cd}^{1,1}(\hat{s}) = \frac{1}{2\hat{s}} d\text{PS}_2 \; \overline{\sum} \, 2\text{Re}\Big\{ \big\langle \mathcal{M}_{ab \to cd}^{0,1} \big| \mathcal{M}_{ab \to cd}^{1,0} \big\rangle \Big\}, \tag{4.84}$$

and the color modified EW–QCD interference contributions,

$$\left[d\tilde{\sigma}_{ab \to cd}^{1,1}(\hat{s}) \right]_{ij} = \frac{1}{2\hat{s}} d\text{PS}_2 \; \overline{\sum} \, 2\text{Re}\Big\{ \big\langle \mathcal{M}_{ab \to cd}^{0,1} \big| \mathbf{T}_i \cdot \mathbf{T}_j \big| \mathcal{M}_{ab \to cd}^{1,0} \big\rangle \Big\}. \tag{4.85}$$

Collinear gluon bremsstrahlung

In case of squark pair production, also singularities due to collinearly emitted gluons have to be considered. The collinear singularities are related to initial state radiation only and no color-modified contributions arise. Therefore, they can be treated in complete analogy to the photonic case with a replacement of the electric charges by color charges and the corresponding replacement of the gauge couplings.

In the collinear cone, defined by $\cos \theta_{ig} > 1 - \delta_\theta$, the real gluon bremsstrahlung cross section is approximated by (see Eq. (4.63)),

$$d\hat{\sigma}_{ab \to cdg}^{2,1}(\Delta E, \delta_\theta)\Big|_{\text{coll.}} = \frac{\alpha_s}{\pi} \sum_i C_F \int_{z_0}^{1 - \Delta E/E_i} dz \, \kappa_{\text{coll.}}(z, \hat{s}) \, d\hat{\sigma}_{ab \to cd}^{1,1}(\hat{s}), \tag{4.86}$$

in terms of the EW–QCD interference contribution $d\hat{\sigma}_{ab \to cd}^{1,1}$ defined in Eq. (4.84) and the

collinear factor $\kappa_{\text{coll.}}$ as given in Eq. (4.64). The sum over i in Eq. (4.86) runs over the color charged particles a, b in the initial state.

The remaining quark mass singularity is absorbed by a redefinition of the (anti-)quark PDF at $\mathcal{O}(\alpha_s)$,

$$f_{i/A}(x, \mu_F) \to f_{i/A}(x, \mu_F) \left(1 + \frac{\alpha_s}{\pi} C_F \, \kappa_{\text{soft}}^{\text{PDF}}\right) + \frac{\alpha_s}{\pi} C_F \int_x^{1-\delta_s} \frac{dz}{z} f_{i/A}\left(\frac{x}{z}, \mu_F\right) \kappa_{\text{coll.}}^{\text{PDF}}(z),$$
$$(4.87)$$

with the same factors $\kappa_{\text{soft}}^{\text{PDF}}$ and $\kappa_{\text{coll.}}^{\text{PDF}}(z)$ as in the photonic case, introduced in Eq. (4.67). Note however that the PDFs at NLO QCD are defined in the $\overline{\text{MS}}$ scheme and the scheme dependent parameter λ_{sc} has to be chosen accordingly ($\lambda_{sc} = 0$) in Eq. (4.67).

The additional $\mathcal{O}(\alpha_s^2 \alpha)$ contributions to the hadronic cross section due to the factorization of initial state gluon singularities are then, cf. Eq. (4.69),

$$d\sigma_{AB \to cdg}^{\text{coll.CT}}(\Delta E) = \frac{\alpha_s}{\pi} C_F \sum_i \int d\tau \, \frac{d\mathcal{L}_{AB}^{ij}}{d\tau} \kappa_{\text{soft}}^{\text{PDF}} \, d\hat{\sigma}_{ab \to cd}^{1,1}(\hat{s})$$

$$+ \frac{\alpha_s}{\pi} C_F \sum_i \int d\tau \int \frac{dx_i}{x_i} \int_{x_i}^{1-\Delta E/E_i} \frac{dz}{z} \, \kappa_{\text{coll.}}^{\text{PDF}}(z) \, d\hat{\sigma}_{ab \to cd}^{1,1}(\hat{s})$$

$$\times \frac{1}{1 + \delta_{ij}} \left[f_{i/A}\left(\frac{x_i}{z}, \mu_F\right) f_{j/B}\left(\frac{\tau}{x_i}, \mu_F\right) + f_{j/A}\left(\frac{\tau}{x_i}, \mu_F\right) f_{i/B}\left(\frac{x_i}{z}, \mu_F\right) \right].$$
$$(4.88)$$

4.2.3 Real quark bremsstrahlung

At the same order of perturbation theory, tree-level real quark and real anti-quark bremsstrahlung processes can contribute to squark and gluino production. These are novel production mechanisms at $\mathcal{O}(\alpha_s^2 \alpha)$, arising from the interference of EW-mediated and QCD-mediated diagrams. In case of squark–anti-squark and squark–squark production, the real quark bremsstrahlung proceeds from (anti-)quark–gluon initial states. In case of gluino–squark production, there are (anti-)quark–(anti-)quark initial states that allow for real quark radiation.

These subprocesses always yield IR-finite results in the limit of a softly radiated quark or anti-quark, since the radiated particle is of fermionic nature. However for squark pair production processes, collinear singularities arise if the gluon in the initial state splits collinearly into a quark–anti-quark pair in both the EW- and QCD-mediated diagrams of a given interference contribution.

The general procedure is similar to the treatment of collinear singularities due to gluon radiation. Integrated over the region of collinear splitting, the cross section for real quark bremsstrahlung factorizes into a collinear factor and the lowest-order cross section [152].

Expressed in an analogous way to Eq. (4.86), it is

$$d\hat{\sigma}^{2,1}_{ig \to cdj}(\delta_\theta)\Big|_{\text{coll.}} = \frac{\alpha_s}{\pi} T_F \int_{z_0}^1 dz \; \kappa^{qg}_{\text{coll.}}(z,\hat{s}) \; d\hat{\sigma}^{1,1}_{ab \to cd}(\hat{s}), \qquad (4.89)$$

with $T_F = 1/2$. Depending on the charges of the produced SUSY particles, the particle labels i, j refer to

$$\begin{aligned} \tilde{q}_a \tilde{q}_a^* : &\quad i = j = u, d, c, s, \bar{u}, \bar{d}, \bar{c}, \bar{s}\,, \\ \tilde{q}_a \tilde{q}_a : &\quad i = q, \quad j = \bar{q}, \\ \tilde{q}_a^* \tilde{q}_a^* : &\quad i = \bar{q}, \quad j = q. \end{aligned} \qquad (4.90)$$

The interference contribution $d\hat{\sigma}^{1,1}_{ab \to cd}$ is defined according to Eq. (4.84) and obtained from the EW-mediated and QCD-mediated tree-level amplitudes; and the collinear factor $\kappa^{qg}_{\text{coll.}}(z,\hat{s})$ is,

$$\kappa^{qg}_{\text{coll.}}(z,\hat{s}) = \frac{1}{2} P_{q \leftarrow g}(z) \left[\ln\left(\frac{\hat{s}(1-z)^2}{z m_q^2} \frac{\delta_\theta}{2} \right) \right] + z(1-z), \qquad (4.91)$$

in terms of the gluon-quark LO splitting function [106],

$$P_{q \leftarrow g}(z) = z^2 + (1-z)^2. \qquad (4.92)$$

The universal quark mass singularity can again be absorbed by a redefinition of the (anti-)quark PDF at $\mathcal{O}(\alpha_s)$,

$$f_{i/A}(x, \mu_F) \to f_{i/A}(x, \mu_F) + \frac{\alpha_s}{\pi} T_F \int_x^1 \frac{dz}{z} f_{g/A}\left(\frac{x}{z}, \mu_F\right) \frac{1}{2} P_{q \leftarrow g}(z) \ln\left(\frac{m_q^2}{\mu_F}\right). \qquad (4.93)$$

Thus, as a result of collinear gluon-quark splitting taking place in the proton, the quark PDF gets contributions from the gluon PDF at higher orders in QCD. The redefinition of the PDF induces as usual an additional $\mathcal{O}(\alpha_s^2 \alpha)$ contribution to the total hadronic cross section,

$$\begin{aligned} d\sigma^{\text{coll.CT}}_{AB \to cdj} = &\frac{\alpha_s}{\pi} T_F \sum_{i=a,b} \int d\tau \int \frac{dx}{x} \int_x^1 \frac{dz}{z} \frac{1}{2} P_{q \leftarrow g}(z) \ln\left(\frac{m_q^2}{\mu_F}\right) d\hat{\sigma}^{1,1}_{ab \to cd}(\hat{s}) \\ &\times \frac{1}{1 + \delta_{ab}} \left[f_{g/A}\left(\frac{x}{z}, \mu_F\right) f_{i/B}\left(\frac{\tau}{x}, \mu_F\right) + f_{i/A}\left(\frac{\tau}{x}, \mu_F\right) f_{g/B}\left(\frac{x}{z}, \mu_F\right) \right]. \end{aligned} \qquad (4.94)$$

Chapter 5
Stop–anti-stop production

In this chapter, we study the electroweak contribution to the hadronic production of diagonal stop–anti-stop pairs within the MSSM,

$$PP \to \tilde{t}_a \tilde{t}_a^*, \qquad a = 1, 2. \tag{5.1}$$

As discussed in Chapter 3, the lighter of the top-squark (stop) mass eigenstates is a candidate for the lightest colored SUSY particle in many SUSY models and thus relatively large production cross sections are expected in particular at hadron colliders. At lowest order in QCD, only diagonal stop–anti-stop pairs can be produced. The corresponding cross section depends on the mass of the produced particles, while no other SUSY parameter enters. As a consequence, experimental bounds on the cross section can easily be translated into lower bounds on the masses. Altogether, this yields pair production of stops being among the most promising SUSY discovery channels at the LHC.

The LO and NLO QCD results for stop–anti-stop production at hadron colliders are well known since many years [19–21]. At NLO QCD, the cross section changes considerably and it becomes dependent on further SUSY parameters such as the stop mixing angle and gluino and sfermion masses. Here, we discuss the hitherto missing part of the EW contribution to the cross section [24,153]. We follow the classification given in Section 3.3 and study both tree-level EW contributions and NLO EW corrections of $\mathcal{O}(\alpha_s^2 \alpha)$. At this order in perturbation theory, one has to deal with singularities of UV and IR origin. The necessary calculational techniques have been introduced in Chapter 4 and we refer to Sections 4.1 and 4.2 for more details.

The outline of this chapter is as follows. In Section 5.1, we recall the analytical expressions for the partonic LO cross sections and set the basic notation. The EW contribution is presented in Section 5.2, where we also include a discussion of the treatment of soft and collinear singularities that arise from virtual and real corrections. Section 5.3 is dedicated to numerical studies. We focus on $\tilde{t}_1 \tilde{t}_1^*$ production at the LHC and present results for hadronic cross sections and for distributions with respect to kinematical variables. Moreover, the
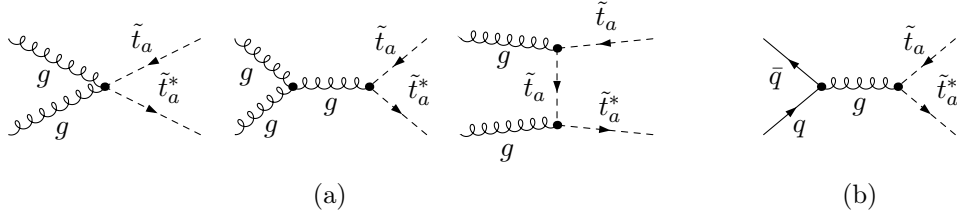
Figure 5.1.: LO Feynman diagrams for stop–anti-stop pair production at the Born level via
(a) gg fusion and (b) $q\bar{q}$ annihilation. For the gg fusion, the u-channel diagram
(with crossed final states) is not shown explicitly.

dependence of the EW contributions on SUSY parameters is further investigated and we
briefly refer to $\tilde{t}_2 \tilde{t}_2^*$ production towards the end of the chapter.

5.1 LO cross sections and notations

At hadron colliders, the dominant production mechanism for diagonal stop–anti-stop pro-
duction proceeds at $\mathcal{O}(\alpha_s^2)$ via two classes of partonic subprocesses,

$$g(p_1)\ g(p_2) \to \tilde{t}_a(p_3)\ \tilde{t}_a^*(p_4) \qquad \text{and} \qquad q(p_1)\ \bar{q}(p_2) \to \tilde{t}_a(p_3)\ \tilde{t}_a^*(p_4), \qquad (5.2)$$

where $q\bar{q}$ denotes representatively the contributing quark flavors. The corresponding Feyn-
man diagrams are shown in Fig. 5.1 (see also Fig. 3.5(d), $\tilde{q}_a \equiv \tilde{t}_a$, for the general classifi-
cation among the colored SUSY particle production processes).

We recall that after the electroweak symmetry breaking the soft-breaking terms in the
MSSM Lagrangian induce a mixing among the particles of identical color and electric
charge. In the squark sector, left- and right-handed gauge eigenstate mix to form the mass
eigenstates. This mixing is proportional to the mass of the SM partner quark, cf.Eqs. (2.96)
and (2.101), and thus non-negligible for squarks of the third generation. We denote the two
stop mass eigenstates by $\tilde{t}_a$ with $a = 1, 2$ in the following. The masses are labeled as $m_{\tilde{t}_a}$.

It is convenient to parameterize the cross sections in terms of the following kinematical
variables,

$$\hat{s} = (p_1 + p_2)^2, \qquad \hat{t} = (p_1 - p_3)^2, \qquad \hat{u} = (p_1 - p_4)^2,$$
$$\hat{t}_{\tilde{t}_a} = \hat{t} - m_{\tilde{t}_a}^2, \qquad \hat{u}_{\tilde{t}_a} = \hat{u} - m_{\tilde{t}_a}^2, \qquad (5.3)$$

with the sum rule $\hat{s} + \hat{t}_{\tilde{t}_a} + \hat{u}_{\tilde{t}_a} = 0$. Furthermore we apply the previously introduced
notation $d\hat{\sigma}_X^{m,\,n}\ [\mathcal{M}_X^{m,\,n}]$ in order to refer to the cross section [matrix element] of the partonic
process X at a given order $\mathcal{O}(\alpha_s^m \alpha^n)$ in the strong and electroweak coupling constants.

The differential partonic cross sections are obtained from the spin- and color-averaged

squared matrix elements,

$$d\hat{\sigma}^{2,0}_{gg\to\tilde{t}_a\tilde{t}_a^*}(\hat{s}) = \frac{1}{2\hat{s}} \overline{\sum} \left|\mathcal{M}^{1,0}_{gg\to\tilde{t}_a\tilde{t}_a^*}(\hat{s},\hat{t},\hat{u})\right|^2 d\mathrm{PS}_2 \,,$$
$$d\hat{\sigma}^{2,0}_{q\bar{q}\to\tilde{t}_a\tilde{t}_a^*}(\hat{s}) = \frac{1}{2\hat{s}} \overline{\sum} \left|\mathcal{M}^{1,0}_{q\bar{q}\to\tilde{t}_a\tilde{t}_a^*}(\hat{s},\hat{t},\hat{u})\right|^2 d\mathrm{PS}_2 \,, \tag{5.4}$$

in terms of the two-particle phase-space measure $d\mathrm{PS}_2 = d\hat{t}/(8\pi\hat{s})$ defined in Eq. (4.76) (evaluated in the c. m. frame) and the lowest-order matrix elements as explicitly given by [20],

$$\overline{\sum}\left|\mathcal{M}^{1,0}_{gg\to\tilde{t}_a\tilde{t}_a^*}\right|^2 = \frac{1}{4}\cdot\frac{1}{64}\cdot 32\pi^2\alpha_s^2\left[C_0\left(1-2\frac{\hat{t}_{\tilde{t}_a}\,\hat{u}_{\tilde{t}_a}}{\hat{s}^2}\right)-C_K\right]$$
$$\times\left[1-2\frac{\hat{s}m_{\tilde{t}_a}^2}{\hat{t}_{\tilde{t}_a}\,\hat{u}_{\tilde{t}_a}}\left(1-\frac{\hat{s}m_{\tilde{t}_a}^2}{\hat{t}_{\tilde{t}_a}\,\hat{u}_{\tilde{t}_a}}\right)\right]\,,$$
$$\overline{\sum}\left|\mathcal{M}^{1,0}_{q\bar{q}\to\tilde{t}_a\tilde{t}_a^*}\right|^2 = \frac{1}{4}\cdot\frac{1}{9}\cdot 64\pi^2\alpha_s^2\,NC_F\,\frac{\hat{t}_{\tilde{t}_a}\,\hat{u}_{\tilde{t}_a}-m_{\tilde{t}_a}^2\,\hat{s}}{\hat{s}^2}\,. \tag{5.5}$$

The $SU(3)_C$ color factors are ($N=3$)

$$C_0 = N(N^2-1) = 24, \qquad C_K = \frac{N^2-1}{N} = \frac{8}{3}, \qquad C_F = \frac{N^2-1}{2N} = \frac{4}{3}\,. \tag{5.6}$$

At the hadronic level, the full differential cross section is obtained by convoluting the partonic cross sections with the respective parton luminosities, cf. Eqs. (3.2) and (3.3),

$$d\sigma^{2,0}_{PP\to\tilde{t}_a\tilde{t}_a^*}(S) = \int_{\tau_0}^1 d\tau\,\frac{d\mathcal{L}^{gg}_{PP}}{d\tau}\,d\hat{\sigma}^{2,0}_{gg\to\tilde{t}_a\tilde{t}_a^*}(\tau S) + \sum_q\int_{\tau_0}^1 d\tau\,\frac{d\mathcal{L}^{q\bar{q}}_{PP}}{d\tau}\,d\hat{\sigma}^{2,0}_{q\bar{q}\to\tilde{t}_a\tilde{t}_a^*}(\tau S)\,, \tag{5.7}$$

where the integration over τ is bounded from below by the production threshold of the process, $\tau_0 = 4m_{\tilde{t}_a}^2/S$. The sum over q runs over the five light quark flavors.

5.2 Electroweak contributions

The EW contributions to hadronic stop–anti-stop pair production up to the one-loop level divide into tree-level contributions and NLO EW corrections. The tree-level contributions, described below in Section 5.2.1, arise from the pure-EW tree-level subprocesses of $\mathcal{O}(\alpha^2)$ and the photon-induced production channels of $\mathcal{O}(\alpha_s\alpha)$. In contrast, the NLO EW corrections are of $\mathcal{O}(\alpha_s^2\alpha)$ and comprise virtual corrections (see Section 5.2.2), real photon and real gluon bremsstrahlung contributions (Section 5.2.3), as well as real quark radiation diagrams (Section 5.2.4).

The complete EW contribution to the hadronic cross section is obtained from the corre-

sponding partonic cross section by convolution and summation as follows,

$$
\begin{aligned}
d\sigma_{PP\to\tilde{t}_a\tilde{t}_a^*}^{\text{EW}}(S) = \int_{\tau_0}^1 d\tau \Bigg\{ & \frac{d\mathcal{L}_{\gamma g}^{PP}}{d\tau} \, d\hat{\sigma}_{\gamma g\to\tilde{t}_a\tilde{t}_a^*}^{1,\,1}(\hat{s}) + \sum_{q=u,d,c,s} \frac{d\mathcal{L}_{q\bar{q}}^{PP}}{d\tau} \, d\hat{\sigma}_{q\bar{q}\to\tilde{t}_a\tilde{t}_a^*}^{0,\,2}(\hat{s}) \\
& + \frac{d\mathcal{L}_{gg}^{PP}}{d\tau} \left[d\hat{\sigma}_{gg\to\tilde{t}_a\tilde{t}_a^*}^{2,\,1}(\hat{s}) + d\hat{\sigma}_{gg\to\tilde{t}_a\tilde{t}_a^*\gamma}^{2,\,1}(\hat{s}) \right] \\
& + \sum_{q=u,d,c,s} \frac{d\mathcal{L}_{q\bar{q}}^{PP}}{d\tau} \left[d\hat{\sigma}_{q\bar{q}\to\tilde{t}_a\tilde{t}_a^*}^{2,\,1}(\hat{s}) + d\hat{\sigma}_{q\bar{q}\to\tilde{t}_a\tilde{t}_a^*\gamma}^{2,\,1}(\hat{s}) + d\hat{\sigma}_{q\bar{q}\to\tilde{t}_a\tilde{t}_a^*g}^{2,\,1}(\hat{s}) \right] \\
& + \sum_{q=u,d,c,s} \left[\frac{d\mathcal{L}_{gq}^{PP}}{d\tau} \, d\hat{\sigma}_{gq\to\tilde{t}_a\tilde{t}_a^*q}^{2,\,1}(\hat{s}) + \frac{d\mathcal{L}_{g\bar{q}}^{PP}}{d\tau} \, d\hat{\sigma}_{g\bar{q}\to\tilde{t}_a\tilde{t}_a^*\bar{q}}^{2,\,1}(\hat{s}) \right] \Bigg\},
\end{aligned}
\tag{5.8}
$$

where again the parton luminosities refer to Eq. (3.3). We will discuss all the partonic cross sections in the following.

Here, the sum over q runs only over the four light quark flavors. As there is no intrinsic bottom content in the proton, the bottom-quark density is generated dynamically from gluon splitting only. Its inclusion in Eq. (5.8) would thus result in a higher-order effect and its contributions to the tree-level EW diagrams and the NLO EW results can be neglected.

The Feynman diagrams and corresponding amplitudes are generated and calculated using `FeynArts` [154] and `FormCalc` with `LoopTools` [83], based on Passarino-Veltman (PV) reduction techniques for the tensor loop integrals [147], which were further developed for 4-point integrals in [155]. Higgs boson masses are computed with `FeynHiggs` [81].

IR and collinear singularities are treated by means of mass regularization as described in Section 4.2. I. e. we regularize the photonic and gluonic IR singularities with a small mass parameter λ and keep the light quark masses in the collinearly singular integrals as regulators.

5.2.1 Tree-level EW contributions

Pure-EW tree-level contributions of $\mathcal{O}(\alpha^2)$

The $q\bar{q}$-induced partonic subprocess

$$
q(p_1)\,\bar{q}(p_2)\ \to\ \tilde{t}_a(p_3)\,\tilde{t}_a^*(p_4),
\tag{5.9}
$$

also allows for stop–anti-stop pair production from EW tree-level diagrams mediated by γ and Z boson exchange. The differential cross section is given by

$$
d\hat{\sigma}_{q\bar{q}\to\tilde{t}_a\tilde{t}_a^*}^{0,\,2}(\hat{s}) = \frac{d\hat{t}}{16\pi\hat{s}^2} \overline{\sum} \left| \mathcal{M}_{q\bar{q}\to\tilde{t}_a\tilde{t}_a^*}^{0,\,1}(\hat{s}) \right|^2,
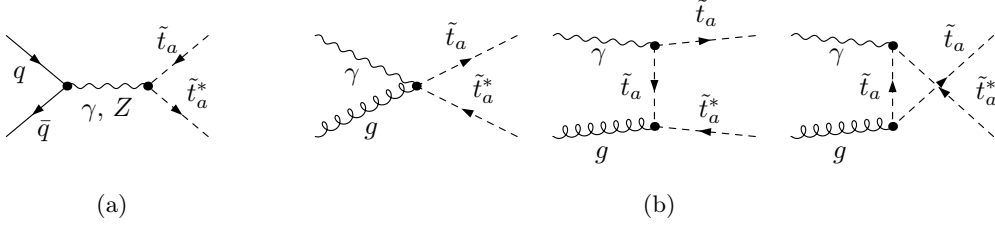\tag{5.10}
$$

Figure 5.2.: Feynman diagrams for tree-level EW contributions to $\tilde{t}_a \tilde{t}_a^*$ production, comprising (a) the pure-EW tree-level channel and (b) the photon-induced subprocess.

where $\mathcal{M}^{0,1}_{q\bar{q}\to\tilde{t}_a\tilde{t}_a^*}$ is the amplitude according to the diagrams depicted in Fig. 5.2(a) (see also Fig. 3.7(a)). Due to the absence of top-quarks in the proton, there are only two s-channel diagrams present that yield a contribution of $\mathcal{O}(\alpha^2)$. Color conservation then implies that the QCD-mediated and EW-mediated tree-level diagrams cannot interfere. Hence there is no $\mathcal{O}(\alpha_s\alpha)$ contribution to the $q\bar{q}$-annihilation channel.

Photon-induced stop–anti-stop production

We also consider the photon-induced mechanisms of the stop–anti-stop production,

$$\gamma(p_1)\ g(p_2)\ \rightarrow\ \tilde{t}_a(p_3)\ \tilde{t}_a^*(p_4), \tag{5.11}$$

arising from the Feynman diagrams illustrated in Fig. 5.2(b) (see also Fig. 3.8(a)). The differential cross section for this subprocess is

$$d\hat{\sigma}^{1,1}_{\gamma g\to\tilde{t}_a\tilde{t}_a^*}(\hat{s}) = \frac{d\hat{t}}{16\pi\hat{s}^2}\ \overline{\sum}\left|\mathcal{M}^{1/2,\,1/2}_{\gamma g\to\tilde{t}_a\tilde{t}_a^*}(\hat{s})\right|^2,$$

$$\overline{\sum}\left|\mathcal{M}^{1/2,\,1/2}_{\gamma g\to\tilde{t}_a\tilde{t}_a^*}\right|^2 = \frac{1}{4}\cdot\frac{1}{8}\cdot 128\pi^2\alpha\alpha_s e_t^2\, NC_F\left[1 - 2\frac{\hat{s}m_{\tilde{t}_a}^2}{\hat{t}_{\tilde{t}_a}\hat{u}_{\tilde{t}_a}}\left(1 - \frac{\hat{s}m_{\tilde{t}_a}^2}{\hat{t}_{\tilde{t}_a}\hat{u}_{\tilde{t}_a}}\right)\right], \tag{5.12}$$

expressed in terms of the reduced Mandelstam variables defined in Eq. (5.3). Photon-induced processes with quarks in the initial state represent contributions of higher orders ($\gamma q \to \tilde{t}_a\tilde{t}_a^* q$, $\gamma\bar{q} \to \tilde{t}_a\tilde{t}_a^*\bar{q}$) and we do not include them in our discussion here.

5.2.2 Virtual corrections

The $\mathcal{O}(\alpha_s^2\alpha)$ virtual corrections to the gg-fusion channel can be expressed in terms of $\mathcal{M}^{1,0}$, the tree-level QCD-mediated amplitude, and $\mathcal{M}^{1,1}$, the one-loop amplitude with EW insertions in the tree-level gg diagrams,

$$d\hat{\sigma}^{2,1}_{gg\to\tilde{t}_a\tilde{t}_a^*}(\hat{s}) = \frac{d\hat{t}}{16\pi\hat{s}^2}\ \overline{\sum}\, 2\,\mathrm{Re}\left\{\left(\mathcal{M}^{1,0}_{gg\to\tilde{t}_a\tilde{t}_a^*}\right)^*\mathcal{M}^{1,1}_{gg\to\tilde{t}_a\tilde{t}_a^*}\right\}. \tag{5.13}$$

The resulting counterterm, self-energy, box, and vertex diagrams are shown in Figs. 5.3 and 5.4, respectively. We refer to $\tilde{t}_1 \tilde{t}_1^*$ production only, however the diagrams for $\tilde{t}_2 \tilde{t}_2^*$ production can be obtained in complete analogy. The diagrams containing a quartic squark vertex (e. g. the diagrams in the last row of Fig. 5.3) deserve some special attention. In order to yield contributions at $\mathcal{O}(\alpha_s^2 \alpha)$, only the weak part of the four-squark vertex has to be taken into account.

The $q\bar{q}$-annihilation channel allows both tree-level QCD and tree-level EW graphs. As a consequence, the $\mathcal{O}(\alpha_s^2 \alpha)$ virtual corrections also comprise interference contributions of tree-level EW and QCD-mediated box diagrams. In total, they can be written as

$$d\hat{\sigma}^{2,1}_{q\bar{q}\to\tilde{t}_a \tilde{t}_a^*}(\hat{s}) = \frac{d\hat{t}}{16\pi\hat{s}^2} \overline{\sum} \, 2\,\mathrm{Re}\left\{\left(\mathcal{M}^{1,0}_{q\bar{q}\to\tilde{t}_a \tilde{t}_a^*}\right)^* \mathcal{M}^{1,1}_{q\bar{q}\to\tilde{t}_a \tilde{t}_a^*} + \left(\mathcal{M}^{0,1}_{q\bar{q}\to\tilde{t}_a \tilde{t}_a^*}\right)^* \mathcal{M}^{2,0}_{q\bar{q}\to\tilde{t}_a \tilde{t}_a^*}\right\},$$
(5.14)

where again $\mathcal{M}^{1,0}$ and $\mathcal{M}^{1,1}$ denote the tree-level QCD amplitude and the corresponding one-loop amplitude with weak insertions (see diagrams in Fig. 5.5); whereas $\mathcal{M}^{0,1}$ is the amplitude from the tree-level EW diagrams shown in Fig. 5.2(a) and $\mathcal{M}^{2,0}$ refers to the pure-QCD one-loop amplitude arising from Fig. 5.6.

In order to obtain an UV-finite result, it is necessary to regularize the diagrams and to renormalize the theory. We proceed as described in Section 4.1, treating UV divergences by dimensional reduction and fixing the renormalization constants in the on-shell scheme. At $\mathcal{O}(\alpha_s^2 \alpha)$, UV singularities only arise from one-loop amplitudes with weak insertions ($\mathcal{M}^{1,1}$) and we have to renormalize the light-flavor quark fields and of the top-squark sector. The appropriate counterterm diagrams, Figs. 5.3(a) and 5.5(a), can be constructed from the Feynman rules given in Table 4.1, where the renormalization constants have to be evaluated at $\mathcal{O}(\alpha)$.

There is no renormalization of the gluon field and the strong coupling constant at $\mathcal{O}(\alpha)$ and the strong sector needs not to be renormalized. In the $q\bar{q}$-annihilation channels, also one-loop QCD amplitudes ($\mathcal{M}^{2,0}$, Fig. 5.6) in combination with tree-level EW diagrams come into play and give contributions at the desired order of perturbation theory. But due to the specific color structure and the absence of t/u-channel tree-level EW diagrams, only UV-finite box diagrams arise.

It is interesting to note that only the diagonal entries of the stop field renormalization constant have to be evaluated as there are no non-diagonal self-energy corrections to the diagrams. In all LO diagrams the stops are produced via couplings to gluons and both the $g\tilde{t}\tilde{t}$ and the $gg\tilde{t}\tilde{t}$ vertices are diagonal in the chiral basis as well as in the mass eigenstate basis. As a result, the counterterm for the stop mixing angle, cf. Eq. (4.25) does not enter the calculation.

Let us briefly comment on the diagrams in the last row of Fig. 5.4, which are loop corrections to the gluon-gluon-Higgs (ggh^0 and ggH^0) vertex. The (heavy-)quark loops

(a)

(b)

(c)

Figure 5.3.: Feynman diagrams for virtual NLO EW corrections to the process $gg \rightarrow \tilde{t}_1 \tilde{t}_1^*$:
(a) counterterm diagrams, (b) self-energy corrections, (c) box diagrams.
The u-channel diagrams with crossed final states are not shown explicitly. In case
of γ exchange, $\tilde{q}_a$ denotes the lighter stop, $\tilde{q}_a \equiv \tilde{t}_1$. For Z/W, $\tilde{\chi}_n^0/\tilde{\chi}_n^\pm$, and $S^0/S^\pm$
exchange, it is $\tilde{q}_a \equiv \tilde{t}_a/\tilde{b}_a$ and $q \equiv t/b$.
As in the following, we refer to $\tilde{t}_1 \tilde{t}_1^*$ production only. The diagrams for $\tilde{t}_2 \tilde{t}_2^*$ production
are obtained in complete analogy. The index i runs over all six quark and lepton
flavors, and a over the mass eigenstates $1, 2$. We use a common label V to denote the
gauge bosons, γ, Z and W. The label S^0 refers to the neutral Higgs (and Goldstone)
bosons h^0, H^0, A^0, G^0, and the label $S^\pm$ to the charged Higgs (and Goldstone) bosons
$H^\pm, G^\pm$. For neutralinos and charginos, we use a common label n to number the
four and two eigenstates, respectively.
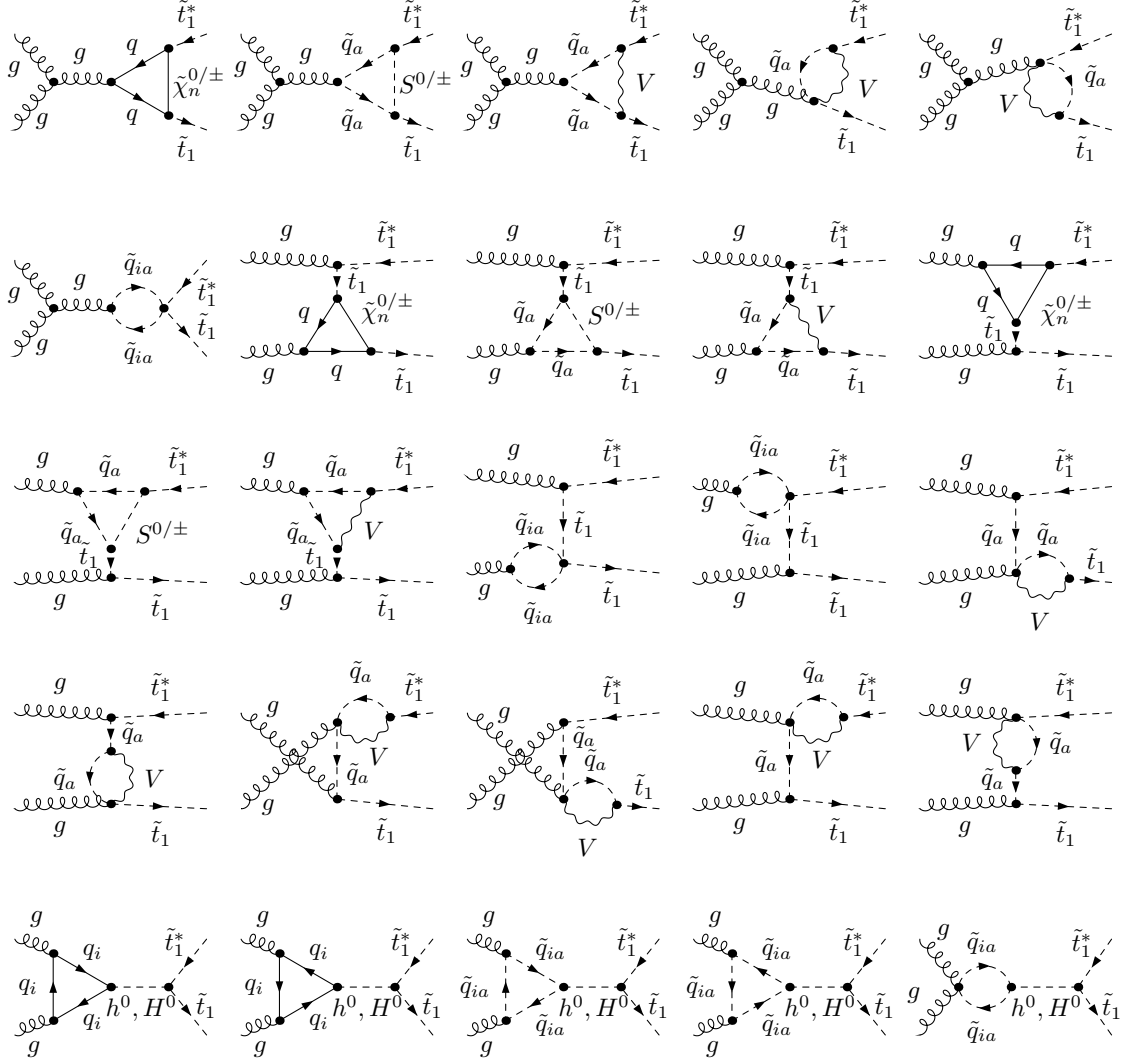
Figure 5.4.: Feynman diagrams for the NLO EW vertex corrections to the process $gg \to \tilde{t}_1 \tilde{t}_1^*$. The u-channel diagrams with crossed final states are not shown explicitly. The notation refers to Fig. 5.3.

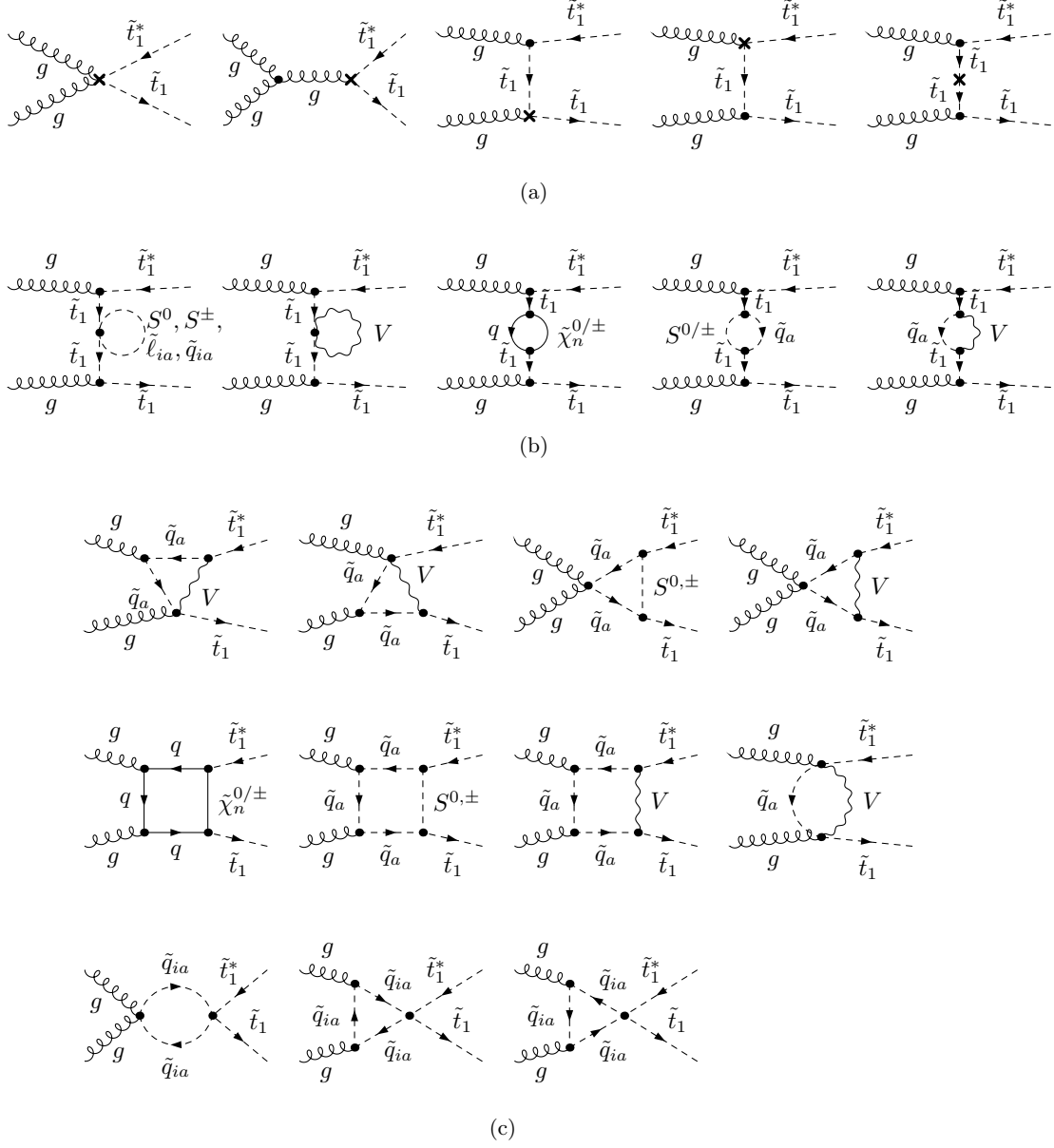(a)   (b)

(c)

(d)
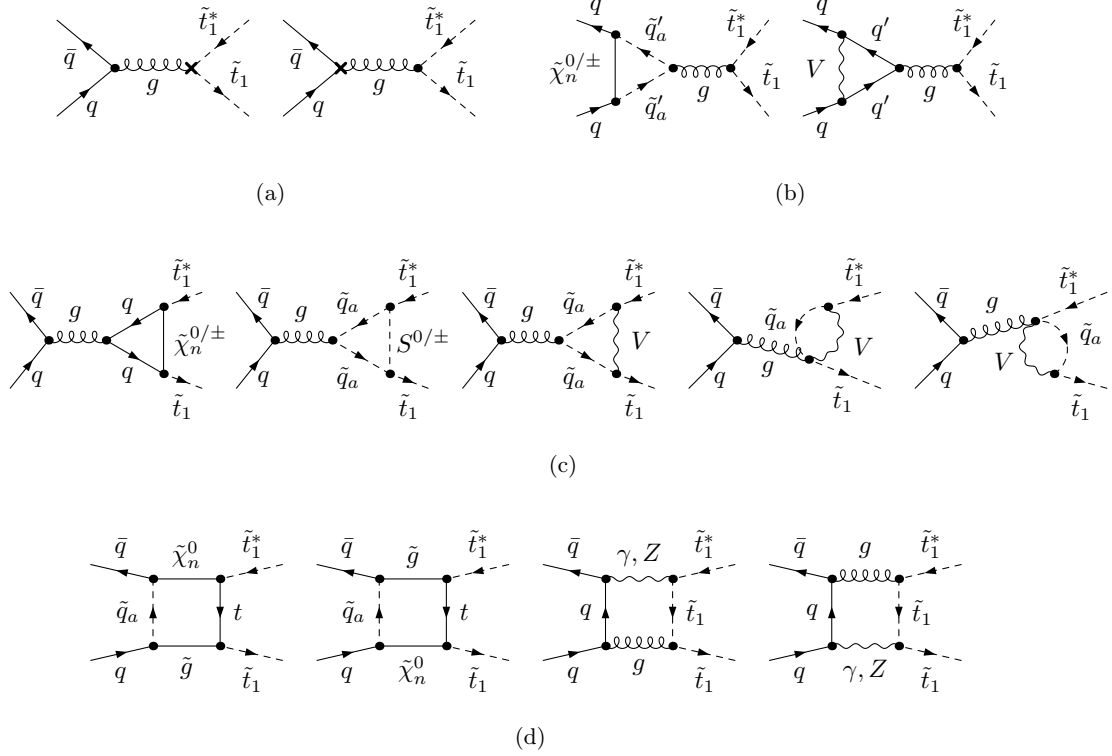
Figure 5.5.: Feynman diagrams for virtual NLO EW corrections to the process $q\bar{q} \rightarrow \tilde{t}_1\tilde{t}_1^*$:
(a) counterterm diagrams, (b+c) vertex corrections, (d) box diagrams. The u-channel diagrams with crossed final states are not shown explicitly. Notation as in Fig. 5.3. In the initial state vertex corrections (b), q' denotes the $SU(2)_L$ partner of q in case of W and $\tilde{\chi}_n^\pm$ exchange, for $V = \gamma, Z$ and $\tilde{\chi}_n^0$ it is $q' \equiv q$.
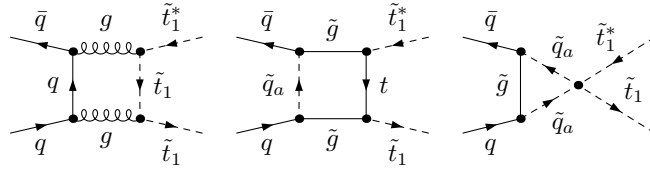

Figure 5.6.: Feynman diagrams for the QCD-mediated box contributions to the process $q\bar{q} \rightarrow \tilde{t}_1\tilde{t}_1^*$. These diagrams interfere with the tree-level EW graphs shown in Fig. 5.2(a) yielding $\mathcal{O}(\alpha_s^2\alpha)$ contributions.

yield a UV-finite contribution and the sum of the diagrams containing squark loops is UV finite as well. Renormalization of the ggh^0 and ggH^0 vertices is thus not required. However these diagrams become resonant if the propagating Higgs boson is heavier than the two final-state stops in sum and the width of the Higgs boson is needed in the propagator to regularize the integral. Indeed there are phenomenologically viable scenarios where $m_{H^0} \geq 2m_{\tilde{t}_1}$ and we will come back to this issue in Section 5.3.4.

Concerning the IR structure of the diagrams we find that in the gg-fusion channel, IR singularities only originate from final-state soft photon radiation. This is different in the $q\bar{q}$-annihilation subprocess, where also photon emission off the initial state quarks enters and additional mass singularities occur. Furthermore, the IR singular structure is extended by the contributions related to the gluons which appear in the 4-point UV finite loop integrals. Owing to the photon-like appearance of the gluon in the box diagrams, the gluonic IR singularities can be handled in analogy to the photonic IR singularities.

5.2.3   Real photon and real gluon corrections

To compensate the IR singularities in the virtual EW corrections, contributions with real photon and real gluon radiation are required. In case of some diagrams, the integration over the photon (gluon) phase space is IR singular in the soft photon (gluon) region or in the collinear limit. The soft singularities recover the structure of the IR singularities arising from virtual photons or gluons and cancel in the sum of real and virtual corrections. Collinear singularities from initial-state radiation remain and have to be absorbed into the PDFs via factorization. We treat the bremsstrahlung processes as described in Section 4.2, using the phase-space slicing method.

gg fusion with real photon radiation

The IR singularities arising from virtual photons in the gg-fusion channel cancel those in the photonic bremsstrahlung process

$$g(p_1) \ g(p_2) \rightarrow \tilde{t}_a(p_3) \ \tilde{t}_a^*(p_4) \ \gamma(k), \tag{5.15}$$

according to the diagrams shown in Fig. 5.7(a). The integration over the photon phase space is IR singular in the soft-photon region ($E_\gamma \rightarrow 0$).

Following the phase-space slicing approach, we isolate the soft singularities by imposing a lower cutoff ΔE on the photon energy. This hard-photon region is thus free of singularities and can be integrated numerically. In the soft region, $E_\gamma < \Delta E$, the integration can be approximated analytically and the squared matrix element factorizes into the lowest-order squared matrix elements and universal factors containing the singularities.

In the eikonal approximation, the cross section for real photon radiation in the soft limit is given in Eq. (4.60). For our specific process, we only have final state radiation and the

(a)

(b)
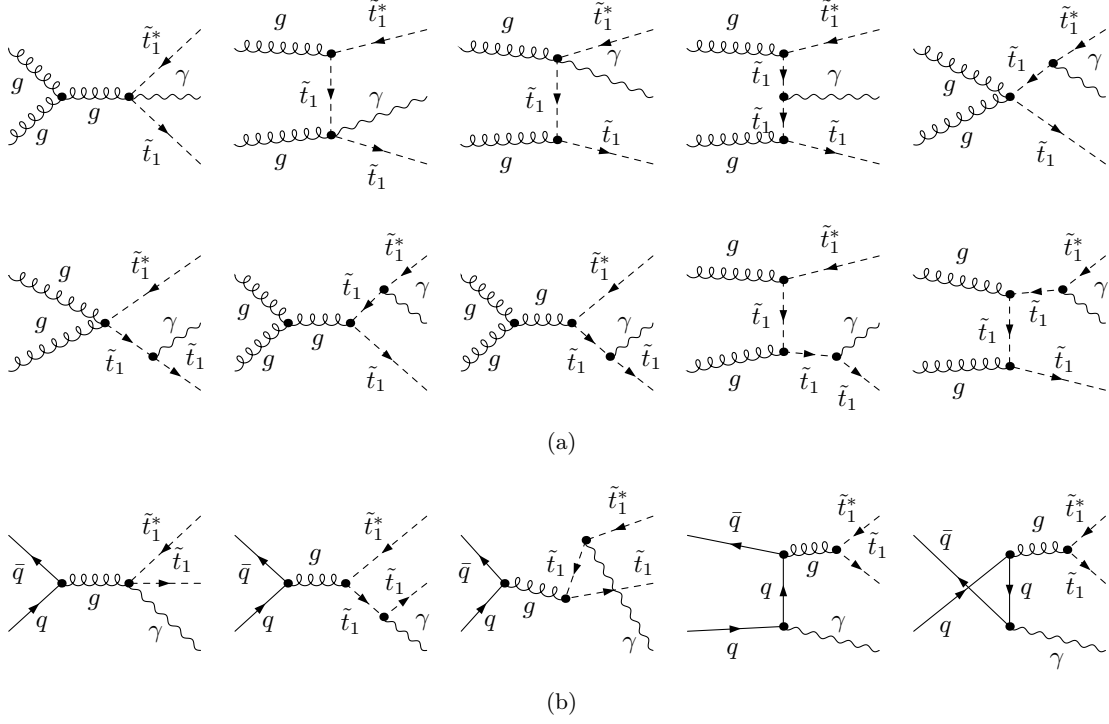
Figure 5.7.: Feynman diagrams for real photon radiation to $\tilde{t}_1\tilde{t}_1^*$ production via (a) gg fusion and (b) $q\bar{q}$ annihilation. In (a), diagrams with crossed initial state are not shown explicitly. The first four diagrams in (a) and the first diagram in (b) give IR-finite contributions, the remaining diagrams cause IR singularities in the soft-photon region. The last two diagrams in (b) also cause collinear singularities.

result reduces to

$$
\begin{aligned}
d\hat{\sigma}^{2,1}_{gg\to\tilde{t}_a\tilde{t}_a^*\gamma}(\hat{s})\Big|_{\text{soft}} &= -\frac{\alpha}{\pi}\, e_t^2\, (2\,\mathcal{I}_{33} - 2\mathcal{I}_{34}) \times d\hat{\sigma}^{2,0}_{gg\to\tilde{t}_a\tilde{t}_a^*}(\hat{s}) \\
&\equiv -\frac{\alpha}{\pi}\, e_t^2\, \delta^{\text{fin}}_{\text{soft}}\, d\hat{\sigma}^{2,0}_{gg\to\tilde{t}_a\tilde{t}_a^*}(\hat{s})\,,
\end{aligned}
\tag{5.16}
$$

in terms of the universal phase-space factors $\mathcal{I}_{ij}$, cf. Eq. (4.61). The complete soft factor for final state radiation for $\tilde{t}_a\tilde{t}_a^*$ production, $\delta^{\text{fin}}_{\text{soft}}$, simplifies in the limit of vanishing quark masses to the following expression,

$$
\begin{aligned}
\delta^{\text{fin}}_{\text{soft}} &= \left[\ln\delta_s^2 - \ln\frac{\lambda^2}{\hat{s}}\right]\left[1 - \frac{\hat{s} - 2m_{\tilde{t}_a}^2}{\hat{s}\beta}\ln\left(\frac{1+\beta}{1-\beta}\right)\right] - \frac{1}{\beta}\ln\left(\frac{1+\beta}{1-\beta}\right) \\
&\quad + \frac{\hat{s} - 2m_{\tilde{t}_a}^2}{\hat{s}\beta}\left[2\,\text{Li}_2\left(\frac{2\beta}{1+\beta}\right) + \frac{1}{2}\ln^2\left(\frac{1+\beta}{1-\beta}\right)\right].
\end{aligned}
\tag{5.17}
$$

Here, e_t is the fractional electric charge of the top-squark, $\delta_s = 2\Delta E/\sqrt{\hat{s}}$, and we introduced the parameter $\beta = \sqrt{1 - (4m_{\tilde{t}_a}^2)/\hat{s}}$.

$q\bar{q}$ annihilation with real photon radiation

In the $q\bar{q}$-annihilation channel, we consider the photon bremsstrahlung process,

$$q(p_1)\,\bar{q}(p_2) \to \tilde{t}_a(p_3)\,\tilde{t}_a^*(p_4)\,\gamma(k), \tag{5.18}$$

corresponding to the diagrams shown in Fig. 5.7(b). This process is IR singular both in the soft-photon region and in the collinear limit ($p_1 \cdot k \to 0$, $p_2 \cdot k \to 0$). To extract the singularities, a second cutoff $\Delta\theta$ is introduced on the angle between the photon and radiating fermion, dividing the photon phase space into soft and collinear parts which contain singularities and a non-collinear, hard part which is free of singularities and can be integrated numerically.

In the soft region, the cross section for the $q\bar{q}$-annihilation channel is approximated by

$$d\hat{\sigma}^{2,1}_{q\bar{q}\to\tilde{t}_a\tilde{t}_a^*\gamma}(\hat{s})\Big|_{\text{soft}} = -\frac{\alpha}{\pi}\left(e_q^2\,\delta^{\text{in}}_{\text{soft}} + e_t^2\,\delta^{\text{fin}}_{\text{soft}} + 2e_qe_t\,\delta^{\text{int}}_{\text{soft}}\right)d\hat{\sigma}^{2,0}_{q\bar{q}\to\tilde{t}_a\tilde{t}_a^*}(\hat{s})\,, \tag{5.19}$$

where the soft factors $\delta^{\text{in,fin,int}}_{\text{soft}}$ refer to the initial state radiation, final state radiation or interference of initial and final state radiation, respectively. The electric charges of the initial-state quark and the final-state top-squark are denoted by e_q and e_t.

The factor $\delta^{\text{fin}}_{\text{soft}}$ is given in Eq. (5.17). Defined by the universal phase-space factors $\mathcal{I}_{ij}$, the remaining two are, in terms of the reduced Mandelstam invariants $\hat{t}_{\tilde{t}_a}$ and $\hat{u}_{\tilde{t}_a}$,

$$
\begin{aligned}
\delta^{\text{in}}_{\text{soft}} &= 2\mathcal{I}_{11} - 2\mathcal{I}_{12} \\
&= \left[\ln\delta_s^2 - \ln\frac{\lambda^2}{\hat{s}}\right]\left[1 + \ln\frac{m_q^2}{\hat{s}}\right] + \frac{1}{2}\ln^2\frac{m_q^2}{\hat{s}} + \ln\frac{m_q^2}{\hat{s}} + \frac{\pi^2}{3}\,,
\end{aligned} \tag{5.20}
$$

$$
\begin{aligned}
\delta^{\text{int}}_{\text{soft}} &= 2\mathcal{I}_{13} - 2\mathcal{I}_{23} \\
&= \left[\ln\delta_s^2 - \ln\frac{\lambda^2}{\hat{s}}\right]\ln\left(\frac{\hat{u}_{\tilde{t}_a}}{\hat{t}_{\tilde{t}_a}}\right) + \text{Li}_2\left(1 + \frac{\hat{s}}{2\hat{t}_{\tilde{t}_a}}(1-\beta)\right) \\
&\quad + \text{Li}_2\left(1 + \frac{\hat{s}}{2\hat{t}_{\tilde{t}_a}}(1+\beta)\right) - \text{Li}_2\left(1 + \frac{\hat{s}}{2\hat{u}_{\tilde{t}_a}}(1-\beta)\right) - \text{Li}_2\left(1 + \frac{\hat{s}}{2\hat{u}_{\tilde{t}_a}}(1+\beta)\right).
\end{aligned}
$$

Similarly, the collinear part of the cross section is proportional to the Born cross section with reduced momentum for one of the partons, cf. Eq. (4.63),

$$d\hat{\sigma}^{2,1}_{q\bar{q}\to\tilde{t}_a\tilde{t}_a^*\gamma}(\hat{s})\Big|_{\text{coll.}} = \frac{2\alpha}{\pi}e_q^2\int_{z_0}^{1-\delta_s} dz\,\kappa_{\text{coll.}}(z,\hat{s})\,d\hat{\sigma}^{2,0}_{q\bar{q}\to\tilde{t}_a\tilde{t}_a^*}(z\hat{s}), \tag{5.21}$$

with the lower integration limit $z_0 = 4m_{\tilde{t}_a}^2/\hat{s}$ and $\kappa_{\text{coll.}}(z,\hat{s})$ as given in Eq. (4.64).

Although IR singularities cancel in sufficiently inclusive observables, quark-mass logarithms in the collinear singularities from initial-state radiation remain and have to be ab-

sorbed into the PDFs. We redefine the (anti-)quark PDF at $\mathcal{O}(\alpha)$ according to Eq. (4.66),

$$f_{i/A}(x,\mu_F) \to f_{i/A}(x,\mu_F)\left(1 + \frac{\alpha}{\pi}\, e_{q_i}^2\, \kappa_{\text{soft}}^{\text{PDF}}\right) + \frac{\alpha}{\pi}\, e_{q_i}^2 \int_x^{1-\delta_s} \frac{dz}{z}\, f_{i/A}\left(\frac{x}{z},\mu_F\right) \kappa_{\text{coll.}}^{\text{PDF}}(z),$$

$$(5.22)$$

yielding an additional contribution to the total hadronic cross section Eq. (5.8),

$$
\begin{aligned}
d\sigma_{PP\to\tilde{t}_a\tilde{t}_a^*\gamma}^{\text{coll.CT}}(S) &= \frac{\alpha}{\pi} \sum_{q=u,d,c,s} e_q^2 \int d\tau\, \frac{d\mathcal{L}_{PP}^{q\bar{q}}}{d\tau} \times \kappa_{\text{soft}}^{\text{PDF}}\, d\hat{\sigma}_{q\bar{q}\to\tilde{t}_a\tilde{t}_a^*}^{2,0}(\hat{s}) \\
&+ \frac{\alpha}{\pi} \sum_{q=u,d,c,s} e_q^2 \int d\tau \int \frac{dx}{x} \int_x^{1-\delta_s} \frac{dz}{z}\, \kappa_{\text{coll.}}^{\text{PDF}}(z)\, d\hat{\sigma}_{q\bar{q}\to\tilde{t}_a\tilde{t}_a^*}^{2,0}(\hat{s}) \\
&\times \left[f_{q/P}\left(\frac{x}{z},\mu_F\right) f_{\bar{q}/P}\left(\frac{\tau}{x},\mu_F\right) + f_{\bar{q}/P}\left(\frac{\tau}{x},\mu_F\right) f_{q/P}\left(\frac{x}{z},\mu_F\right) \right],
\end{aligned}
$$

$$(5.23)$$

as specified in Eq. (4.69). The collinear factors $\kappa_{\text{soft}}^{\text{PDF}}$ and $\kappa_{\text{coll.}}^{\text{PDF}}(z)$, defined in Eq. (4.67), have to be evaluated in the *DIS* factorization scheme ($\lambda_{sc} = 1$).

$q\bar{q}$ annihilation with real gluon radiation

Third, gluon radiation at the appropriate order $\mathcal{O}(\alpha_s^2\alpha)$ has to be taken into account,

$$q(p_1)\, \bar{q}(p_2) \to \tilde{t}_a(p_3)\, \tilde{t}_a^*(p_4)\, g(k), \tag{5.24}$$

to cancel the IR singularities of the $q\bar{q}$-annihilation channel related to the virtual gluon. The necessary contributions originate from the interference of QCD-based and EW-based Born level diagrams, as shown in Fig. 5.8. Not all of the interference terms contribute. Due to the color structure, only the interference between initial- and final-state gluon radiation is non-zero. Correspondingly, the integration over the gluon phase-space in Eq. (5.24) is singular in the soft-gluon region but collinear singularities do not arise.

The color correlation between the amplitudes induced by real gluon radiation has been discussed in Section 4.2.2. The general result for a cross section in the soft limit is given by Eq. (4.74) and for the particular case of four (s)quarks interacting in Eq. (4.83). For the soft-gluon part of the $q\bar{q}$-channel we write the result in a way similar to Eqs. (5.16) and (5.19),

$$d\hat{\sigma}_{q\bar{q}\to\tilde{t}_a\tilde{t}_a^*g}^{2,1}(\hat{s})\Big|_{\text{soft}} = -\frac{\alpha_s}{\pi}\, \delta_{\text{soft}}^{\text{int}} \times \overline{\sum} 2\,\text{Re}\left\{ \left\langle \mathcal{M}_{q\bar{q}\to\tilde{t}_a\tilde{t}_a^*}^{0,1} \Big| \mathbf{T}_1 \cdot \mathbf{T}_3 \Big| \mathcal{M}_{q\bar{q}\to\tilde{t}_a\tilde{t}_a^*}^{1,0} \right\rangle \right\} \frac{d\hat{t}}{16\pi\hat{s}^2},$$

$$(5.25)$$

where the color-modified interference contribution in terms of the color-charge operators $\mathbf{T}_i$ is defined in Eq. (4.81). $\mathcal{M}_{q\bar{q}\to\tilde{t}_a\tilde{t}_a^*}^{0,1}$ denotes the tree-level EW amplitude (γ and Z boson

(a)

(b)

Figure 5.8.: Feynman diagrams for real gluon radiation to $\tilde{t}_1 \tilde{t}_1^*$ production from (a) tree-level QCD diagrams and (b) tree-level EW diagrams. Due to the color structure, only QCD-EW interference terms between initial- and final-state gluon radiation are non-vanishing and contribute at $\mathcal{O}(\alpha_s^2 \alpha)$. These contributions cause IR singularities in the soft-gluon regions. In (a), the last diagram with crossed initial state is not shown explicitly.

exchange) and $\mathcal{M}^{1,0}_{q\bar{q}\to\tilde{t}_a\tilde{t}_a^*}$ refers to the tree-level QCD amplitude (g exchange). As anticipated above, the other two terms in Eq. (4.83) vanish owing to the specific color structure of the process. Explicitly, the cross section can be written as follows,

$$
d\hat{\sigma}^{2,1}_{q\bar{q}\to\tilde{t}_a\tilde{t}_a^* g}(\hat{s})\Big|_{\text{soft}} = -\frac{\alpha_s}{\pi}\,\delta^{\text{int}}_{\text{soft}}\,NC_F\left[\frac{8e_q e_t}{\hat{s}^2} + \frac{\left((U^{\tilde{t}}_{1a})^2 - 2e_t\sin^2\theta_W\right)\left(\epsilon - 4e_q\sin^2\theta_W\right)}{\sin^2\theta_W\cos^2\theta_W\,\hat{s}(\hat{s}-m_Z^2)}\right]
$$
$$
\times\,\frac{16\pi^2\alpha\alpha_s}{4\cdot 9}\left[\hat{t}_{\tilde{t}_a}\hat{u}_{\tilde{t}_a} - m_{\tilde{t}_a}^2\,\hat{s}\right]\frac{d\hat{t}}{16\pi\hat{s}^2}\,,
$$

(5.26)

involving the top-squark mixing matrix $U^{\tilde{t}}$ and $\epsilon = \pm 1$ for up- and down-type initial-state quarks, respectively.

5.2.4 Real quark radiation

To complete the list of EW contributions to stop–anti-stop pair production, also real quark and real anti-quark radiation has to addressed,

$$
g(p_1)\,q(p_2)\,\to\,\tilde{t}_a(p_3)\,\tilde{t}_a^*(p_4)\,q(k) \qquad \text{for}\quad q = u,d,c,s,\bar{u},\bar{d},\bar{c},\bar{s}. \tag{5.27}
$$

These tree-level processes give an (soft and collinear) IR-finite contribution of the order $\mathcal{O}(\alpha_s^2\alpha)$ through the interference between the QCD-based diagrams in Fig. 5.9(a) and the
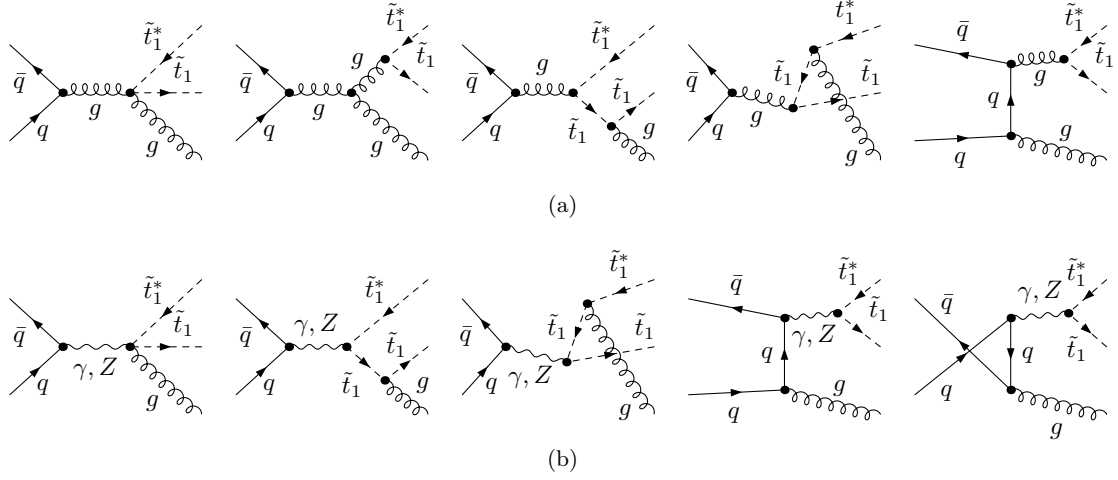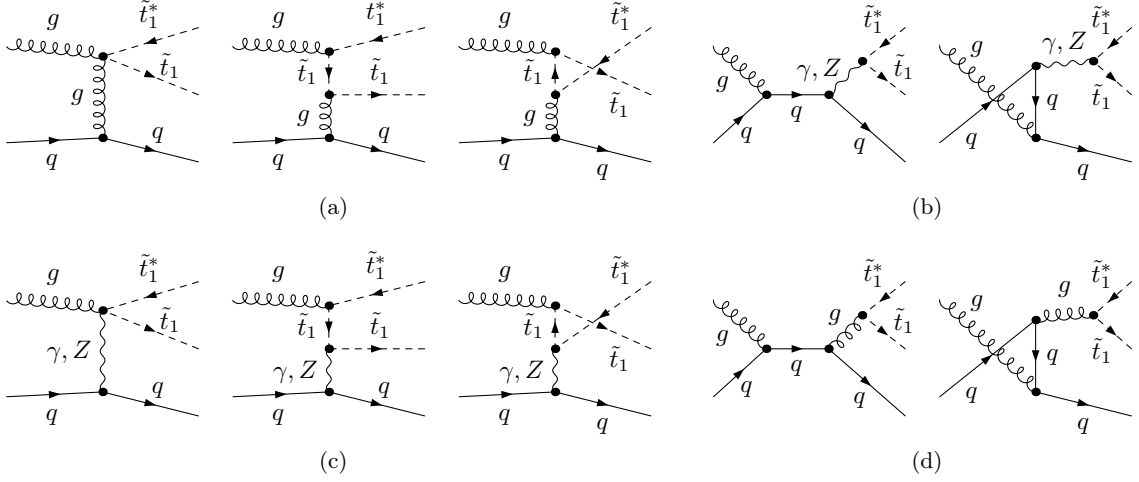
Figure 5.9.: Feynman diagrams for real quark radiation to $\tilde{t}_1\tilde{t}_1^*$ production from (a,d) tree-level QCD diagrams and (b,c) tree-level EW diagrams. Only QCD-EW interference terms between (a) and (b) and between (c) and (d) are non-vanishing and contribute at $\mathcal{O}(\alpha_s^2\alpha)$.

EW-based diagrams in Fig. 5.9(b) and between those in Fig. 5.9(c) and Fig. 5.9(d). In terms of the respective amplitudes (in the usual notation), the cross section reads

$$d\hat{\sigma}^{2,\,1}_{gq\to\tilde{t}_a\tilde{t}_a^*q}(\hat{s}) = \frac{1}{2\hat{s}}\overline{\sum} 2\,\mathrm{Re}\left\{\left(\mathcal{M}^{3/2,\,0}_{gq\to\tilde{t}_a\tilde{t}_a^*q}\right)^*\mathcal{M}^{1/2,\,1}_{gq\to\tilde{t}_a\tilde{t}_a^*q}\right\} d\mathrm{PS}_3. \qquad (5.28)$$

Due to the fact that the heavy-flavor top-squarks can only directly couple to the initial-state gluons but not to the (light-flavor) quarks, the number of non-zero interference terms is strongly reduced and we expect vanishing contributions from this subprocess only.

5.3 Numerical results

For the numerical discussion we focus on the production of light top-squark pairs $\tilde{t}_1\tilde{t}_1^*$ in proton–proton collisions at LHC energies.

We present the results in terms of the following hadronic observables: the integrated cross section, σ, the differential cross section with respect to the invariant mass of the top-squark pair, ($d\sigma/dM_{\mathrm{inv}}$ with $M^2_{\mathrm{inv}} = (p_3 + p_4)^2$), the differential cross sections with respect to the transverse momentum, ($d\sigma/dp_T$), to the rapidity, ($d\sigma/dy$), and to the pseudo-rapidity, ($d\sigma/d\eta$), of one of the final-state top-squarks. The energy and momentum (thus also y and η) of the two stops are equal in the $2 \to 2$ processes and differ only in the $2 \to 3$ processes if one of the stops radiates off a photon or gluon. As both stops radiate statistically with equal probability, the distributions with respect to the stop or the anti-stop do not differ meaningfully. Here, we give distributions with respect to the stop $\tilde{t}_1(p_3)$.

One has to take care of the fact that each top-squark observed in the laboratory system under a certain angle θ can originate from two different constellations at parton level: parton

$a(b)$ out of hadron $A(B)$ and vice-versa, corresponding to $\theta \rightarrow (\pi - \theta)$. Both parton-level configurations have to be added correctly for hadronic distributions (for explicit formulas see e. g. [156]). Note that the two boost factors β relating the two partonic c. m. systems with the laboratory system differ by a relative sign, as do the rapidity and the pseudo-rapidity of each particle. This fact is of particular importance in the collinear cones of the cross section, Eqs. (4.63) and (4.69), where we have to keep track of which parton radiates off the photon or gluon and enters the hard-scattering process with reduced momentum, resulting in different Lorentz boosts between the c. m. and the laboratory frame.

Assuming that the forward-scattered parton a carries the momentum fraction x of hadron A and the backward-scattered parton b the momentum fraction τ/x of hadron B, the boost factor β is given by

$$\beta = \frac{x - \tau/x}{x + \tau/x} \, . \tag{5.29}$$

The rapidity of one of the final state top-squarks in the laboratory system, $y(\equiv y_3)$, is related to the rapidity in the partonic c. m. frame, $y^{\text{cm}} = \text{artanh}(p_z^{\text{cm}}/E^{\text{cm}})$, via a Lorentz transformation,

$$y = y^{\text{cm}} - \text{artanh}(-\beta) = y^{\text{cm}} + \frac{1}{2} \ln \frac{x^2}{\tau} \, . \tag{5.30}$$

The pseudo-rapidity η is related to $\eta^{\text{cm}} = -\ln(\tan \theta^{\text{cm}}/2)$ in the c.m. frame via

$$\eta = \text{arsinh} \left(\frac{1}{2} \sqrt{\frac{m_{\tilde{t}_a}^2}{p_T^2} + \cosh^2 \eta^{\text{cm}}} \left(\frac{x}{\sqrt{\tau}} - \frac{\sqrt{\tau}}{x} \right) + \frac{1}{2} \sinh \eta^{\text{cm}} \left(\frac{\sqrt{\tau}}{x} + \frac{x}{\sqrt{\tau}} \right) \right), \tag{5.31}$$

which can be derived using the representation

$$p = \left(\sqrt{m_{\tilde{t}_a}^2 + p_T^2 \cosh^2 \eta}, \, 0, \, p_T, \, p_T \sinh \eta \right) \tag{5.32}$$

for the top-squark momentum $p \equiv p_3$. Since the final state particles are massive, rapidity and pseudo-rapidity do not coincide; in the limit $m_{\tilde{t}_a} \rightarrow 0$ one obtains $\eta = y$.

We introduce the following conventions for the discussion of the results. We will analyze the different gauge invariant, IR (soft and collinear) finite subsets of the EW contributions described in the previous section, referred to by their initial-state particles. The sum of the virtual corrections and of the $\mathcal{O}(\alpha_s^2 \alpha)$ contributions to real photon and gluon radiation via gg fusion ($q\bar{q}$ annihilation) will be labeled as "gg- ($q\bar{q}$-) channel contributions", respectively. The photon-induced subprocesses of $\mathcal{O}(\alpha_s \alpha)$ will be referred to as "γg-channel contributions". We also discuss the contributions of the real quark emission processes ("gq-channel contributions" of $\mathcal{O}(\alpha_s^2 \alpha)$) and the tree-level EW contributions to the $q\bar{q}$ annihilation of

$\mathcal{O}(\alpha^2)$. The sum of these channels will be labeled as "the EW contribution" according to Eq. (5.8). The relative EW contribution is defined as

$$\delta = (\mathcal{O}_{\mathrm{NLO}} - \mathcal{O}_{\mathrm{LO}})/\mathcal{O}_{\mathrm{LO}} \equiv \Delta\mathcal{O}_{\mathrm{NLO}}/\mathcal{O}_{\mathrm{LO}}, \qquad (5.33)$$

where $\mathcal{O}$ is a generic observable and $\mathcal{O}_{\mathrm{NLO}}$ is the sum of the LO contribution according to Eq. (5.7) and the EW contribution $\Delta\mathcal{O}_{\mathrm{NLO}}$.

The contents of this section are the following. First of all, we fix the input parameters for the numerical evaluation in Subsection 5.3.1. We start the discussion of numerical results with the presentation of integrated hadronic cross sections in Subsection 5.3.2. Next, in Subsection 5.3.3, we investigate the EW contributions from the distinct channels in differential distributions with respect to kinematical variables. In order to obtain experimentally more realistic results for the cross sections we also apply typical sets of kinematical cuts. A study of the dependence on the various SUSY parameters is given in Subsection 5.3.4. Finally, in Section 5.3.5, we also comment on the production of a pair of heavier stops $\tilde{t}_2\tilde{t}_2^*$.

5.3.1   Input parameters and conventions

The numerical results depend on the following input parameters.

The SM particle masses and gauge couplings are chosen as described in Appendix B.1. In particular, the top-quark mass m_t has been set to $m_t = 170.9$ GeV. The current value of the top-quark mass, $m_t = 173.1 \pm 1.3$ GeV [157], increases the top-squark mass $m_{\tilde{t}_1}$ by 0.6%, which reduces the total cross section by $\approx 3\%$. The changes for the relative corrections are completely negligible.

In the SUSY sector, we consider the SPS1a' parameter point suggested by the SPA convention [158] as a reference, unless stated otherwise. The low-energy $\overline{\mathrm{DR}}$ soft-breaking parameters are obtained with the help of a spectrum calculator (`Softsusy 2.0.18` [75]) at the (SUSY) scale $Q_{\mathrm{SUSY}} = 1$ TeV. To be consistent with the renormalization scheme we are using, we take the on-shell squark masses and the on-shell stop mixing angle as input parameters for our actual calculation (see Appendix B.2). In the SPS1a' scenario, the on-shell mass of the lighter stop is

$$m_{\tilde{t}_1} = 359.5 \text{ GeV} \qquad \text{(SPS1a')}, \qquad (5.34)$$

the other squark masses are given in Table B.1 on p. 218.

For the parton distributions, we use the set MRST 2004 QED [107], as already mentioned previously. Factorization and renormalization scales are chosen equal at the central value $\mu_F = \mu_R = m_{\tilde{t}_1}$. A study of the remaining QED-based scale dependence is not possible at the present stage since the QED and QCD evolution are not separated in the available parton densities. The scale dependence cannot be checked in a consistent way owing to the
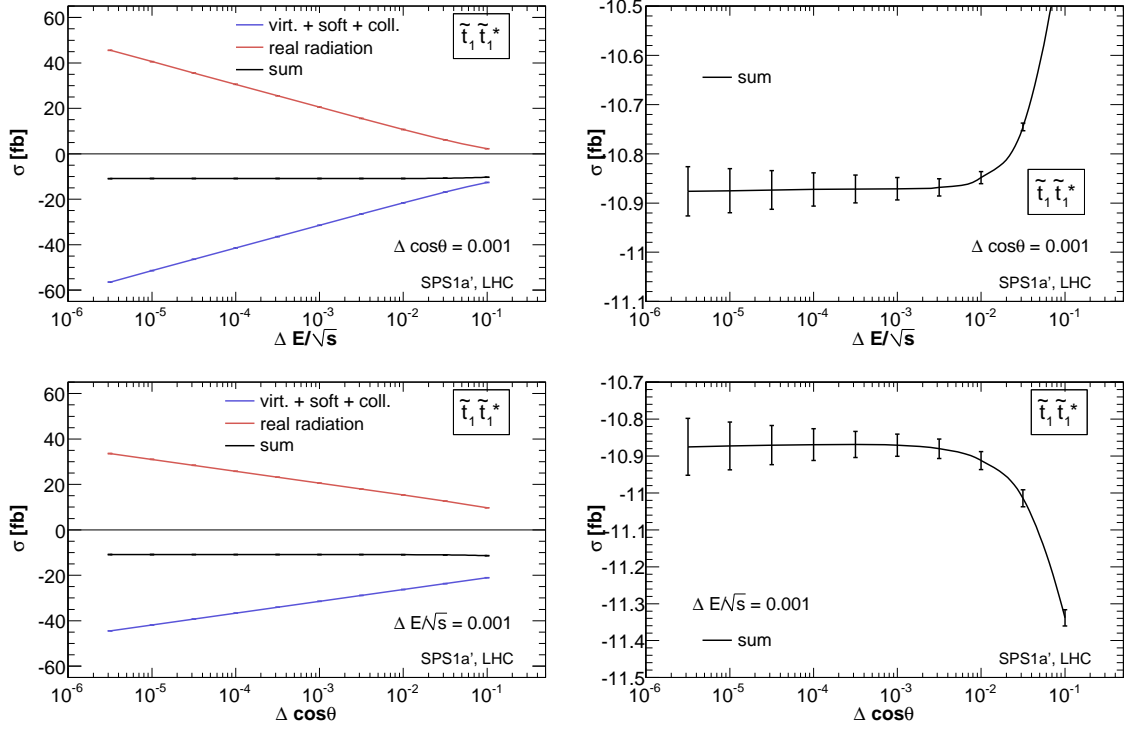
Figure 5.10.: Dependence of hadronic cross section contributions in the $q\bar{q}$ channel on the cutoff parameters ΔE (upper plots, $\delta_\theta = 0.001$ fixed) and δ_θ (lower plots, $\Delta E = 0.001\sqrt{\hat{s}}$ fixed). Left panels: Shown are the partial contributions (virtual corrections plus soft and collinear parts and the hard, non-collinear part) and the sum of all contributions for stop–anti-stop pair production at the LHC within the SPS1a' scenario. Right panels: Zoom on the sum of all contributions, the error bars represent integration uncertainties.

NLO QCD effects in the parton densities, which are not included in our calculation. For this reason we do not present a study of the scale dependence here. An important next step in improving the theoretical predictions would be to combine the NLO electroweak and QCD corrections.

As explained, the treatment of the IR-singular bremsstrahlung is done using the phase-space slicing method. We illustrate the method and its stability in terms of the more involved case of $q\bar{q}$ corrections, where two cutoff parameters are needed. The photon/gluon phase space is split into a soft part ($E_{\gamma/g} < \Delta E$), a collinear part ($E_{\gamma/g} > \Delta E$ and $\cos\theta > 1 - \delta_\theta$, θ being the angle between the photon/gluon and the radiating fermion), and a hard, non-collinear part ($E_{\gamma/g} > \Delta E$ and $\cos\theta < 1 - \delta_\theta$). The cutoff parameters for the photon and for the gluon phase space are chosen to be equal. As shown in Fig. 5.10, the sum of all contributions does not depend on the parameters when they are small enough. This is in accordance with the discussion in Section 5.2.3 that for small enough cutoff

(sub-)process	LO $\mathcal{O}(\alpha_s^2)$	EW contr. per channel $\mathcal{O}(\alpha_s^2\alpha)$	$\mathcal{O}(\alpha_s\alpha)$	$\mathcal{O}(\alpha^2)$	EW contr. δ
gg	2347	-11.5			-0.49%
$q\bar{q}$	327	-10.9		1.18	-2.97%
γg			38.1		
gq		$< 10^{-3}$			
inclusive $\tilde{t}_1\tilde{t}_1^*$	**2674**	**-22.3**	**38.1**	**1.18**	**0.64%**

Table 5.1.: Numerical results for the integrated cross sections for light stop–anti-stop pair production at the LHC within the SPS1a' scenario [158]. Shown are the leading order results, the EW contributions from the distinct channels, and the relative corrections δ, as defined in the text. All cross sections are given in femtobarn [fb].

parameters the soft and collinear contributions can be treated approximately according to Eq. (5.16), (5.19), (5.21), and (5.26), respectively. In the following numerical analysis, we use $\Delta E = 0.001\sqrt{\hat{s}}$ and $\delta_\theta = 0.001$.

5.3.2 Hadronic cross sections

In Table 5.1 we show results for the integrated hadronic cross section for $\tilde{t}_1\tilde{t}_1^*$ production at the LHC within the SPS1a' scenario. The LO cross sections and the absolute and relative EW contributions as introduced above are presented for the gg fusion, the $q\bar{q}$ annihilation, the γg fusion, and the real quark radiation gq channel separately. The γg and gq channel contribute at NLO only.

At the LHC, stop–anti-stop pairs are mainly produced via gg fusion which is enhanced by the high gluon density. The $q\bar{q}$ channels contribute to the integrated hadronic cross section at LO with less than 15%. Including EW contributions, we find that the corrections from the gg and the $q\bar{q}$ channels are of similar size. This is related to the fact that the $q\bar{q}$ channels get additional interference contributions from QCD- and EW-mediated diagrams which are not present at the Born level. However, both the $\mathcal{O}(\alpha_s^2\alpha)$ corrections to the gg and $q\bar{q}$ channels are negative and range at the percentage level only, whereas the γg contribution is positive and of even larger size. In total, the EW contribution to the integrated hadronic cross section is below 1%.

For the $q\bar{q}$ channel, also the results of the tree-level electroweak contribution is given In Table 5.1. As expected from the couplings and the structure of the pure s-channel diagrams, it is smaller by roughly one order of magnitude compared to the NLO EW corrections. Let us mention again that we neglect for this channel the contributions of bottom quarks in the initial state, motivated by the suppressed size of the loop-generated b-quark density. Initial-state b quarks would give rise to additional tree-level EW contributions of $\mathcal{O}(\alpha^2)$, generated by s-channel Higgs boson exchange and t-channel chargino exchange

diagrams. The latter yield possibly large results as the $b\tilde{\chi}^{\pm}\tilde{t}$ coupling is enhanced by the top-quark mass. However for a consistent treatment, also the EW–QCD interference terms of $\mathcal{O}(\alpha_s\alpha)$ of these diagrams and the QCD Born amplitudes have to be considered and they turn out to be of comparable size but of opposite sign. As a result, the $b\bar{b}$-induced $\mathcal{O}(\alpha_s\alpha + \alpha^2)$ contributions are smaller by about a factor of 20 compared to $q\bar{q}$-induced $\mathcal{O}(\alpha_s^2\alpha)$ corrections and can safely be neglected. In the following discussion of differential distributions we do not include any of the pure-EW tree-level channels.

Furthermore, the real quark radiation processes give only vanishing contributions which are limited in precision by the numerical integration error and we neglect these subprocesses below.

5.3.3 Differential distributions

The interplay of the dominant three production channels is illustrated in Fig. 5.11 where the absolute EW contributions per channel are shown as distributions with respect to M_{inv}, p_T, y, or η. Owing to the alternating signs, compensations occur where in particular the γg channel plays an important role.

In order to illustrate the numerical impact of the EW contributions on the LO cross section, we show in Fig. 5.12 the relative EW contributions δ for the gg and the $q\bar{q}$ channel, respectively, as distributions with respect to the invariant mass M_{inv} and the transverse momentum p_T of the stop $\tilde{t}_1(p_3)$. The EW corrections in the p_T distribution reach typically -10% in the gg channel, and -20% in the $q\bar{q}$ channel, for large values of p_T. In the invariant mass distributions, they are somewhat smaller, but still sizeable, at the 10% level for large M_{inv}.

The increase of the EW corrections in the high-p_T and high-M_{inv} region is influenced by the virtual corrections that comprise contributions from the massive gauge bosons. At high energies, W and Z bosons behave essentially as massless particles. They lead to similar collinear effects as photons, described by large double logarithmic contributions of W and Z boson masses. Contrarily to the photonic case, these double logarithms are not canceled in the sum of virtual and real gauge boson corrections since weak boson radiation leads to a different hadronic final state and is thus not included in our calculations. It is a well-known fact that EW virtual corrections to many hadron collider processes become large and negative at high energies and suggestions have been made to include the separately-finite but same-order contributions from gauge boson emission in the full EW result [159]. Even though additional gauge bosons in the final state induce different signatures, they should be included if (partially) inclusive final states are considered, in order to agree better with realistic experimental measurements. In [159] several example processes have been studied and it was found that the cross sections for weak boson emission are substantial in the high-energy region and that the EW virtual and real gauge boson corrections partially cancel. On the other hand, in our case and similar SUSY particle production processes, the double
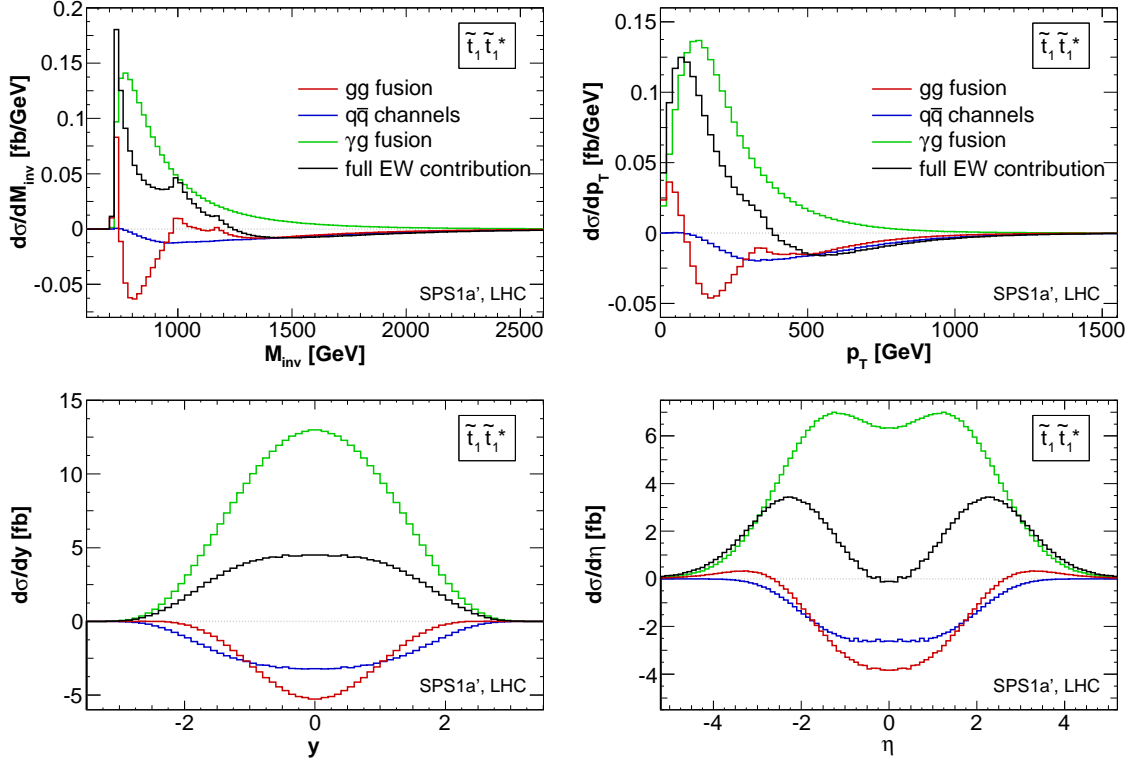
Figure 5.11.: Comparison of EW contributions from the dominant partonic channels to $\tilde{t}_1\tilde{t}_1^*$ production, for the distributions of the invariant mass of the stop pair, the transverse momentum $p_T(\tilde{t}_1^*)$, the rapidity $y(\tilde{t}_1^*)$, and the pseudo-rapidity $\eta(\tilde{t}_1^*)$ (from upper left to lower right). y and η are given in the laboratory frame.

logarithmic contributions from gauge boson exchange in the virtual diagrams cannot be the only source of the increase of EW corrections. If important, also corrections of higher order were expected to become sizable and should be resummed (see e. g. [160]) for a reliable cross section prediction. However, in [161], the two-loop corrections to sfermion pair production at linear colliders were estimated by the dominating contributions from box diagrams with weak boson exchange and only moderate effects of a few percent were found in the high-energy region. In summary, it would be interesting to further investigate the impact of weak boson exchange in the virtual corrections to stop–anti-stop production and to consider the corresponding real radiation processes in order to study possibly cancellations.

As a second feature of the relative corrections shown in Fig. 5.12, we observe small peaks in the gg invariant mass distribution. Their position can be determined best in the overlaid panel which gives a detailed view of the region of interest. The peaks precisely correspond to two-particle thresholds related to $\tilde{b}_1\tilde{b}_1^*$, $\tilde{b}_2\tilde{b}_2^*$, and $\tilde{t}_2\tilde{t}_2^*$ pairs in gg box diagrams (Fig. 5.3(c)) and Higgs boson-mediated vertex diagrams (last three diagrams in Fig. 5.4) [in the considered scenario, the masses of the involved squarks are $m_{\tilde{b}_1} = 495.3\,\text{GeV}$, $m_{\tilde{b}_2} =$
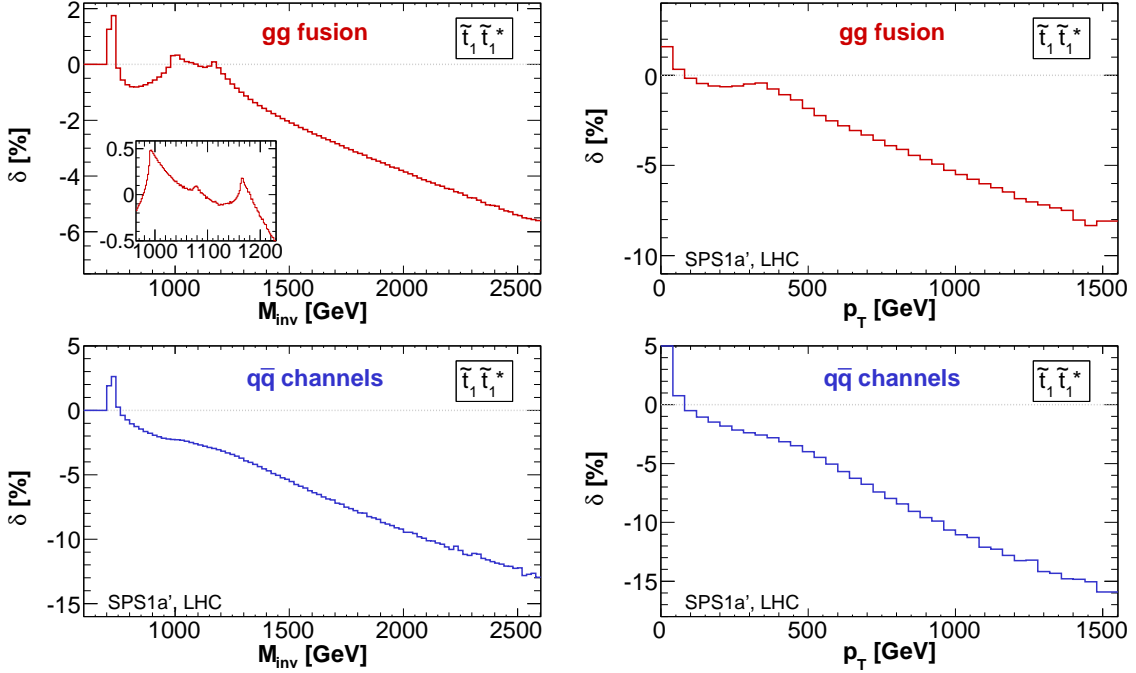
Figure 5.12.: Relative EW corrections to $\tilde{t}_1 \tilde{t}_1^*$ production at the LHC within the SPS1a' scenario. The upper plots refer to the $\mathcal{O}(\alpha_s^2 \alpha)$ corrections to the gg-fusion channel, the lower plots those of the $q\bar{q}$ channels. Shown are the invariant mass distribution of the $\tilde{t}_1 \tilde{t}_1^*$ pair (left panels) and the distributions with respect to the transverse momentum of the $\tilde{t}_1^*$ (right panels). In the upper left plot, the small panel gives a detailed view of the relative EW corrections in the region where squark threshold effects occur.

$538.1 \,\text{GeV}$, $m_{\tilde{t}_2} = 581.9 \,\text{GeV}$]. Thresholds from the squarks of the first two generations are CKM suppressed. The threshold effects appear also in the p_T distribution, around $300 \,\text{GeV}$, but they are smeared out and much less pronounced.

Finally, Fig. 5.13 shows the EW contribution of the dominant channels, including the photon-induced subprocesses, relative to the full LO cross section. We find a similar behavior as for the NLO EW corrections in the single channels. It is obvious that, although small for the total cross section, the higher-order EW contributions cannot be neglected for differential distributions where, in the high-p_T and high-M_{inv} range, they are of the same order of magnitude as the NLO QCD corrections.

For realistic experimental analyses, cuts on the kinematically allowed phase space of the stops have to be applied. They can be realized by a lower cut on the transverse momenta of the final-state particles to focus on high-p_T jets. Moreover, detectability of the final-state particles requires a minimal angle between the particles and the beam axis. Therefore, we set a cut on the pseudo-rapidity of the stops restricting the scattering angle θ to a central
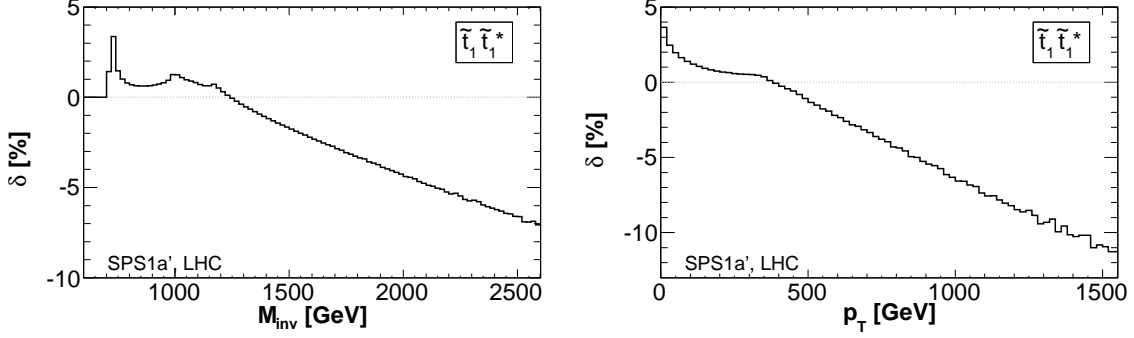
Figure 5.13.: Same as Fig. 5.12, but shown is the full EW contribution from all partonic subprocesses to $\tilde{t}_1\tilde{t}_1^*$ production at the LHC within the SPS1a' scenario.

channel (SPS1a')	unconstrained EW contr.	$p_T < 150\,\text{GeV}$ & $|\eta| < 2.5$	$p_T < 250\,\text{GeV}$ & $|\eta| < 2.5$
gg	2234	1262 (-46%)	661 (-72%)
$q\bar{q}$	316	278 (-12%)	226 (-28%)
γg	38.1	21.0 (-45%)	12.2 (-68%)

Table 5.2.: Integrated hadronic cross section at $\mathcal{O}(\alpha_s^2\alpha)$ within the SPS1a' scenario for the different production channels. Comparison of the full (unconstrained) results and cross sections where cuts on the pseudo-rapidities η and on the transverse momenta p_T of the outgoing top-squarks are applied (in femtobarn). The relative changes compared to the full results are given in brackets.

region. We apply two exemplary sets of cuts,

$$\text{cuts 1:} \quad p_T \geq 150\,\text{GeV and } |\eta| \leq 2.5 \quad (\text{i.e. } 9.4^\circ \leq \theta \leq 170.6^\circ),$$

$$\text{cuts 2:} \quad p_T \geq 250\,\text{GeV and } |\eta| \leq 2.5.$$

The differential cross sections and the influence of cuts are the content of Figs. 5.14 and 5.15. Displayed are the hadronic cross sections at NLO EW for the three dominant subprocesses (gg fusion, $q\bar{q}$ annihilation, γg induced), differential with respect to p_T, M_{inv} and to y, η, respectively. We show both the full (unconstrained) distributions and the distributions with cuts applied. The reduction of the integrated cross section owing to the application of cuts is summarized in Table 5.2.

The application of cuts reduces the gg- and γg-channel contributions strongly, cutting off the peak of the p_T distributions. The reduction is less pronounced in the $q\bar{q}$ channels where the p_T distribution is harder. The p_T-cuts also shift the threshold of the invariant mass distributions towards higher values affecting again mainly the gg and γg channels in
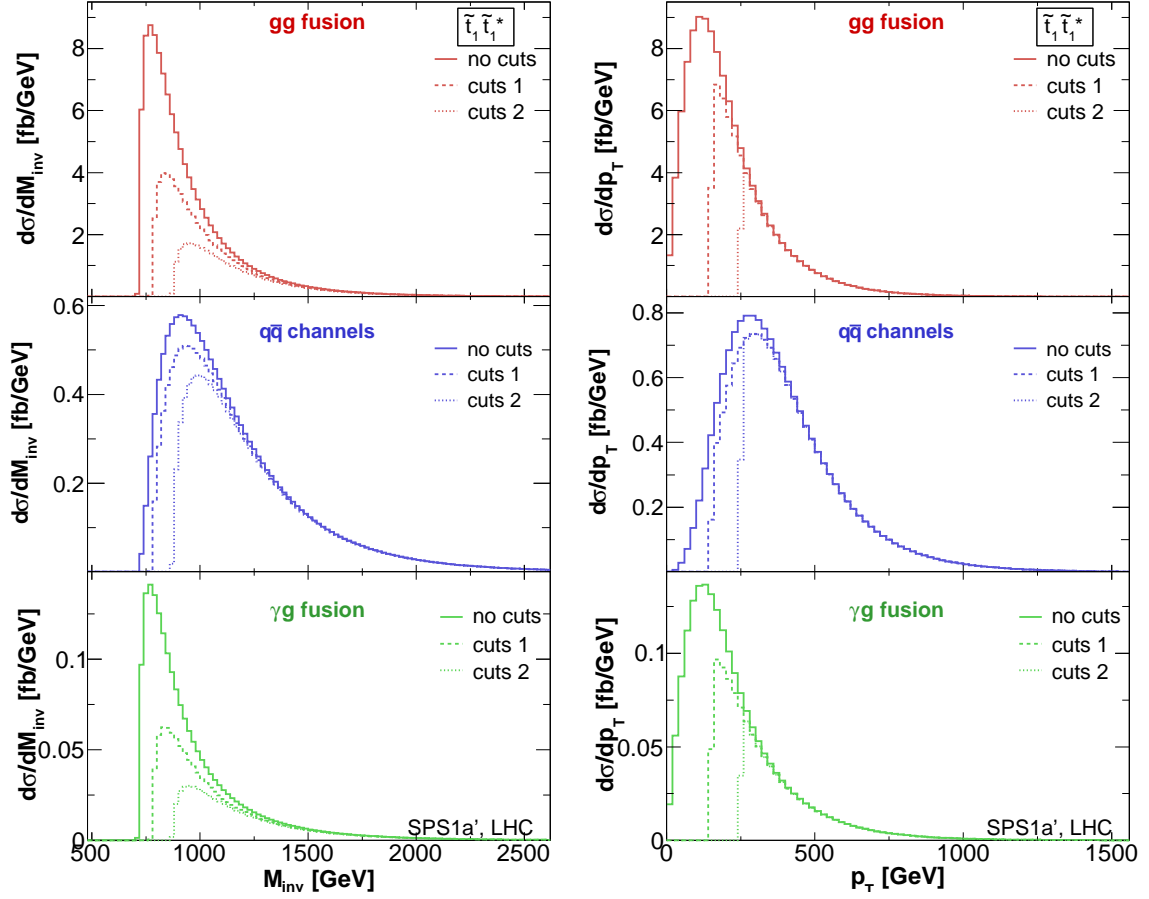
Figure 5.14.: Comparison of NLO EW differential hadronic cross sections (solid lines) and the distributions where kinematical cuts on the final top-squarks are applied for all three production channels, gg fusion (upper red plots), $q\bar{q}$ channels (middle blue plots), and γg fusion (lower green plots). Cuts 1 (dashed lines): $\mathbf{p_T \geq 150\ GeV}$, $\mathbf{|\eta| \leq 2.5}$, cuts 2 (dotted lines): $\mathbf{p_T \geq 250\ GeV}$, $\mathbf{|\eta| \leq 2.5}$. Distributions with respect to the invariant mass of the stop pair (left) and the transverse momentum $p_T(\tilde{t}_1)$ (right) are shown for $\tilde{t}_1\tilde{t}_1^*$ production at the LHC within the SPS1a' scenario.
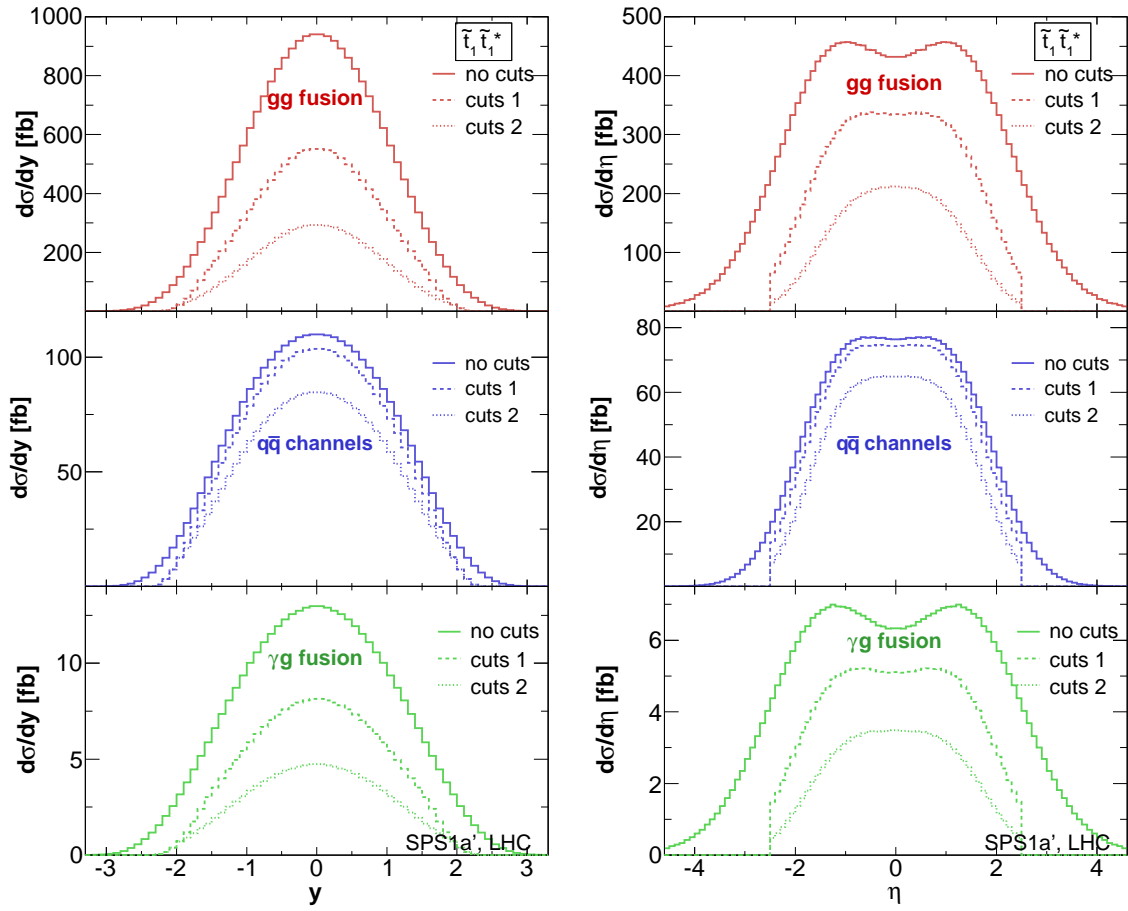
Figure 5.15.: Same as Fig. 5.14, but with respect to the rapidity $y(\tilde{t}_1^*)$ (left) and the pseudo-rapidity $\eta(\tilde{t}_1^*)$ (right).

height and shape. The situation for the rapidity distribution is similar. In the $q\bar{q}$ channel, the harder p_T distribution goes along with a narrower η distribution, as shown in the right panels of Fig. 5.15. Most of the stops produced via $q\bar{q}$ annihilation can be found in the central region. In contrast, stops from gg or γg fusion are often produced in the strong forward (or backward) direction, and the application of cuts on the pseudo-rapidity thus reduces the number of gg or γg based events significantly.

5.3.4   Dependence on SUSY parameters

How sensitive are the EW contributions to SUSY parameters as the soft-breaking parameters or the mass of the final state particle? This question shall be briefly answered in this section, where we investigate the dependence of the EW contributions on the SUSY parameters.

Different SUSY scenarios

To start with, we compare in Table 5.3 the integrated hadronic cross sections and the contributions from the three dominant partonic channels for $\tilde{t}_1 \tilde{t}_1^*$ production at the LHC within different SUSY scenarios. We consider four different mSUGRA-type Snowmass Points and Slopes (SPS) benchmark scenarios, specified by the universal mSUGRA parameters at the GUT scale as given in Eqs. (B.12)–(B.15). The on-shell stop mass $m_{\tilde{t}_1}$ is

$$m_{\tilde{t}_1} = \begin{cases} 992.4 \text{ GeV} & \text{(SPS2),} \qquad 649.7 \text{ GeV} \quad \text{(SPS3),} \\ 545.0 \text{ GeV} & \text{(SPS4),} \qquad 224.9 \text{ GeV} \quad \text{(SPS5)} \end{cases}, \tag{5.35}$$

in the four scenarios, respectively (see Appendix B.2 for more details on the input parameters).

The integrated hadronic cross sections depend strongly on the mass of the final-state particle, $m_{\tilde{t}_1}$. At LO, the stop mass is the only SUSY parameter that enters, cf. Eq. (5.5) and the results from different SUSY scenarios can directly be compared. For the example scenarios SPS2 and SPS4, we find that the LO cross section reduces by almost a factor of 50 if the stop mass is doubled.

The EW contributions, however, vary nontrivially among the different scenarios as other SUSY parameters enter via the particles and couplings in the loop-diagrams.

In scenarios where the top-squark $\tilde{t}_1$ is of intermediate or high mass (as SPS1a', SPS2, and SPS3) the NLO contributions are below 1%. The corrections to the $q\bar{q}$ and the gg channels are negative. In contrast, the γg contribution is always positive and of the same size as the other corrections or even larger.

scenario	(sub-) process	LO $\mathcal{O}(\alpha_s^2)$	EW contr. per channel			EW contr. δ
			$\mathcal{O}(\alpha_s^2\alpha)$	$\mathcal{O}(\alpha_s\alpha)$	$\mathcal{O}(\alpha^2)$	
SPS2	gg	4.31	-5.35×10^{-2}			-1.24%
	$q\bar{q}$	1.54	-12.4×10^{-2}		0.65×10^{-2}	-7.64%
	γg			18.6×10^{-2}		
	incl. $\tilde{t}_1\tilde{t}_1^*$	**5.86**	$\mathbf{-17.8 \times 10^{-2}}$	$\mathbf{18.6 \times 10^{-2}}$	$\mathbf{0.65 \times 10^{-2}}$	**0.26%**
SPS3	gg	77.2	-1.71			-2.21%
	$q\bar{q}$	18.5	-1.51		0.07	-7.75%
	γg			2.13		
	incl. $\tilde{t}_1\tilde{t}_1^*$	**95.8**	**-3.22**	**2.13**	**0.07**	**-1.07%**
SPS4	gg	226	-10.2			-4.49%
	$q\bar{q}$	46.1	-4.82		0.20	-10.0%
	γg			5.28		
	incl. $\tilde{t}_1\tilde{t}_1^*$	**273**	**-15.0**	**5.28**	**0.20**	**-3.49%**
SPS5	gg	25043	288			1.15%
	$q\bar{q}$	2340	-15.0		6.66	-0.36%
	γg			284		
	incl. $\tilde{t}_1\tilde{t}_1^*$	**27383**	**273**	**284**	**6.66**	**2.06%**

Table 5.3.: Numerical results for the integrated cross sections for light stop–anti-stop pair production at the LHC within different SPS scenarios [162]. Shown are the leading order results, the EW contributions from the distinct channels, and the relative corrections δ, as defined in the text. The results for the SPS1a' scenario are given in Table 5.1. All cross sections are given in femtobarn [fb].

The SPS4 scenario is characterized by a large $\tan\beta$ $(\tan\beta(m_Z) = 50)$. The large value of $\tan\beta$ has an important impact in the Higgs sector, where the couplings to down-type (s)fermions are enhanced. Also, the L–R mixing of the stop eigenstates is affected. Compared to the other considered scenarios, the stop mixing angle is rather large in the SPS4 scenario $(\theta_{\tilde{t}} = 35°)$, and the lighter of the stops has an important left-handed component. Both effects combine to enhance the $\mathcal{O}(\alpha_s^2\alpha)$ corrections from the gg and $q\bar{q}$ channels (-15%) over the γg contribution (5%).

The situation is different again in scenarios where the top-squark is very light, i.e. lighter than half of m_{H^0}, the mass of the heavier neutral Higgs boson H^0, where a large fraction of the squarks appears through production and decay of H^0 particles. This is the case in the SPS5 scenario $[m_{H^0} = 698.7\,\text{GeV}$ and $\Gamma(H^0) = 8.8\,\text{GeV}$, obtained with `FeynHiggs` [81]]. As the H^0 boson can go on-shell in the respective diagrams (last row of Fig. 5.4), we insert

the width Γ_{H^0} in the Higgs boson propagator to regularize the diagrams,

$$\frac{1}{p^2 - m_{H^0}^2} \longrightarrow \frac{1}{p^2 - m_{H^0}^2 + i m_{H^0}\Gamma_{H^0}} \tag{5.36}$$

By doing so, the order in perturbation theory with respect to the electroweak coupling α of the diagrams is reduced by one-half. Thus also the squared resonant Higgs boson diagrams give contributions at $\mathcal{O}(\alpha_s^2\alpha)$ and we include them in the sum of the EW corrections. In numbers, the interference contribution of the QCD Born diagram and the full gg-induced virtual corrections amounts to 26.8 fb (in the SPS5 scenario), whereas the squared Higgs boson diagrams dominate and contribute with 96.2 fb. The large size of those can be understood by the fact that large threshold contributions arise from the $\tilde{t}_1$'s running in the loops if the Higgs boson is produced on-shell. As a result, the EW contributions in the gg channel are positive and add up together with the γg fusion contribution of similar size to yield positive EW corrections of 2.1% relative to the inclusive LO result.

Dependence on soft-breaking and SUSY parameters

In order to study the dependence of the EW contributions on the various SUSY parameters in more detail, we consider the ratio of the EW contribution in each of the three dominant channels to the combined $gg + q\bar{q}$ Born cross section, $\delta_{tot} = \{\sigma_{gg}^{2,1}, \sigma_{q\bar{q}}^{2,1}, \sigma_{\gamma g}^{1,1}\}/(\sigma_{gg}^{2,0} + \sigma_{q\bar{q}}^{2,0})$. We focus on those parameters that determine the top-squark mass, cf. Eqs. (2.93) and (2.96), and vary each quantity out of the set $m_{\tilde{Q}_3}$, $m_{\tilde{U}_3}$, $\tan\beta$, A_t, or μ around its SPS1a' value while keeping all other parameters fixed to those of the default SPS1a' scenario[20]. Again, as we did for the SPS5 scenario, we include the squared Higgs boson-mediated diagrams in the gg channel contributions in scenarios where $m_{H^0} > 2m_{\tilde{t}_1}$. The results are displayed in the left panels of Figs. 5.16 – 5.20. Simultaneously, we show the mass of the light stop $\tilde{t}_1$ as a function of the varied parameter in the respective right panels (black solid lines). The parameter configuration of the SPS1a' scenario is marked by a vertical gray dotted line in all the figures.

We find the following general behaviors. The γg contributions stem from tree-level diagrams and the only relevant parameter is thus the top-squark mass $m_{\tilde{t}_1}$. In all scenarios, the γg fusion channel is as important as the $\mathcal{O}(\alpha_s^2\alpha)$ EW corrections to the $q\bar{q}$ and gg processes. The $q\bar{q}$ corrections, being practically always negative, involve many different SUSY particles in the loops, although the relative corrections show only small variations. The gg contributions are more sensitive to the considered SUSY parameters. The plots

---

[20]The following plots are taken from [24], where a slightly different convention for the SUSY input parameters has been used. In particular, the soft-breaking parameters correspond to on-shell quantities which directly determine the on-shell stop mass. At the central SPS1a' value, the resulting stop mass is $m_{\tilde{t}_1} = 322\,\text{GeV}$. Furthermore, the factorization and renormalization scale have been set to $\mu_{R,F} = 2m_{\tilde{t}_1}$. The general features of the presented results are basically unaffected by these conventions.
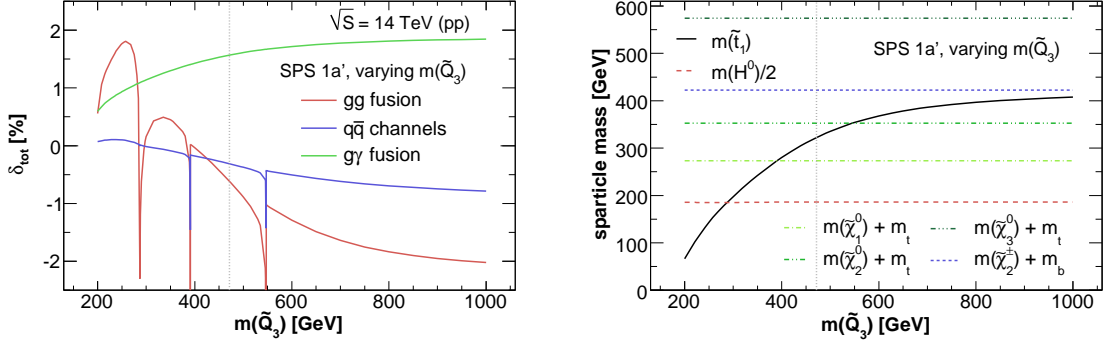
Figure 5.16.: Left: EW contributions from the dominant partonic channels to $\tilde{t}_1 \tilde{t}_1^*$ production relative to the combined $(gg+q\bar{q})$ LO cross section as a function of the soft-breaking parameter $m_{\tilde{Q}_3}$, where $m_{\tilde{Q}_3}$ is varied around the SPS1a' value (gray dotted line). Right: Mass of $\tilde{t}_1$, half of the mass of H^0, sums of the masses of the top-quark and $\tilde{\chi}_1^0$, $\tilde{\chi}_2^0$, and $\tilde{\chi}_3^0$, respectively, and sum of the masses of the b-quark and $\tilde{\chi}_2^{\pm}$ as a function of $m_{\tilde{Q}_3}$. All other parameters are chosen according to the SPS1a' scenario.
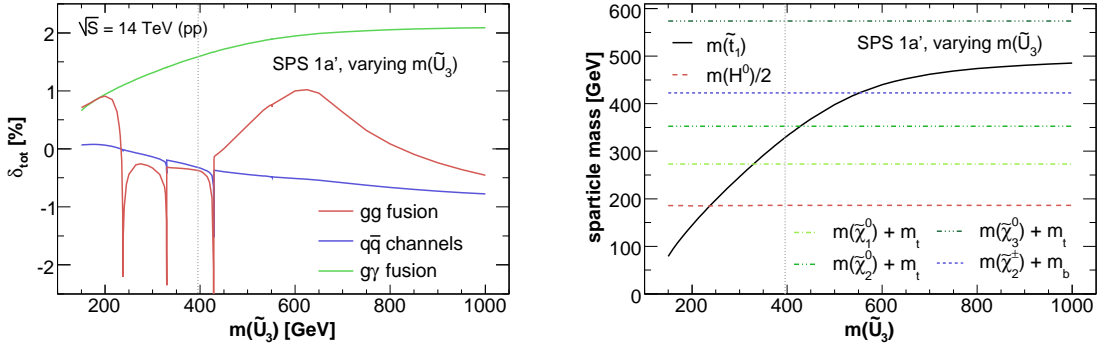
Figure 5.17.: Same as Fig. 5.16, but for variation of the soft-breaking parameter $m_{\tilde{U}_3}$.

show striking peaks (some of them are also visible in $q\bar{q}$ annihilation), which correspond to threshold effects and can be explained by the SUSY particle masses displayed at the right panels of Figs. 5.16 – 5.20. They occur in the Higgs boson-exchange diagrams when $m_{\tilde{t}_1} = m_{H^0}/2$ (red long-dashed lines in the figures), and in the top-squark wave function renormalization when $m_{\tilde{t}_1}$ equals the sum of masses of a neutralino and the top-quark (green dash-dotted lines) or of a chargino and the bottom-quark (blue dashed lines). The chargino-induced peaks are less pronounced than those from neutralinos and not visible in Fig. 5.17 and Fig. 5.20.

Outside of such singular parameter configurations, over a wide range of SUSY parameters, the combined EW contributions to stop–anti-stop pair production are only weakly parameter dependent.
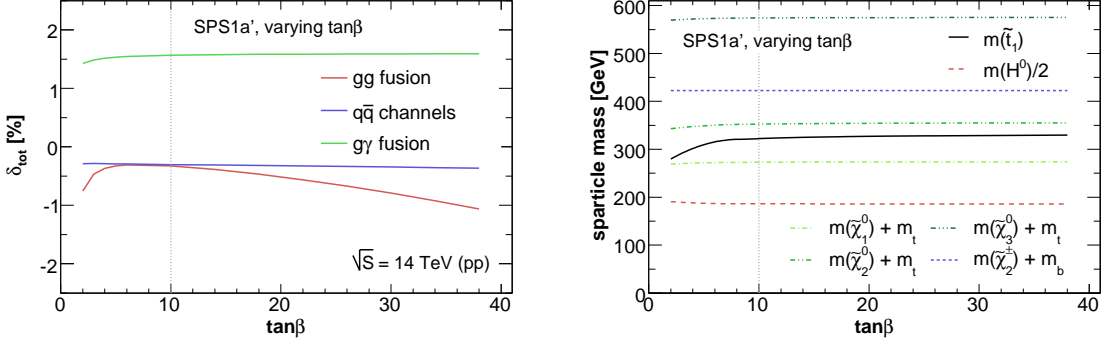
Figure 5.18.: Same as Fig. 5.16, but for variation of $\tan\beta$.
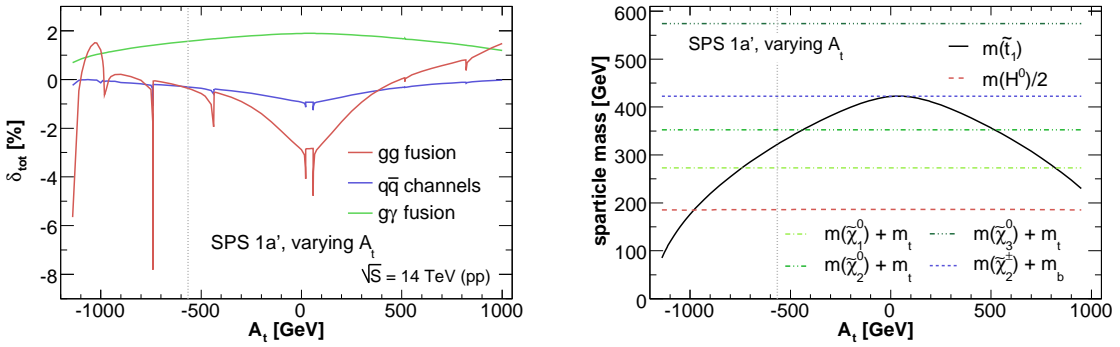
Figure 5.19.: Same as Fig. 5.16, but for variation of trilinear coupling parameter A_t.
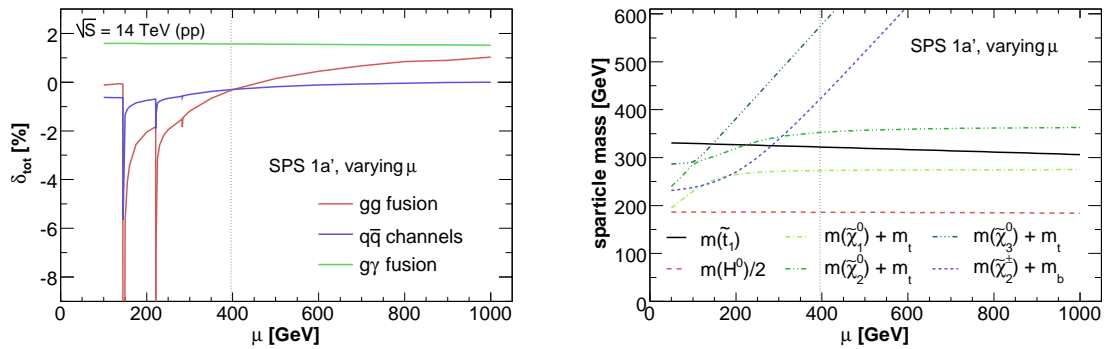
Figure 5.20.: Same as Fig. 5.16, but for variation of the Higgs parameter μ.

scenario	(sub-) process	LO $\mathcal{O}(\alpha_s^2)$	EW contr. per channel			EW contr. δ
			$\mathcal{O}(\alpha_s^2\alpha)$	$\mathcal{O}(\alpha_s\alpha)$	$\mathcal{O}(\alpha^2)$	
SPS1a'	gg	153	-24.9			-16.3%
	$q\bar{q}$	33.1	-6.65		0.32	-19.1%
	γg			3.78		
	gq		$< 10^{-3}$			
	incl. $\tilde{t}_2\tilde{t}_2^*$	**186**	**-31.6**	**3.78**	**0.32**	**-14.8%**

Table 5.4.: Numerical results for the integrated cross sections for heavy stop–anti-stop pair production at the LHC within the SPS1a' scenario. Notation as in Tables 5.1 and 5.3. All cross sections are given in femtobarn [fb].

5.3.5 Production of $\tilde{t}_2\tilde{t}_2^*$ pairs

To conclude our studies on stop–anti-stop production, let us briefly comment on the case of $\tilde{t}_2\tilde{t}_2^*$ pairs. The $\tilde{t}_2$ is considerably heavier than the first mass eigenstate $\tilde{t}_1$ and we expect only small integrated cross sections at hadron colliders. The process is thus less interesting for experimental searches. However, as the $\tilde{t}_2$ is more left-handed than the $\tilde{t}_1$ in many SUSY scenarios, the relative EW contributions to the cross section can become sizable.

We present results for the integrated hadronic cross section for $\tilde{t}_2\tilde{t}_2^*$ production at the LHC within the SPS1a' scenario in Table 5.4. As usual, we give the LO cross sections and the absolute and relative EW contributions from the various partonic subprocesses. In the SPS1a' scenario, the on-shell mass of the heavier stop is $m_{\tilde{t}_2} = 581.9$ GeV, cf. Table B.1.

For the LO cross section we find results of similar size as those for $\tilde{t}_1\tilde{t}_1^*$ production within the SPS4 scenario, where the mass of the lighter stop is comparable. As already argued above, the stop mixing does not enter at LO and the only SUSY parameter that determines the cross section is the mass of the final state particle. Including EW effects, however, we find important differences between the results for $\tilde{t}_1\tilde{t}_1^*$ and $\tilde{t}_2\tilde{t}_2^*$ production. In the latter case, the NLO EW corrections of $\mathcal{O}(\alpha_s^2\alpha)$ from the gg-induced and $q\bar{q}$-induced channels give the dominant contribution while the chirality-independent photon-induced subprocess is suppressed from the high stop mass. The pure-EW tree-level channel is slightly enhanced for the mostly left-handed $\tilde{t}_2\tilde{t}_2^*$ production due to the mixing angle that enters in the $Z\tilde{t}_a\tilde{t}_a^*$ coupling. Compared to the $\mathcal{O}(\alpha_s\alpha)$ contributions, however, this channel is smaller by two orders of magnitude. In total, the EW contributions to $\tilde{t}_2\tilde{t}_2^*$ production alter the LO prediction by almost -15%.

The interplay of the various EW contributions is further investigated in Fig. 5.21, where the absolute EW contributions per channel are shown as distributions with respect to M_{inv}, p_T, y, or η. The absolute size of the full EW contribution is dominated by the gg channel which profits from the high gluon luminosity. Different to $\tilde{t}_1\tilde{t}_1^*$ (cf. Fig. 5.11), no threshold
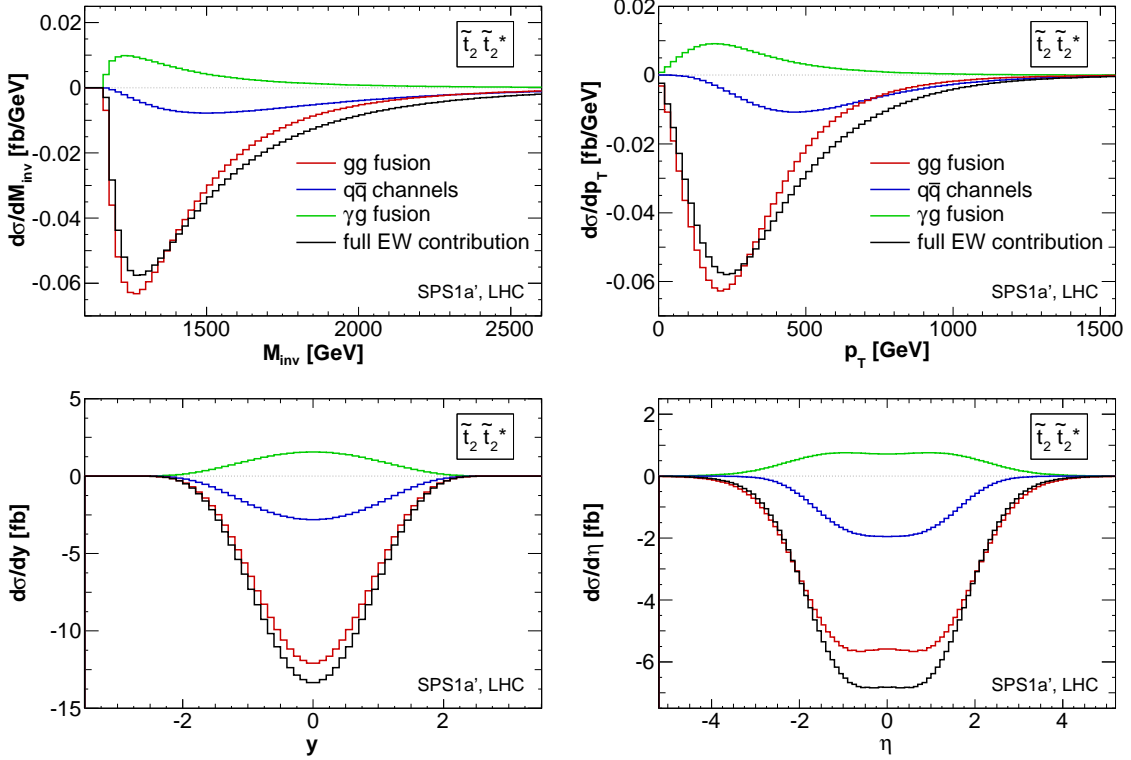
Figure 5.21.: Comparison of EW contributions from the dominant partonic channels to $\tilde{t}_2\tilde{t}_2^*$ production at the LHC within the SPS1a' scenario, for the distributions of the invariant mass of the stop pair, the transverse momentum $p_T(\tilde{t}_2^*)$, the rapidity $y(\tilde{t}_2^*)$, and the pseudo-rapidity $\eta(\tilde{t}_2^*)$ (from upper left to lower right). y and η are given in the laboratory frame.

effects arise in the M_{inv} distribution, as the $\tilde{t}_2$ is the heaviest among all squarks.

Finally, we present the EW contributions relative to the LO results from gg- and $q\bar{q}$-induced $\tilde{t}_2\tilde{t}_2^*$ production in Fig. 5.22 and also give the full EW contribution relative to the inclusive LO cross section in Fig. 5.23. In correspondence with the results of Table 5.4, the relative corrections in the gg and $q\bar{q}$ channels are comparable. In the high-p_T and high-M_{inv} region they grow up to -20% in the gg channel and even -30% for the $q\bar{q}$-induced subprocess. The γg subprocess is less important and the inclusive EW contribution, shown in Fig. 5.23, amounts to -20% and -25% in the given kinematical ranges of the M_{inv} and p_T distributions, respectively.

To summarize, the integrated cross sections for $\tilde{t}_2\tilde{t}_2^*$ production are suppressed by the heavy mass of the final-state particles and the EW contributions are small in absolute size. However as the latter depend on the stop mixing angle, they are enhanced for mostly left-handed mass eigenstates and alter the LO prediction considerably in particular in the high-energy ranges.
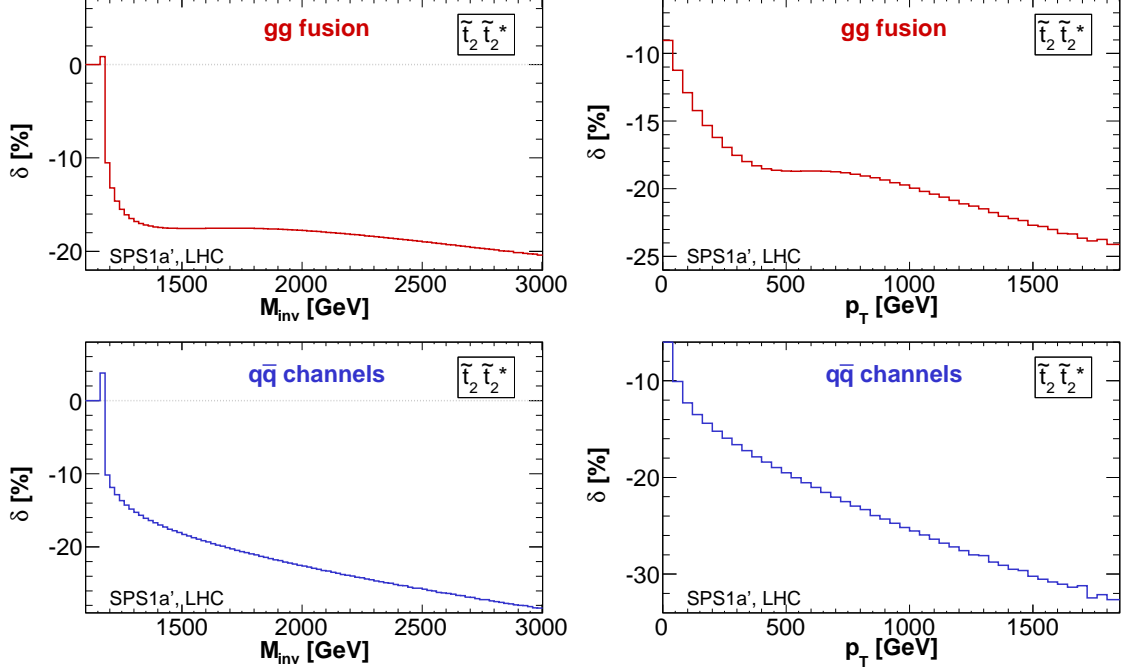
Figure 5.22.: Relative EW corrections to $\tilde{t}_2\tilde{t}_2^*$ production at the LHC within the SPS1a' scenario. The upper plots refer to the $\mathcal{O}(\alpha_s^2\alpha)$ corrections to the gg fusion channel, the lower plots those of the $q\bar{q}$ channels. Shown are the invariant mass distribution of the $\tilde{t}_2\tilde{t}_2^*$ pair (left panels) and the distributions with respect to the transverse momentum of the $\tilde{t}_2^*$ (right panels).
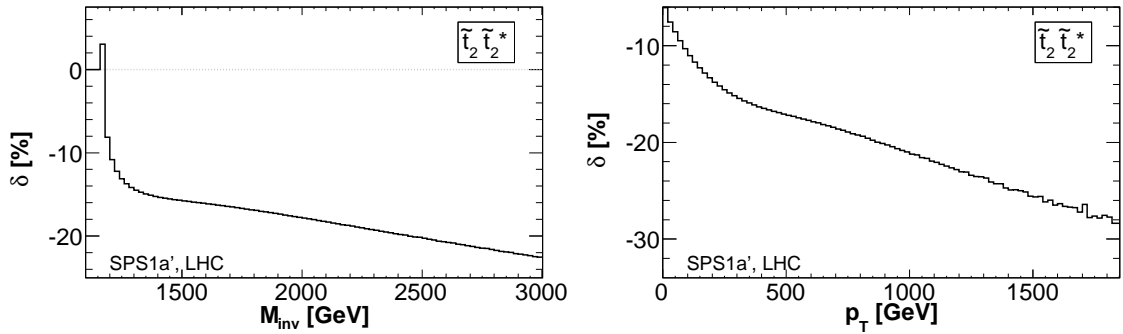
Figure 5.23.: Same as Fig. 5.22, but shown is the full EW contribution from all partonic subprocesses to $\tilde{t}_2\tilde{t}_2^*$ production at the LHC within the SPS1a' scenario.

Chapter 6
Gluino–squark production

In this chapter, we consider the associated production of squarks and gluinos at hadron colliders and study the EW contributions within the MSSM framework. We restrict the discussion to (anti-)squarks of the first two generations,

$$PP \to \tilde{g}\tilde{q}_a,$$
$$PP \to \tilde{g}\tilde{q}_a^*, \qquad q = u, d, c, s; \quad a = L, R. \tag{6.1}$$

We recall that this is motivated by the fact that both $\tilde{g}\tilde{t}$ and $\tilde{g}\tilde{b}$ production are suppressed by the heavy-quark parton density inside hadrons. Furthermore, as light-flavor squarks are almost degenerate in mass and typically decay into a light quark and a LSP, they are hard to distinguish in experiments. Stops and sbottoms, in contrast, lead to distinct final-state signatures and will experimentally be distinguishable from squarks of the first two generations. Experimental analyses are thus mostly based on inclusive gluino–squark production, as indicated in Eq. (6.1).

In many SUSY models, gluinos and squarks have intermediate masses around $\mathcal{O}(500 - 1000 \text{ GeV})$ and are heavier than the lighter stop $\tilde{t}_1$ and other sfermions and gauginos. However owing to the color charge and the high multiplicity of light-flavor squarks and gluinos, the inclusive $\tilde{g}\tilde{q}$ cross section is expected to be comparable to or even larger than those of $\tilde{t}_1\tilde{t}_1^*$ production (see last chapter) and sfermion or gaugino pair production processes. Among the various squark and gluino production processes, it is the dominant one if squarks and gluinos are of comparable masses (see Chapter 3). The cascade decays of the final state particles result in multijet and $\not{E}_T$ signatures and simple cuts will allow a good discrimination between signal and SM backgrounds [163]. In summary, gluino–squark production constitutes one of the most promising channels in the hunt for SUSY.

This chapter is organized in analogy to the previous discussion on stop–anti-stop production. In Section 6.1, we recapitulate the well-known LO cross section for gluino–squark production at the partonic and the hadronic level [19]. We refer to [20,21] for the results at NLO QCD. Here, we focus on the EW contributions, first published in [25]. In Section 6.1 the various subprocesses are presented and based on the techniques introduced in Chapter 4
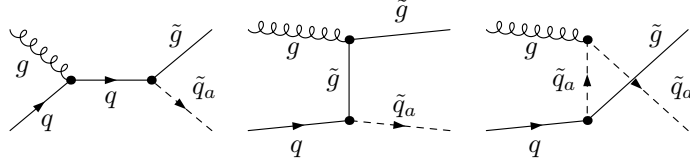
Figure 6.1.: LO Feynman diagrams for gluino–squark production at the Born level.

we give details about the treatment of UV and IR singularities. Numerical results for the hadronic cross sections and distributions with respect to gluino–squark production at the LHC are discussed in Section 6.3.

6.1 LO cross section and conventions

At hadron colliders, the LO contribution to the production of a gluino in association with an (anti-)squark $\tilde{q}_a^{(*)}$ is QCD based and related to the following partonic processes:

$$g(p_1)\, q(p_2) \;\rightarrow\; \tilde{g}(p_3)\, \tilde{q}_a(p_4), \qquad g(p_1)\, \bar{q}(p_2) \;\rightarrow\; \tilde{g}(p_3)\, \tilde{q}_a^*(p_4), \tag{6.2}$$

where the initial-state quark and the final-state squark are of the same flavor q. Due to CP symmetry the unpolarized cross sections of these two processes are equal; so in the following we will refer to the first partonic process only. The corresponding Feynman diagrams are shown in Fig. 6.1 (see also Fig. 3.5(b) for the general classification among the colored SUSY particle production processes).

Since the quarks of the first two generations are treated as massless, in the case of the squarks of the first two generations weak eigenstates are also mass eigenstates and we will distinguish squarks with same flavor by means of their chiralities, $\tilde{q}_a = \tilde{q}_L, \tilde{q}_R$. Furthermore, the masses of the squarks of the second generation coincide with those in the first generation. We denote the mass of squark $\tilde{q}_a$ by $m_{\tilde{q}_a}$, and the gluino mass by $m_{\tilde{g}}$.

Cross sections and matrix elements are given in the usual notation, i.e. superscripts m, n specify the order in perturbation theory $\mathcal{O}(\alpha_s^m \alpha^n)$ and the subscript refers to the respective partonic process. We parameterize the results in terms of the (reduced) Mandelstam variables defined in analogy to Eq. (5.3) by

$$\hat{s} = (p_1 + p_2)^2, \qquad \hat{t} = (p_1 - p_3)^2, \qquad \hat{u} = (p_1 - p_4)^2,$$
$$\hat{t}_{\tilde{g}/\tilde{q}_a} = \hat{t} - m^2_{\tilde{g}/\tilde{q}_a}, \quad \hat{u}_{\tilde{g}/\tilde{q}_a} = \hat{u} - m^2_{\tilde{g}/\tilde{q}_a}. \tag{6.3}$$

The differential partonic cross section for the process $gq \rightarrow \tilde{g}\tilde{q}_a$ reads

$$d\hat{\sigma}^{2,0}_{gq \rightarrow \tilde{g}\tilde{q}_a}(\hat{s}) = \frac{d\hat{t}}{16\pi\hat{s}^2} \overline{\sum} \left| \mathcal{M}^{1,0}_{gq \rightarrow \tilde{g}\tilde{q}_a}(\hat{s},\hat{t},\hat{u}) \right|^2 , \tag{6.4}$$

in terms of the squared spin- and color-averaged lowest-order matrix element [20],

$$
\overline{\sum}\left|\mathcal{M}_{gq\to\tilde{g}\tilde{q}_a}^{1,0}\right|^2 = \frac{1}{4}\cdot\frac{1}{24}\cdot 16\pi^2\alpha_s^2\left[C_0\left(1-2\frac{\hat{s}\,\hat{u}_{\tilde{q}_a}}{\hat{t}_{\tilde{g}}^2}\right)-C_K\right]
$$
$$
\times\left[-\frac{\hat{t}_{\tilde{g}}}{\hat{s}}+\frac{2(m_{\tilde{g}}^2-m_{\tilde{q}_a}^2)\hat{t}_{\tilde{g}}}{\hat{s}\hat{u}_{\tilde{q}_a}}\left(1+\frac{m_{\tilde{g}}^2}{\hat{t}_{\tilde{g}}}+\frac{m_{\tilde{q}_a}^2}{\hat{u}_{\tilde{q}_a}}\right)\right],
$$

(6.5)

with the color factors defined in Eq. (5.6), ($C_0 = 24$, $C_K = 8/3$).

As usual, the hadronic cross section is then given by a convolution of the partonic cross section with the respective parton luminosities, cf. Eq. (3.3),

$$
d\sigma_{PP\to\tilde{g}\tilde{q}_a}^{2,0}(S) = \int_{\tau_0}^1 d\tau\,\frac{d\mathcal{L}_{PP}^{gq}}{d\tau}\,d\hat{\sigma}_{gq\to\tilde{g}\tilde{q}_a}^{2,0}(\tau S),
$$

(6.6)

with the production threshold $\tau_0 = (m_{\tilde{g}} + m_{\tilde{q}_a})^2/S$.

6.2   Electroweak contributions

In contrast to squark–(anti-)squark production processes, which allow for $q\bar{q}$ initial states at LO, gluino–squark final states cannot be produced at $\mathcal{O}(\alpha^2)$. But again, we include photon-induced gluino–squark production at the tree level being part of the EW contributions, described below in Section 6.2.1. At NLO EW, gluino–squark production comprises virtual corrections (see Section 6.2.2) and real photon radiation at $\mathcal{O}(\alpha_s^2\alpha)$ (Section 6.2.3). Further $\mathcal{O}(\alpha_s^2\alpha)$ contributions arise from interference of EW- and QCD-mediated real-quark radiation diagrams, which will be discussed in Section 6.2.4.

The complete EW contribution to the hadronic cross section is defined by

$$
d\sigma_{PP\to\tilde{g}\tilde{q}_a}^{\mathrm{EW}}(S) = \int_{\tau_0}^1 d\tau\left\{\frac{d\mathcal{L}_{\gamma q}^{PP}}{d\tau}\,d\hat{\sigma}_{\gamma q\to\tilde{g}\tilde{q}_a}^{1,1}(\hat{s}) + \frac{d\mathcal{L}_{gq}^{PP}}{d\tau}\left[d\hat{\sigma}_{gq\to\tilde{g}\tilde{q}_a}^{2,1}(\hat{s})+d\hat{\sigma}_{gq\to\tilde{g}\tilde{q}_a\gamma}^{2,1}(\hat{s})\right]\right.
$$
$$
+\sum_{q_i=u,d,c,s}\frac{d\mathcal{L}_{qq_i}^{PP}}{d\tau}\,d\hat{\sigma}_{qq_i\to\tilde{g}\tilde{q}_a q_i}^{2,1}(\hat{s}) + \sum_{q_i=u,d,c,s;\ q_i\neq q}\frac{d\mathcal{L}_{q\bar{q}_i}^{PP}}{d\tau}\,d\hat{\sigma}_{q\bar{q}_i\to\tilde{g}\tilde{q}_a\bar{q}_i}^{2,1}(\hat{s})
$$
$$
\left.+\sum_{q_i=u,d,c,s}\frac{d\mathcal{L}_{q_i\bar{q}_i}^{PP}}{d\tau}\,d\hat{\sigma}_{q_i\bar{q}_i\to\tilde{g}\tilde{q}_a\bar{q}}^{2,1}(\hat{s})\right\},
$$

(6.7)

in terms of the respective partonic cross sections (see below) and parton luminosities, cf. Eq. (3.3).
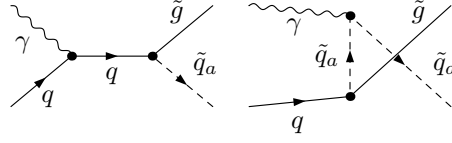
Figure 6.2.: Feynman diagrams for the tree-level EW contribution to $\tilde{g}\tilde{q}_a$ production from the photon-induced subprocess.

6.2.1 Tree-level EW contributions

Photon-induced gluino–squark production

We consider the photon-induced subprocesses as an independent production channel to gluino–squark production. Formally of different orders, the photon–quark induced diagrams shown in Fig. 6.2.1 (see also Fig. 3.8(b)) contribute at tree level to the same final state and can be important, as we have seen in the case of stop–anti-stop production in Chapter 5.

The partonic differential cross section reads

$$d\hat{\sigma}^{1,\,1}_{\gamma q \to \tilde{g}\tilde{q}_a}(\hat{s}) = \frac{d\hat{t}}{16\pi\hat{s}^2} \overline{\sum} \left| \mathcal{M}^{1/2,\,1/2}_{\gamma q \to \tilde{g}\tilde{q}_a}(\hat{s},\hat{t},\hat{u}) \right|^2 , \tag{6.8}$$

$$\overline{\sum} \left| \mathcal{M}^{1/2,\,1/2}_{\gamma q \to \tilde{g}\tilde{q}_a} \right|^2 = \frac{1}{4} \cdot \frac{1}{3} \cdot 32\pi^2 \alpha_s \alpha\, e_q^2\, N C_K \left[-\frac{\hat{t}_{\tilde{g}}}{\hat{s}} + \frac{2(m_{\tilde{g}}^2 - m_{\tilde{q}_a}^2)\hat{t}_{\tilde{g}}}{\hat{s}\hat{u}_{\tilde{q}_a}} \left(1 + \frac{m_{\tilde{g}}^2}{\hat{t}_{\tilde{g}}} + \frac{m_{\tilde{q}_a}^2}{\hat{u}_{\tilde{q}_a}} \right) \right] ,$$

expressed in terms of the reduced Mandelstam variables, Eq. (6.3).

Due to color conservation, photon–gluon induced partonic processes are only possible in combination with an additionally radiated quark and thus represent contributions of higher order. Since they are suppressed by the photon PDF compared to the bremsstrahlung processes Eq. (6.10) and Eq. (6.14), we do not include them in our discussion here.

6.2.2 Virtual corrections

The first class of NLO contributions of EW origin are the virtual corrections,

$$d\hat{\sigma}^{2,\,1}_{gq \to \tilde{g}\tilde{q}_a}(\hat{s}) = \frac{d\hat{t}}{16\pi\hat{s}^2} \overline{\sum} 2\,\mathrm{Re}\left\{ \left(\mathcal{M}^{1,\,0}_{gq \to \tilde{g}\tilde{q}_a} \right)^* \mathcal{M}^{1,\,1}_{gq \to \tilde{g}\tilde{q}_a} \right\}, \tag{6.9}$$

where $\mathcal{M}^{1,\,1}$ is the one-loop amplitude with EW insertions in the (QCD-based) tree-level gq diagrams, leading to the self-energy, vertex, box, and counterterm diagrams shown in Figs. 6.3 and 6.4.

In order to obtain a UV-finite result, both the quark and the squark sector require renormalization and we proceed as described in Section 4.1, imposing on-shell conditions according to [79,128,129]. Here, in the limit of no L–R mixing, the independent parameters

(a)

(b)
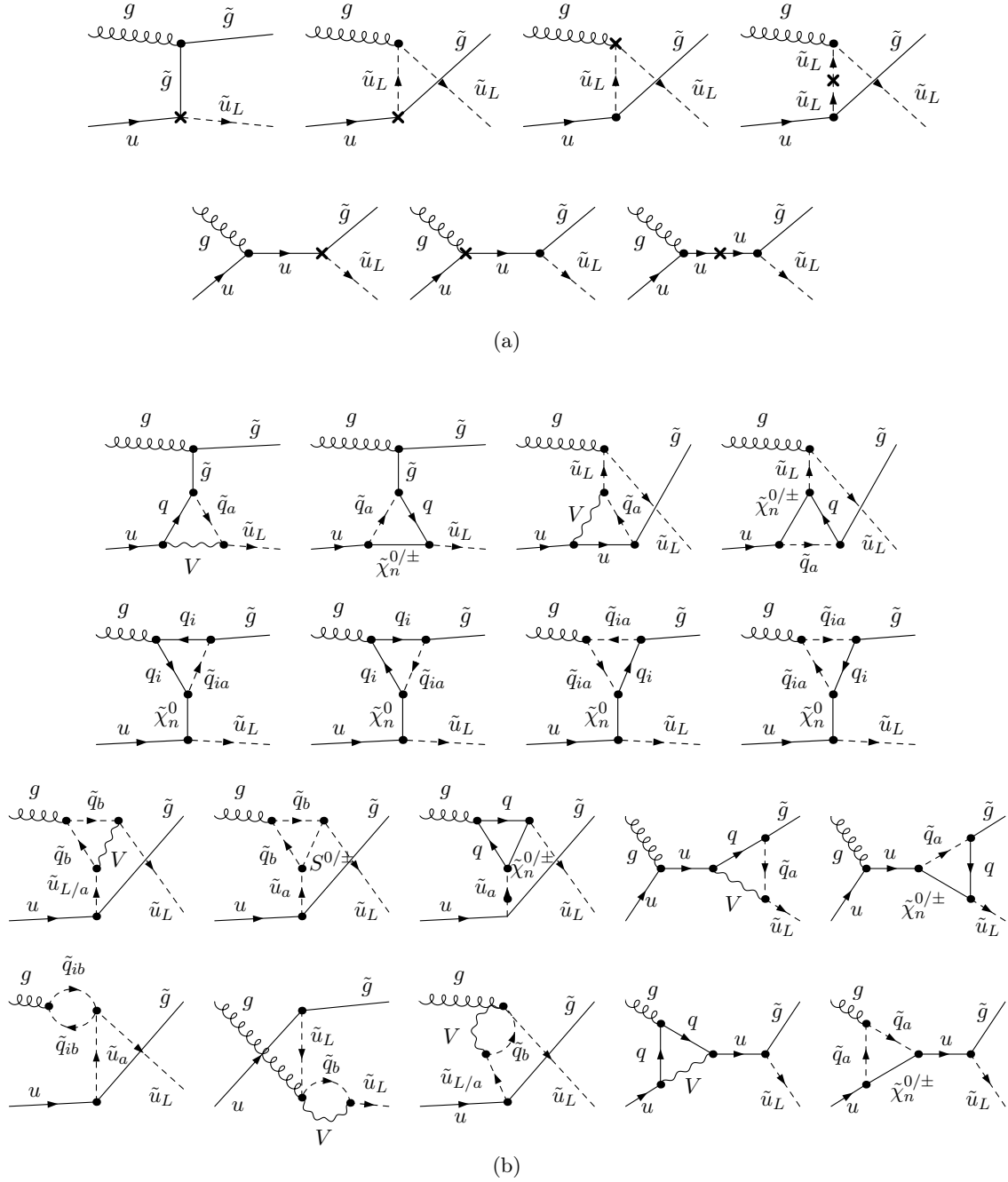
Figure 6.3.: Feynman diagrams for virtual NLO EW corrections to the process $gu \to \tilde{g}\tilde{u}_L$:
(a) counterterm and (b) vertex corrections. In case of γ exchange, q denotes an u
quark, and $\tilde{q}_a \equiv \tilde{u}_L$. For Z/W boson, $\tilde{\chi}_n^0 / \tilde{\chi}_n^{\pm}$, and $S^0 / S^{\pm}$ exchange, it is $q \equiv u/d$
and $\tilde{q}_a \equiv \tilde{u}_a / \tilde{d}_a$.
As in the following, we refer to $gu \to \tilde{g}\tilde{u}_L$ production only. The diagrams for
(s)quarks of different flavor, charge, and chirality can be obtained in complete anal-
ogy. The notation of the particles refers to Fig. 5.3.

(a)

(b)
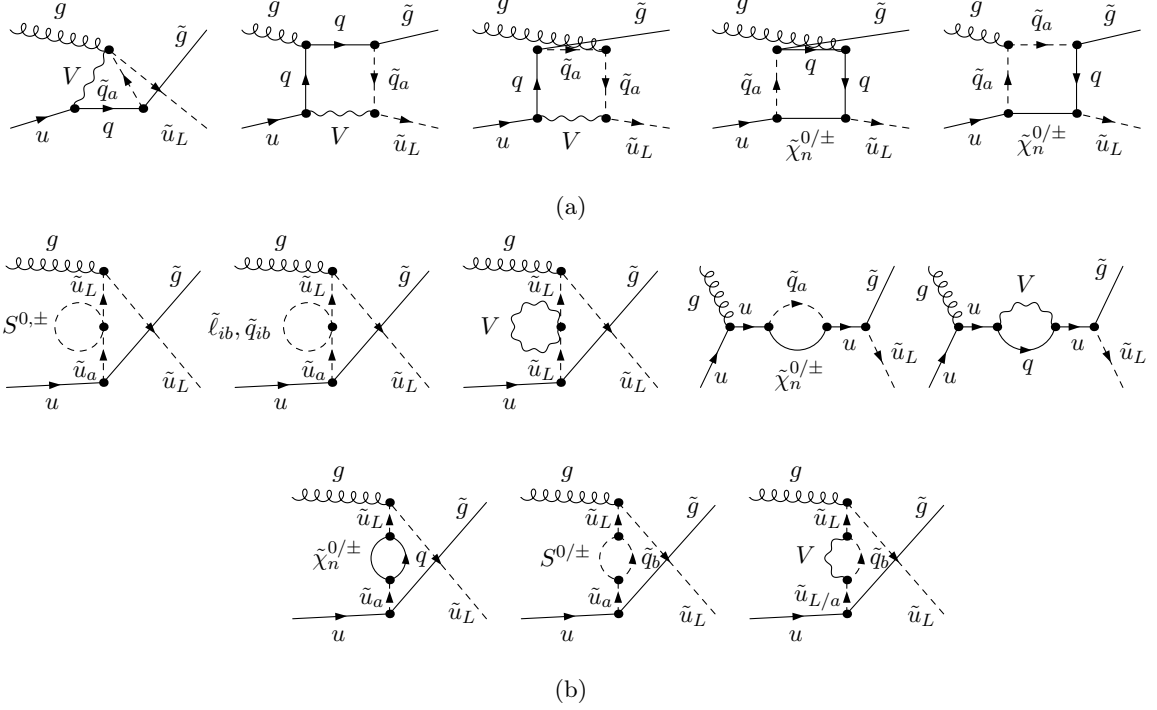
Figure 6.4.: Feynman diagrams for NLO EW (a) box diagrams and (b) self-energy corrections for the process $gu \to \tilde{g}\tilde{u}_L$. The notation is the same as in Fig. 6.3.

for a given squark isospin doublet are the masses of the two up-type squarks $\tilde{u}_{L,R}$ and the mass of the right-handed down-type squark $\tilde{d}_R$ (see Eq. (2.104)). As for the stop–anti-stop production, we do not need to renormalize the strong sector. Gluino–squark production at LO can only proceed via QCD diagrams and the NLO corrections (and thus the UV singularities) are of pure EW origin.

Parts of the diagrams are IR singular due to the exchange of soft photons. If the initial-state quarks split into a quark and a photon, singularities also arise in the collinear region. As described before, we regularize the soft singularities by a small photon mass and keep finite quark masses in the collinearly divergent integrals.

6.2.3 Real photon corrections

To compensate the IR singularities in the virtual corrections, we have to include the tree-level photon bremsstrahlung process, cf. the diagrams in Fig. 6.5,

$$g(p_1) \; q(p_2) \; \to \; \tilde{g}(p_3) \; \tilde{q}_a(p_4) \; \gamma(k). \tag{6.10}$$
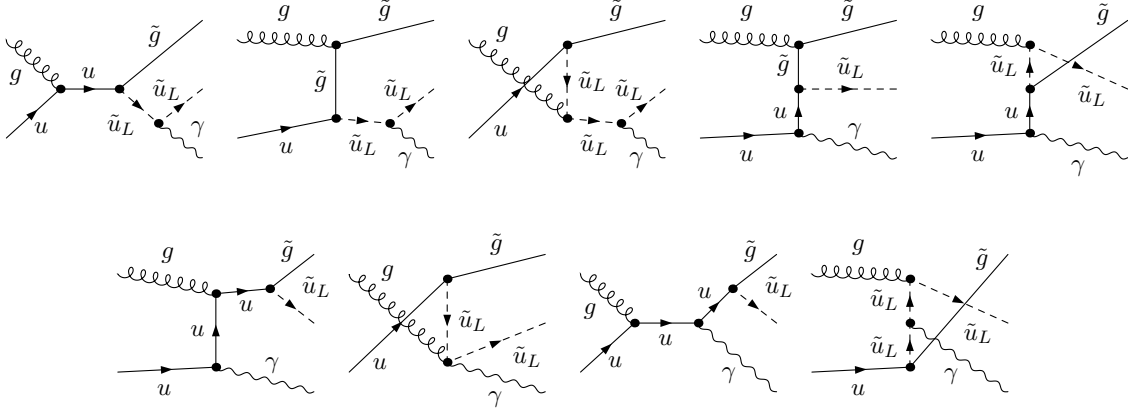
Figure 6.5.: Feynman diagrams for real photon radiation to $\tilde{g}\tilde{u}_L$ production. The first six diagrams are IR divergent, the last three are IR finite.

The integral over the photon phase space is divergent in the soft region ($E_\gamma \to 0$) and in the collinear region ($k \cdot p_2 \to 0$). We use the two-cutoff phase-space slicing method (cf. Section 4.2.1), and exclude the singular regions from the numerical integration by imposing a cut $\Delta E \equiv \delta_s \sqrt{\hat{s}}/2$ on the photon energy and a cut δ_θ on the cosine of the angle between the photon and the quark. In the singular regions the integrands can be approximated analytically as follows.

The differential cross section integrated over the soft region can be parameterized as

$$d\hat{\sigma}^{2,1}_{gq \to \tilde{g}\tilde{q}_a \gamma}(\hat{s})\Big|_{\text{soft}} = -\frac{\alpha}{\pi}\left(e_q^2\,\delta^{\text{in}}_{\text{soft}} + e_q^2\,\delta^{\text{fin}}_{\text{soft}} + e_q^2\,\delta^{\text{int}}_{\text{soft}}\right)d\hat{\sigma}^{2,0}_{gq \to \tilde{g}\tilde{q}_a}(\hat{s})\,. \tag{6.11}$$

The factors $\delta^{\text{in,fin,int}}_{\text{soft}}$ refer respectively to initial state radiation, final state radiation, or interference of initial and final state radiation. Note that there is only one charged particle in the initial and in the final state (both with fractional electric charge e_q). The soft factors are then directly given by the universal phase-space factors $\mathcal{I}_{ij}$, cf. Eq. (4.61),

$$\delta^{\text{in}}_{\text{soft}} = \mathcal{I}_{22} = \frac{1}{2}\left[\ln\delta_s^2 - \ln\frac{\lambda^2}{\hat{s}}\right] + \frac{1}{2}\ln\frac{m_q^2}{\hat{s}},$$

$$\delta^{\text{fin}}_{\text{soft}} = \mathcal{I}_{44} = \frac{1}{2}\left[\ln\delta_s^2 - \ln\frac{\lambda^2}{\hat{s}}\right] - \frac{1}{2\beta}\ln\left(\frac{1+\beta}{1-\beta}\right),$$

$$\delta^{\text{int}}_{\text{soft}} = 2\,\mathcal{I}_{24} = \left[\ln\delta_s^2 - \ln\frac{\lambda^2}{\hat{s}}\right]\ln\left(\frac{-\hat{t}_{\tilde{q}_a}}{m_q\,m_{\tilde{q}_a}}\right) - \frac{1}{4}\ln^2\frac{m_{\tilde{q}_a}^2}{\hat{s}} - \text{Li}_2\left(1 - \frac{\hat{s}}{m_q^2}\right) + \frac{1}{4}\ln^2\frac{1-\beta}{1+\beta}$$

$$+\,\text{Li}_2\left(1 + \frac{\hat{s} + m_{\tilde{q}_a}^2 - m_{\tilde{g}}^2}{2\hat{t}_{\tilde{q}_a}}(1+\beta)\right) + \text{Li}_2\left(1 + \frac{\hat{s} + m_{\tilde{q}_a}^2 - m_{\tilde{g}}^2}{2\hat{t}_{\tilde{q}_a}}(1-\beta)\right),$$

$$\tag{6.12a}$$

in terms of the squark velocity $\beta = \sqrt{1 - m_{\tilde{q}_a}^2 / (E_{\tilde{q}_a})^2}$.

In the collinear region the differential cross section reads

$$
d\hat{\sigma}^{2,1}_{gq \to \tilde{g}\tilde{q}_a \gamma}(\hat{s}) \Big|_{\text{coll.}} = \frac{\alpha}{\pi} e_q^2 \int_{z_0}^{1-\delta_s} dz \; \kappa_{\text{coll.}}(z, \hat{s}) \; d\hat{\sigma}^{2,0}_{gq \to \tilde{g}\tilde{q}_a}(z\hat{s}),
\tag{6.13}
$$

with the lower integration limit $z_0 = (m_{\tilde{g}} + m_{\tilde{q}_a})^2 / \hat{s}$ and $\kappa_{\text{coll.}}(z, \hat{s})$ as given in Eq. (4.64).

After adding virtual and real corrections, the mass singularity related to Eq. (6.13) does not cancel and has to be absorbed into the quark PDF choosing a factorization scheme, see Eq. (4.66). Using the redefined PDF, we obtain an additional $\mathcal{O}(\alpha_s^2 \alpha)$ contribution to the total hadronic cross section according to Eq. (4.69).

6.2.4 Real quark radiation

For each production process of a gluino in association with a squark $\tilde{q}_a$ of a given chirality a and flavor q, there are eleven quark–quark or quark–anti-quark induced subprocesses with an additional real quark or anti-quark in the final state:

$$
\begin{aligned}
q(p_1) \; q_i(p_2) &\to \tilde{g}(p_3) \; \tilde{q}_a(p_4) \; q_i(k) & \text{for} \quad q_i &= u, d, c, s; \\
q(p_1) \; \bar{q}_i(p_2) &\to \tilde{g}(p_3) \; \tilde{q}_a(p_4) \; \bar{q}_i(k) & \text{for} \quad q_i &= u, d, c, s; \; q_i \neq q; \\
q_i(p_1) \; \bar{q}_i(p_2) &\to \tilde{g}(p_3) \; \tilde{q}_a(p_4) \; \bar{q}(k) & \text{for} \quad q_i &= u, d, c, s.
\end{aligned}
\tag{6.14}
$$

These tree-level processes give an (soft and collinear) IR-save contribution of order $\mathcal{O}(\alpha_s^2 \alpha)$ through the interference between the EW diagrams in Fig. 6.6(a) and the QCD diagrams in Fig. 6.6(b) and between those in Fig. 6.7(a) and Fig. 6.7(b), where the example of $\tilde{g}\tilde{u}_L$ production has been considered.

In specific SUSY scenarios, internal gauginos or squarks can be on-shell. The poles are regularized introducing the particle width in the corresponding propagator. If both EW- and QCD-mediated diagrams provide intermediate on-shell squarks, the non-vanishing interference contribution corresponds to the production of a squark pair at order $\mathcal{O}(\alpha_s \alpha)$ with the subsequent decay of one of the two squarks,

$$
\begin{aligned}
q \; q_i &\to \tilde{q}_a \; \tilde{q}_i, & \tilde{q}_i &\to \tilde{g} \; q_i \,; \\
q \; \bar{q}_i &\to \tilde{q}_a \; \tilde{q}_i^*, & \tilde{q}_i^* &\to \tilde{g} \; \bar{q}_i \,; \\
q_i \; \bar{q}_i &\to \tilde{q}_a \; \tilde{q}_a^*, & \tilde{q}_a^* &\to \tilde{g} \; \bar{q} \,.
\end{aligned}
\tag{6.15}
$$

To avoid double counting, these resonating squark contributions have to be subtracted [20]. The pole term has thereby been isolated in the narrow-width approximation (see e. g. [164] for a detailed introduction to the method).

(a)

(b)
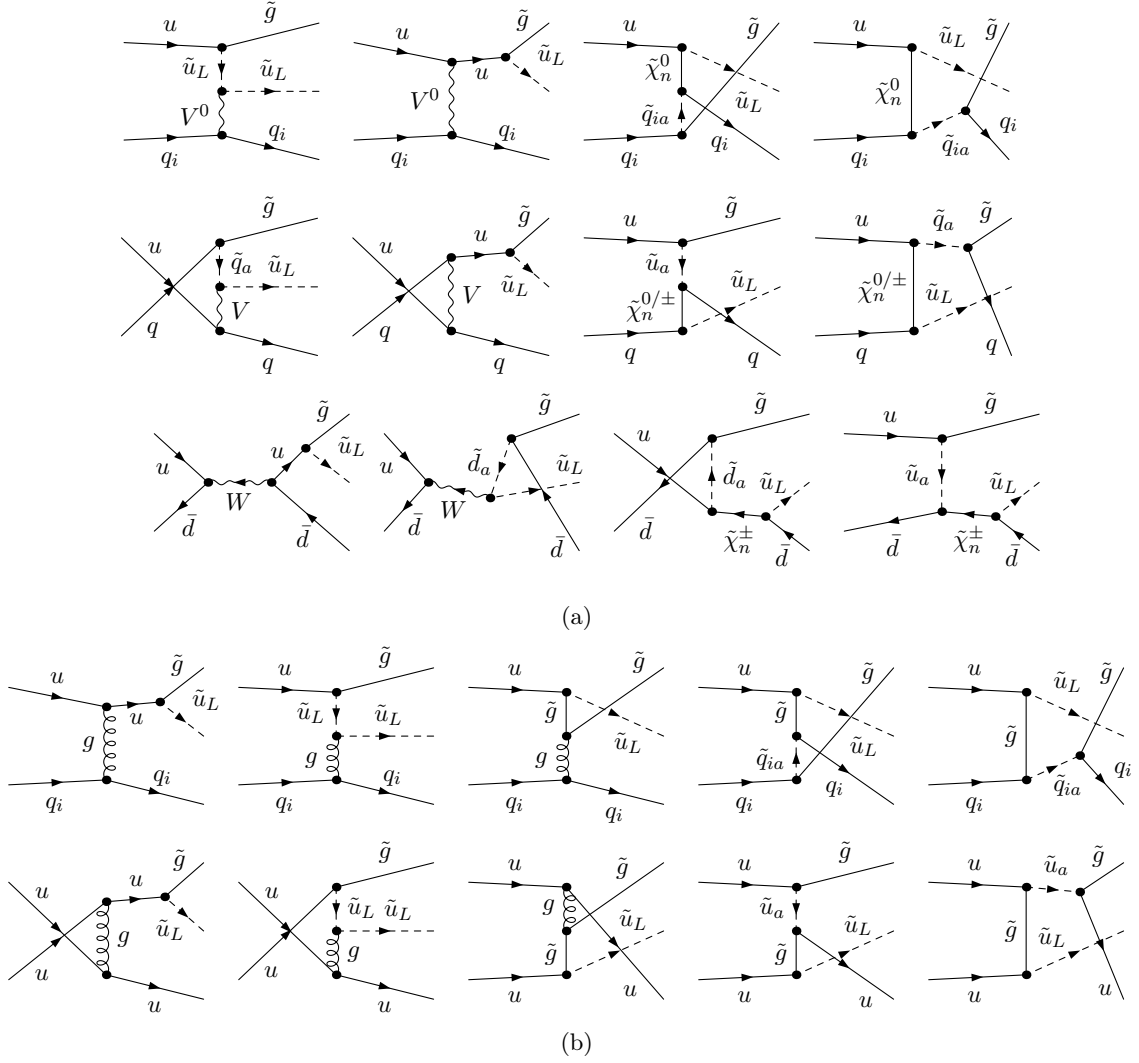
Figure 6.6.: Feynman diagrams for real quark radiation to $\tilde{g}\tilde{u}_L$ production via $uq_i \to \tilde{g}\tilde{u}_L q_i$, with $q_i = u,\ d,\ c,\ s,\ \bar{d},\ \bar{c},\ \bar{s}$. Only interference terms from (a) EW-mediated and (b) QCD-mediated diagrams contribute at $\mathcal{O}(\alpha_s^2\alpha)$. In panel (a), the diagrams of the second row contribute only for $q_i = u, d$ and the diagrams of the third row only for $q_i = \bar{d}$. In panel (b), the diagrams of the second row contribute only for $q_i = u$.

(a)

(b)
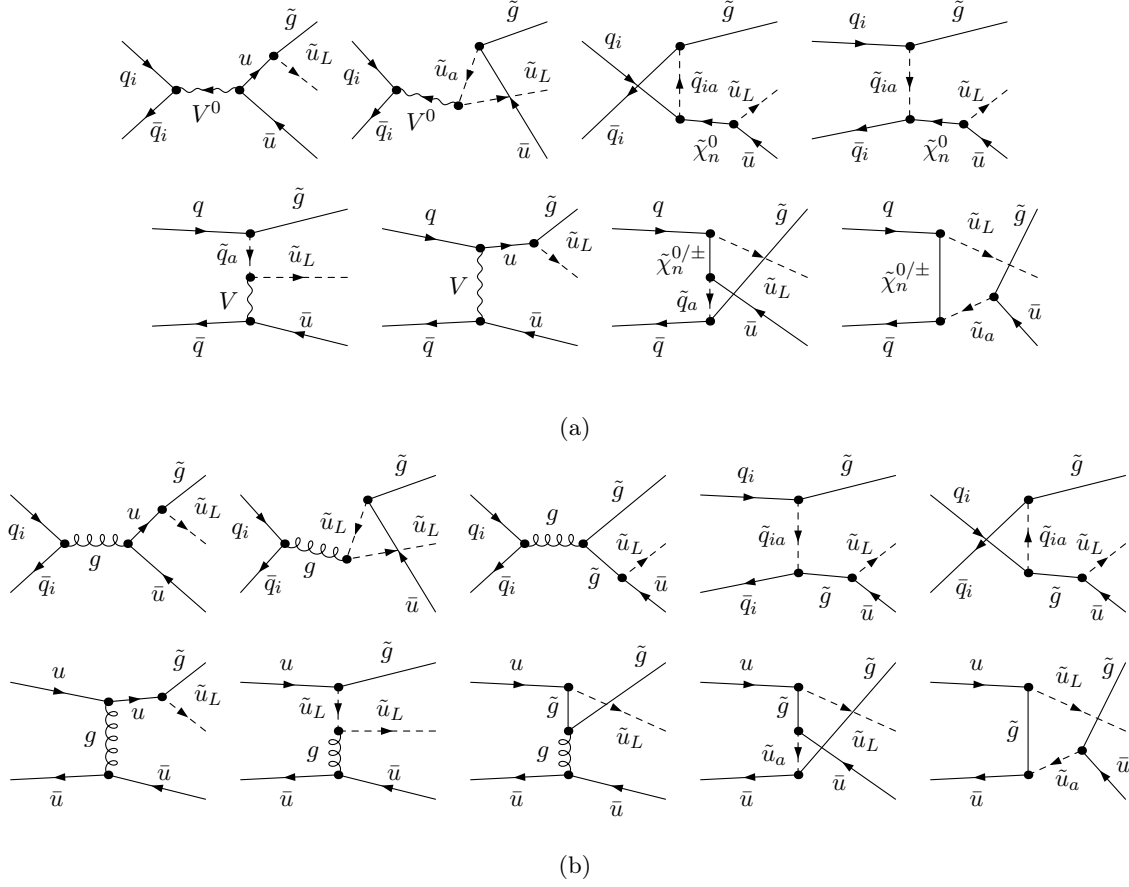
Figure 6.7.: Feynman diagrams for real quark radiation to $\tilde{g}\tilde{u}_L$ production via $q_i\bar{q}_i \to \tilde{g}\tilde{u}_L\bar{u}$, with $q_i = u$, d, c, s. Only interference terms from (a) EW-mediated and (b) QCD-mediated diagrams contribute at $\mathcal{O}(\alpha_s^2\alpha)$. In panel (a), the diagrams of the second row contribute only for $q_i = u, d$. In panel (b), the diagrams of the second row contribute only for $q_i = u$.

6.3 Numerical results

We present results both for the production of left- and right-handed, up- and down-type squarks separately and for the inclusive gluino–squark production at the LHC. We mainly stick to the conventions introduced in Section 5.3 and discuss the integrated hadronic cross section, σ, and the differential cross sections with respect to the invariant mass of the gluino–squark pair, $d\sigma/dM_{\text{inv}}$, and with respect to the transverse momentum, $(d\sigma/dp_T(\tilde{g})$, $d\sigma/dp_T(\tilde{q}_a))$ and to the pseudo rapidity, $(d\sigma/d\eta(\tilde{g})$, $d\sigma/d\eta(\tilde{q}_a))$, of one of the final-state particles, respectively. $\eta(\tilde{g})$, $\eta(\tilde{q}_a)$ are defined in the laboratory frame according to Eq. (5.31).

In particular, we refer to the three different gauge invariant, IR (soft and collinear) finite subsets of the EW contributions described in the previous section as follows. The sum

of the virtual corrections and of the $\mathcal{O}(\alpha_s^2 \alpha)$ contributions to real photon radiation will be labeled as "*gq* channel contributions". The photon-induced gluino–squark production processes as "*γq* channel contributions" and the real quark emission subprocesses will be referred to as "*qq* channel contributions". Again, we label the sum of the three channels as "the EW contribution", and the relative EW contribution is defined as in Eq. (5.33).

The input parameters are defined as described in Section 5.3.1 and Appendix B. We again consider the SPS1a' scenario [158] as a reference, unless stated otherwise. In this scenario, the on-shell masses of the light-flavor squarks and the gluino are

$$
\begin{aligned}
m_{\tilde{u}_L} &= 560.7 \text{ GeV}, \quad m_{\tilde{u}_R} = 543.3 \text{ GeV}, \qquad\qquad \text{(SPS1a')} \\
m_{\tilde{d}_L} &= 566.4 \text{ GeV}, \quad m_{\tilde{d}_R} = 539.4 \text{ GeV}, \quad m_{\tilde{g}} = 609.0 \text{ GeV},
\end{aligned}
\tag{6.16}
$$

see also Table B.1. We use the set MRST 2004 QED [107] for the parton distributions. For factorization and renormalization, a common scale has been chosen for all processes, $\mu_F = \mu_R = (m_{\tilde{g}} + m_{\tilde{u}_L})/2$. As explained, the treatment of the IR-singular bremsstrahlung is done using the phase-space slicing method. In the following numerical analysis, the two cutoff parameters are set to $\Delta E = 0.001 \sqrt{\hat{s}}$ and $\delta_\theta = 0.001$. Internal checks were performed to ensure that for these values the soft- and collinear approximations are valid and that the full result is independent on the cutoff parameters.

6.3.1 Hadronic cross sections

We show in Table 6.1 the results for the integrated hadronic cross sections for gluino–squark production at the LHC. The LO cross sections and the absolute and relative EW contributions are presented for the *gq* channel, the photon-induced *γq* subprocess, and the real-quark *qq* channel separately.

We consider left- and right-handed, up- and down-type squark production separately. Since light quark masses are negligible, squarks of the first two generations are mass degenerate and cannot be distinguished experimentally. The cross sections for e.g. $\tilde{g}\tilde{u}_L$, $\tilde{g}\tilde{c}_L$ (and by CP symmetry also for $\tilde{g}\tilde{u}_L^*$, $\tilde{g}\tilde{c}_L^*$) production differ only through the parton luminosity and we present in the following always their sum, although denoted by the dominant contribution, e.g. $\tilde{g}\tilde{u}_L$. The last line in Table 6.1 contains the inclusive ('$\tilde{g}\tilde{q}$') results.

Being of QCD origin, the LO cross section of the partonic process $gq \rightarrow \tilde{g}\tilde{q}_a$ is independent of the chirality and of the flavor of the produced squark $\tilde{q}_a$. Since all considered squark masses are of the same order, the LO hadronic cross sections for up-type squark production are about twice as large as the cross sections for down-type squark production. In contrast, the EW contributions depend strongly on the chirality of the squarks and, to a less extent, on the squark flavors. The MSSM is a chiral theory and for the production of right-handed squarks some of the one-loop and *qq* channel diagrams are suppressed by the couplings. The EW contribution to all left-handed squarks, i.e. to $\tilde{g}\tilde{u}_L$ and $\tilde{g}\tilde{d}_L$ production,

name	process	sub-process	LO $\mathcal{O}(\alpha_s^2)$	EW contr. per channel $\mathcal{O}(\alpha_s^2\alpha)$	$\mathcal{O}(\alpha_s\alpha)$	EW contr. δ
$\tilde{g}\tilde{u}_L$	$\tilde{g}\tilde{u}_L + \tilde{g}\tilde{u}_L^* + \tilde{g}\tilde{c}_L + \tilde{g}\tilde{c}_L^*$	gq	6485	-156		-2.41%
		γq			4.21	
		qq		4.88		
		incl.	**6485**	**-151**	**4.21**	**-2.27%**
$\tilde{g}\tilde{u}_R$	$\tilde{g}\tilde{u}_R + \tilde{g}\tilde{u}_R^* + \tilde{g}\tilde{c}_R + \tilde{g}\tilde{c}_R^*$	gq	6907	7.53		0.11%
		γq			4.57	
		qq		0.87		
		incl.	**6907**	**8.40**	**4.57**	**0.19%**
$\tilde{g}\tilde{d}_L$	$\tilde{g}\tilde{d}_L + \tilde{g}\tilde{d}_L^* + \tilde{g}\tilde{s}_L + \tilde{g}\tilde{s}_L^*$	gq	3524	-100		-2.85%
		γq			0.68	
		qq		3.55		
		incl.	**3524**	**-96.8**	**0.68**	**-2.73%**
$\tilde{g}\tilde{d}_R$	$\tilde{g}\tilde{d}_R + \tilde{g}\tilde{d}_R^* + \tilde{g}\tilde{s}_R + \tilde{g}\tilde{s}_R^*$	gq	3911	1.05		0.03%
		γq			0.77	
		qq		0.31		
		incl.	**3911**	**1.36**	**0.77**	**0.05%**
	inclusive $\tilde{g}\tilde{q}$		**20827**	**-238**	**10.2**	**-1.09%**

Table 6.1.: Numerical results for the integrated cross sections for gluino–squark production at the LHC within the SPS1a' scenario [158]. Shown are the leading order results, the EW contributions from the distinct channels, and the relative corrections δ, as defined in the text. All cross sections are given in femtobarn [fb].

is dominated by the (negative) gq channel contributions, and alters the LO cross section by about -2%. For right-handed squarks, i. e. for $\tilde{g}\tilde{u}_R$ and $\tilde{g}\tilde{d}_R$ production, the qq and γq channels contribute at almost the same order of magnitude as the (positive) gq channel and the full EW contribution ranges at the 0.1% level.

Summing up all processes for the inclusive $\tilde{g}\tilde{q}$ production, the gq channel corrections to right-handed squarks are negligible compared to those to left-handed squarks and the size of the relative contribution is roughly halved. The qq and γq channels give both positive contributions at the sub-percent level. The full EW contribution to gluino–squark production amounts -1% within the SPS1a' scenario.

The corresponding NLO QCD corrections have been estimated using `Prospino` [111]. They are positive and their percentage impact is independent of the flavor and the chirality of the produced squark. Using the PDF set MRST 2004 QED, the relative NLO QCD corrections at the scale $\mu_F, \mu_R = \frac{1}{2}(m_{\tilde{q}} + m_{\tilde{g}})$ amount to 28% of the LO contribution, with a remaining scale uncertainty of the total cross section at NLO QCD of the order of 10%.
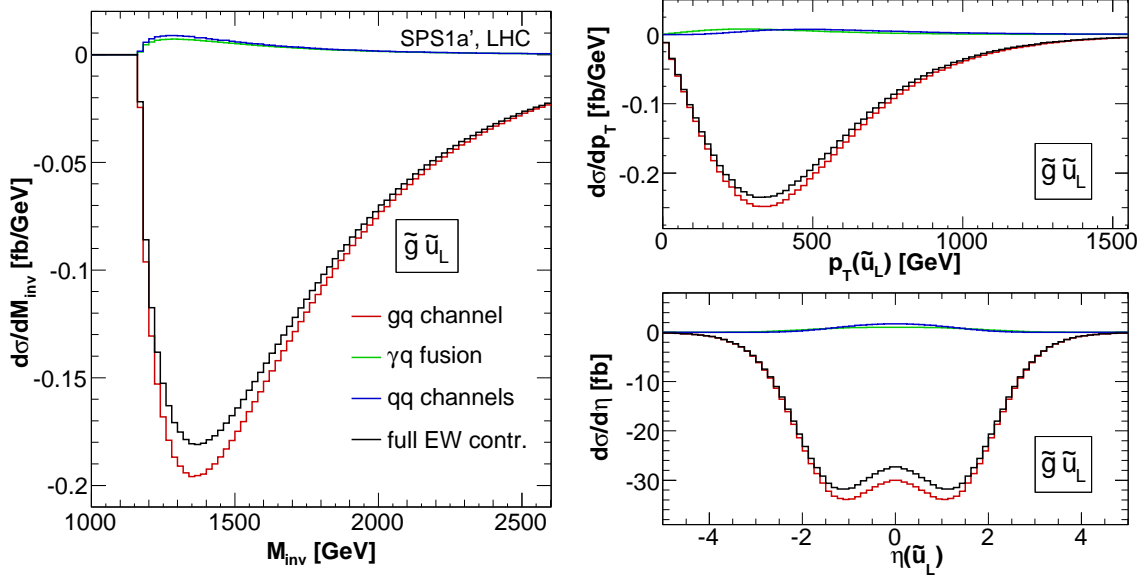
Figure 6.8.: Comparison of gq, γq, and qq channel contributions to $\tilde{g}\tilde{u}_L$ production. The total EW contribution is also given. Shown are the invariant mass distributions (left), and the transverse momentum and pseudo rapidity distributions (right panels).

6.3.2 Differential distributions

The interplay of the various EW contributions is illustrated in Figs. 6.8 and 6.9 for $\tilde{g}\tilde{u}_L$ and $\tilde{g}\tilde{u}_R$ production, respectively, where the absolute contributions from the three partonic channels are given as distributions with respect to the invariant mass $M_{\text{inv}} = (p_3 + p_4)^2$ of the squark and the gluino, as well as the transverse momentum p_T and the pseudo rapidity η of the squark. The plots for the production of a left- and right-handed down-type squark in association with a gluino are given in Figs. 6.10 and 6.11, respectively. They reveal a very similar behavior, as expected from the discussion above.

In Figs. 6.8 and 6.10, one clearly sees that for left-handed squark production the virtual and real photon corrections to the gq channel dominate the EW contributions over the whole phase space. For right-handed squark production, Figs. 6.9 and Fig. 6.11, the situation is more involved; in particular in the central region ($|\eta| < 1$) the γq channel contribution is the leading one while the other two are comparable.

Next, we consider the complete EW contribution relative to the LO result, δ. In Fig. 6.12, the distributions with respect to M_{inv}, and to p_T and η of both the squark and the gluino are given, for all four $\tilde{g}\tilde{u}_L$, $\tilde{g}\tilde{d}_L$, $\tilde{g}\tilde{u}_R$, $\tilde{g}\tilde{d}_R$ production processes. Again, the shape of the relative corrections is similar for up- and down-type squarks of the same chirality, and also the size is comparable. For right-handed squark production, the distributions are almost flat and relative EW contributions are negligible.
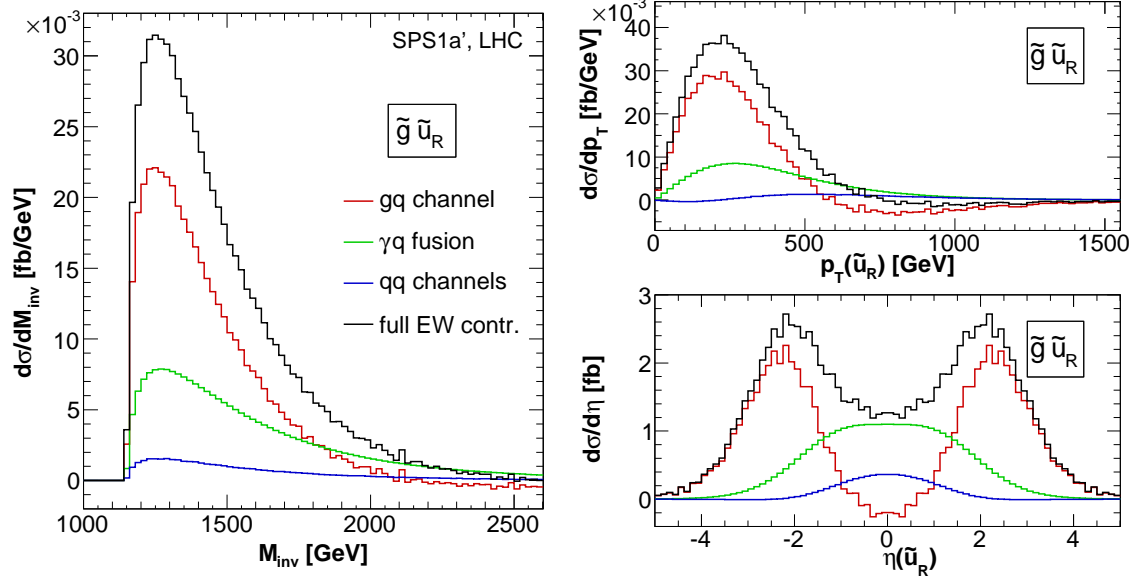
Figure 6.9.: Same as Fig. 6.8 for $\tilde{g}\tilde{u}_R$ production.
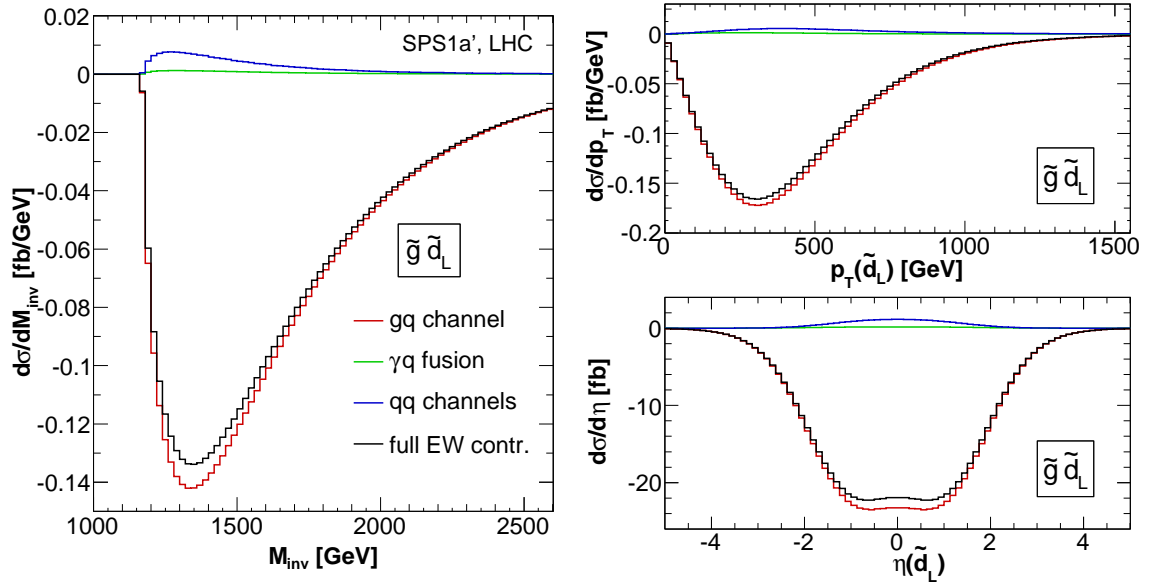
Figure 6.10.: Same as Fig. 6.8 for $\tilde{g}\tilde{d}_L$ production.
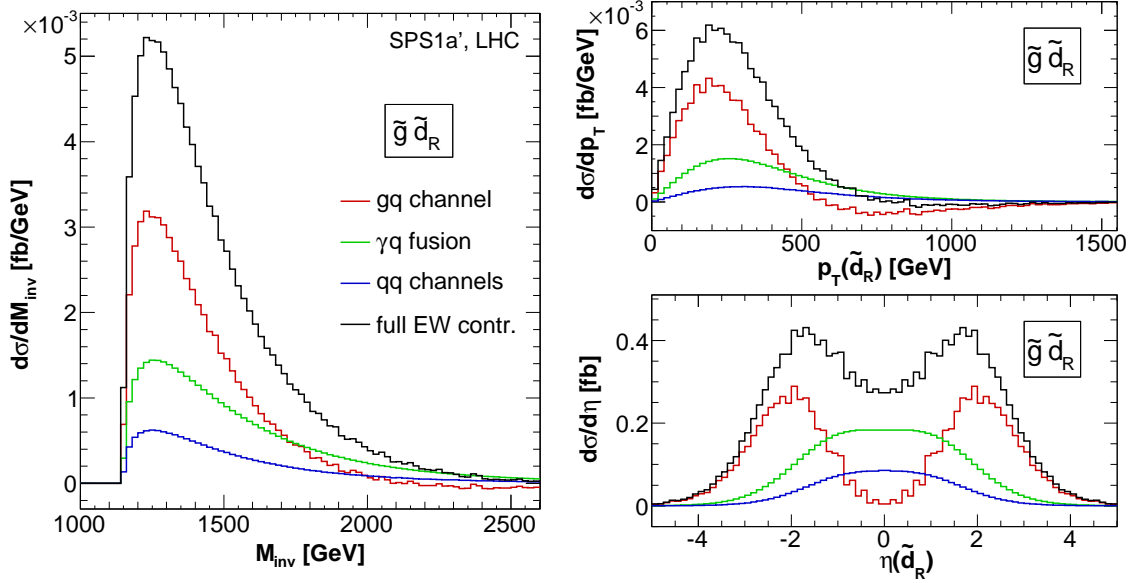
Figure 6.11.: Same as Fig. 6.8 for $\tilde{g}\tilde{d}_R$ production.

For left-handed squarks, the EW contribution in the M_{inv} distribution amounts -2% near threshold and increases up to -4% in the considered M_{inv} range ($M_{\text{inv}} < 2600$ GeV). Larger corrections arise in the p_T distribution, where the EW contributions reach the -10% level for $p_T > 1500$ GeV. The distributions with respect to $p_T(\tilde{g})$ and $p_T(\tilde{q})$ differ slightly because of the different contributions they receive from real-photon and real-quark radiation processes. In particular the qq channels affect the p_T of the squark more, reducing (in absolute size) the EW contribution in the high-p_T range.

With respect to η, the EW contribution is largest in the central region (-3% for left-handed squarks). Differences between $\eta(\tilde{g})$ and $\eta(\tilde{q})$ are related to the real emission processes, and also to the different masses of the two final particles which affect the definition of η already at the lowest order.

In order to study the behavior of the EW contribution close to the threshold we consider the distribution of the "cumulative invariant mass", defined as

$$\sigma(M_{\text{inv}}^{\text{cut}}) = \int_{m_{\tilde{g}}+m_{\tilde{q}_a}}^{M_{\text{inv}}^{\text{cut}}} \frac{d\sigma}{dM_{\text{inv}}} \, dM_{\text{inv}}. \tag{6.17}$$

In Fig. 6.13 the cumulative invariant mass including the EW contribution and the relative yield of the EW contribution is depicted for the case of $\tilde{g}\tilde{u}_L$ (left panel) and $\tilde{g}\tilde{u}_R$ (right panel) production. For left-handed squarks, the relative EW contribution increases in absolute size as $M_{\text{inv}}^{\text{cut}}$ increases. This is a clear signal that the relative yield of the EW corrections increases in high-M_{inv} region, a general feature that can also be seen in Fig. 6.12.
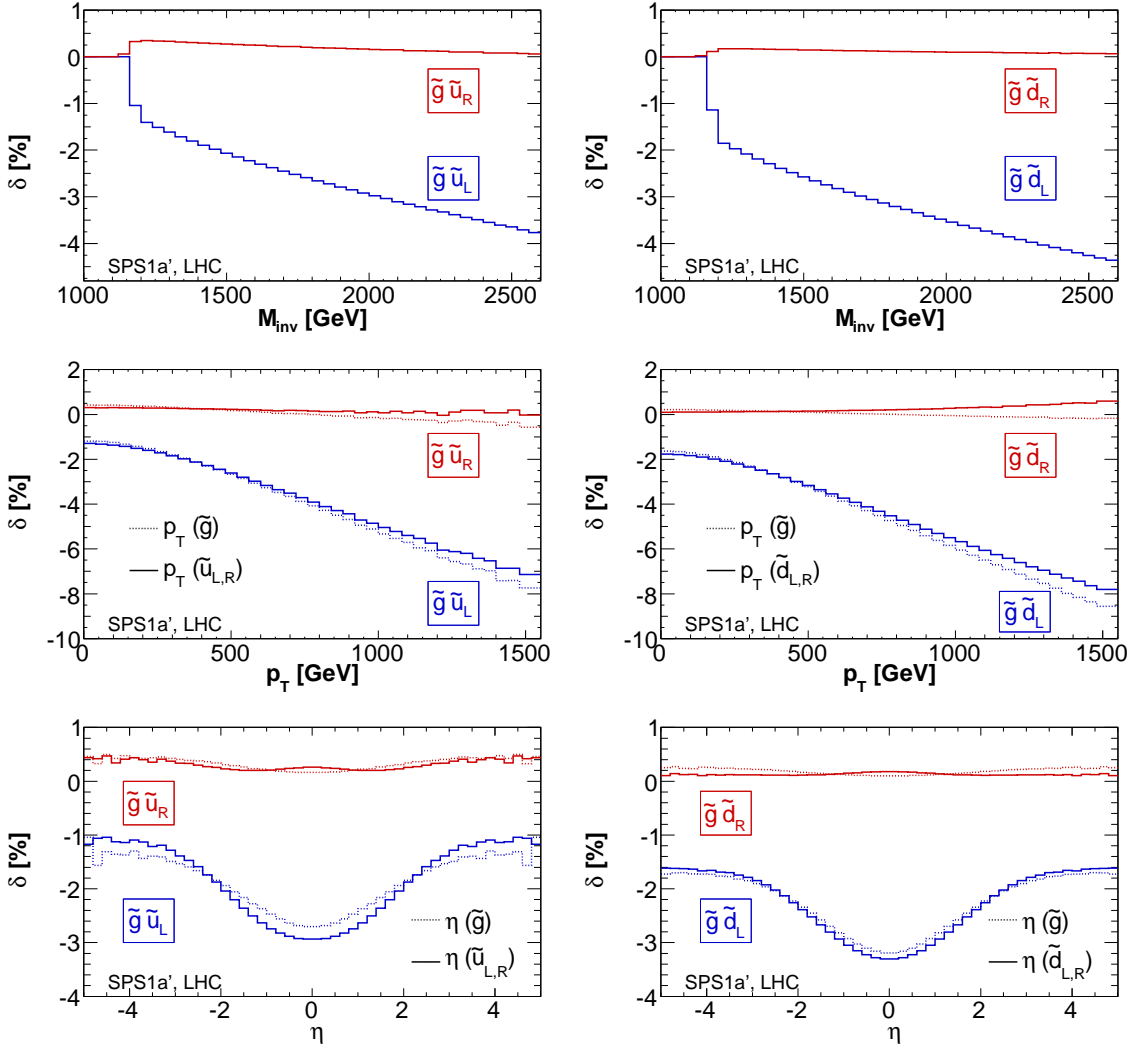
Figure 6.12.: Relative EW contribution to gluino–squark production at the LHC within the SPS1a' scenario. The left plots refer to $\tilde{g}\tilde{u}_L$ and $\tilde{g}\tilde{u}_R$ production, the right plots to $\tilde{g}\tilde{d}_L$ and $\tilde{g}\tilde{d}_R$ production. Shown are the invariant mass distribution (top panels), the distributions with respect to the transverse momentum (middle panels) of the gluino (dashed lines) and of the squark (solid lines), and the distributions with respect to the pseudo rapidity (bottom panels) of the gluino (dashed) and the squark (solid).
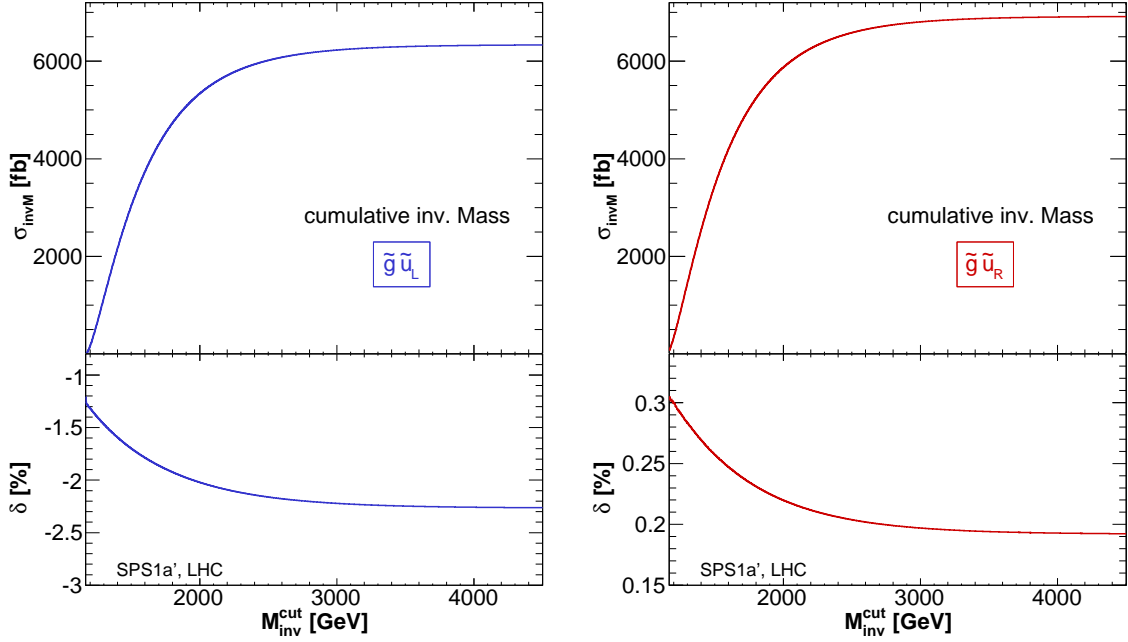
Figure 6.13.: NLO cumulative invariant mass and relative EW contribution to the same observable, cf. Eq. (6.17), for left- and right-handed up-type squark production in association with a gluino.

Interestingly, the situation is reversed for right-handed squarks. In absolute numbers, the relative EW contribution to the cumulative invariant mass decreases for increasing $M_{\text{inv}}^{\text{cut}}$: In the high-invariant mass range the virtual corrections to the gq channel receive negative contributions from Sudakov-like double and single logarithms resulting from gauge boson corrections and the positive, non-logarithmically enhanced part of the amplitude is suppressed.

In experimental analyses, usually cuts on the kinematically allowed phase space of the final state particles are applied. These include lower cuts p_T^{cut} on the transverse momenta, to focus on high-p_T jets, and cuts on the pseudo rapidity η^{cut} to restrict the scattering angles to the central region in the detector. In contrast to Section 5.3, where two explicit sets of cuts have been investigated, we now illustrate the hadronic cross sections as a function of these cuts,

$$\sigma(p_T^{\text{cut}}) = \int_{p_T^{\text{cut}}}^{\infty} \frac{d\sigma}{dp_T}\, dp_T, \qquad \sigma(\eta^{\text{cut}}) = \int_{-\eta^{\text{cut}}}^{\eta^{\text{cut}}} \frac{d\sigma}{d\eta}\, d\eta, \qquad (6.18)$$

as shown in Fig. 6.14, together with the corresponding relative corrections. Since the difference of LO and NLO results are small, only the NLO hadronic cross sections are
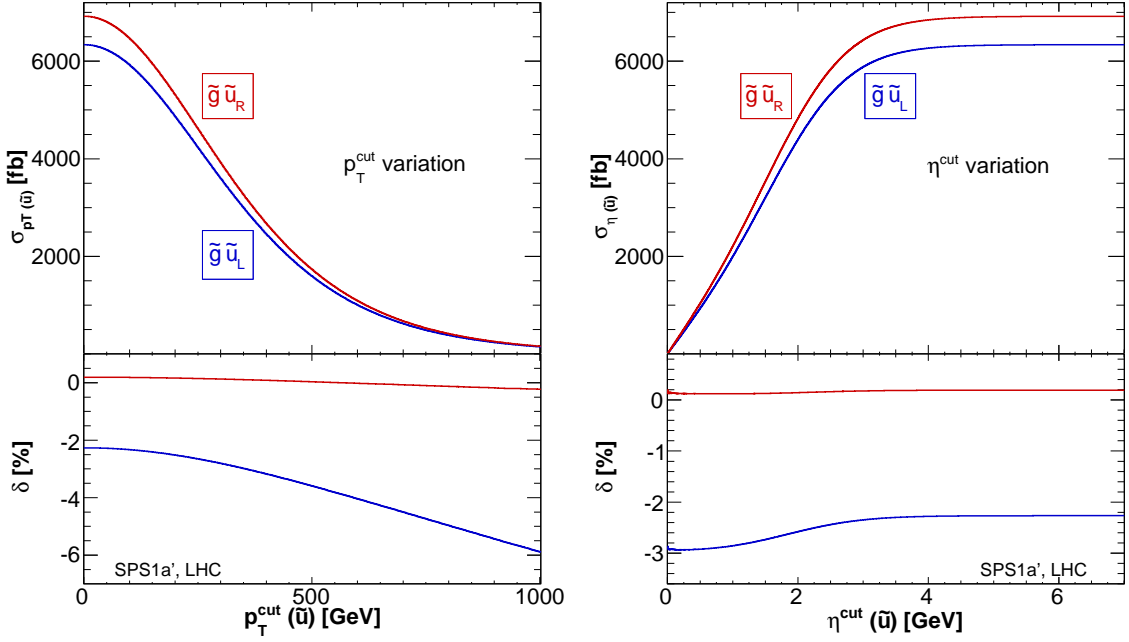
Figure 6.14.: Hadronic cross sections and relative corrections as a function of p_T^{cut} (left panels) and η^{cut} (right panels), cf. Eq. (6.18), for up-type squark production in association with a gluino. The cuts refer to p_T and η of the produced squark.

plotted. We refer to cuts on p_T and η of the (up-type) squark. As argued above, results are similar for down-type squarks and for cuts on $p_T(\tilde{g})$ or $\eta(\tilde{g})$. As we can see from the left panel of Fig. 6.14, a cut on p_T enlarges the relative EW contribution. The total cross section is about halved for $p_T^{\mathrm{cut}} = 300$ GeV. A cut on η, see right panel of Fig. 6.14, affects the EW contribution only weakly. The cross section, however, falls rapidly for $\eta^{\mathrm{cut}} < 3$.

Finally, we consider inclusive gluino–squark production and show in Fig. 6.15 the differential hadronic cross sections at NLO EW (i.e. LO plus EW contribution), together with the relative corrections δ, with respect to M_{inv} and to $p_T(\tilde{q})$. The relative EW contribution grows in the high-M_{inv} and high-p_T range, but owing to the small corrections for right-handed squarks, it remains at the percent level only.

6.3.3   Dependence on SUSY parameters

We complete our report by investigating the stability of the EW contributions against a variation of the SUSY parameters. Similarly as we proceeded for the stops in the last chapter, we first compare the results within different SPS scenarios and then study the behavior of the EW contributions as a function of the final-state particle masses.
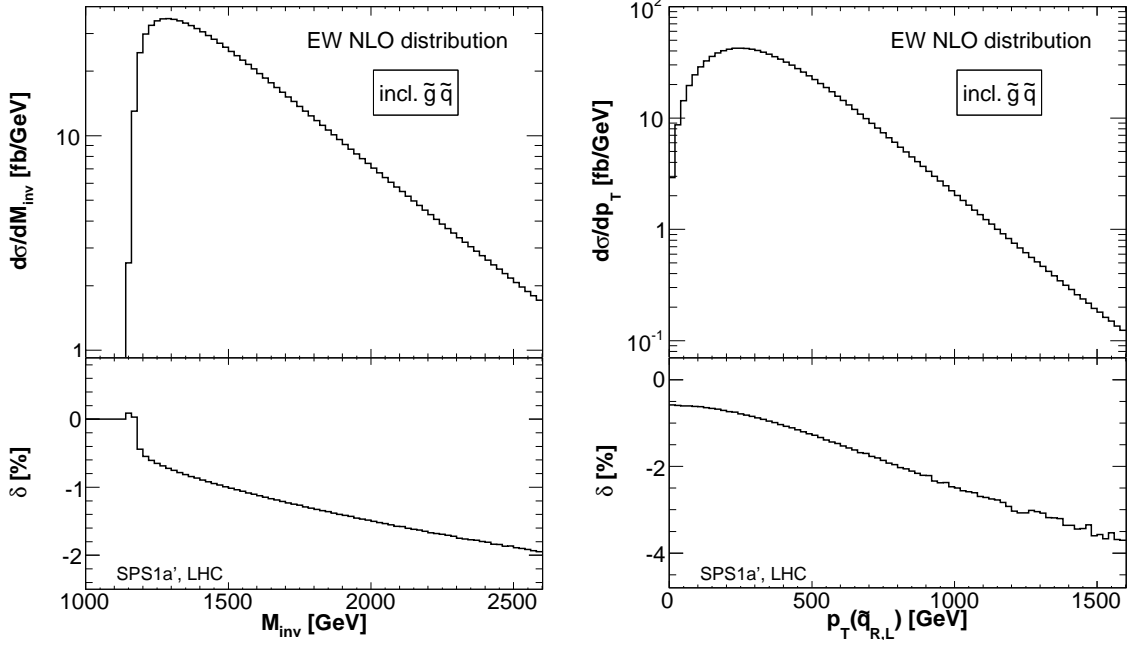
Figure 6.15.: Hadronic cross sections including the EW contribution (upper panels) and relative EW contribution (lower panels) for inclusive $\tilde{g}\tilde{q}$ production. Left panel: differential distribution with respect to the invariant mass of the squark and the gluino. Right panel: differential distribution with respect to the transverse momentum of the produced squark.

Different SUSY scenarios

We discuss gluino–squark production at the LHC within the SPS2, SPS3, SPS4, and SPS5 scenario. The input parameters for these exemplary mSUGRA scenarios are defined in Appendix B.2. In particular, the gluino and average light-flavor squark masses are the following (see also Table B.1),

$$
\begin{aligned}
m_{\tilde{g}} &= 785 \text{ GeV}, & m_{\tilde{q}} &\sim 1.5 \text{ TeV} & \text{(SPS2)}, \\
m_{\tilde{g}} &= 940 \text{ GeV}, & m_{\tilde{q}} &\sim 850 \text{ GeV} & \text{(SPS3)}, \\
m_{\tilde{g}} &= 735 \text{ GeV}, & m_{\tilde{q}} &\sim 750 \text{ GeV} & \text{(SPS4)}, \\
m_{\tilde{g}} &= 725 \text{ GeV}, & m_{\tilde{q}} &\sim 650 \text{ GeV} & \text{(SPS5)}.
\end{aligned}
\tag{6.19}
$$

Note that in the SPS2 and SPS4 scenarios, the squarks are heavier than gluinos and can go on-shell in some of the real quark radiation diagrams. Correspondingly, as described in Section 6.2.4, we subtract the resonance contributions from the qq channels within these two scenarios in order to avoid double counting in an inclusive analysis of squark and gluino final states.

The integrated hadronic cross sections and contributions from the partonic subprocesses for gluino-squark production are displayed in Table 6.2. As we have seen above, differences between up- and down-type squarks in the final state are PDF effects mainly, resulting in different integrated hadronic cross sections but comparable relative EW contributions. We thus only distinguish between left-handed and right-handed squarks and give inclusive results for $\tilde{g}\tilde{q}_L$ and $\tilde{g}\tilde{q}_R$ production.

Compared to stop–anti-stop production, we find a milder variation of the results among the various scenarios. This can be explained by the fact that the sum of the masses of the final state particles ranges in a similar order of magnitude in all the considered scenarios. Still, going from the SPS2 to SPS4 scenario, the squark masses are halved and the LO cross section raises by a factor of ten. Concerning the EW contributions, the results confirm our observations from the SPS1a' scenario: The NLO EW corrections to the gq channel are relatively large and negative for $\tilde{g}\tilde{q}_L$ production, while they are negligibly and positive in case of $\tilde{g}\tilde{q}_R$ production. The photon-induced subprocesses depend to a less extent on the helicity of the produced squark and range in the same order as the gq-channel corrections for $\tilde{g}\tilde{q}_R$ production. The qq-induced real quark bremsstrahlung processes give small contributions only, both in scenarios where squarks can and cannot become resonant. In total, the EW contributions amount to typically -3% and 0.2% for $\tilde{g}\tilde{q}_L$ and $\tilde{g}\tilde{q}_R$ production, respectively.

Dependence on squark and gluino masses

At LO, the only SUSY parameters that enter the production cross section are the masses of the final state particles. These parameters are thus crucial for the total size of the cross section and it is instructive to investigate in more detail the dependence of the cross section and the EW contribution on the squark and gluino masses. To this aim, we set the independent squark masses of the first and second generation to a common value $m(\tilde{q})$, which is varied for the 'squark mass variation' and fixed (to 500 GeV) for the 'gluino mass variation'. The fourth, dependent squark mass is computed at each SUSY point according to Eq. (B.7). All other SUSY parameters are kept at their SPS1a' values[21]. We give the results in Fig. 6.16 for the variation of the common squark mass $m(\tilde{q})$ (left) and the variation of the gluino mass (right). In the upper panels, the total cross sections including the EW contribution, and in the lower panels, the relative EW contribution are shown. Up-type squark production contributes twice as large as down-type squark production to the inclusive result. Again, this is due to the respective parton densities. The relative EW contribution to right-handed squark production can be neglected ($< 0.5\%$) for the considered parameter points. For left-handed squarks the corrections vary around -2%

---

[21]The following two plots are taken from [25], where the factorization and renormalization scale have been set to $\mu_{R,F} = 1$ TeV. All other input parameters agree with the conventions made in this thesis. The general behavior of the results presented here is expected to be unaffected by the choice of scales.

scenario	name	sub-process	LO $\mathcal{O}(\alpha_s^2)$	EW contr. per channel		EW contr. δ
				$\mathcal{O}(\alpha_s^2\alpha)$	$\mathcal{O}(\alpha_s\alpha)$	
SPS2	$\tilde{g}\tilde{q}_L$	gq	200.2	-867×10^{-2}		-4.33%
		γq			10.2×10^{-2}	
		qq		5.89×10^{-2}		
		incl.	**200.2**	$\mathbf{-861\times10^{-2}}$	$\mathbf{10.2\times10^{-2}}$	$\mathbf{-4.25\%}$
	$\tilde{g}\tilde{q}_R$	gq	203.0	5.52×10^{-2}		0.03%
		γq			10.3×10^{-2}	
		qq		2.66×10^{-2}		
		incl.	**203.0**	$\mathbf{8.19\times10^{-2}}$	$\mathbf{10.3\times10^{-2}}$	$\mathbf{0.09\%}$
SPS3	$\tilde{g}\tilde{q}_L$	gq	835.0	-29.3		-3.51%
		γq			0.69	
		qq		0.93		
		incl.	**835.0**	$\mathbf{-28.4}$	**0.69**	$\mathbf{-3.31\%}$
	$\tilde{g}\tilde{q}_R$	gq	920.6	0.68		0.07%
		γq			0.77	
		qq		0.13		
		incl.	**920.6**	**0.81**	**0.77**	$\mathbf{0.17\%}$
SPS4	$\tilde{g}\tilde{q}_L$	gq	2584	-82.3		-3.18%
		γq			1.49	
		qq		2.56		
		incl.	**2584**	$\mathbf{-79.7}$	**1.49**	$\mathbf{-3.03\%}$
	$\tilde{g}\tilde{q}_R$	gq	2758	1.66		0.06%
		γq			1.60	
		qq		0.38		
		incl.	**2758**	**2.03**	**1.60**	$\mathbf{0.13\%}$
SPS5	$\tilde{g}\tilde{q}_L$	gq	3729	-109		-2.93%
		γq			2.20	
		qq		3.64		
		incl.	**3729**	$\mathbf{-106}$	**2.20**	$\mathbf{-2.78\%}$
	$\tilde{g}\tilde{q}_R$	gq	4048	3.13		0.08%
		γq			2.42	
		qq		0.50		
		incl.	**4048**	**3.63**	**2.42**	$\mathbf{0.15\%}$

Table 6.2.: Numerical results for the integrated cross sections for gluino–squark production at the LHC within different SPS scenarios. Shown are the leading order results, the EW contributions from the distinct channels, and the relative corrections δ. All cross sections are given in femtobarn [fb].
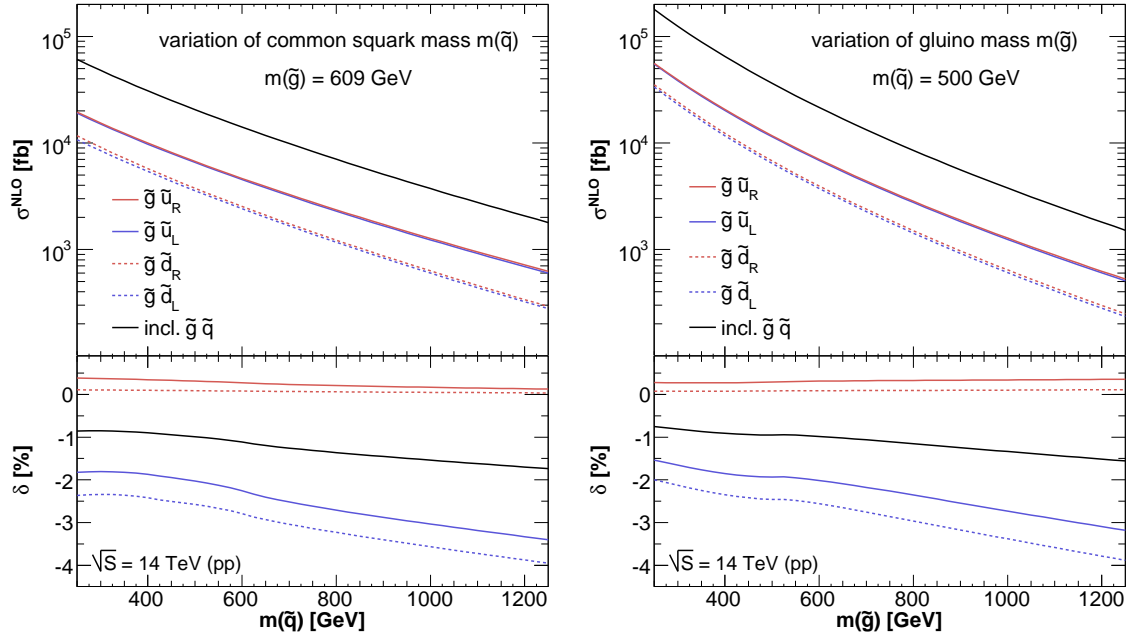
Figure 6.16.: Hadronic cross sections as a function of a common squark mass (left panel) and of the gluino mass (right panel). Masses of squarks of the first and second generation are set equal to $m(\tilde{q})$. All other parameters are fixed to their SPS1a' values. Shown are the hadronic cross sections at EW NLO and the relative EW contribution for $\tilde{g}\tilde{u}_R$, $\tilde{g}\tilde{u}_L$, $\tilde{g}\tilde{d}_R$, $\tilde{g}\tilde{d}_L$ production and inclusive $\tilde{g}\tilde{q}$ production.

for light masses ($m(\tilde{g}) < 600$ GeV) and grow up to -4% for squark and gluino masses at the TeV range. One observes a change in the slope of the relative corrections at the point $m(\tilde{g}) = m(\tilde{q})$ since the cross section depends also on the difference of the masses. If squarks are heavier than gluinos, the resonance contributions from the qq channels have been subtracted again and the final contributions from these channels are tiny.

As a consequence, the relative EW contribution to inclusive gluino–squark production depends only weekly on the final state masses and is rather small ($\approx -1\%$).

Chapter 7

Diagonal squark–squark production

We conclude our studies on the hadronic production of colored SUSY particles by considering same-sign squark–squark final states. In general, these include all combinations of left- and right-handed squarks (or anti-squarks) of any flavor. Here, we restrict ourselves to the production of diagonal squark–squark pairs,

$$
\begin{aligned}
PP &\rightarrow \tilde{q}_a \tilde{q}_a, \\
PP &\rightarrow \tilde{q}_a^* \tilde{q}_a^*,
\end{aligned}
\qquad q = u, d, c, s; \quad a = L, R. \tag{7.1}
$$

The production of squark–squark pairs of the third generation is suppressed by the vanishing top-quark and small bottom-quark density inside protons and shall not be considered here.

In the context of all squark and gluino production processes, $\tilde{q}_a \tilde{q}_a$ production is of particular interest at the proton-proton collider LHC. The partonic process proceeds at LO from qq-induced diagrams only. $\tilde{q}\tilde{q}^*$ and $\tilde{g}\tilde{g}$ production require $q\bar{q}$ or gg initial states instead, see Section 3.3. Since the final-state SUSY particles are very massive, an important contribution to the hadronic cross sections arises from the high-x region where valence-quark densities dominate over sea-quark and gluon densities. As a result, $\tilde{q}\tilde{q}$ production has generally a higher tree-level yield than $\tilde{q}\tilde{q}^*$ production and can be comparable to $\tilde{g}\tilde{g}$ production depending on the precise squark–gluino mass configuration (see also Fig. 3.6).

Concerning the EW contributions to $\tilde{q}_a \tilde{q}_a$ production, the application of our previously obtained results is nontrivial. In contrast to $\tilde{t}_a \tilde{t}_a^*$ and $\tilde{g}\tilde{q}_a$ final states, $\tilde{q}_a \tilde{q}_a$ pairs can be produced from both QCD- and EW-mediated t- and u-channel diagrams that give non-zero interferences already at tree-level. As a consequence, many types of $\mathcal{O}(\alpha_s^2 \alpha)$ interferences occur at NLO EW between amplitudes of $\mathcal{O}(\alpha_s \alpha)$ and $\mathcal{O}(\alpha_s)$ as well as between the pure-QCD one-loop amplitudes of $\mathcal{O}(\alpha_s^2)$ and the tree-level EW amplitudes of $\mathcal{O}(\alpha)$. This leads to a complicated structure of both photonic and gluonic IR singularities. Moreover a UV-finite result is obtained only if also the strong sector is renormalized.

We annotate that this project is work in progress [115]. The purpose of this chapter is thus mainly to give an overview of the characteristic features of $\tilde{q}_a \tilde{q}_a$ production and to settle the technical details related to UV and IR singularities. A complete numerical analysis still

remains to be done and is postponed to [115]. In particular, a detailed investigation of the EW contributions for inclusive squark–squark production, also including non-diagonal and mixed-flavor squark–squark pairs, is beyond the scope of this report.

The outline of this chapter is as follows. As in the previous analyses, we first recall the LO cross section (Section 7.1) and then discuss the EW contributions (Section 7.2), divided into tree-level and NLO EW contributions. We consider the various virtual and real corrections and explain the treatment of UV and IR singularities. In Section 7.3 we present a first, preliminary numerical investigation of $\tilde{q}_a\tilde{q}_a$ production at the LHC for the example of $\tilde{u}_a\tilde{u}_a$ final states.

7.1 LO cross sections and notations

The LO contribution to the production of diagonal squark–squark pairs at hadron colliders proceeds from QCD-mediated tree-level diagrams via the following partonic processes:

$$q(p_1)\,q(p_2)\ \rightarrow\ \tilde{q}_a(p_3)\,\tilde{q}_a(p_4), \qquad \bar{q}(p_1)\,\bar{q}(p_2)\ \rightarrow\ \tilde{q}_a^*(p_3)\,\tilde{q}_a^*(p_4), \tag{7.2}$$

where the initial-state quarks and the final-state squarks are of the same flavor q. The unpolarized cross sections of these two processes are related by charge conjugation and in the following we will refer to the first partonic process only. The corresponding Feynman diagrams are shown in Fig. 7.1(a) (see also Fig. 3.5(c) for the general classification among the colored SUSY particle production processes).

Again, we distinguish the light-flavor squarks by means of their chiralities, $\tilde{q}_a = \tilde{q}_L, \tilde{q}_R$ and neglect the L–R mixing. The mass of a squark $\tilde{q}_a$ is denoted by $m_{\tilde{q}_a}$. Different to $\tilde{t}_a\tilde{t}_a^*$ and $\tilde{g}\tilde{q}_a$ production, the masses of the final-state particles are not the only SUSY parameters that enter the LO result for $\tilde{q}_a\tilde{q}_a$ production. At LO, squark–squark pairs are produced via gluino-exchange diagrams, which introduce a dependence of the cross section on the gluino mass, $m_{\tilde{g}}$. For the parameterization of matrix elements and cross sections, we use again (reduced) Mandelstam variables, cf. Eq. (6.3),

$$\hat{s} = (p_1 + p_2)^2, \qquad \hat{t} = (p_1 - p_3)^2, \qquad \hat{u} = (p_1 - p_4)^2,$$
$$\hat{t}_{\tilde{q}_a/\tilde{g}} = \hat{t} - m_{\tilde{q}_a/\tilde{g}}^2, \quad \hat{u}_{\tilde{q}_a/\tilde{g}} = \hat{u} - m_{\tilde{q}_a/\tilde{g}}^2. \tag{7.3}$$

The differential partonic cross section for the process $qq \to \tilde{q}_a\tilde{q}_a$, in the usual notation with superscripts m, n specifying the order in perturbation theory $\mathcal{O}(\alpha_s^m \alpha^n)$, can then be written as

$$d\hat{\sigma}^{2,0}_{qq\to\tilde{q}_a\tilde{q}_a}(\hat{s}) = \frac{d\hat{t}}{16\pi\hat{s}^2} \overline{\sum}\left|\mathcal{M}^{1,0}_{qq\to\tilde{q}_a\tilde{q}_a}(\hat{s},\hat{t},\hat{u})\right|^2 , \tag{7.4}$$

Figure 7.1.: Feynman diagrams for diagonal squark–squark production (a) at LO via QCD-mediated amplitudes and (b) from EW-mediated t- and u-channel diagrams.

in terms of the squared spin- and color-averaged lowest-order matrix element [20],

$$
\begin{aligned}
\overline{\sum}\left|\mathcal{M}^{1,0}_{qq\to\tilde{q}_a\tilde{q}_a}\right|^2 = {} & \frac{1}{2}\cdot\frac{1}{4}\cdot\frac{1}{9}\cdot 16\pi^2\alpha_s^2\, C_F \\
& \times\left[N\left(\hat{t}_{\tilde{q}_a}\,\hat{u}_{\tilde{q}_a}-m_{\tilde{q}_a}^2\hat{s}+m_{\tilde{g}}^2\hat{s}\right)\left(\frac{1}{\hat{t}_{\tilde{g}}}+\frac{1}{\hat{u}_{\tilde{g}}}\right)-4\frac{m_{\tilde{g}}^2\,\hat{s}}{t_{\tilde{g}}\,u_{\tilde{g}}}\right].
\end{aligned}
\tag{7.5}
$$

Since we have two identical particles in the final state, an additional factor of $1/2$ has been inserted in Eq. (7.5) in order to avoid double counting in the amplitudes. The color factors are defined in Eq. (5.6), ($N = 3$, $C_F = 4/3$). The hadronic cross section results immediately after convolution with the respective parton luminosity, cf. Eq. (3.3),

$$
d\sigma^{2,0}_{PP\to\tilde{q}_a\tilde{q}_a}(S) = \int_{\tau_0}^1 d\tau\,\frac{d\mathcal{L}^{qq}_{PP}}{d\tau}\,d\hat{\sigma}^{2,0}_{qq\to\tilde{q}_a\tilde{q}_a}(\tau S).
\tag{7.6}
$$

Here, the production threshold is given by $\tau_0 = 4m_{\tilde{q}_a}^2/S$.

7.2 Electroweak contributions

We divide the EW contributions to $\tilde{q}_a\tilde{q}_a$ production into three classes, which will be described below. First, see Section 7.2.1, tree-level EW contributions of $\mathcal{O}(\alpha^2)$ and $\mathcal{O}(\alpha_s\alpha)$ arise from EW-mediated diagrams and their interference with the LO QCD-mediated diagrams. Note that $\tilde{q}_a\tilde{q}_a$ final states cannot be produced at lowest order from photon-induced channels, different to $\tilde{t}_a\tilde{t}_a^*$ and $\tilde{g}\tilde{q}_a$ production. The second class of EW contributions are the NLO EW corrections of $\mathcal{O}(\alpha_s^2\alpha)$. The sum of virtual corrections, described in Section 7.2.2, and real photon and real gluon bremsstrahlung processes (Section 7.2.3) is UV and IR finite after proper renormalization and a careful treatment of soft and collinear singularities. Third, real-quark radiation contributes at the same order of perturbation theory and has to be considered (see Section 7.2.4).

The total EW contribution to the hadronic cross section is then given by

$$
d\sigma_{PP\to\tilde{q}_a\tilde{q}_a}^{\text{EW}}(S) = \int_{\tau_0}^{1} d\tau \left\{ \frac{d\mathcal{L}_{qq}^{PP}}{d\tau} \left[d\hat{\sigma}_{qq\to\tilde{q}\tilde{q}_a}^{0,\,2}(\hat{s}) + d\hat{\sigma}_{qq\to\tilde{q}\tilde{q}_a}^{1,\,1}(\hat{s}) \right] \right.
$$
$$
+ \frac{d\mathcal{L}_{qq}^{PP}}{d\tau} \left[d\hat{\sigma}_{qq\to\tilde{q}_a\tilde{q}_a}^{2,\,1}(\hat{s}) + d\hat{\sigma}_{qq\to\tilde{q}_a\tilde{q}_a\gamma}^{2,\,1}(\hat{s}) + d\hat{\sigma}_{qq\to\tilde{q}_a\tilde{q}_a g}^{2,\,1}(\hat{s}) \right]
$$
$$
\left. + \frac{d\mathcal{L}_{gq}^{PP}}{d\tau}\ d\hat{\sigma}_{gq\to\tilde{q}_a\tilde{q}_a\bar{q}}^{2,\,1}(\hat{s}) \right\}, \tag{7.7}
$$

in terms of the respective partonic cross sections explained below and parton luminosities, cf. Eq. (3.3). It is a peculiarity of same-sign squark–squark production that there is no summation over light quark flavors in Eq. (7.7). Charge conservation enforces the initial-state quarks and the final-state squarks to have the same flavor configuration (i.e. all up-type, all down-type, or both pairs of mixed-flavor particles). Neglecting CKM quark mixing, the quarks and squarks have also to belong to the same generation.

7.2.1 Tree-level EW contributions

The qq-induced squark–squark production process,

$$
q(p_1)\ q(p_2)\ \to\ \tilde{q}_a(p_3)\ \tilde{q}_a(p_4), \tag{7.8}
$$

can also proceed from EW-mediated tree-level diagrams [113]. The structure of the diagrams is restricted by charge and $\mathcal{R}$-parity conservation. Only diagrams with t- and u-channel neutralino exchange are allowed, as depicted in Fig. 7.1(b). We denote the respective amplitude by $\mathcal{M}_{qq\to\tilde{q}_a\tilde{q}_a}^{0,\,1}$.

We obtain the differential cross section for $\tilde{q}_a\tilde{q}_a$ production at $\mathcal{O}(\alpha^2)$ as follows,

$$
d\hat{\sigma}_{qq\to\tilde{q}_a\tilde{q}_a}^{0,\,2}(\hat{s}) = \frac{d\hat{t}}{16\pi\hat{s}^2} \overline{\sum} \left| \mathcal{M}_{qq\to\tilde{q}_a\tilde{q}_a}^{0,\,1}(\hat{s},\hat{t},\hat{u}) \right|^2. \tag{7.9}
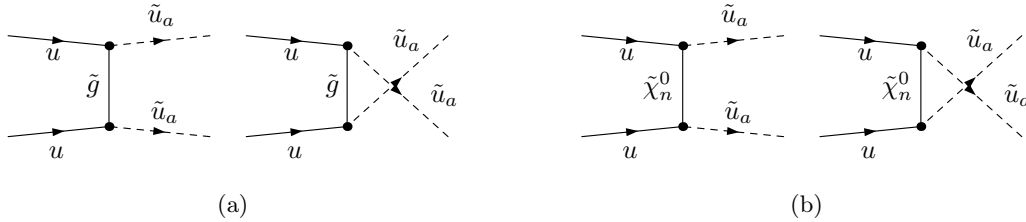$$

Furthermore, the EW-mediated and the dominant QCD-mediated tree-level amplitudes give a non-zero interference contribution of $\mathcal{O}(\alpha_s\alpha)$,

$$
d\hat{\sigma}_{qq\to\tilde{q}_a\tilde{q}_a}^{1,\,1}(\hat{s}) = \frac{d\hat{t}}{16\pi\hat{s}^2} \overline{\sum} 2\text{Re}\left\{ \left(\mathcal{M}_{qq\to\tilde{q}_a\tilde{q}_a}^{0,\,1} \right)^* \mathcal{M}_{qq\to\tilde{q}_a\tilde{q}_a}^{1,\,0} \right\}, \tag{7.10}
$$

which we include into the sum of EW contributions, Eq. (7.7).

7.2.2 Virtual corrections

As a consequence of the existence of both tree-level QCD and tree-level EW amplitudes, the $\mathcal{O}(\alpha_s^2\alpha)$ virtual corrections to $\tilde{q}_a\tilde{q}_a$ production involve EW as well as QCD loop diagrams.

(a)

(b)

(c)

Figure 7.2.: Feynman diagrams for the virtual NLO EW corrections to $uu \to \tilde{u}_a \tilde{u}_a$ that arise from tree-level QCD diagrams with EW one-loop insertions: (a) counterterm, (b) vertex correction and (c) box diagrams. These diagrams interfere with tree-level QCD diagrams to give contributions of $\mathcal{O}(\alpha_s^2 \alpha)$. The counterterm diagrams have to be computed according to the Feynman rules in Table 4.2, where the renormalization constants have to be evaluated at $\mathcal{O}(\alpha)$. Diagrams with respect to vertex corrections at the lower $u\tilde{g}\tilde{u}_a$ vertex are not shown explicitly in (b).
The notation of the particles refers to Fig. 5.3. In case of $V \equiv \gamma$ exchange, q denotes an u quark, and $\tilde{q}_a \equiv \tilde{u}_a$. For Z/W boson and $\tilde{\chi}_n^0 / \tilde{\chi}_n^{\pm}$ exchange, it is $q \equiv u/d$ and $\tilde{q}_a \equiv \tilde{u}_a / \tilde{d}_a$. The squark index b runs over the two chirality eigenstates L, R.

(a)

(b)

(c)

Figure 7.3.: Feynman diagrams for the virtual NLO EW corrections to $uu \to \tilde{u}_a \tilde{u}_a$ that arise from tree-level EW diagrams with QCD one-loop insertions: (a) counterterm, (b) vertex correction, and (c) box diagrams. These diagrams interfere with tree-level QCD diagrams to give contributions of $\mathcal{O}(\alpha_s^2 \alpha)$. The counterterm diagrams have to be computed according to the Feynman rules in Table 4.2, where the renormalization constants have to be evaluated at $\mathcal{O}(\alpha_s)$. Diagrams with respect to vertex corrections at the lower $u\tilde{\chi}_n^0 \tilde{u}_a$ vertex are not shown explicitly in (b).

More precisely, the virtual contributions to the partonic cross section at $\mathcal{O}(\alpha_s^2 \alpha)$ are given by the following interference terms,

$$d\hat{\sigma}_{qq \to \tilde{q}_a \tilde{q}_a}^{2,1}(\hat{s}) = \frac{d\hat{t}}{16\pi\hat{s}^2} \overline{\sum} 2 \operatorname{Re} \left\{ \left(\mathcal{M}_{qq \to \tilde{q}_a \tilde{q}_a}^{1,0}\right)^* \mathcal{M}_{qq \to \tilde{q}_a \tilde{q}_a}^{1,1\,(\gamma)} + \left(\mathcal{M}_{qq \to \tilde{q}_a \tilde{q}_a}^{1,0}\right)^* \mathcal{M}_{qq \to \tilde{q}_a \tilde{q}_a}^{1,1\,(g)} \right\}$$
$$+ \frac{d\hat{t}}{16\pi\hat{s}^2} \overline{\sum} 2 \operatorname{Re} \left\{ \left(\mathcal{M}_{qq \to \tilde{q}_a \tilde{q}_a}^{0,1}\right)^* \mathcal{M}_{qq \to \tilde{q}_a \tilde{q}_a}^{2,0} \right\},$$
(7.11)

where again $\mathcal{M}^{1,0}$ and $\mathcal{M}^{0,1}$ denote the tree-level QCD and EW amplitudes, respectively. The one-loop amplitude $\mathcal{M}^{1,1\,(\gamma)}$ arises from tree-level QCD diagrams with EW insertions (shown in Fig. 7.2), while $\mathcal{M}^{1,1\,(g)}$ refers to the tree-level EW diagrams with QCD insertions (see Fig. 7.3). Both one-loop amplitudes interfered with $\mathcal{M}^{1,0}$ give non-zero contributions at the right order $\mathcal{O}(\alpha_s^2 \alpha)$. At the same level of perturbation theory, the interference contribution of the tree-level EW amplitude $\mathcal{M}^{0,1}$ and the pure-QCD one-loop amplitude $\mathcal{M}^{2,0}$ arising from the diagrams shown in Fig. 7.4 has to be considered. In the diagrams containing a four-squark vertex, we take into account either the strong or the weak interaction component in order to match the classification of amplitudes and to avoid double counting.

The full set of virtual corrections is UV finite after renormalization of the theory and we have to include the proper set of counterterms. In general, we proceed as described in

Section 4.1, treating UV divergences by dimensional reduction and imposing on-shell conditions to fix the renormalization constants. The counterterm diagrams for $\tilde{q}_a \tilde{q}_a$ production can be constructed from the Feynman rules listed in Table 4.2. However, care has to be taken to evaluate the counterterms and renormalization constants at the right order.

In the first set of virtual corrections, shown in Fig. 7.2, UV singularities only arise from gluino-mediated amplitudes with weak insertions ($\mathcal{M}^{1,1\,(\gamma)}$). We have to renormalize the quark and squark sector and to include diagrams with counterterms of $\mathcal{O}(\alpha)$ for the $q\tilde{g}\tilde{q}_a$ vertex, see Fig. 7.2(a). At this order of perturbation theory, we do not need to renormalize the gluino or the strong coupling.

In the second subset of virtual corrections, Fig. 7.3, we have to deal with UV singularities arising from neutralino-mediated amplitudes with strong insertions ($\mathcal{M}^{1,1\,(g)}$). In order to obtain a UV-finite result, we include diagrams containing counterterms for the $q\tilde{\chi}^0\tilde{q}_a$ vertex, Fig. 7.3(a). The renormalization constants have to be evaluated at $\mathcal{O}(\alpha_s)$ and no renormalization of the neutralino is required. Since the gluino does not enter this subset of one-loop amplitudes, it is thus sufficient to renormalize the quark and squark sector.

The third set of virtual corrections, depicted in Fig. 7.4, refers to pure-QCD one-loop amplitudes, i.e. gluino-mediated diagrams with strong insertions ($\mathcal{M}^{2,0}$). In this case, renormalization of the quark and squark sector as well as of the gluino and the strong $q\tilde{g}\tilde{q}$ Yukawa coupling $\hat{g}_s$ is required. The renormalization constants in the appropriate counterterm diagrams, Fig. 7.4(a), have to be evaluated at $\mathcal{O}(\alpha_s)$. Note that in order to match the definition of the strong coupling constant used in the extraction of the PDFs, we define the strong coupling g_s in the $\overline{\text{MS}}$ scheme and subtract the contributions from heavy particles in the running of α_s, cf. Eq. (4.49). Accordingly, we regularize the loop integrals of this set of virtual corrections using dimensional regularization. This prescription induces a finite difference between g_s and $\hat{g}_s$ at the one-loop level and thus violates the supersymmetric relation between the two couplings. Requiring the physical amplitudes to preserve this SUSY relation, we implement an unsymmetric renormalization scheme for g_s and $\hat{g}_s$ and add a finite shift in the definition of the renormalization constant for $\hat{g}_s$ which restores SUSY, cf. Eq. (4.50) [136].

The virtual corrections also provide photonic and gluonic IR singularities, which we treat by means of mass regularization as described in Section 4.2.

In $\mathcal{M}^{1,1\,(\gamma)}$, IR singularities arise if two external particles exchange a low-energetic massless photon and if one of the massless initial-state quarks splits collinearly into a quark and a photon. In order to obtain an IR-finite result, real photon radiation at $\mathcal{O}(\alpha_s^2 \alpha)$ has to be added. In contrast in $\mathcal{M}^{1,1\,(g)}$, massless gluons running in the loops give rise to IR singularities in the soft and collinear limit. Similarly, the diagrams contributing to $\mathcal{M}^{2,0}$ suffer from gluonic IR singularities. Hence we have to include real gluon bremsstrahlung at $\mathcal{O}(\alpha_s^2 \alpha)$ in order to cancel the IR singularities. Owing to the photon-like appearance of the gluon in the respective diagrams, it is again possible to regularize these IR singularities
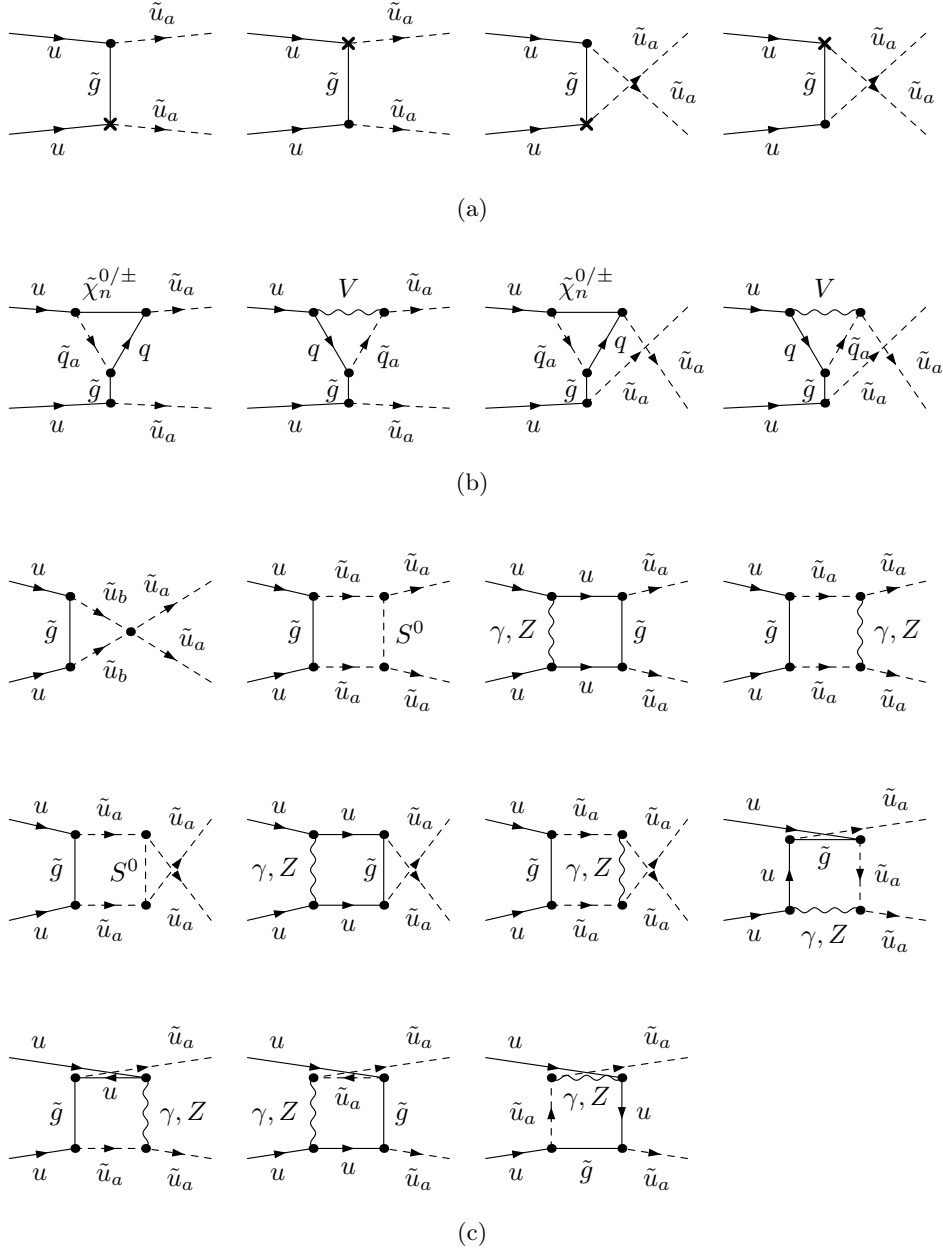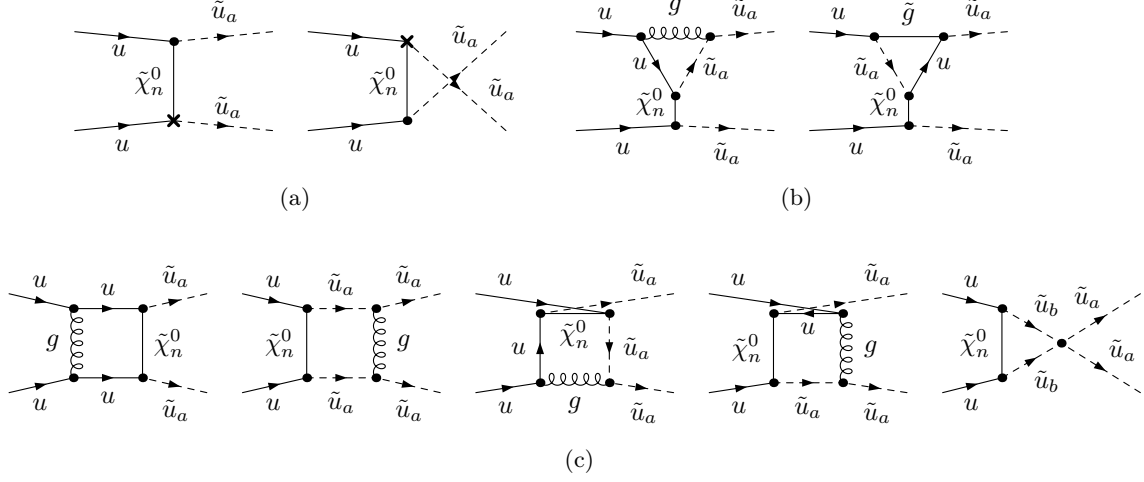
(a)

(b)

(c)

(d)
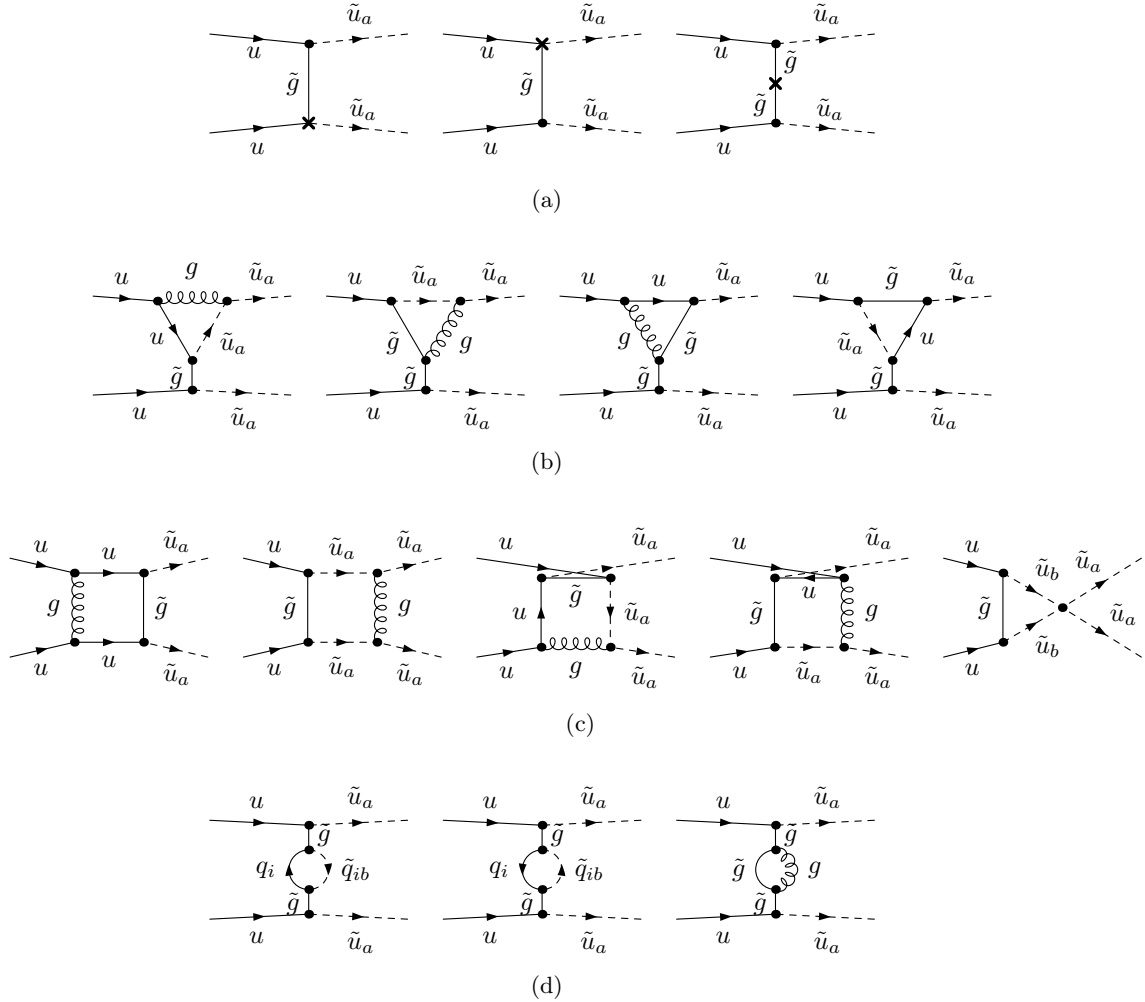
Figure 7.4.: Feynman diagrams for the virtual NLO EW corrections to $uu \to \tilde{u}_a \tilde{u}_a$ that arise from tree-level QCD diagrams with QCD one-loop insertions: (a) counterterm, (b) vertex correction, (c) box, and (d) self-energy diagrams. These diagrams interfere with tree-level EW diagrams to give contributions of $\mathcal{O}(\alpha_s^2 \alpha)$. The counterterm diagrams have to be computed according to the Feynman rules in Table 4.2, where the renormalization constants have to be evaluated at $\mathcal{O}(\alpha_s)$. Here, all diagrams with cross final states and diagrams with respect to vertex corrections at the lower $u\tilde{g}\tilde{u}_a$ vertex in (b) are not shown explicitly. Labels b and i are helicity and generation indices, respectively.
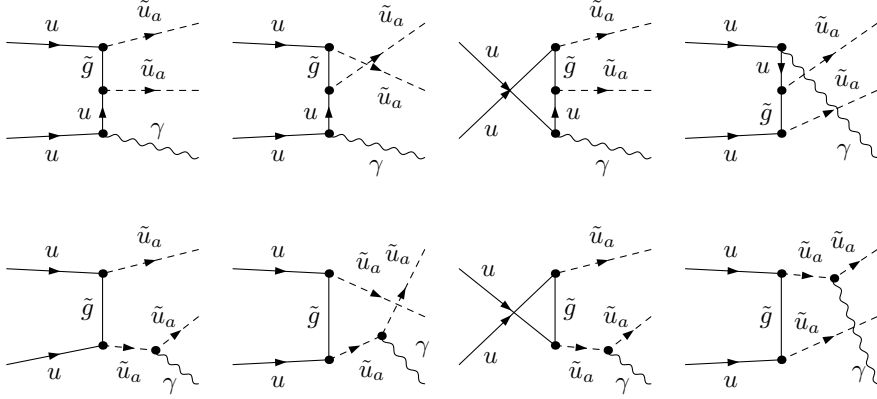
Figure 7.5.: Feynman diagrams for real photon radiation to $\tilde{u}_a\tilde{u}_a$ production. All diagrams are IR singular in the soft photon region, the diagrams in the first row also contain initial-state collinear singularities.

by a fictious gluon mass. The computation of real photon and gluon radiation processes is described in the next section.

7.2.3 Real photon and real gluon corrections

Real photon radiation

The IR singularities arising from photon exchange in the virtual corrections cancel those in the photonic bremsstrahlung process

$$q(p_1)\ q(p_2) \rightarrow \tilde{q}_a(p_3)\ \tilde{q}_a(p_4)\ \gamma(k), \tag{7.12}$$

according to the diagrams shown in Fig. 7.5. The integral over the photon phase space is divergent in the soft region ($E_\gamma \rightarrow 0$) and in the collinear region ($k{\cdot}p_1 \rightarrow 0$, $k{\cdot}p_2 \rightarrow 0$). We again apply the two-cutoff phase-space slicing method described in Section 4.2.1 and impose a cut $\Delta E \equiv \delta_s\sqrt{\hat{s}}/2$ on the photon energy and a cut δ_θ on the cosine of the angle between the photon and the quark to exclude the singular regions from the numerical integration. In the singular regions the integrands can be approximated analytically.

In the soft region, the differential cross section factorizes from the LO QCD cross section,

$$d\hat{\sigma}^{2,1}_{qq\rightarrow\tilde{q}_a\tilde{q}_a\gamma}(\hat{s})\Big|_{\text{soft}} = -\frac{\alpha}{\pi}\left(e_q^2\,\delta^{\text{in}}_{\text{soft}} + e_q^2\,\delta^{\text{fin}}_{\text{soft}} + 2e_q^2\,\delta^{\text{int}}_{\text{soft}}\right)d\hat{\sigma}^{2,0}_{qq\rightarrow\tilde{q}_a\tilde{q}_a}(\hat{s}), \tag{7.13}$$

where the soft factors $\delta^{\text{in}}_{\text{soft}}$, $\delta^{\text{fin}}_{\text{soft}}$, $\delta^{\text{intf}}_{\text{soft}}$ refer as usual to initial state, final state, and interference of initial and final state radiation, respectively, and are defined by the universal phase-space factors $\mathcal{I}_{ij}$, Eq. (4.61). For the process under consideration, the soft factors

are given by

$$\delta_{\text{soft}}^{\text{in}} = 2\,\mathcal{I}_{11} + 2\,\mathcal{I}_{12} = \left[\ln\delta_s^2 - \ln\frac{\lambda^2}{\hat{s}}\right]\left[1 - \ln\frac{m_q^2}{\hat{s}}\right] - \frac{1}{2}\ln^2\frac{m_q^2}{\hat{s}} + \ln\frac{m_q^2}{\hat{s}} - \frac{\pi^2}{3}\,,$$

$$\begin{aligned}
\delta_{\text{soft}}^{\text{fin}} = 2\,\mathcal{I}_{33} + 2\,\mathcal{I}_{34} &= \left[\ln\delta_s^2 - \ln\frac{\lambda^2}{\hat{s}}\right]\left[1 + \frac{\hat{s} - 2m_{\tilde{q}_a}^2}{\hat{s}\beta}\ln\left(\frac{1+\beta}{1-\beta}\right)\right] - \frac{1}{\beta}\ln\left(\frac{1+\beta}{1-\beta}\right) \\
&\quad - \frac{\hat{s} - 2m_{\tilde{q}_a}^2}{\hat{s}\beta}\left[2\,\text{Li}_2\left(\frac{2\beta}{1+\beta}\right) + \frac{1}{2}\ln^2\left(\frac{1+\beta}{1-\beta}\right)\right],
\end{aligned} \tag{7.14}$$

$$\begin{aligned}
\delta_{\text{soft}}^{\text{int}} = 2\,\mathcal{I}_{13} + 2\,\mathcal{I}_{23} &= \left[\ln\delta_s^2 - \ln\frac{\lambda^2}{\hat{s}}\right]\ln\left(\frac{m_q^2\,m_{\tilde{q}_a}^2}{\hat{t}_{\tilde{q}_a}\hat{t}_{\tilde{q}_a}}\right) - \frac{1}{2}\ln^2\frac{m_q^2}{\hat{s}} - 2\text{Li}_2\left(1 - \frac{\hat{s}}{m_q^2}\right) \\
&\quad + \frac{1}{2}\ln^2\left(\frac{1+\beta}{1-\beta}\right) + \text{Li}_2\left(1 + \frac{\hat{s}}{2\hat{t}_{\tilde{q}_a}}(1-\beta)\right) + \text{Li}_2\left(1 + \frac{\hat{s}}{2\hat{t}_{\tilde{q}_a}}(1+\beta)\right) \\
&\quad + \text{Li}_2\left(1 + \frac{\hat{s}}{2\hat{u}_{\tilde{q}_a}}(1-\beta)\right) + \text{Li}_2\left(1 + \frac{\hat{s}}{2\hat{u}_{\tilde{q}_a}}(1+\beta)\right).
\end{aligned}$$

The squark velocity β is given by $\beta = \sqrt{1 - 4m_{\tilde{q}_a}^2/\hat{s}}$. The contributions to the soft factors are analogous to those of stop–anti-stop production, cf. Eqs. (5.17) and (5.20). They differ in relative signs since $\tilde{q}_a\tilde{q}_a$ production involves particles only and no anti-(s)quarks do arise.

In the collinear region the differential cross section reads,

$$d\hat{\sigma}_{qq\to\tilde{q}_a\tilde{q}_a\gamma}^{2,1}(\hat{s})\Big|_{\text{coll.}} = \frac{2\alpha}{\pi}\,e_q^2\int_{z_0}^{1-\delta_s}dz\,\kappa_{\text{coll.}}(z,\hat{s})\,d\hat{\sigma}_{qq\to\tilde{q}_a\tilde{q}_a}^{2,0}(z\hat{s}), \tag{7.15}$$

with the lower integration limit $z_0 = 4m_{\tilde{q}_a}^2/\hat{s}$ and the collinear factor $\kappa_{\text{coll.}}(z,\hat{s})$ as defined in Eq. (4.64). Finally we again have to absorb the universal quark mass singularity into the quark PDF. In order to do so we redefine the quark PDF according to Eq. (4.66) choosing the *DIS* factorization scheme (we use the PDF set MRST 2004 QED in the numerical applications). The resulting additional $\mathcal{O}(\alpha_s^2\alpha)$ contribution to the total hadronic cross section Eq. (7.7) is given by

$$d\sigma_{PP\to\tilde{q}_a\tilde{q}_a\gamma}^{\text{coll.CT}}(S) = \frac{2\alpha}{\pi}\,e_q^2\int d\tau\,\frac{d\mathcal{L}_{PP}^{qq}}{d\tau}\,\kappa_{\text{soft}}^{\text{PDF}}\,d\hat{\sigma}_{q\bar{q}\to\tilde{q}_a\tilde{q}_a}^{2,0}(\hat{s}) \tag{7.16}$$

$$+ \frac{2\alpha}{\pi}\,e_q^2\int d\tau\int\frac{dx}{x}\int_x^{1-\delta_s}\frac{dz}{z}\,\kappa_{\text{coll.}}^{\text{PDF}}(z)\,d\hat{\sigma}_{q\bar{q}\to\tilde{q}_a\tilde{q}_a}^{2,0}(\hat{s})\times f_{q/P}\left(\frac{x}{z},\mu_F\right)f_{q/P}\left(\frac{\tau}{x},\mu_F\right),$$

as specified in Eq. (4.69). The collinear factors $\kappa_{\text{soft}}^{\text{PDF}}$ and $\kappa_{\text{coll.}}^{\text{PDF}}(z)$, defined in Eq. (4.67), have to be evaluated in the *DIS* factorization scheme accordingly ($\lambda_{sc} = 1$).

(a)

(b)

Figure 7.6.: Feynman diagrams for real gluon radiation to $\tilde{u}_a\tilde{u}_a$ production from (a) tree-level QCD diagrams and (b) tree-level EW diagrams. Only QCD-EW interference terms contribute at $\mathcal{O}(\alpha_s^2\alpha)$.

Real gluon radiation

Second, we have to include gluon bremsstrahlung at $\mathcal{O}(\alpha_s^2\alpha)$,

$$q(p_1)\ q(p_2) \to \tilde{q}_a(p_3)\ \tilde{q}_a(p_4)\ g(k), \tag{7.17}$$

to cancel the gluonic IR singularities in the virtual corrections. Contributions of the right order in perturbation theory originate from the interference of QCD-based and EW-based Born level diagrams, as shown in Fig. 7.6(a) and (b), respectively. IR singularities arise in the phase-space integration in the regions where the gluon becomes soft ($E_\gamma \to 0$) or collinear to one of the initial-state quarks ($k\cdot p_1 \to 0$, $k\cdot p_2 \to 0$).

As discussed in Section 4.2.2, the differential cross section integrated over the soft gluon region factorizes from lowest-order matrix elements of $\mathcal{O}(\alpha_s\alpha)$, but owing to the color

charge of the emitted gluon a rearrangement of the color structure becomes necessary. For the process Eq. (7.17), the result can be expressed as follows, cf. Eq. (4.83),

$$
d\hat{\sigma}^{2,1}_{qq\to\tilde{q}_a\tilde{q}_a g}(\hat{s})\Big|_{\text{soft}} = -\frac{\alpha_s}{\pi}\left\{\frac{4}{3}\left(2\mathcal{I}_{11}+2\mathcal{I}_{33}-4\mathcal{I}_{23}\right)\times d\hat{\sigma}^{1,1}_{qq\to\tilde{q}_a\tilde{q}_a}(\hat{s})\right.
$$
$$
+2\left(\mathcal{I}_{12}+\mathcal{I}_{34}-2\mathcal{I}_{23}\right)\times\left[d\tilde{\sigma}^{1,1}_{qq\to\tilde{q}_a\tilde{q}_a}(\hat{s})\right]_{12} \tag{7.18}
$$
$$
\left.+2\left(2\mathcal{I}_{13}-2\mathcal{I}_{23}\right)\times\left[d\tilde{\sigma}^{1,1}_{qq\to\tilde{q}_a\tilde{q}_a}(\hat{s})\right]_{13}\right\}.
$$

Here, the $\mathcal{O}(\alpha_s\alpha)$ cross sections refer to the interference contribution from the tree-level EW and QCD amplitudes, cf. Eq. (7.10), and to the color-modified EW–QCD interference contributions, cf. Eqs. (4.80) and (4.81),

$$
\left[d\tilde{\sigma}^{1,1}_{qq\to\tilde{q}_a\tilde{q}_a}(\hat{s})\right]_{ij} = \frac{1}{2\hat{s}}d\text{PS}_2\,\overline{\sum}\,2\text{Re}\left\{\left\langle\mathcal{M}^{0,1}_{qq\to\tilde{q}_a\tilde{q}_a}\Big|\mathbf{T}_i\cdot\mathbf{T}_j\Big|\mathcal{M}^{1,0}_{ab\to\tilde{q}_a\tilde{q}_a}\right\rangle\right\}, \tag{7.19}
$$

in terms of the color-charge operators $\mathbf{T}_i$, defined Eq. (4.73).

Also in the collinear region, the differential cross section factorizes into a universal collinear factor $\kappa_{\text{coll.}}$, defined in Eq. (4.64), and the EW–QCD interference contribution. In complete analogy to the case of photon radiation, Eq. (7.15), we write the result as

$$
d\hat{\sigma}^{2,1}_{qq\to\tilde{q}_a\tilde{q}g}(\hat{s})\Big|_{\text{coll.}} = \frac{2\alpha_s}{\pi}\,C_F\int_{z_0}^{1-\delta_s}dz\,\kappa_{\text{coll.}}(z,\hat{s})\,d\hat{\sigma}^{1,1}_{qq\to\tilde{q}_a\tilde{q}_a}(\hat{s}). \tag{7.20}
$$

To fully get rid of the initial-state collinear singularities we have to absorb them into the quark PDFs by a second redefinition as specified in Eq. (4.87). This yields a further $\mathcal{O}(\alpha_s^2\alpha)$ contribution to the hadronic cross section, as given in Eq. (4.88),

$$
d\sigma^{\text{coll.CT}}_{PP\to\tilde{q}_a\tilde{q}_a g}(S) = \frac{2\alpha_s}{\pi}\,C_F\int d\tau\,\frac{d\mathcal{L}^{qq}_{PP}}{d\tau}\kappa^{\text{PDF}}_{\text{soft}}\,d\hat{\sigma}^{1,1}_{qq\to\tilde{q}_a\tilde{q}_a}(\hat{s}) \tag{7.21}
$$
$$
+\frac{2\alpha_s}{\pi}\,C_F\int d\tau\int\frac{dx}{x}\int_x^{1-\delta_s}\frac{dz}{z}\,\kappa^{\text{PDF}}_{\text{coll.}}(z)\,d\hat{\sigma}^{1,1}_{qq\to\tilde{q}_a\tilde{q}_a}(\hat{s})\times f_{q/P}\left(\frac{x}{z},\mu_F\right)f_{q/P}\left(\frac{\tau}{x},\mu_F\right).
$$

Note that the redefinition of PDFs at higher orders in QCD, respectively their global fitting in the extraction from experiments, is usually performed in the $\overline{\text{MS}}$ factorization scheme. Accordingly, the collinear factors $\kappa^{\text{PDF}}_{\text{soft}}$ and $\kappa^{\text{PDF}}_{\text{coll.}}(z)$, cf. Eq. (4.67), have to be evaluated in the $\overline{\text{MS}}$ scheme (i.e. with $\lambda_{sc}=0$).

7.2.4 Real quark radiation

The complete list of real radiation processes at $\mathcal{O}(\alpha_s^2\alpha)$ also includes processes with an additional quark or anti-quark in the final state. They arise from quark-gluon initial states
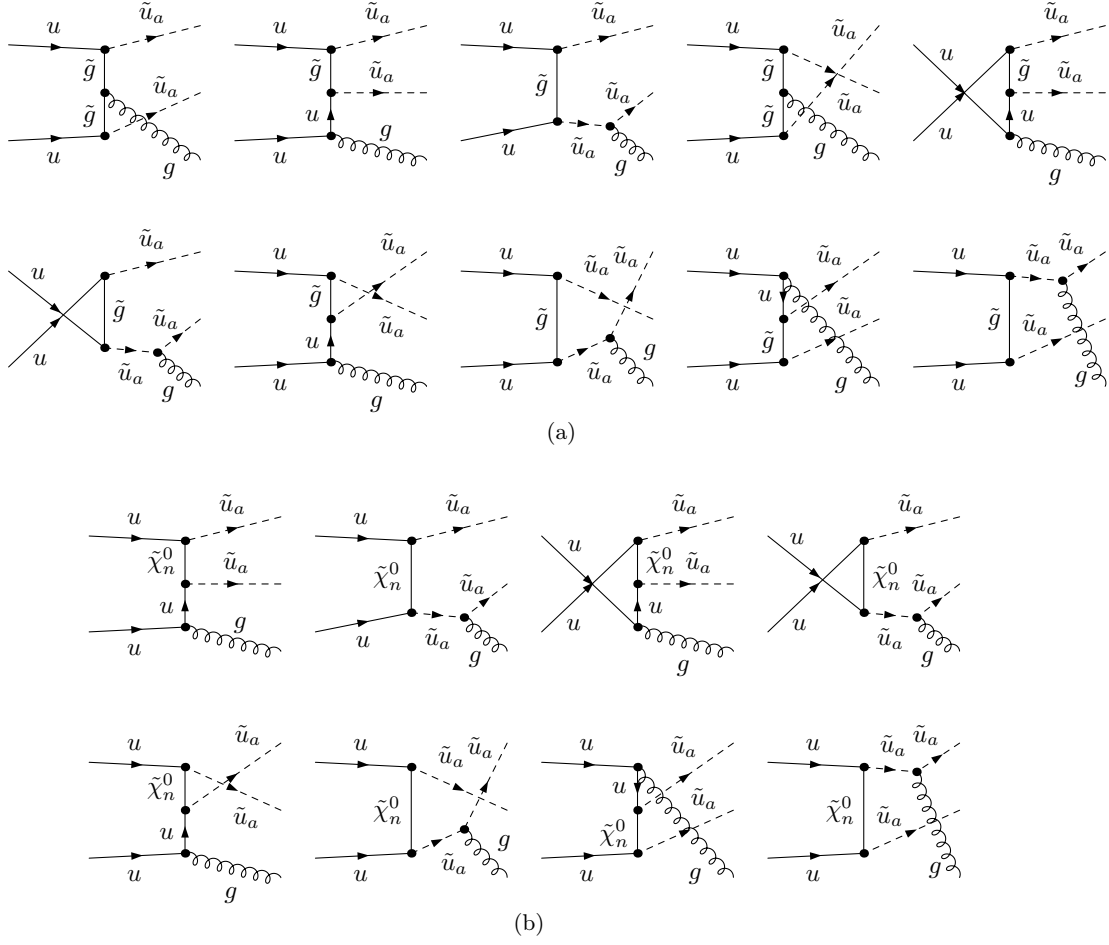
(a)

(b)
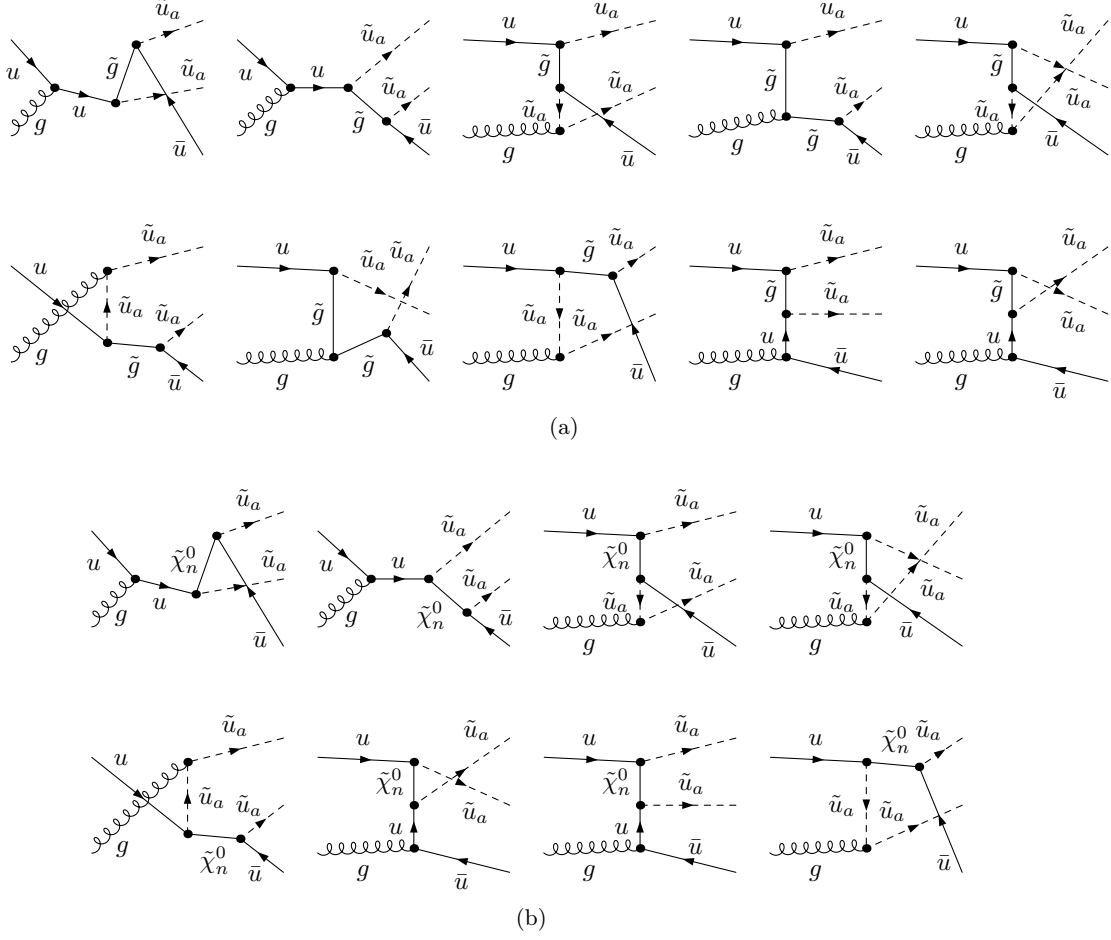
Figure 7.7.: Feynman diagrams for real quark radiation to $\tilde{u}_a \tilde{u}_a$ production from (a) tree-level QCD diagrams and (b) tree-level EW diagrams. Only the QCD–EW interference terms contribute at $\mathcal{O}(\alpha_s^2 \alpha)$.

in the interference of QCD-mediated and EW-mediated tree-level diagrams. Charge conservation enforces that a $\tilde{q}_a \tilde{q}_a$ pair can be produced in association with an real anti-quark only (while $\tilde{q}_a^* \tilde{q}_a^*$ production allows for real quark radiation). Furthermore, since the strong $q \tilde{g} \tilde{q}_a$ couplings are diagonal in flavor, the radiated quark has to have the same flavor as the produced squarks. Thus the only subprocess to be considered is

$$q(p_1)\ g(p_2) \rightarrow \tilde{q}_a(p_3)\ \tilde{q}_a(p_4)\ \bar{q}(k). \tag{7.22}$$

The resulting cross section contribution to the cross section can be written as

$$d\hat{\sigma}^{2,1}_{gq \rightarrow \tilde{q}_a \tilde{q}_a \bar{q}}(\hat{s}) = \frac{1}{2\hat{s}} \overline{\sum} 2\,\mathrm{Re}\left\{ \left(\mathcal{M}^{3/2,\,0}_{gq \rightarrow \tilde{q}_a \tilde{q}_a \bar{q}} \right)^* \mathcal{M}^{1/2,\,1}_{gq \rightarrow \tilde{q}_a \tilde{q}_a \bar{q}} \right\} d\mathrm{PS}_3, \tag{7.23}$$

in terms of the amplitude $\mathcal{M}^{3/2,\,0}$ related to the QCD-mediated diagrams depicted in Fig. 7.7(a), and the amplitude $\mathcal{M}^{1/2,\,1}$ describing the EW-mediated diagrams of Fig. 7.7(b). No summation over different quark species has to be included. Different to $\tilde{t}_a \tilde{t}_a^*$ and $\tilde{g}\tilde{q}_a$ production, there is only one real quark radiation channel contributing to the production of a pair of same-sign squarks $\tilde{q}_a$ of a given helicity and flavor.

The phase-space integration in Eq. (7.23) is finite in the region of vanishing quark energies $E_{\bar{q}} \to 0$. However quark mass singularities arise when the initial-state gluon and the final-state (anti-)quark are collinear in both the QCD- and EW-mediated diagrams ($k \cdot p_2 \to 0$). The extraction of collinear singularities can be performed in a similar way as we did before, applying a cut δ_θ on the cosine of the angle between the gluon and the quark to split off the singular region from the numerical phase-space integration. Integrated over the collinear region, the cross section reads, cf. Eq. (4.89),

$$d\hat{\sigma}^{2,\,1}_{qg \to \tilde{q}_a \tilde{q}_a \bar{q}}(\delta_\theta)\Big|_{\text{coll.}} = \frac{\alpha_s}{\pi}\, T_F \int_{z_0}^{1} dz\; \kappa^{qg}_{\text{coll.}}(z, \hat{s})\; d\hat{\sigma}^{1,\,1}_{qq \to \tilde{q}_a \tilde{q}_a}(\hat{s}), \qquad (7.24)$$

where the quark–gluon collinear factor $\kappa^{qg}_{\text{coll.}}(z, \hat{s})$ is defined in Eq. (4.91) and $T_F = 1/2$. The collinear singularities are again absorbed into the quark PDF by an appropriate redefinition at $\mathcal{O}(\alpha_s)$, specified in Eq. (4.93). This results in an additional $\mathcal{O}(\alpha_s^2 \alpha)$ contribution to the hadronic cross section as follows,

$$
\begin{aligned}
d\sigma^{\text{coll.CT}}_{PP \to \tilde{q}_a \tilde{q}_a \bar{q}} = {} & \frac{\alpha_s}{\pi}\, T_F \int d\tau \int \frac{dx}{x} \int_x^1 \frac{dz}{z}\, \frac{1}{2} P_{q \leftarrow g}(z)\, \ln\!\left(\frac{m_{\tilde{q}}^2}{\mu_F}\right)\, d\hat{\sigma}^{1,\,1}_{qq \to \tilde{q}_a \tilde{q}_a}(\hat{s}) \\
& \times \left[f_{g/P}\!\left(\frac{x}{z}, \mu_F\right) f_{q/P}\!\left(\frac{\tau}{x}, \mu_F\right) + f_{q/P}\!\left(\frac{\tau}{x}, \mu_F\right) f_{g/P}\!\left(\frac{x}{z}, \mu_F\right) \right],
\end{aligned}
\qquad (7.25)
$$

where $P_{q \leftarrow g}(z) = z^2 + (1-z)^2$ is the gluon-quark splitting function.

In specific SUSY scenarios, internal neutralinos and gluinos in the diagrams shown in Fig. 7.7 can be on-shell and the widths of the particles have to be inserted in the corresponding propagators in order to regularize the poles. Physical resonances do not occur. This is different to the case of real quark radiation in gluino–squark production processes, where internal squarks can go on-shell in both the EW- and the QCD-mediated diagrams (see Section 6.2.4).

7.3 Numerical results

We evaluate our results numerically for the important case of $\tilde{u}_a \tilde{u}_a$ production. Among the various squark–squark production processes, we expect largest hadronic cross sections at the LHC for first-generation up-type squarks $\tilde{u}_a$ since these are produced from uu initial states at tree-level and thus enhanced by purely valence-quark PDFs. Again, we present

the integrated hadronic cross section, σ, the differential cross section with respect to the invariant mass of the squark–squark pair, $d\sigma/dM_{\mathrm{inv}}$, and with respect to the average transverse momentum, $d\sigma/dp_T$, and lab-frame pseudo rapidity, $d\sigma/d\eta$, of the (indistinguishable) squarks, respectively. In analogy to the previous numerical discussions, we label the various EW contributions according to the initial-state particles of the respective subprocesses. All presented results are preliminary yet.

The input parameters are defined as described in Section 5.3.1 and Appendix B. For the SUSY parameters, we consider the SPS1a' scenario [158] as a reference. In this scenario, the on-shell masses of the first-generation up-type squarks are

$$m_{\tilde{u}_L} = 560.7 \text{ GeV}, \qquad m_{\tilde{u}_R} = 543.3 \text{ GeV}, \qquad \text{(SPS1a')} \qquad (7.26)$$

Again, we use the set MRST 2004 QED [107] for the parton distributions with identified factorization and renormalization scales $\mu_F = \mu_R = 560$ GeV ($\approx m_{\tilde{u}_L}$, chosen for later convenience if inclusive squark–squark final states are considered).

For the calculation of the IR singular bremsstrahlung contributions, three independent sets of energy and angle cutoff parameters have to be considered. The phase space of the real photon in process Eq. (7.12) and the phase space of the real gluon in process Eq. (7.17) are divided into a soft, a hard collinear, and a hard non-collinear region, respectively. The phase space of the real (anti-)quark in process Eq. (7.22) is cut into a collinear and a non-collinear part. In Fig. 7.8 we briefly investigate the stability of the phase-space slicing method. Shown are the partial hadronic cross section contributions (virtual corrections plus soft and collinear parts and the hard, non-collinear part) and the sum of all contributions as a function of the angle cutoff δ_θ (and $\Delta E = 0.001\sqrt{\hat{s}}$ fixed). We refer to the photonic corrections of $\mathcal{O}(\alpha_s^2\alpha)$ (upper plots, cf. Fig. 7.2) and gluonic corrections of $\mathcal{O}(\alpha_s^2\alpha)$ (lower plots, cf. Figs. 7.3 and 7.4), only. In both cases, the summed result does not depend on the parameters when they are chosen small enough, and the method is applicable. However the choice of appropriate cutoff parameters in case of gluonic corrections has to be done with care. In the small cutoff region, close to the singular regions in phase space, the separate contributions are huge and cancel down to the percentage level. Thus one looses roughly two digits in precision and the relative errors of the summed result are large in comparison to the case of photonic corrections. The situation is similar in case of variation of the energy cutoff parameter and not shown explicitly, here. The numerical integration over singular regions is avoided by the alternative dipole subtraction method (see Section 4.2.1), resulting in an improvement in the integration errors of typically one order of magnitude [145]. For a future precision analysis on squark–squark production, we strongly suggest to implement the dipole subtraction method and to perform careful cross checks on the reliability of the results obtained from both methods.

In the following numerical analysis, the energy cut off parameters are set to $\Delta E = 0.001\sqrt{\hat{s}}$ and the cuts on the (cosine of) the angle are set to $\delta_\theta = 0.0001$.
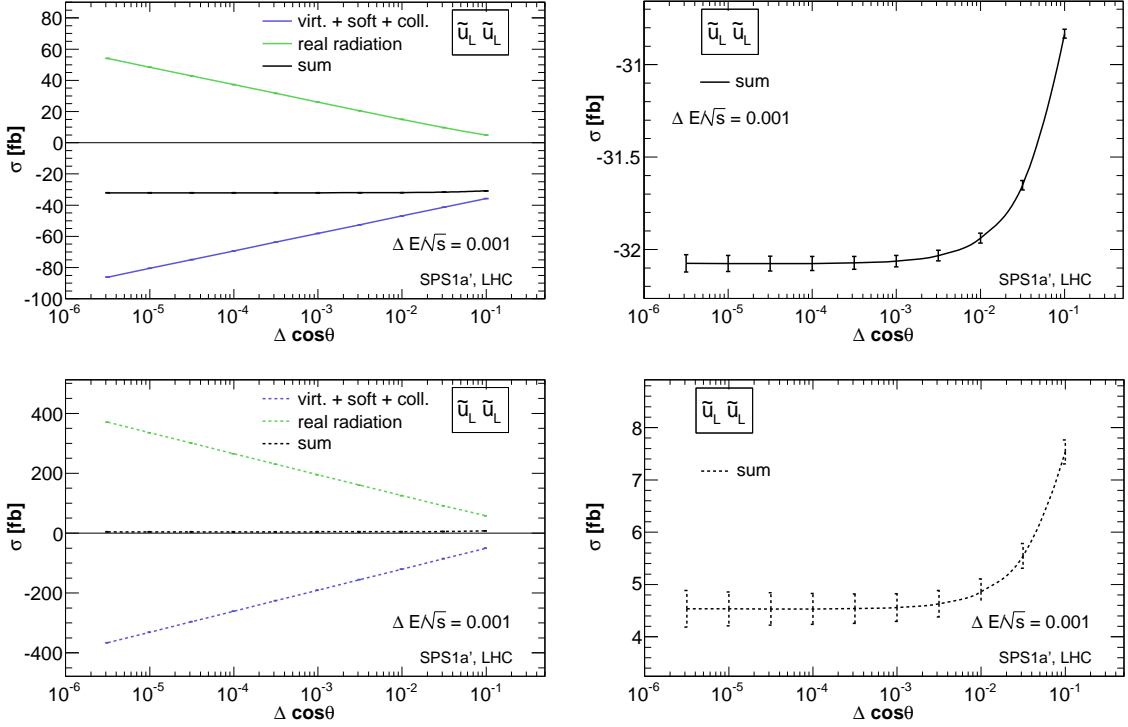
Figure 7.8.: Dependence of hadronic cross section contributions on the cutoff parameter δ_θ ($\Delta E = 0.001\sqrt{\hat{s}}$ fixed), for the photonic corrections of $\mathcal{O}(\alpha_s^2\alpha)$ (upper plots, cf. Fig. 7.2), and for the gluonic corrections of $\mathcal{O}(\alpha_s^2\alpha)$ (lower plots, cf. Figs. 7.3 and 7.4), to $\tilde{u}_L\tilde{u}_L$ production at the LHC within the SPS1a' scenario. Left panels: Shown are the partial contributions (virtual corrections plus soft and collinear parts and the hard, non-collinear part) and the sum of all contributions. Right panels: Sum of all contributions. The error bars represent integration uncertainties.

7.3.1 Hadronic cross sections

The results for the integrated hadronic cross sections for $\tilde{u}_L\tilde{u}_L$ and $\tilde{u}_R\tilde{u}_R$ production at the LHC are displayed in Table 7.1. The LO cross sections and the various absolute and relative EW contributions are presented. For the quark–quark induced (uu) channel, we give the relative impact of the IR-finite sum of $\mathcal{O}(\alpha_s^2\alpha)$ NLO EW corrections and the $\mathcal{O}(\alpha_s\alpha + \alpha^2)$ tree-level EW channels, separately. The gluon-quark induced (gu) real quark radiation process contributes at NLO only.

In case of left-handed squark–squark production, the uu-induced NLO EW corrections are relatively large and alter the LO cross section by about -6%. Moreover, the tree-level pure-EW and EW–QCD processes give important contributions (20%). The real quark radiation is suppressed by one order of magnitude in comparison. As expected from our previous investigations on $\tilde{t}_a\tilde{t}_a^*$ and $\tilde{g}\tilde{q}_a$ production, the impact of the EW contributions for

process	sub-process	LO $\mathcal{O}(\alpha_s^2)$	EW contr. per channel			EW contr. δ
			$\mathcal{O}(\alpha_s^2\alpha)$	$\mathcal{O}(\alpha_s\alpha)$	$\mathcal{O}(\alpha^2)$	
$\tilde{\mathbf{u}}_\mathbf{L}\tilde{\mathbf{u}}_\mathbf{L}$	uu	479	-27.5			-5.75%
				78.5	13.5	19.9%
	gu		-2.32			
	incl.	**479**	$\mathbf{-29.8}$	**78.5**	**13.5**	$\mathbf{13.0\%}$
$\tilde{\mathbf{u}}_\mathbf{R}\tilde{\mathbf{u}}_\mathbf{R}$	uu	528	-3.55			-0.67%
				26.3	1.72	5.30%
	gu		-0.77			
	incl.	**528**	$\mathbf{-4.32}$	**26.3**	**1.72**	$\mathbf{4.63\%}$
inclusive $\tilde{\mathbf{u}}_\mathbf{a}\tilde{\mathbf{u}}_\mathbf{a}$		**1006**	$\mathbf{-34.2}$	**105**	**15.2**	$\mathbf{8.52\%}$

Table 7.1.: Numerical results for the integrated cross sections for $\tilde{u}_L\tilde{u}_L$ and $\tilde{u}_R\tilde{u}_R$ production at the LHC within the SPS1a' scenario [158]. Shown are the leading order results, the EW contributions from the distinct channels, and the corrections relative to the LO result, δ. All cross sections are given in femtobarn [fb].

right-handed $\tilde{u}_R\tilde{u}_R$ production is less pronounced. The $\mathcal{O}(\alpha_s^2\alpha)$ corrections range below the percent level. Summing up tree-level and one-loop EW contributions, the LO cross section for inclusive $\tilde{u}_L\tilde{u}_L$ and $\tilde{u}_R\tilde{u}_R$ production increases by 8.5%.

We recall that only $\tilde{u}_a\tilde{u}_a$ final states are considered. Cross section for the charge conjugated process of $\tilde{u}_a^*\tilde{u}_a^*$ production and for second-generation $\tilde{c}_a\tilde{c}_a$, $\tilde{c}_a^*\tilde{c}_a^*$ final states differ only in the PDF factor and can easily be included. At the LHC however, these are strongly suppressed by the sea-quark parton densities (the LO production channels proceed from $\bar{u}\bar{u}$, cc, and $\bar{c}\bar{c}$ initial states, respectively) and negligible hadronic contributions are expected. This is different to squark–anti-squark production [26], where the dependence of the EW contributions on the flavor and generation of the produced squarks is much more involved.

7.3.2 Differential distributions

We further investigate the interplay of the EW contributions in Fig. 7.9. We only consider $\tilde{u}_L\tilde{u}_L$ production, since the EW corrections are suppressed for right-handed squarks. Shown are the absolute EW contributions as distributions with respect to M_{inv}, p_T, y, or η. We refer to the tree-level EW subprocesses of $\mathcal{O}(\alpha_s\alpha + \alpha^2)$, the $\mathcal{O}(\alpha_s^2\alpha)$ corrections divided into the two gauge-invariant subsets of photonic and gluonic corrections, as well as the gu-induced EW contributions due to real quark radiation. Owing to the alternating signs,
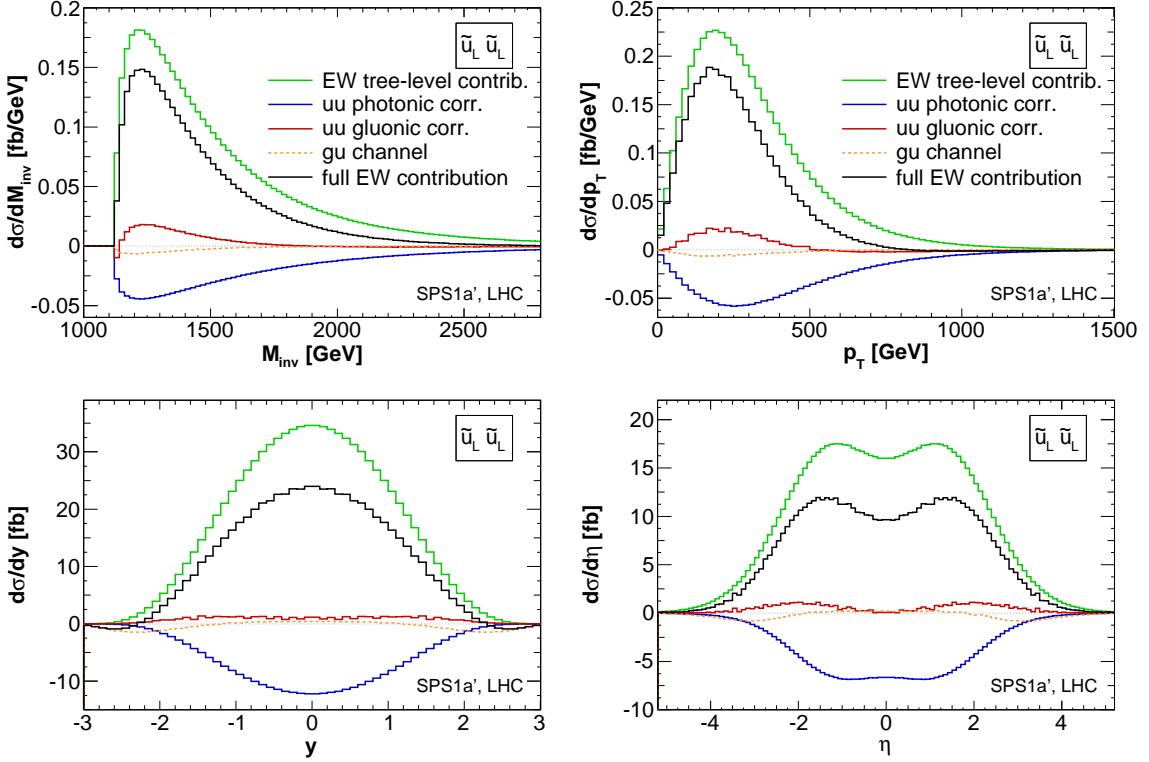
Figure 7.9.: Comparison of absolute EW contributions from the various channels to $\tilde{u}_L \tilde{u}_L^*$ production, as distributions of the invariant mass of the squark–squark pair, the transverse momentum p_T, the rapidity y, and the pseudo-rapidity η of one of the squarks (from upper left to lower right). y and η are given in the laboratory frame.

compensations occur in particular between the photonic and gluonic NLO EW corrections. The sum of EW contributions is dominated by the tree-level EW processes over largest regions in phase-space.

Focussing on the $\mathcal{O}(\alpha_s^2 \alpha)$ EW corrections to the uu channel, we consider in Fig. 7.10 the hadronic contributions of the two gauge-invariant subsets of photonic and gluonic corrections relative to the LO Born cross section. The numerical impact of the EW contributions on the invariant mass distribution is moderate, ranging at the percent level. In the p_T distributions, both the photonic and gluonic EW corrections grow for large values of p_T and reach the -10% and -20% level, respectively.

Finally we present the differential hadronic cross section at NLO EW, including all EW contributions up to $\mathcal{O}(\alpha_s^2 \alpha)$ (i. e. including the tree-level EW subprocesses), as a function of the invariant mass and p_T in Fig. 7.11. In the respective lower panels, the EW contributions relative to the LO result are given. Close to the threshold, in particular the tree-level EW processes alter the LO prediction considerably ($\approx 20\%$). In the high-M_{inv} and high-p_T regions, the EW contributions turn negative and are dominated by the $\mathcal{O}(\alpha_s^2 \alpha)$ corrections.
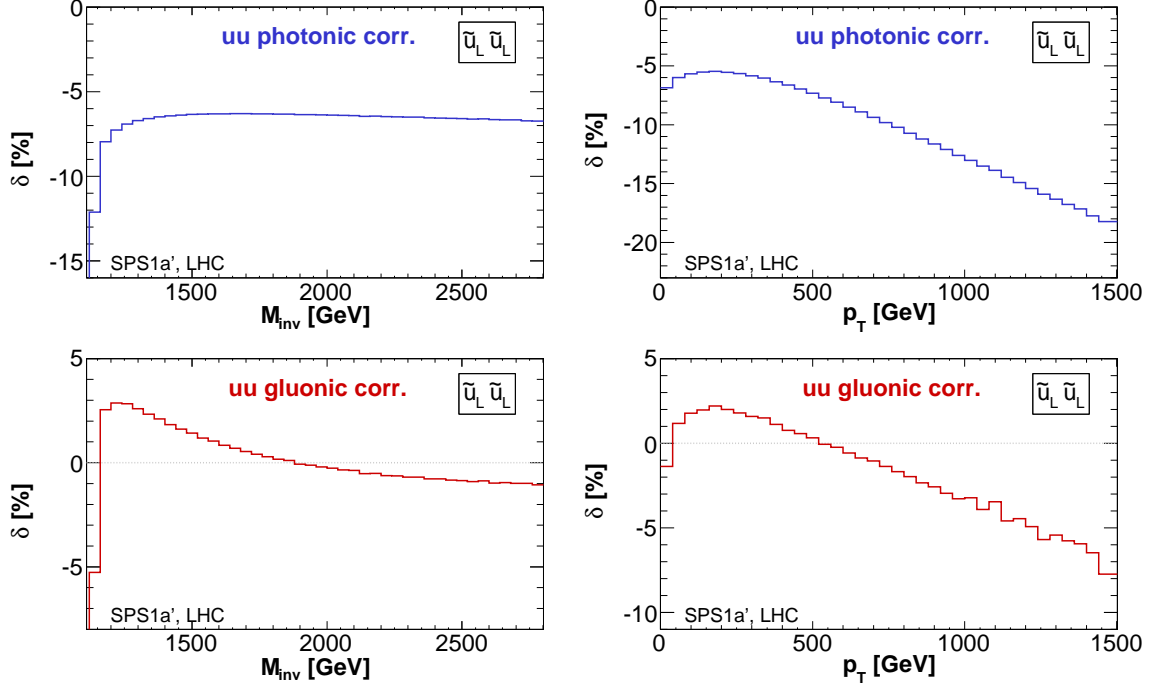
Figure 7.10.: Relative $\mathcal{O}(\alpha_s^2\alpha)$ EW corrections to $\tilde{u}_L\tilde{u}_L$ production at the LHC within the SPS1a' scenario. The upper plots refer to the IR-finite subset of photonic corrections to the uu channel, the lower plots to that of gluonic corrections. Shown are the invariant mass distribution of the $\tilde{u}_L\tilde{u}_L$ pair (left panels) and the distributions with respect to the transverse momentum $p_T(\tilde{u}_L)$ (right panels).

7.4 Outlook: non-diagonal and mixed-flavor squark–squark production

Squark–squark final states also allow for non-diagonal and mixed-flavor squark pairs. Experimentally, the inclusive squark–squark production is most relevant since light-flavor squarks are hard to distinguish in detectors (even though squarks of different helicities could be distinguishable by their decay chains in principle). Having worked out the technical details concerning the cancellation of UV and IR singularities for $\tilde{q}_a\tilde{q}_a$ production, the application of our methods to non-diagonal and/or mixed-flavor squark–squark production is straight-forward. It is thus planned to extend our studies to inclusive final-state analyses [115]. However the EW contributions depend sensitively on the chirality and the flavor of the produced particles. Different to the calculation of flavor-blind QCD corrections, we have to perform separate computations for different species of squarks.

At parton level, the squark–squark production processes can be divided into three classes (and the same applies to the charge conjugated processes). First, diagonal and non-diagonal
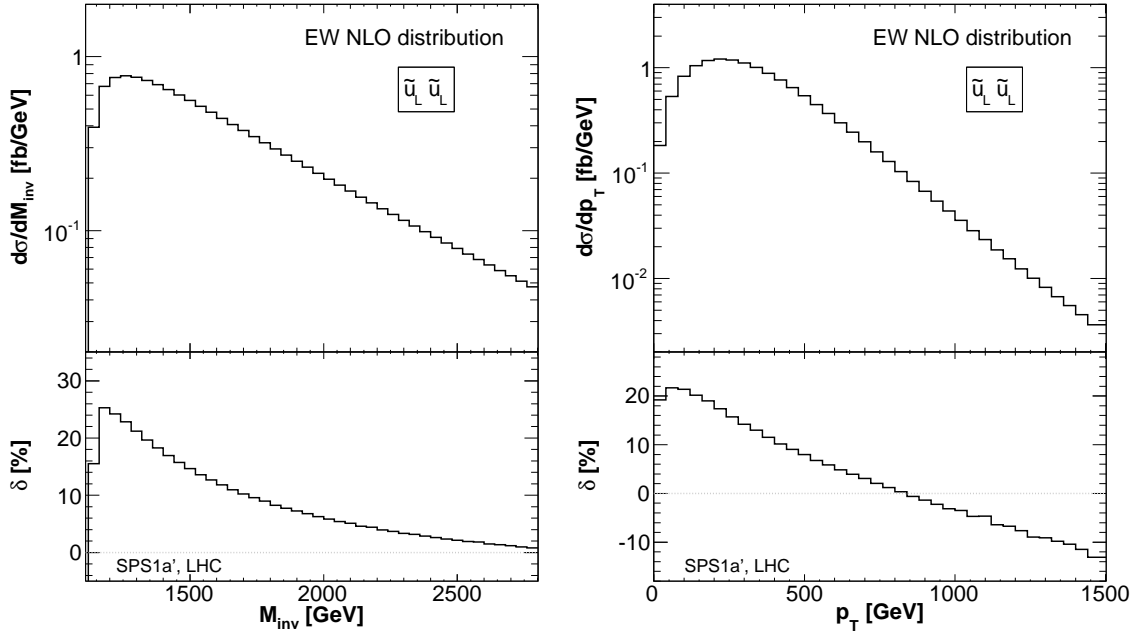
Figure 7.11.: Hadronic cross sections including the full EW contribution (upper panels) and relative EW contribution (lower panels) for $\tilde{u}_L \tilde{u}_L$ production. Shown are the invariant mass distribution of the $\tilde{u}_L \tilde{u}_L$ pair (left panels) and the distributions with respect to the transverse momentum $p_T(\tilde{u}_L)$ (right panels).

squark-squark production has to be addressed, with both squarks having the same flavor q,

$$qq \to \tilde{q}_a \tilde{q}_b, \qquad \begin{aligned} q &= u,d,c,s, \\ a,b &= L,R. \end{aligned} \qquad (7.27a)$$

A second class of processes describes squark–squark pairs of different flavor q,q' but with the squarks belonging to the same generation,

$$qq' \to \tilde{q}_a \tilde{q}'_b, \qquad \begin{aligned} (q,q') &= (u,d),\ (c,s), \\ a,b &= L,R. \end{aligned} \qquad (7.27b)$$

Third, the two squarks can be of different flavor and different generation

$$qq' \to \tilde{q}_a \tilde{q}'_b, \qquad \begin{aligned} (q,q') &= (u,c),\ (u,s),\ (d,c),\ (d,s), \\ a,b &= L,R. \end{aligned} \qquad (7.27c)$$

We summarize the three classes and respective parton-level Feynman diagrams in Fig. 7.12. All production processes can proceed from both QCD-mediated and EW-mediated tree-level amplitudes, yielding cross section contributions of $\mathcal{O}(\alpha_s^2)$ and $\mathcal{O}(\alpha^2)$, respectively. However

subprocess	strong contribution	electroweak contribution
$qq \to \tilde{q}_a \tilde{q}_b$ same flavor		
$qq' \to \tilde{q}_a \tilde{q}'_b$ different flavor, same generation		
$qq' \to \tilde{q}_a \tilde{q}'_b$ different flavor, different generation		

Figure 7.12.: Parton-level Feynman diagrams at LO for same-sign squark–squark production in hadronic collisions. All classes of production processes allow for both QCD-mediated and EW-mediated tree-level amplitudes. Depending on the flavor (q, q') and chirality $(a, b = L, R)$ structure of the final-state particles, the subset of contributing diagrams is different. In the first row, diagrams with crossed final states are only possible for diagonal $\tilde{q}_a \tilde{q}_a$ pairs $(a = L, R)$. In the second row, the diagram with crossed final states is present for left-handed $\tilde{q}_L \tilde{q}'_L$ pairs only.

the subset of non-zero diagrams and interference contributions is different for the processes Eqs. 7.27a–7.27c and depends on the flavor and chirality of the produced particles. The $\mathcal{O}(\alpha_s \alpha)$ interference of tree-level EW and tree-level QCD diagrams is only non-zero in case of diagonal $\tilde{q}_a \tilde{q}_a$ and same-generation $\tilde{q}_L \tilde{q}'_L$ final states. This structure of EW- and QCD-mediated diagrams carries over to EW NLO corrections at $\mathcal{O}(\alpha_s^2 \alpha)$ and requires a separate treatment of the various process classes.

Chapter 8

SUSY with $\mathcal{R}$-parity violation and
a $\tilde{\tau}_1$ as lightest SUSY particle

In the MSSM, an additional symmetry, $\mathcal{R}$-parity, is postulated to exclude lepton and baryon number violating operators from the superpotential that lead to rapid proton decay. In this chapter we investigate an alternative protective symmetry, baryon-triality B_3 [34–37], which prohibits only the baryon number violating operators. We focus on B_3 mSUGRA models where the lightest stau $\tilde{\tau}_1$ is the LSP. Since B_3 models allow for lepton number and $\mathcal{R}$-parity violation, the LSP can decay and is not constrained to be electrically neutral from cosmological observations.

We assume one non-zero B_3 coupling λ'_{ijk} at the GUT scale Λ_{GUT}, which can generate further B_3 couplings at the weak scale. In Section 8.1 we study the renormalization group equations and give numerical examples. The new couplings lead to additional $\tilde{\tau}_1$ decays, providing distinct collider signatures. We classify the $\tilde{\tau}_1$ decays and describe their dependence on the mSUGRA parameters in Section 8.2. Third, we exploit our results for single slepton production at the LHC in Section 8.3. As an explicit numerical example, we investigate single smuon production, focussing on like-sign dimuons in the final state. Also considered are final states with three or four muons.

The results presented in this chapter are published in [165].

B_3 mSUGRA models

B_3 mSUGRA models are based on the minimal particle content of a supersymmetric extension of the Standard Model (SSM). The most general renormalizable superpotential of the SSM is given in Eq. (2.42). It divides into Yukawa terms and a Higgs mixing term contained in $\mathcal{W}_{\mathcal{R}}$, Eq. (2.43a), and L- and B-violating terms parameterized in $\mathcal{W}_{\not{\mathcal{R}}}$, Eq. (2.43b). The assumption of $\mathcal{R}$-parity conservation excludes $\mathcal{W}_{\not{\mathcal{R}}}$ from the theory and is a defining property of the MSSM. In contrast, in models with conserved baryon-triality B_3 [34–37], only the baryon number violating $\overline{U}\,\overline{D}\,\overline{D}$ operator in $\mathcal{W}_{\not{\mathcal{R}}}$ is prohibited (and also dangerous dimension-five operators).

The most general B_3 SSM has more than 200 parameters. The number of parameters can be lowered by specific assumptions on the SUSY breaking mechanism. Within the MSSM, the most widely studied constrained model is minimal supergravity (mSUGRA), see Section 2.3.3. The 124 free parameters of the MSSM are reduced to only five, M_0, $M_{1/2}$, A_0, $\tan\beta$, $\text{sgn}(\mu)$, which are fixed at the GUT scale Λ_{GUT}, cf. Eq. (2.55). Correspondingly, in the B_3 mSUGRA model [166,167], there are six free parameters at the GUT scale,

$$M_0, \ M_{1/2}, \ A_0, \ \tan\beta, \ \text{sgn}(\mu), \ \text{and a single} \quad \lambda'_{ijk} \neq 0, \tag{8.1}$$

where the λ'_{ijk} coupling allows for the L-violating $L_i Q_j \overline{D}_k$ operator in $\mathcal{W}_{\mathcal{R}}$, Eq. (2.43b).

The B_3 SSM has some distinguishing features compared to the MSSM [31,168], which can have a strong impact on (hadron) collider phenomenology [169,170]:

- Lepton number and lepton flavor violating processes take place.

- The renormalization group equations (RGEs) get additional contributions [166,171, 172], resulting in modified low-energy SUSY couplings and SUSY particle spectra.

- Neutrino masses can be generated as experimentally observed [173][22].

- The LSP is not stable and can decay via the B_3 couplings.

- Supersymmetric particles can be produced singly, possibly on resonance.

Since the LSP is not stable, we are not restricted to the lightest neutralino $\tilde{\chi}_1^0$ as the LSP [10]. A first investigation of the parameter space has shown that there are extensive regions with a neutralino, a stau or a sneutrino LSP [166,167]. We shall focus here on a $\tilde{\tau}_1$ LSP. $\tilde{\tau}_1$ LSP scenarios have been studied in the literature [166,167,174–176]. As we discuss in the next section, we go beyond this work in several aspects.

We concentrate on models with only one non-vanishing λ'_{ijk} being present at Λ_{GUT}, similar to the dominant top Yukawa in the SM. Allowing for more than one coupling leads to stricter bounds [31,168,177–180]. The bounds for a single λ'_{ijk} lie between $\mathcal{O}(1)$ and $\mathcal{O}(10^{-4})$ depending on the flavor indices and SUSY particle masses. A summary of present bounds on the RPV couplings is given e.g. in [31,177]. The most stringent bound applies to λ'_{111} due to the non-observation of neutrinoless double beta decay. In general, the bounds can be up to four orders of magnitude stronger at Λ_{GUT} if one includes the generation of neutrino masses [166,179]. We therefore assume below that $\lambda'_{ijk} \lesssim \mathcal{O}(10^{-2})$ and require it to be consistent with the observed neutrino masses.

---

[22]The bilinear term $\kappa^i L_i H_u$ in the superpotential Eq. (2.43b) induces mixing between the neutrinos and neutralinos and thus one massive neutrino is obtained at tree level. A second neutrino mass as required from experiments is supplied by higher-order contributions to the neutrino mass matrix by B_3-coupling induced quark-squark and lepton-slepton loops. See e.g. [36,37] for more details.

New phenomenology

If SUSY particles are produced at colliders, they typically induce long cascade decay chains to the LSP in the detector. The nature of the LSP and its possible decay modes are thus essential in all supersymmetric signatures. The $\tilde{\tau}_1$ LSP might decay via the dominant $L_i Q_j \overline{D}_k$ operator; for example via a 4-body decay in the presence of a non-vanishing λ'_{211}, [23]

$$\tilde{\tau}_1^- \xrightarrow{\lambda'_{211}} \tau^- \mu^- u \bar{d} \,. \tag{8.2}$$

In this context, an important feature of B$_3$ mSUGRA models is that additional B$_3$ couplings are generated via the RGE running of non-vanishing B$_3$ couplings (see below). These new couplings can lead to 2-body decays of the $\tilde{\tau}_1$ LSP. For example, λ'_{211} will generate λ_{233} which allows for the decay

$$\tilde{\tau}_1^- \xrightarrow{\lambda_{233}} \mu^- \nu_\tau \,. \tag{8.3}$$

Even though $\lambda_{233} \ll \lambda'_{211}$, this might be the dominant decay mode. The decay (8.2) is suppressed by phase space and heavy propagators. In Section 8.2, we will analyze in detail the conditions for a dominance of the 2-body decay over the 4-body decay. We provide for the first time an extensive study of B$_3$ $\tilde{\tau}_1$ LSP decays and extend and specify thus the results of [176], where a first estimate has been performed. Since typically all heavy SUSY particles decay to the LSP, the various LSP signatures are important for studies both on pair and on singly produced SUSY particles.

As an interesting application of our results, we then consider in Section 8.3 resonant single slepton production at the LHC. This process is possible in B$_3$ scenarios with a non-zero λ'_{ijk} coupling via $q\bar{q}$ annihilation at parton level,

$$\bar{u}_j d_k \xrightarrow{\lambda'_{ijk}} \tilde{\ell}_{Li}^- \qquad \text{and} \qquad \bar{d}_j d_k \xrightarrow{\lambda'_{ijk}} \tilde{\nu}_i. \tag{8.4}$$

Note that single slepton production allows to study two B$_3$ couplings at a time, depending on the scenario. The slepton is always produced via a λ', whereas the decay of the $\tilde{\tau}_1$ LSP in the decay chain of the slepton might proceed via a generated λ, cf. Eq. (8.3).

Single slepton production within a $\tilde{\chi}_1^0$ LSP scenario leads to like-sign dileptons in the final state and has thus a very promising signature for experimental studies, see Refs. [181, 182]. As we will see, also in $\tilde{\tau}_1$ LSP scenarios one obtains like-sign dilepton events and, additionally, events with three or four leptons in the final state. We provide a classification of all possible signatures for resonant single slepton production in B$_3$ mSUGRA models with a $\tilde{\tau}_1$ LSP. As an numerical example, we calculate event rates for like-sign dimuon events as well as for three- and four-muon events, at the LHC. We also discuss backgrounds and cuts for like-sign dimuon events.

---

[23] In this chapter, we denote charged sleptons and anti-sleptons by $\tilde{\ell}^-$ and $\tilde{\ell}^+$ for clarification.

Resonant slepton production at hadron colliders via the $L_iQ_j\overline{D}_k$ operator was first investigated in [183], using tree-level production cross sections. Three-lepton final states and like-sign dilepton events were investigated in [181,182]. Ref. [184] considered scenarios with a gravitino LSP. Experimental studies by the DØ collaboration at the Tevatron were performed in Refs. [185] assuming a $\tilde{\chi}_1^0$ LSP and a non-vanishing λ'_{211}. The NLO QCD corrections to the cross section were computed in [186–188]. The SUSY-QCD corrections were included by [187]. The latter can modify the NLO QCD prediction by up to 35%.

8.1 The low-energy spectrum of the B$_3$ mSUGRA model with a $\tilde{\tau}_1$ LSP

At the GUT scale, the B$_3$ mSUGRA model is defined by six input parameters, cf. Eq. (8.1). We now discuss the low-energy spectrum. SUSY particle masses and couplings are obtained by running the respective RGEs down to the weak scale.

We explicitly take into account the mixing of different quark flavors, described by the CKM matrix (see the discussion in Section 2.3.4). We restrict ourselves to the extreme (but nontrivial) cases of quark mixing taking place completely in the up- or down-quark sector, respectively. In scenarios with "up-type mixing" the quark Yukawa matrices are given by Eq. (2.88), in scenarios with "down-type mixing" we consider Eq. (2.90).

As a first consequence of the nontrivial quark rotation matrices, the RGEs of the B$_3$ couplings are not independent but highly coupled. Therefore, a single non-zero λ'_{ijk} at the GUT scale generates a set of other non-zero B$_3$ couplings at lower scales. The size of the dynamically generated B$_3$ couplings depends sensitively on the composition of the quark Yukawa matrices. Assuming a diagonal charged-lepton Yukawa matrix $\mathbf{Y}_E$, only those couplings can be generated which violate the same lepton number as λ'_{ijk}, i.e. λ'_{imn} and λ_{ill}. No additional source of lepton number violation is introduced. Phenomenologically particularly relevant is the generation of λ_{i33}, which we discuss in detail in Section 8.1.3.

Second, the λ'_{ijk} coupling also has to be rotated from the weak into the quark mass basis for a comparison with experimental data. In case of up-type mixing, the $L_iQ_j\overline{D}_k$ interactions of the superpotential in the quark mass basis are, in terms of the $SU(2)_L$-component superfields $L_i = (N_i, E_i)^T$, (see e.g. [180]),

$$\lambda'_{ijk}\left[N_iD_j^m - E_i(\mathbf{V}_{\text{CKM}}^+)_{jl}U_l^m\right]\overline{D}_k^m. \tag{8.5}$$

In the case of down-mixing they are

$$\lambda'_{ijk}\left[N_i(\mathbf{V}_{\text{CKM}})_{jl}D_l^m - E_iU_j^m\right](\mathbf{V}_{\text{CKM}}^\dagger)_{nk}\overline{D}_n^m. \tag{8.6}$$

However for slepton production cross sections, we do not take into account these CKM

effects. If needed, the corresponding rescaling of the λ' coupling can be done easily. Furthermore the sub-dominant interactions, which include non-diagonal matrix elements of $\mathbf{V}_{\mathrm{CKM}}$, do not allow for large production cross sections since λ' enters only quadratically.

8.1.1 SUSY particle spectra

The low-energy SUSY particle masses depend strongly on the universal mSUGRA parameters, Eq. (2.55), and only weakly on $\lambda' \lesssim \mathcal{O}(10^{-2})$ [167]. Therefore, the general discussions of the MSSM particle spectrum of Section 2.3.4 also apply for the B$_3$ SSM. For later reference, we cite here known approximate expressions for the relevant SUSY particle masses in terms of the mSUGRA parameters [189] that also do hold.

Owing to the small electron and muon mass, the L–R mixing for sleptons of the first and second generation can safely be neglected. The gauge and mass eigenstates thus coincide and the masses are approximately given by

$$
\begin{aligned}
m_{\tilde{\ell}_R}^2 &= M_0^2 + 0.15 M_{1/2}^2 - \sin^2 \theta_W m_Z^2 \cos 2\beta, \\
m_{\tilde{\ell}_L}^2 &= M_0^2 + 0.52 M_{1/2}^2 - (0.5 - \sin^2 \theta_W) m_Z^2 \cos 2\beta, \\
m_{\tilde{\nu}}^2 &= M_0^2 + 0.52 M_{1/2}^2 + 0.5 m_Z^2 \cos 2\beta,
\end{aligned}
\tag{8.7}
$$

where $m_{\tilde{\ell}_{R,L}}$ denotes the mass of a right-/left-handed selectron or smuon, respectively, and $m_{\tilde{\nu}}$ denotes the mass of a left-handed electron or muon sneutrino.

For sfermions of the third generation, the L–R mixing has to be taken into account. The stau mass eigenstates $\tilde{\tau}_{1,2}$ are obtained by diagonalizing the stau mass matrix, cf. Eqs. (2.92) and (2.95), yielding for the masses $m_{\tilde{\tau}_{1,2}}$,

$$
m_{\tilde{\tau}_{1,2}}^2 = m_\tau^2 + \frac{1}{2} \left[(A^{LL} + C^{RR}) \mp \sqrt{(A^{LL} - C^{RR})^2 + 4 m_\tau^2 (B^{LR})^2} \right],
\tag{8.8}
$$

$$
\begin{aligned}
\text{with} \quad A^{LL} &= m_{\tilde{L}_3}^2 - \left(\frac{1}{2} - \sin^2 \theta_W \right) m_Z^2 \cos 2\beta, \\
B^{LR} &= A_\tau - \mu \tan \beta, \\
C^{RR} &= m_{\tilde{E}_3}^2 - \sin^2 \theta_W \, m_Z^2 \cos 2\beta.
\end{aligned}
\tag{8.9}
$$

The left- and right-handed third generation soft-breaking parameters $m_{\tilde{L}_3}$ and $m_{\tilde{E}_3}$ depend on the mSUGRA parameters (approximately) as follows,

$$
\begin{aligned}
m_{\tilde{E}_3}^2 &= M_0^2 + 0.15 M_{1/2}^2 - \frac{2}{3} X_\tau, \\
m_{\tilde{L}_3}^2 &= M_0^2 + 0.52 M_{1/2}^2 - \frac{1}{3} X_\tau, \\
X_\tau &\equiv 10^{-4} (1 + \tan^2 \beta) \left(M_0^2 + 0.15 M_{1/2}^2 + 0.33 A_0^2 \right),
\end{aligned}
\tag{8.10}
$$

where X_τ parameterizes the influence of the tau Yukawa coupling. Note, that X_τ can have a strong impact on the stau masses due to its $\tan^2\beta$ dependence, even though X_τ is suppressed by a factor 10^{-4}. We will investigate this effect on the $\tilde{\tau}_1$ decay branching ratios in the next section. In Eq. (8.9), A_τ is the trilinear coupling of the left- and right-handed stau to the Higgs boson. In mSUGRA models, it is $A_\tau = A_0$ at the GUT scale.

The neutralino masses simplify in many mSUGRA models, assuming that the lightest neutralino is bino-like and the second lightest is wino-like (see Section 2.3.4 and Eq. (2.117)). The masses can be approximated in terms of the universal gaugino mass $M_{1/2}$,

$$m_{\tilde{\chi}_1^0} \simeq M_1 = 0.41 M_{1/2}, \qquad m_{\tilde{\chi}_2^0} \simeq M_2 = 0.84 M_{1/2}, \qquad (8.11)$$

where Eq. (2.116) has been applied.

8.1.2 Reference scenarios with a $\tilde{\tau}_1$ LSP

For the purpose of numerical studies and as future reference points, two specific sets of B_3 mSUGRA scenarios with a $\tilde{\tau}_1$ LSP have been defined in [165],

Set A: $\quad M_0 = 0\,\text{GeV}, \ M_{1/2} = 500\,\text{GeV}, \ A_0 = 600\,\text{GeV}, \ \tan\beta = 13, \ \text{sgn}(\mu) = +1,$
a single $\lambda'_{ijk} \neq 0|_{\text{GUT}}$, $\qquad\qquad\qquad\qquad\qquad\qquad\qquad\qquad$ (8.12a)

Set B: $\quad M_0 = 0\,\text{GeV}, \ M_{1/2} = 700\,\text{GeV}, \ A_0 = 1150\,\text{GeV}, \ \tan\beta = 26, \ \text{sgn}(\mu) = +1,$
a single $\lambda'_{ijk} \neq 0|_{\text{GUT}}$. $\qquad\qquad\qquad\qquad\qquad\qquad\qquad\qquad$ (8.12b)

The scenarios are carefully chosen in accordance with bounds from B-physics, EW precision observables (the anomalous magnetic moment of the muon), Higgs boson searches at LEP, and neutrino physics (see [165] and references therein).

In Table 8.1, we show the supersymmetric mass spectra of the parameter sets A and B (8.12). We have neglected the mass dependence on the different non-zero B_3 couplings which is valid if $\lambda'_{ijk} \lesssim \mathcal{O}(10^{-2})$ [167]. The main B_3 effect on the spectrum is that we allow for a $\tilde{\tau}_1$ LSP. Note that one naturally obtains a $\tilde{\tau}_1$ LSP spectrum for $M_{1/2} \gg M_0$. The large $M_{1/2}$ raises the lightest neutralino mass Eq. (8.11) faster than the right-handed slepton masses (8.7). It also drives the gluino and indirectly via the RGEs the squark masses up. We thus see in Table 8.1 squark and gluino masses $\gtrsim 1\,\text{TeV}$, while the slepton masses are below 500 GeV. Another general feature of a $\tilde{\tau}_1$ LSP scenario is that the second lightest neutralino and the lightest chargino are also heavier than the sleptons. Therefore the only conventional supersymmetric decays of the left-handed sleptons are via the lightest neutralino. Depending on the dominant B_3 coupling and its size, the left-handed sleptons can also decay into two jets.

	masses [GeV]			masses [GeV]	
	Set A	Set B		Set A	Set B
$\tilde{\tau}_1$	179	146	$\tilde{\chi}_1^0$	203	290
$\tilde{e}_R$	193	266	$\tilde{\chi}_2^0$	380	544
$\tilde{\tau}_2$	340	453	$\tilde{\chi}_3^0$	571	754
$\tilde{e}_L$	340	471	$\tilde{\chi}_4^0$	587	765
$\tilde{\nu}_\tau$	326	437	$\tilde{\chi}_1^\pm$	383	549
$\tilde{\nu}_e$	329	461	$\tilde{\chi}_2^\pm$	583	761
$\tilde{t}_1$	841	1160	h^0	113	115
$\tilde{b}_1$	970	1300	H^0	643	795
$\tilde{u}_R$	1010	1370	A^0	642	795
$\tilde{t}_2$	1010	1340	H^+	648	799
$\tilde{b}_2$	995	1340			
$\tilde{u}_L$	1040	1410	$\tilde{g}$	1150	1560

Table 8.1.: SUSY particle masses for the B_3 mSUGRA sets A and B as defined in Eq. (8.12), evaluated for a renormalization scale Q_{SUSY}, Eq. (8.20), using `Softsusy 2.0.10` [75]. The variation due to different $\lambda'_{ijk} \neq 0|_{\mathrm{GUT}}$ and quark mixing is below the percent level. The masses in the second generation coincide with those in the first generation.

Nearly all SUSY particles in Set B ($M_{1/2} = 700$ GeV) are heavier than in Set A ($M_{1/2} = 500$ GeV). The most important difference for the phenomenology at colliders arises from the different values of $\tan\beta$ ($\tan\beta = 13$ in Set A, $\tan\beta = 26$ in Set B). According to Eq. (8.10), the soft breaking parameters of the stau decrease for increasing $\tan\beta$ and thus both stau mass eigenstates are reduced for large values of $\tan\beta$. Furthermore, the mass of the lighter stau is reduced due to the larger L–R mixing proportional to B^{LR}, Eq. (8.9). This effect can be seen in Table 8.1, where the mass of the $\tilde{\tau}_1$ LSP is 179 GeV in Set A but only 146 GeV in Set B. The $\tilde{\tau}_1$ mass and $\tan\beta$ strongly influence the possible 2- and 4-body $\tilde{\tau}_1$ LSP branching ratios. We will investigate this topic in detail in Section 8.2.

8.1.3 Renormalization group equations

One of the most important consequences of including B_3 effects in SUSY models is that the LSP is no longer stable. This is of special interest for phenomological studies if the LSP couples directly to the dominant B_3 operator. This leads to large LSP decay widths and to distinctive final-state signatures.

In the scenarios considered here, cf.Eq. (8.1), the dominant coupling is a λ'_{ijk}; for $i \neq 3$ it does not couple to the $\tilde{\tau}_1$ LSP. However, as the RGEs of the B_3 couplings are coupled via non-diagonal entries of Yukawa matrices, a λ'_{ijk} generates dynamically other B_3 couplings. Among those, we want to focus on the λ_{i33} which do couple directly to the $\tilde{\tau}_1$ LSP.

The aim of the next two sections is to study the RGEs of the dominant λ'_{ijk} and to quantitatively determine the generated λ_{i33}. We then use these results to predict the low-energy spectrum of B$_3$ mSUGRA scenarios. We will also derive approximate formulas that allow for a numerical implementation of the running of the couplings.

The full renormalization group equations for the B$_3$ couplings λ'_{ijk} and λ_{i33} are [166,171, 172],

$$16\pi^2 \frac{d}{dt}\lambda'_{ijk} = \lambda'_{ijl}\,\gamma^{D_k}_{D_l} + \lambda'_{ilk}\,\gamma^{Q_j}_{Q_l} + \lambda'_{ljk}\,\gamma^{L_i}_{L_l} - \left(\mathbf{Y}_D\right)_{jk}\gamma^{L_i}_{H_1}, \tag{8.13}$$

$$16\pi^2 \frac{d}{dt}\lambda_{i33} = \lambda_{i3l}\,\gamma^{E_3}_{E_l} + \lambda_{il3}\,\gamma^{L_3}_{L_l} + \lambda_{l33}\,\gamma^{L_i}_{L_l} - \left(\mathbf{Y}_E\right)_{33}\gamma^{L_i}_{H_1} + \left(\mathbf{Y}_E\right)_{i3}\gamma^{L_3}_{H_1}, \tag{8.14}$$

with $t = \ln\mu_R$; μ_R being the renormalization scale. The anomalous dimensions γ are listed in [166] at one-loop level and in [172] at two-loop level. The RGEs simplify considerably under the assumption of the single B$_3$ coupling dominance hypothesis [183,190]. Products of two or more B$_3$ couplings including quadratic contributions of the dominant coupling can be neglected for $\lambda' \lesssim \mathcal{O}(10^{-2})$. In this limit, the one-loop anomalous dimensions read

$$\begin{aligned}
\gamma^{Q_i}_{Q_j} &= \left(\mathbf{Y}_D\mathbf{Y}_D^+\right)_{ij} + \left(\mathbf{Y}_U\mathbf{Y}_U^+\right)_{ij} - \delta^i_j\Big(\frac{1}{30}g_1^2 + \frac{3}{2}g_2^2 + \frac{8}{3}g_3^2\Big), \\
\gamma^{D_i}_{D_j} &= 2\left(\mathbf{Y}_D^+\mathbf{Y}_D\right)_{ji} - \delta^i_j\Big(\frac{2}{15}g_1^2 + \frac{8}{3}g_3^2\Big), \\
\gamma^{L_i}_{L_j} &= \left(\mathbf{Y}_E\mathbf{Y}_E^+\right)_{ij} - \delta^i_j\Big(\frac{3}{10}g_1^2 + \frac{3}{2}g_2^2\Big), \\
\gamma^{E_i}_{E_j} &= 2\left(\mathbf{Y}_E^+\mathbf{Y}_E\right)_{ji} - \delta^i_j\Big(\frac{6}{5}g_1^2\Big), \\
\gamma^{L_i}_{H_1} &= -3\lambda'_{iaq}\left(\mathbf{Y}_D\right)_{aq} - \lambda_{ibq}\left(\mathbf{Y}_E\right)_{bq},
\end{aligned} \tag{8.15}$$

where g_1, g_2, g_3 are the three gauge couplings[24].

From Eqs. (8.14) and (8.15), we see that the terms related to $\gamma^{L_i}_{H_1}$ allow for the dynamical generation of λ_{i33} by a non-zero λ'_{iaq} coupling [and vice-versa for Eq. (8.13)]. All other terms in Eq. (8.14) only alter the running of λ_{i33} once it is generated.

The RGEs can be further simplified. At one-loop level, all B$_3$ couplings but the dominant λ'_{ijk} and the generated λ_{i33} can be neglected in the RGEs since they must be generated first by λ' and thus contribute at two-loop level only. Also, since we work in a diagonal charged lepton Yukawa basis, the last term in Eq. (8.14), proportional to $\left(\mathbf{Y}_E\right)_{i3}$ does not contribute to the running of λ_{i33}. It is only non-zero if $i = 3$, but owing to the ij-antisymmetry of λ_{ijk}

---

[24]This is the usual notation of gauge couplings in mSUGRA models. In order to study the unification of the running couplings, it is helpful to have a proper normalization of the gauge couplings. In particular, the normalization of the $U(1)_Y$ generator, which can be arbitrarily normalized within the SM, is fixed by the GUT relation to the generators of the non-Abelian groups. Assuming $SU(5)$ unification, we define $g_1 = \sqrt{5/3}g'$, $g_2 = g$, $g_3 = g_s$, and $\alpha_i = g_i^2/(4\pi)$.
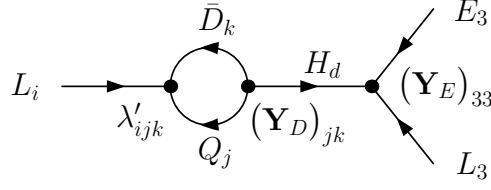
Figure 8.1.: Superfield diagram for the dynamical generation of λ_{i33} by λ'_{ijk} at one-loop order.

no coupling is generated in this case ($\lambda_{333} = 0$). Next, in scenarios of intermediate $\tan\beta$ ($\tan\beta = \mathcal{O}(10)$), a general ordering of the parameters in the anomalous dimensions is [165]

$$g_3^2 > \left(\mathbf{Y}_U\right)_{33}^2 > g_2^2 > g_1^2 > \left(\mathbf{Y}_D\right)_{33}^2 > \left(\mathbf{Y}_E\right)_{33}^2, \tag{8.16}$$

and all other entries of the $\mathbf{Y}$ matrices are smaller by at least one order of magnitude. The contributions to the RGEs are thus largest for diagonal anomalous dimensions. As a result, the RGEs for a non-zero λ'_{ijk} at the GUT scale and a generated λ_{i33} reduce to

$$
\begin{aligned}
16\pi^2 \frac{d}{dt}\lambda'_{ijk} = {} & \lambda'_{ijk}\Big[-\frac{7}{15}g_1^2 - 3g_2^2 - \frac{16}{3}g_3^2 \\
& + \left(\mathbf{Y}_D\right)_{33}^2\big(2\delta_{k3} + \delta_{j3} + 3\,\delta_{j3}\,\delta_{k3}\big) + \left(\mathbf{Y}_U\right)_{33}^2\delta_{j3} + \left(\mathbf{Y}_E\right)_{33}^2\delta_{i3}\Big],
\end{aligned}
\tag{8.17a}
$$

$$
16\pi^2 \frac{d}{dt}\lambda_{i33} = \lambda_{i33}\left[-\frac{9}{5}g_1^2 - 3g_2^2 + 4\left(\mathbf{Y}_E\right)_{33}^2\right] + 3\lambda'_{ijk}\left(\mathbf{Y}_E\right)_{33}\left(\mathbf{Y}_D\right)_{jk}. \tag{8.17b}
$$

A similar analytical approximation for the generation of λ is derived in [176]. But the effect of the gauge couplings is neglected there. See also Ref. [191].

The last term in Eq. (8.17b) induces the dynamical generation of λ_{i33}. Diagrammatically, this process can be understood as shown in Fig. 8.1. We see that at one-loop the lepton-doublet superfield L_i mixes with the Higgs doublet superfield H_d via the B_3 coupling λ'_{ijk} and the down quark Yukawa coupling $\left(\mathbf{Y}_D\right)_{jk}$. H_d then couples via the tau Yukawa coupling $\left(\mathbf{Y}_E\right)_{33}$ purely leptonically. The resulting effective interaction is of the λ_{i33}-type.

It is important to notice that the generation is related to $\left(\mathbf{Y}_D\right)_{jk}$. Whether a given λ'_{ijk} can generate λ_{i33} or not depends on whether $\left(\mathbf{Y}_D\right)_{jk} \neq 0$. For $j \neq k$ it thus depends crucially on the origin of the CKM mixing: is it dominantly down-type or up-type mixing. In case of down-type mixing, all entries of the $\mathbf{Y}_D$ matrix are non-zero and all λ'_{ijk} can therefore generate a λ_{i33}. In contrast, if the quark mixing takes place in the up-sector, only the diagonal entries of $\mathbf{Y}_D$ are non-zero and $j = k$ is required. The flavor and size of the generated coupling depends on $\tan\beta$ and on the precise j,k configuration. A strong ordering is expected that goes along with the ordering of the entries of the $\mathbf{Y}_D$ matrix.

In order to study the running of the B$_3$ couplings, the RGEs for the Yukawa matrix elements $(\mathbf{Y}_D)_{jk}$, $(\mathbf{Y}_U)_{33}$, and $(\mathbf{Y}_E)_{33}$ and the gauge couplings are also needed. The full RGEs for the Yukawa couplings are given in [166,171]. Applying the single coupling dominance hypothesis, neglecting quadratic terms in λ'_{ijk}, and considering only the dominant terms Eq. (8.16), they read

$$16\pi^2 \frac{d}{dt}(\mathbf{Y}_U)_{33} = (\mathbf{Y}_U)_{33} \left[-\frac{13}{15}g_1^2 - 3g_2^2 - \frac{16}{3}g_3^2 + 6(\mathbf{Y}_U)_{33}^2 + (\mathbf{Y}_D)_{33}^2 \right], \qquad (8.18a)$$

$$16\pi^2 \frac{d}{dt}(\mathbf{Y}_E)_{33} = (\mathbf{Y}_E)_{33} \left[-\frac{9}{5}g_1^2 - 3g_2^2 + 4(\mathbf{Y}_E)_{33}^2 + 3(\mathbf{Y}_D)_{33}^2 \right], \qquad (8.18b)$$

$$16\pi^2 \frac{d}{dt}(\mathbf{Y}_D)_{jk} = (\mathbf{Y}_D)_{jk} \left[-\frac{7}{15}g_1^2 - 3g_2^2 - \frac{16}{3}g_3^2 \right.$$
$$\left. + (\mathbf{Y}_D)_{33}^2 \left(3 + \delta_{j3} + 2\delta_{k3} \right) + (\mathbf{Y}_U)_{33}^2 \delta_{j3} + (\mathbf{Y}_E)_{33}^2 \right]. \qquad (8.18c)$$

The one-loop order RGEs for the three gauge couplings within the MSSM are given by

$$16\pi^2 \frac{d}{dt}g_i = b_i\,g_i^3, \qquad (8.19)$$

with $b_i = \{33/5,\,1,\,-3\}$ for $i = 1,\,2,\,3$. Thus in total, a set of nine coupled differential equations, Eqs. (8.17a) - (8.19), has to be solved[25].

Numerical results

For the numerical implementation of the RGEs we start from the framework provided by `Softsusy 2.0.10` [75]. First, `Softsusy` evaluates all necessary parameters at the SUSY scale Q_{SUSY},

$$Q_{\text{SUSY}} = \sqrt{m_{\tilde{t}_1}(Q_{\text{SUSY}})\,m_{\tilde{t}_2}(Q_{\text{SUSY}})}\,. \qquad (8.20)$$

In a second step, we apply the ($\mathcal{R}$-parity conserving) RGEs Eqs. (8.18) and (8.19) to run the Yukawa couplings and gauge couplings up to the GUT scale. Here we add the B$_3$ couplings $\lambda'_{ijk} \neq 0|_{\text{GUT}}$ and $\lambda_{i33} = 0|_{\text{GUT}}$ and evolve these couplings down to the scale Q using the above given B$_3$ RGEs (8.17a) and (8.17b). We have implemented the RGEs using a standard Runge Kutta formalism [192].

In Fig. 8.2, we show the running of different λ'_{2jk} couplings (with $\lambda'_{ijk} = 0.01|_{\text{GUT}}$), for the two cases of down- and up-mixing. In the lower panels, the scale dependence of the generated $\lambda_{323} = -\lambda_{233}$ coupling is studied. Here, we refer to the parameters of Set A.

We see that the dominant λ'_{ijk} coupling grows by about a factor of 3, running from the GUT scale to the weak scale. This effect is mainly due to the gauge couplings, see Ref. [191],

---

[25]In case of $j = k = 3$ only 8 equations need to be solved. But this implies that the slepton has to be produced by parton quarks of the third generation which is strongly suppressed due to their negligible parton density.
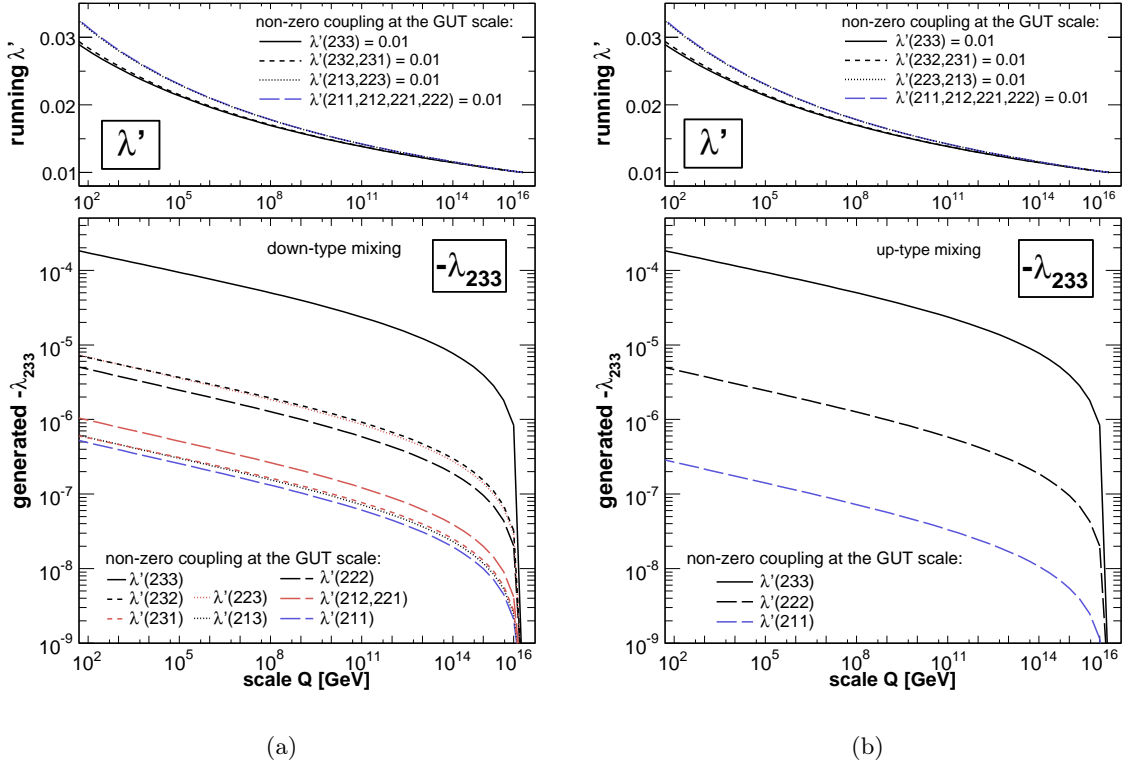
Figure 8.2.: Running of B₃ couplings assuming a single non-zero $\lambda' = 0.01$ coupling at the GUT scale (upper panel) leading to a non-zero λ_{233} coupling (lower panel) at lower scales within the B₃ mSUGRA scenario Set A for (a) down-type and (b) up-type mixing.

where the Yukawa couplings were omitted. Including the Yukawa couplings reduces this effect, maximally for $j = k = 3$.

The generated λ_{233} coupling is at least two orders of magnitude smaller than the original λ' coupling. Furthermore its size depends sensitively on the flavor structure (ijk) of the generating λ' coupling. This reflects the dependence on the Yukawa matrix $(\mathbf{Y}_D)_{jk}$. In case of down-type mixing, the ordering of the corresponding entries is

$$(\mathbf{Y}_D)_{33} > (\mathbf{Y}_D)_{23,32} > (\mathbf{Y}_D)_{22} > (\mathbf{Y}_D)_{12,21} > (\mathbf{Y}_D)_{13,31} > (\mathbf{Y}_D)_{11}, \qquad (8.21)$$

reflecting precisely the ordering of the generated couplings in Fig. 8.2(a). Small differences between the couplings generated by λ'_{i23} (λ'_{i13}) or λ'_{i32} (λ'_{i31}) are related to the different running of the respective λ' and $(\mathbf{Y}_D)_{jk}$ coupling, depending in turn on whether j or k equals 3. In the case of up-type mixing, Fig. 8.2(b), not all λ' couplings can generate a λ. Since the down Yukawa coupling is diagonal, $j = k$ is required. Other couplings can generate λ_{i33} at higher loop levels only and are not included in our approximations.

Set	λ'_{ijk}		λ_{i33} (down-type mixing)		λ_{i33} (up-type mixing)	
A	Eq. (8.17a)	Softsusy	Eq. (8.17b)	Softsusy	Eq. (8.17b)	Softsusy
λ'_{211}	2.82×10^{-2}	2.85×10^{-2}	-3.96×10^{-7}	-3.89×10^{-7}	-2.17×10^{-7}	-2.13×10^{-7}
λ'_{231}	2.58×10^{-2}	2.61×10^{-2}	-4.65×10^{-7}	-4.80×10^{-7}	0	$+2.06 \times 10^{-12}$
λ'_{223}	2.81×10^{-2}	2.83×10^{-2}	-5.55×10^{-6}	-5.73×10^{-6}	0	-8.45×10^{-9}
λ'_{233}	2.55×10^{-2}	2.58×10^{-2}	-1.41×10^{-4}	-1.42×10^{-4}	-1.42×10^{-4}	-1.43×10^{-4}
λ'_{311}	2.81×10^{-2}	2.84×10^{-2}	0	0	0	0

Table 8.2.: Comparison of our approximations Eq. (8.17a) and Eq. (8.17b), and `Softsusy` results, for λ'_{ijk} and the generated coupling λ_{i33} at the SUSY scale Q_{SUSY}. We choose different couplings $\lambda'_{ijk} = 0.01$ at the GUT scale as given in the first column of the table. The running of λ'_{ijk} is the same for down- and up-type quark mixing. The generation of λ_{i33} depends on the quark mixing assumptions and the values at the SUSY scale are given separately. The remaining mSUGRA parameters are these of Set A.

Even though the specific scenario Set A has been studied, the results can easily be generalized: The running of the dominant coupling λ' is mainly driven by gauge interactions, Eq. (8.17a), and thus depends only weakly on the precise SUSY parameters. The dependence of the generated coupling λ on SUSY parameters is more involved but we expect $\tan\beta$ to have the largest impact. In general, the generated λ coupling scales with $\tan^2\beta$,

$$\lambda_{i33} \propto \tan^2\beta\,, \tag{8.22}$$

if $\tan^2\beta \gg 1$. This is due to the fact that the down-quark Yukawa couplings $\left(\mathbf{Y}_D\right)_{jk}$ [and the tau Yukawa coupling $\left(\mathbf{Y}_E\right)_{33}$] are proportional to $1/\cos\beta = \sqrt{1 + \tan^2\beta}$, cf.Eqs. (2.81) and (2.66). Therefore the magnitude of the generated λ coupling for other scenarios can be estimated by rescaling λ of Fig. 8.2 according to Eq. (8.22).

Comparison with the program `Softsusy`

How reliable are our approximations of the RGEs? In order to answer this question we compare our results for λ'_{ijk} and the generated coupling λ_{i33} at the SUSY scale, Eq. (8.20), with an unpublished version of `Softsusy`[26]. This version of `Softsusy` contains the complete one-loop RGEs for λ'_{ijk} (8.13) and λ_{i33} (8.14), without our approximations.

In Table 8.2, we compare our results and the results of `Softsusy` for the case of down-type mixing and up-type mixing assuming different couplings $\lambda'_{ijk} = 0.01$ at the GUT scale. All other parameters are chosen according to Set A specified in Eq. (8.12). At the SUSY scale, the differences between the results for the case of down-type mixing, are less than 2% for all λ'_{ijk} couplings and less than 4% for the λ_{i33}, respectively. In case of up-type

---

[26]`Softsusy 3.0` which includes $\mathcal{R}$-parity violation and has been released meanwhile [193].

mixing, we find the same for the couplings λ'_{ijk} with $j = k$. However for $j \neq k$ and up-type mixing, we observe a discrepancy between our results and `Softsusy` for the coupling λ_{233} generated by $\lambda'_{223} \neq 0|_{\text{GUT}}$ and $\lambda'_{231} \neq 0|_{\text{GUT}}$, respectively. This behavior can easily be understood. The off-diagonal Yukawa matrix elements $(\mathbf{Y}_D)_{jk}$ are equal to zero at the weak scale for up-type mixing. Running from the weak scale to the GUT scale generates Yukawa couplings $(\mathbf{Y}_D)_{jk}$, $j \neq k$, at the one-loop level [166,171]. The generation of λ_{233} via Eq. (8.17b) occurs therefore formally at two-loop level and has been neglected in our approximation. In `Softsusy` this two-loop effect is taken into account and small couplings are generated also for $j \neq k$ and up-type mixing. Compared to the case of down-type mixing, the λ_{233} couplings are suppressed by five (with $\lambda'_{231} = 0.01|_{\text{GUT}}$) and three (with $\lambda'_{223} = 0.01|_{\text{GUT}}$) orders of magnitude. Note that the generation of $(\mathbf{Y}_D)_{jk}$ is not the only two-loop effect that enters the full RGEs [166,171,172].

Therefore, our approximation for the generation of λ_{i33} by a non-zero λ'_{ijk} at the GUT scale (8.17b) breaks down in the case of up-type mixing and $j \neq k$. But concerning $\tilde{\tau}_1$ LSP decays, the corresponding 2-body decay branching ratio for λ_{i33} is negligible compared to the 4-body decay branching ratio via λ'_{ijk} and our approximations are applicable for such phenomenological studies. For example, the 2-body decay branching ratio for up-type mixing and $\lambda'_{231} = 0.01|_{\text{GUT}}$ or $\lambda'_{223} = 0.01|_{\text{GUT}}$ is less than 10^{-4} in Set A.

We conclude that our approximations are valid for the signal and decay rates that we study in this work. We also note that we have provided an independent check of the yet-to-be published version of `Softsusy`. Using a different set of mSUGRA parameters leads to a similar level of agreement.

8.2 $\tilde{\tau}_1$ LSP decays in B_3 mSUGRA models

As we have seen, a non-vanishing coupling λ'_{ijk} at the GUT scale generates an additional coupling λ_{i33} at the weak scale which is (roughly) at least two orders of magnitude smaller than λ'_{ijk}. In this section, we first compare the possible decay modes of the LSP via these two couplings for B_3 mSUGRA scenarios with different LSP candidates. Second, we further investigate the dependence of the $\tilde{\tau}_1$ decay modes on the mSUGRA parameters.

8.2.1 General LSP decay modes

First, let us discuss B_3 scenarios with a $\tilde{\chi}_1^0$ LSP. The leading order decay modes of the $\tilde{\chi}_1^0$ LSP via the dominant λ'_{ijk} and the generated λ_{i33} couplings are all three body decays,

$$
\tilde{\chi}_1^0 \xrightarrow{\lambda'_{ijk}} \begin{cases} \ell_i^+ \, \bar{u}_j \, d_k \\ \ell_i^- \, u_j \, \bar{d}_k \end{cases} , \qquad \tilde{\chi}_1^0 \xrightarrow{\lambda'_{ijk}} \begin{cases} \bar{\nu}_i \, \bar{d}_j \, d_k \\ \nu_i \, d_j \, \bar{d}_k \end{cases} , \tag{8.23}
$$

and

$$\tilde{\chi}_1^0 \xrightarrow{\lambda_{i33}} \begin{cases} \ell_i^+ \, \bar{\nu}_\tau \, \tau^- \\ \ell_i^- \, \nu_\tau \, \tau^+ \end{cases}, \qquad \tilde{\chi}_1^0 \xrightarrow{\lambda_{i33}} \begin{cases} \bar{\nu}_i \, \tau^+ \, \tau^- \\ \nu_i \, \tau^- \, \tau^+ \end{cases}. \qquad (8.24)$$

The corresponding amplitudes depend linearly on the respective B$_3$ couplings, yielding partial widths that depend quadratically on λ'_{ijk} and λ_{i33}, respectively. Therefore, the $\tilde{\chi}_1^0$ decay via the generated coupling λ_{i33} is heavily suppressed and a $\tilde{\chi}_1^0$ LSP decays predominantly via λ'_{ijk} into SM particles.

The situation changes for B$_3$ mSUGRA scenarios with a $\tilde{\tau}_1$ LSP. First we consider scenarios where the $\tilde{\tau}_1$ does not couple directly to the $L_i Q_j \overline{D}_k$ operator, i.e. $i = 1, 2$. In this case, the $\tilde{\tau}_1$ must first couple to a virtual gaugino. The gaugino then couples to a virtual sfermion which then decays via λ'_{ijk}, resulting in a 4-body decay of the $\tilde{\tau}_1$ LSP. The possible decay modes via a virtual neutralino are

$$\tilde{\tau}_1^- \xrightarrow{\lambda'_{ijk}} \begin{cases} \tau^- \, \ell_i^+ \, \bar{u}_j \, d_k \\ \tau^- \, \ell_i^- \, u_j \, \bar{d}_k \\ \tau^- \, \bar{\nu}_i \, \bar{d}_j \, d_k \\ \tau^- \, \nu_i \, d_j \, \bar{d}_k \end{cases}. \qquad (8.25)$$

4-body decays via a virtual chargino are also possible but suppressed due to the higher chargino mass in comparison to the lightest neutralino mass, $m(\tilde{\chi}_1^\pm) > m(\tilde{\chi}_1^0)$. Furthermore, the (mainly right-handed) $\tilde{\tau}_1$ LSP couples stronger to the (bino-like) lightest neutralino than to the (wino-like) lightest chargino. On the other hand, the $\tilde{\tau}_1$ can directly decay via λ_{i33} into only two SM particles

$$\tilde{\tau}_1^- \xrightarrow{\lambda_{i33}} \begin{cases} \tau^- \, \bar{\nu}_i \\ \tau^- \, \nu_i \\ \ell_i^- \, \nu_\tau \end{cases}. \qquad (8.26)$$

We show in Fig. 8.3 (Fig. 8.4), example diagrams for the 4-body (2-body) decay of a $\tilde{\tau}_1$ LSP via λ'_{2jk} (λ_{233}). Although the 2-body decay suffers from the small coupling, the 4-body decay is phase space suppressed as well as by heavy propagators. Which decay mode dominates does strongly depend on the parameters at the GUT scale. We will discuss in detail this topic in the next section.

As a third type of B$_3$ mSUGRA scenarios we want to mention $\tilde{\tau}_1$ LSP scenarios with a dominant λ'_{3jk} coupling. Here, the dominant B$_3$ operator couples directly to the $\tilde{\tau}_1$ LSP and allows for a 2-body decay of the $\tilde{\tau}_1$ into two jets,

$$\tilde{\tau}_1^- \xrightarrow{\lambda'_{3jk}} \bar{u}_j d_k . \qquad (8.27)$$
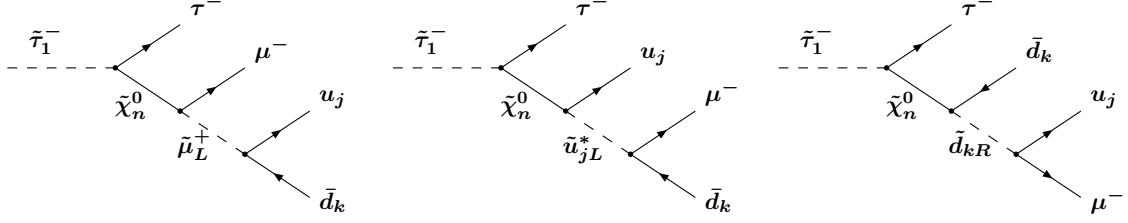
Figure 8.3.: Feynman diagrams for the 4-body decay $\tilde{\tau}_1^- \to \tau^- \mu^- u_j \bar{d}_k$ of the $\tilde{\tau}_1$ LSP via λ'_{2jk}. The $\tilde{\tau}_1$ LSP decays via a virtual neutralino $\tilde{\chi}_n^0$ ($n = 1, 2, 3, 4$) into a tau τ^-, a muon μ^-, an up-type quark u_j and a down-type anti-quark $\bar{d}_k$.
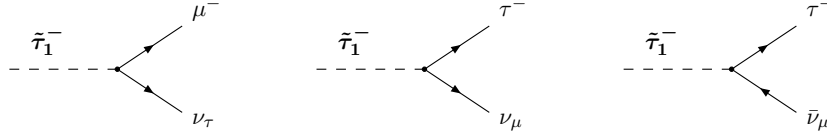
Figure 8.4.: Feynman diagrams leading to the 2-body decays of a $\tilde{\tau}_1$ LSP via a generated coupling λ_{233}. The $\tilde{\tau}_1$ decays either into a muon μ^- and a neutrino or into a τ^- and a neutrino.

λ'_{3jk} can not generate λ_{333} via the RGEs, because λ_{ijk} has to be anti-symmetric in the indices i, j. λ_{3nn} with $n \neq 3$ will be generated by the muon ($n = 2$) or electron ($n = 1$) Higgs Yukawa coupling, cf.Eq. (8.17b). But since these Yukawa couplings are so small, the decay via λ_{3nn} is too small to be seen.

For $j = 3$, the up-type quark in Eq. (8.27) is a top quark and hence the decay Eq. (8.27) is kinematically forbidden for $m_{\tilde{\tau}_1} < m_t$. Instead, the $\tilde{\tau}_1$ LSP decays in a 3-body decay mode via a virtual top quark or a virtual tau sneutrino into a W boson and two jets, where at least one jet is a b jet,

$$\tilde{\tau}_1^- \xrightarrow{\lambda'_{33k}} W^- \bar{b} \, d_k \,. \tag{8.28}$$

We present the squared matrix element and the partial width of this process in Appendix C.2, which to our knowledge has not been given in the literature so far.

8.2.2 Dependence of $\tilde{\tau}_1$ decays on mSUGRA parameters

In this section, we investigate the GUT scale conditions that lead to 2-body decays of the $\tilde{\tau}_1$ LSP. We assume a non-vanishing λ'_{2jk} coupling at the GUT scale. This can easily be generalized to λ'_{1jk}. We point out that the branching ratios of the $\tilde{\tau}_1$ LSP do not depend on the magnitude of λ'_{ijk}, since they cancel in the ratio. The following discussion is therefore also applicable to scenarios where the couplings are too small to produce a significant number of single slepton events at the LHC but where the $\tilde{\tau}_1$ LSP is produced in cascade decays of pair produced SUSY particles.
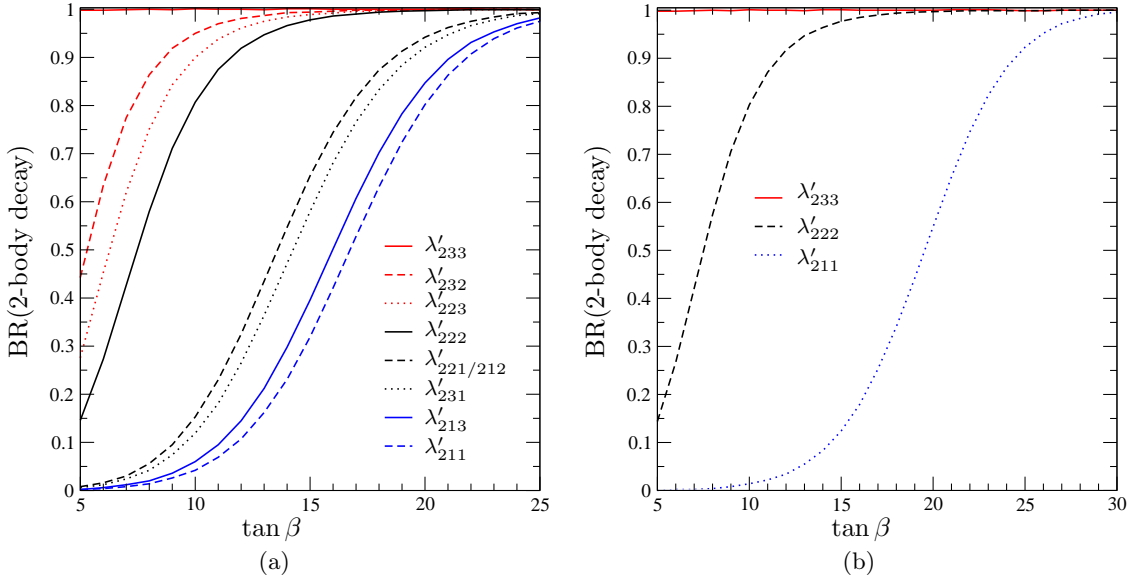
Figure 8.5.: 2-body decay branching ratio as a function of $\tan\beta$ for different dominating λ'_{2jk} couplings at the GUT scale. The mSUGRA parameters are $M_0 = 0$ GeV, $M_{1/2} = 500$ GeV, $A_0 = 600$ GeV, $\mathrm{sgn}(\mu) = +1$. The quark mixing is in the (a) down sector, (b) up sector (couplings λ'_{2jk} for which the 2-body decay branching ratio nearly vanishes are not shown).

For the numerical implementation, we use `Softsusy 2.0.10` [75] to calculate the mass spectrum at the SUSY scale, Q_{SUSY}, Eq. (8.20). In addition, we use our own program to calculate λ'_{ijk} and λ_{i33} at the SUSY scale as described above. We than pipe the mass spectrum and the couplings through `Isawig 1.200`, which is linked to `Isajet 7.75` [194]. `Isajet` calculates the 2-body partial width of the SUSY particles and produces an output for `Herwig` [195]. We use a special version of `Herwig 6.510`[27] which also calculates the 4-body decays of the $\tilde{\tau}_1$ LSP . As an output, we consider the total 2-body decay branching ratio of the $\tilde{\tau}_1$ LSP, BR_2. It is defined as

$$\mathrm{BR}_2 = \frac{1}{1 + \Gamma_4/\Gamma_2}, \tag{8.29}$$

where Γ_2 and Γ_4 denote the sums of the partial widths for the 2- and 4-body decays, respectively.

We first show in Fig. 8.5 the $\tan\beta$ dependence of the 2-body decay branching ratio. We give values for different non-vanishing couplings λ'_{2jk} at the GUT scale and we consider both quark mixing in the down and in the up sector.

Nearly all $\tilde{\tau}_1$ LSPs will decay via a 2-body decay for large values of $\tan\beta$, i.e. $\tan\beta \gtrsim 30$,

---

[27]The version of `Herwig` used in this paper was written by Peter Richardson and is available upon request.

and down-type mixing. In case of up-type mixing this is also true for λ'_{211}, λ'_{222} and λ'_{233}.

This behavior can be easily explained with the help of Eq. (8.29). The partial widths Γ_2, Γ_4 can be approximated by [166]

$$\Gamma_2 \ \propto \ \lambda^2_{233} \, m_{\tilde{\tau}_1} \,, \tag{8.30}$$

$$\Gamma_4 \ \propto \ \lambda'^2_{2jk} \, \frac{m^7_{\tilde{\tau}_1}}{m^2_{\tilde{\chi}} m^4_{\tilde{f}}} \,. \tag{8.31}$$

$m_{\tilde{\chi}}$ denotes the mass of the relevant gaugino and $m_{\tilde{f}}$ denotes the mass of the virtual sfermion which couples directly to $L_2 Q_j \overline{D}_k$, Fig. 8.3. As we argued above, the generated coupling λ_{233} scales roughly with $\tan^2\beta$, cf.Eq. (8.22). Therefore, Γ_2 scales with $\tan^4\beta$. At the same time, λ'_{211} is hardly affected by $\tan\beta$. This is the main effect that enhances BR$_2$ for large $\tan\beta$. Furthermore, increasing $\tan\beta$ increases the contribution from the tau Yukawa couplings to the various RGEs. This is encoded in the function X_τ, Eq. (8.10) which is proportional to $(1 + \tan^2\beta)$. As can be seen in Eq. (8.10), increasing $\tan\beta$ and X_τ reduces the mass of the right- and left-handed stau and therefore, with Eq. (8.8), the mass of the $\tilde{\tau}_1$ LSP, $m_{\tilde{\tau}_1}$. Furthermore, the off-diagonal matrix elements B^{LR} of the stau mass matrix also increase with $\tan\beta$. This leads to a stronger mixing between the right- and left-handed stau and lowers the mass of the $\tilde{\tau}_1$, cf. Eq. (8.8). Note that Γ_4/Γ_2 is proportional to $m^6_{\tilde{\tau}_1}$. According to Eq. (8.29), the 2-body decay branching ratio therefore strongly increases for decreasing $m_{\tilde{\tau}_1}$.

We observe in Fig. 8.5(a) also a large hierarchy between the different couplings λ'_{2jk}. For example, a dominant λ'_{233} coupling leads to BR$_2 \approx 100\%$ for any value of $\tan\beta$, whereas for λ'_{211} this is only the case for $\tan\beta \gtrsim 25$. This hierarchy reflects the hierarchy of the down quark Yukawa matrix elements, Eq. (8.21), which enter as the dominant term in the RGE of λ_{233}, Eq. (8.17b).

For up-type quark mixing, Fig. 8.5(b), and $j \neq k$ the down-quark Yukawa matrix elements and therefore BR$_2$ are nearly vanishing.

We investigate the dependence of BR$_2$ on A_0 in Fig. 8.6(a), for a dominant coupling λ'_{211} and down-type mixing. We see a minimum at $A_0 \approx 250\,\text{GeV}$. Here, BR$_2$ is reduced by up to 70% compared to $A_0 = \pm 1\,\text{TeV}$. The minimum and the position of the minimum is dominated by the following two effects.

The right-handed stau couples to a left-handed stau (tau sneutrino) and a neutral Higgs boson (charged Higgs boson) via a trilinear scalar interaction $(\mathbf{a}_E)_{33}$, cf. Eq. (2.51). The coupling $(\mathbf{a}_E)_{33}$ has dimension one and in mSUGRA models it is equal to $A_0 \times (\mathbf{Y}_E)_{33}$ at the GUT scale. The RGE of the right-handed scalar tau mass, $m_{\tilde{\tau}_R}$, depends in the following way on $(\mathbf{a}_E)^2_{33}$ [166]:

$$\frac{dm^2_{\tilde{\tau}_R}}{dt} = +4(\mathbf{a}_E)^2_{33} + \dots \,. \tag{8.32}$$
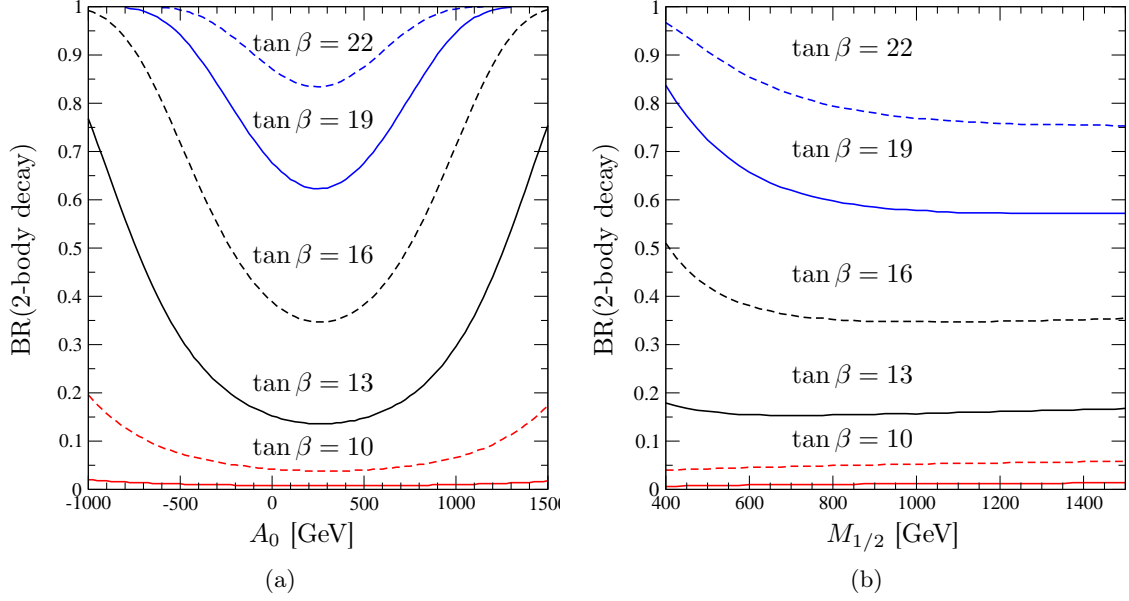
Figure 8.6.: 2-body decay branching ratio as a function of (a) A_0 (with $M_{1/2} = 500$ GeV) and (b) $M_{1/2}$ (with $A_0 = 600$ GeV) for non vanishing λ'_{211} at the GUT scale and different $\tan\beta$. We assume quark mixing in the down sector and consider $M_0 = 0$ GeV, $\mathrm{sgn}(\mu) = +1$. The lowest curve (solid red) corresponds to $\tan\beta = 7$.

This term decreases $m_{\tilde{\tau}_R}$ when we go from the GUT scale to the SUSY scale Q_{SUSY} due to the plus sign. The (negative) contribution of this term to $m_{\tilde{\tau}_R}^2$ is proportional to the integral of $(\mathbf{a}_E)_{33}^2$ from $t_{\min} = \ln(\Lambda_{\mathrm{GUT}})$ to $t_{\max} = \ln(m_Z)$. For the mSUGRA parameters given in Fig. 8.6(a), $M_0 = 0$ GeV, $M_{1/2} = 500$ GeV, $\mathrm{sgn}(\mu) = +1$, the integral of $(\mathbf{a}_E)_{33}^2$ is minimal at $A_0 \approx 180$ GeV and, therefore, $m_{\tilde{\tau}_R}$ is maximal. For $m_{\tilde{\tau}_1} = m_{\tilde{\tau}_R}$ this also leads to a maximum of $\Gamma_4/\Gamma_2 \sim m_{\tilde{\tau}_1}^6$ and hence to a minimum of BR_2.

But the lightest stau is an admixture of the right- and left-handed stau. The off-diagonal mass matrix elements B^{LR} also depend on the value of $(\mathbf{a}_E)_{33}$ at Q_{SUSY}, parameterized through $A_\tau = (\mathbf{a}_E)_{33}/(\mathbf{Y}_E)_{33}$. For $A_0 = 180$ GeV we find $A_\tau \approx -110$ GeV. A negative value of A_τ enhances the effect of L–R mixing which decreases $m_{\tilde{\tau}_1}$. Therefore, the maximum of $m_{\tilde{\tau}_1}$ as a function of A_0 is shifted to $A_0 \approx 250$ GeV compared to $m_{\tilde{\tau}_R}$. Note however that the A_τ dependence of stau L–R mixing is sub-dominant around the minimum because of $\mu \tan\beta \gg A_\tau$.

Next, we study the dependence of BR_2 on the universal gaugino mass $M_{1/2}$. We show this behavior in Fig. 8.6(b), again for a dominant λ'_{211} and down-type mixing. The 2-body decay branching ratios approach a constant value for increasing $M_{1/2}$. Both, the squared mass of the gauginos, Eq. (8.11), and the squared masses of the sfermions, Eq. (8.7), depend

186
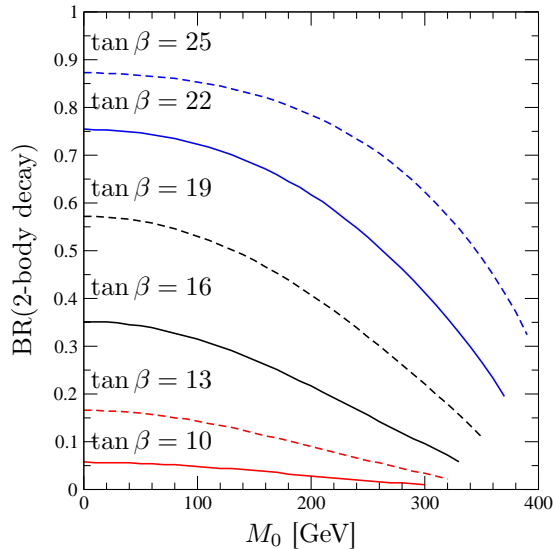
Figure 8.7.: 2-body decay branching ratio as a function of M_0 for non vanishing λ'_{211} at the GUT scale and different $\tan\beta$. We assume quark mixing in the down sector. The other mSUGRA parameters are $M_{1/2} = 1400$ GeV, $A_0 = 600$ GeV, sgn(μ) = +1.

linearly on $M_{1/2}^2$. Therefore,

$$\lim_{M_{1/2}\to\infty} \Gamma_4/\Gamma_2 \propto \frac{m_{\tilde{\tau}_1}^6}{m_{\tilde{\chi}}^2 m_{\tilde{f}}^4} = \text{constant}. \tag{8.33}$$

The dependence of BR_2 on $M_{1/2}$ for $M_{1/2} \lesssim 1$ TeV is more involved, because the ratio Γ_4/Γ_2 depends also on the other mSUGRA parameters, mainly through the running sfermion masses, cf. Eq. (8.7). For example, we observe in Fig. 8.6(b) that the slope of BR_2 for $M_{1/2} \lesssim 1$ TeV strongly depends on $\tan\beta$. For $\tan\beta = 10$, the slope is small and positive whereas for $\tan\beta \gtrsim 13$ the slope is negative. The magnitude of the slope also increases when we consider larger values of $\tan\beta$. This behavior is again related to the tau Yukawa coupling $(\mathbf{Y}_E)_{33}$ and its effects on the $\tilde{\tau}_1$ mass described by the function X_τ, Eq. (8.10). For large values of $M_{1/2}$, the influence of X_τ on the $\tilde{\tau}_1$ mass nearly vanishes. But as we go to smaller values of $M_{1/2}$ the (negative) contributions due to $(\mathbf{Y}_E)_{33}$ become more and more important. For example, for $\tan\beta = 22$ and $M_{1/2} = 1$ TeV ($M_{1/2} = 400$ GeV) the X_τ term reduces the mass of the right-handed stau by 3% (10%) compared to vanishing $(\mathbf{Y}_E)_{33}$. This reduction of $m_{\tilde{\tau}_1}$ will also reduce Γ_4/Γ_2 resulting in an increase of BR_2. This effect is more pronounced for large $\tan\beta$ because X_τ is proportional to $(1 + \tan^2\beta)$. If we neglect the effect of $(\mathbf{Y}_E)_{33}$, the BR_2 curves in Fig. 8.6(b) all get a small positive slope.

Finally, we show in Fig. 8.7 the dependence of BR_2 on the universal soft-breaking scalar mass M_0. Here, we have chosen a rather large value of $M_{1/2}$, $M_{1/2} = 1400$ GeV, because

187

(a)   (b)
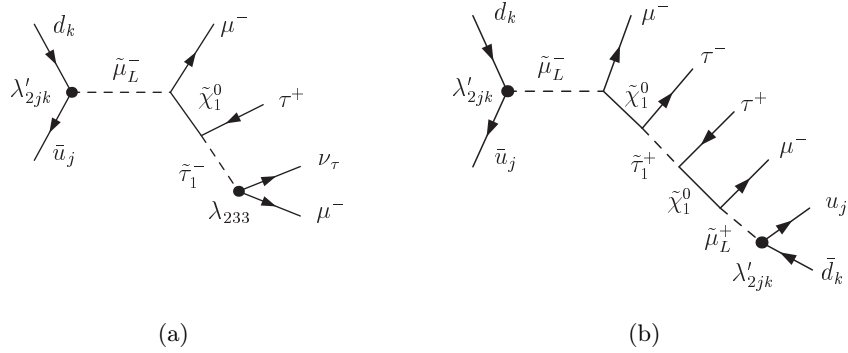
Figure 8.8.: Example Feynman graphs for single slepton production in $\tilde{\tau}_1$ LSP scenarios where the slepton decay proceeds (a) via the generated λ_{233} coupling (2-body decay mode) and (b) via the dominant λ'_{2jk} coupling (4-body decay mode).

otherwise a $\tilde{\tau}_1$ LSP would exist only in a small interval of M_0. The lines in the Figure terminate at values of M_0 above which the $\tilde{\tau}_1$ is no longer the LSP.

The behavior of BR_2 can easily be understood. Increasing M_0 increases the mass of the sfermions, Eq. (8.7), but not the mass of the gauginos. Therefore, the nominator of $\Gamma_4/\Gamma_2 \propto m_{\tilde{\tau}_1}^6/(m_{\tilde{\chi}}^2 m_{\tilde{f}}^4)$ is a polynomial of order $\mathcal{O}(M_0^6)$, whereas the denominator is only a polynomial of order $\mathcal{O}(M_0^4)$. Therefore, the 2-body decay branching ratios fall off for increasing M_0 as shown in Fig. 8.7.

8.3 Resonant single slepton production at the LHC

We now apply the previous discussion to resonant single slepton production in B$_3$ mSUGRA scenarios with a $\tilde{\tau}_1$ LSP. Charged sleptons $\tilde{\ell}_{Li}$ and sneutrinos $\tilde{\nu}_i$ can be produced singly on resonance at the LHC via $q_k \bar{q}_j$ annihilation processes. The production cross section is proportional to $|\lambda'_{ijk}|^2$ and therefore large slepton production rates are expected in scenarios with a dominant λ'_{ijk} coupling. The RGE generation of λ_{i33} is important for the subsequent slepton decay in $\tilde{\tau}_1$ LSP scenarios. As discussed in the previous section, a non-vanishing λ_{i33} introduces new 2-body decay channels for the $\tilde{\tau}_1$ LSP. The interplay of these 2-body decays and the 4-body decays via λ'_{ijk} determines the final-state signatures. In Fig. 8.8, example Feynman graphs for single slepton production and the subsequent decay in $\tilde{\tau}_1$ LSP scenarios are shown.

This section is divided into a phenomenological investigation of slepton production in general, Section 8.3.1, and an explicit numerical example (single smuon production), including a detailed analysis of final-state signatures and a discussion of the background.

8.3.1 Slepton production and slepton decays

It is the aim of this section to first give a general overview of the possible final states for these reactions, see Section 8.3.1, and second to discuss the special cases $\lambda'_{2jk} \neq 0|_{\mathrm{GUT}}$ and $\lambda'_{3jk} \neq 0|_{\mathrm{GUT}}$ in more detail (Sects. 8.3.1 and 8.3.1).

General signatures

In the last section, the ratio of 2- to 4-body $\tilde{\tau}_1$ LSP decay rates and its dependence on various SUSY parameters has been studied. Now, we focus on single slepton production in $\tilde{\tau}_1$ LSP scenarios and are interested in the general decay patterns, independent of the precise SUSY parameters. We first give an overview over all possible final states and signatures which could be used as the starting point for an experimental analysis.

A (left-handed) charged slepton or sneutrino can be produced directly via λ'_{ijk} and has several decay modes:

$$\bar{u}_j\, d_k \to \tilde{\ell}^-_{Li} \to \left\{ \begin{array}{l} \bar{u}_j d_k \\ \ell^-_i\, \tilde{\chi}^0_m \\ \nu_i\, \tilde{\chi}^-_n \end{array} \right. , \qquad (8.34)$$

$$\bar{d}_j\, d_k \to \tilde{\nu}_i \to \left\{ \begin{array}{l} \bar{d}_j\, d_k \\ \nu_i\, \tilde{\chi}^0_m \\ \ell^-_i\, \tilde{\chi}^+_n \end{array} \right. . \qquad (8.35)$$

Both can decay via the B_3 coupling, which is the inverse production process. It is however suppressed by $|\lambda'_{ijk}|^2$. If $\lambda'_{ijk} \leq \mathcal{O}(10^{-2})$, it contributes typically at the percent level. The dominant decay channels are 2-body decays into a lepton-gaugino pair. Further 3- and more-body decays are expected to be negligible, due to phase space suppression.

In case of $j = 3$, the hadronic production of a charged slepton cannot proceed via two quarks as given in Eq. (8.34), due to the vanishing top-quark parton density inside a proton. Instead, the slepton can for example be produced via a $g\bar{d}_k$ initiated Compton process in association with a single top quark. Furthermore, the decay into $t\bar{d}_k$ may be kinematically forbidden. In this case, the slepton decays into a $Wb\bar{d}_k$ final state (cf. Appendix C.2). Sneutrino production for $j = 3$ is possible, Eq. (8.35), but due to the low bottom-quark density small cross sections are expected. We do not consider $j = 3$ any further here and refer the reader to [175, 196] for a detailed investigation of this topic.

For the following discussion, we assume that the produced slepton predominantly decays into a lepton and the lightest neutralino. This assumption is motivated by the fact that we consider $\tilde{\tau}_1$ LSP scenarios. In these scenarios, sleptons are light compared to gauginos and decays into heavier neutralinos or charginos will be kinematically excluded or strongly suppressed. See also the computed branching ratios in explicit SUSY models in [167].

The produced $\tilde{\chi}_1^0$ is not the lightest SUSY particle and will decay further into the $\tilde{\tau}_1$ LSP,

$$\tilde{\chi}_1^0 \rightarrow \tau^{\mp} \tilde{\tau}_1^{\pm}. \tag{8.36}$$

Since the neutralino is a Majorana fermion, both charge conjugated decays are possible. In most $\tilde{\tau}_1$ LSP scenarios this is the only possible decay mode of the neutralino. However, in some scenarios, the right-handed sleptons $\tilde{\mu}_R$ and $\tilde{e}_R$ are lighter than the $\tilde{\chi}_1^0$ and the additional channels $\tilde{\chi}_1^0 \rightarrow \tilde{\ell}_R^{\pm} \ell^{\mp}$ are open (for $\ell = \mu, e$). The $\tilde{\ell}_R$ subsequently decays into the $\tilde{\tau}_1$ LSP, a τ, and a lepton via a virtual neutralino

$$\tilde{\chi}_1^0 \rightarrow \ell^{\mp} \tilde{\ell}_R^{\pm}, \qquad \tilde{\ell}_R^{\pm} \rightarrow \begin{cases} \ell^{\pm} \tau^{\mp} \tilde{\tau}_1^{\pm} \\ \ell^{\pm} \tau^{\pm} \tilde{\tau}_1^{\mp} \end{cases}. \tag{8.37}$$

These decay chains have smaller BRs than the decays in Eq. (8.36). However, they lead to an additional lepton pair in the final state and could be, therefore, of special interest for experimental analyses.

Scenarios with $\lambda'_{2jk} \neq 0|_{\mathrm{GUT}}$, $\lambda_{233} \ll \lambda'_{2jk}$

Let us now study more detailed the final-state signatures in a scenario with $\lambda'_{2jk} \neq 0|_{\mathrm{GUT}}$ and a generated λ_{233} coupling which is small but non-zero at lower scales. In these scenarios, resonant single $\tilde{\mu}_L$ and resonant single $\tilde{\nu}_\mu$ production at hadron colliders is possible,

$$\bar{u}_j \, d_k \rightarrow \tilde{\mu}_L^- \rightarrow \bar{u}_j \, d_k / \mu^- \, \tilde{\chi}_1^0,$$
$$\bar{d}_j \, d_k \rightarrow \tilde{\nu}_\mu \rightarrow \bar{d}_j \, d_k / \nu_\mu \, \tilde{\chi}_1^0. \tag{8.38}$$

As explained above, a small fraction of the sleptons decay via the inverse production process. They predominantly decay into a lepton and the lightest neutralino, $\tilde{\chi}_1^0$. The decays involving heavier neutralinos or charginos are typically not accessible.

The difference between $\tilde{\mu}_L$ and $\tilde{\nu}_\mu$ production concerns the flavor of the initial quarks (which is related to different parton density functions and is thus important for the hadronic cross sections), and the nature of the lepton resulting from the slepton decay. In both processes a neutralino is produced in the predominant decay, which in turn decays into the $\tilde{\tau}_1$ LSP, Eqs. (8.36) and (8.37). Finally, the $\tilde{\tau}_1$ decays either via the dominant λ'_{2jk} coupling (4-body decay) or via the generated λ_{233} coupling (2-body decay). For the 4-body decays, only the decays via virtual neutralinos have to be considered. Decay modes via virtual charginos are suppressed due to the larger mass and their weaker couplings to the predominantly right-handed $\tilde{\tau}_1$ LSP. The complete cascade decay chains are listed in Tab. 8.3.

A classification of all possible final-state signatures is given in Tab. 8.4, for $\tilde{\mu}_L$ and for $\tilde{\nu}_\mu$ production. For completeness, we include here the direct B$_3$ decays via λ'_{2jk}, which

	$\bar{u}_j \, d_k \xrightarrow{\lambda'} \tilde{\mu}_L^- \longrightarrow \bar{u}_j \, d_k / \mu^- \, \tilde{\chi}_1^0$	
	or	
	$\bar{d}_j \, d_k \xrightarrow{\lambda'} \tilde{\nu}_\mu \longrightarrow \bar{d}_j \, d_k / \nu_\mu \tilde{\chi}_1^0$	
	$\tilde{\chi}_1^0 \to \tau^+ \, \tilde{\tau}_1^-$ $\left[\tilde{\chi}_1^0 \to \tau^+ \, \tilde{\tau}_1^- \, \ell^+ \ell^- \right]$	$\tilde{\chi}_1^0 \to \tau^- \, \tilde{\tau}_1^+$ $\left[\tilde{\chi}_1^0 \to \tau^- \, \tilde{\tau}_1^+ \, \ell^- \ell^+ \right]$
λ'_{2jk}	$\tilde{\tau}_1^- \to \tau^- \mu^- \, u_j \, \bar{d}_k$ $\tilde{\tau}_1^- \to \tau^- \mu^+ \bar{u}_j d_k$ $\tilde{\tau}_1^- \to \tau^- \nu_\mu \, d_j \, \bar{d}_k$ $\tilde{\tau}_1^- \to \tau^- \bar{\nu}_\mu \, \bar{d}_j \, d_k$	$\tilde{\tau}_1^+ \to \tau^+ \mu^+ \, \bar{u}_j \, d_k$ $\tilde{\tau}_1^+ \to \tau^+ \mu^- \, u_j \, \bar{d}_k$ $\tilde{\tau}_1^+ \to \tau^+ \bar{\nu}_\mu \, \bar{d}_j \, d_k$ $\tilde{\tau}_1^+ \to \tau^+ \nu_\mu \, d_j \, \bar{d}_k$
λ_{233}	$\tilde{\tau}_1^- \to \tau^- \nu_\mu$ $\tilde{\tau}_1^- \to \tau^- \bar{\nu}_\mu$ $\tilde{\tau}_1^- \to \mu^- \nu_\tau$	$\tilde{\tau}_1^+ \to \tau^+ \bar{\nu}_\mu$ $\tilde{\tau}_1^+ \to \tau^+ \nu_\mu$ $\tilde{\tau}_1^+ \to \mu^+ \bar{\nu}_\tau$

Table 8.3.: Slepton decay chains with all possible final states for single $\tilde{\mu}_L^-$ and single $\tilde{\nu}_\mu$ production via λ'_{2jk}, respectively. The charge conjugated processes are not shown explicitly. Slepton decays into heavier neutralinos or charginos are neglected. The $\tilde{\chi}_1^0$ decays predominantly into a $\tilde{\tau}_1$ LSP and a τ. In some scenarios, decays as in Eq. (8.37) are possible, they are cited in brackets. Owing to the Majorana type nature of the neutralino two charge conjugated decays of the neutralino are possible (second and third column). In the first column the B$_3$ coupling involved in the subsequent 4- or 2-body $\tilde{\tau}_1$ decays are given.

usually contribute at the percent level for couplings at the order of $\mathcal{O}(10^{-2})$. Neutrinos do not give a signal in a detector and are denoted as missing transverse energy $\not{E}_T$. Final state quarks are treated as indistinguishable jets j.

The 4-body decays via λ'_{2jk} and the 2-body decays via the inverse production process lead to two jets in the final state. In contrast, the 2-body decays via λ_{233} are purely leptonic. Many cascade decay chains provide missing transverse energy. Furthermore, since we are considering $\tilde{\tau}_1$ LSP scenarios, there is always at least one τ among the final state particles. The experimentally most promising signatures are probably those involving a large number of muons, e. g. like-sign dimuons and three or four final-state muons. If the $\tilde{\chi}_1^0$ decays only into $\tilde{\tau}_1 \tau$, there are two signatures including like-sign dimuons for $\tilde{\mu}_L$ production. For $\tilde{\nu}_\mu$ production, muons can be produced singly only. But if the decays Eq. (8.37) are open, both slepton production processes allow for dimuon and trimuon production. In case of $\tilde{\mu}_L$ production, even four final state muons are possible. Additionally, depending on how easily taus will be identified, an analysis could be based on like-sign $\mu\tau$-pairs.

The final-state signatures depend sensitively on which particle is the LSP. Compared to slepton production in the $\tilde{\chi}_1^0$ LSP scenarios [181–183,185], there are three main differences here. First, for a $\tilde{\tau}_1$ LSP we have always one or two taus in the final state, which in $\tilde{\chi}_1^0$ LSP scenarios is only possible for smuon production if heavier neutralinos are involved in the

	$\tilde{\mu}_L^-$ production					$\tilde{\nu}_\mu$ production				
λ'_{2jk}	$\tau^+\tau^-$	$\mu^-\mu^\pm$			jj	$\tau^+\tau^-$	$\mu^\pm$		$\not{E}_T$	jj
	$\tau^+\tau^-$	μ^-		$\not{E}_T$	jj	$\tau^+\tau^-$			$\not{E}_T$	jj
	$[\,\tau^+\tau^-$	$\mu^-\mu^-\mu^\pm\mu^+$			$jj\,]$	$[\,\tau^+\tau^-$	$\mu^-\mu^\pm\mu^+$		$\not{E}_T$	$jj\,]$
	$[\,\tau^+\tau^-$	$\mu^-\mu^-\mu^+$		$\not{E}_T$	$jj\,]$	$[\,\tau^+\tau^-$	$\mu^-\mu^+$		$\not{E}_T$	$jj\,]$
	$[\,\tau^+\tau^-$	$\mu^-\mu^\pm$	e^+e^-		$jj\,]$	$[\,\tau^+\tau^-$	$\mu^\pm$	e^+e^-	$\not{E}_T$	$jj\,]$
	$[\,\tau^+\tau^-$	μ^-	e^+e^-	$\not{E}_T$	$jj\,]$	$[\,\tau^+\tau^-$		e^+e^-	$\not{E}_T$	$jj\,]$
λ_{233}	$\tau^\pm$	$\mu^-\mu^\mp$		$\not{E}_T$		$\tau^\pm$	$\mu^\mp$		$\not{E}_T$	
	$\tau^+\tau^-$	μ^-		$\not{E}_T$		$\tau^+\tau^-$			$\not{E}_T$	
	$[\,\tau^\pm$	$\mu^-\mu^-\mu^\mp\mu^+$		$\not{E}_T$	$]$	$[\,\tau^\pm$	$\mu^-\mu^\mp\mu^+$		$\not{E}_T$	$]$
	$[\,\tau^+\tau^-$	$\mu^-\mu^-\mu^+$		$\not{E}_T$	$]$	$[\,\tau^+\tau^-$	$\mu^-\mu^+$		$\not{E}_T$	$]$
	$[\,\tau^\pm$	$\mu^-\mu^\mp$	e^+e^-	$\not{E}_T$	$]$	$[\,\tau^\pm$	$\mu^\mp$	e^+e^-	$\not{E}_T$	$]$
	$[\,\tau^+\tau^-$	μ^-	e^+e^-	$\not{E}_T$	$]$	$[\,\tau^+\tau^-$		e^+e^-	$\not{E}_T$	$]$
inv. prod.					jj					jj

Table 8.4.: Summary of all possible final states for single slepton production via λ'_{2jk}. Decays involving the dominant λ'_{2jk} coupling and involving the generated λ_{233} coupling are listed separately, cf. Tab. 8.3. If kinematically allowed, the $\tilde{\chi}_1^0$ may also decay into a light-flavor lepton-slepton pair which gives rise to an additional $\mu^+\mu^-$ or e^+e^- pair in the final state. The corresponding signatures are given in brackets. The decay via the inverse production process is also listed.

decay chain. These heavy neutralinos then decay into the lightest neutralino and possibly taus. Second, the generation of a λ coupling can be neglected in $\tilde{\chi}_1^0$ LSP scenarios. As argued above, λ only allows for additional 3-body decays which are thus not phase-space enhanced compared to the 3-body decays via the dominant λ' coupling. As a consequence, purely leptonic final-state signatures are absent in $\tilde{\chi}_1^0$ LSP scenarios. Third, due to the modified spectra in $\tilde{\chi}_1^0$ LSP scenarios, also $\tilde{\nu}_\mu$ production can provide like-sign dimuon events. In this case, $\tilde{\nu}_\mu$ can often decay into a μ and a chargino. Like-sign dimuons arise either if the chargino directly decays via λ' into a μ and two quarks, or if the chargino first decays into the $\tilde{\chi}_1^0$ LSP and then the $\tilde{\chi}_1^0$ LSP decays via λ' into a μ and two quarks.

This discussion can easily be translated to scenarios with $\lambda'_{1jk} \neq 0$ by replacing the muons by electrons (and vice-versa). Since there is typically no difference in mass between sleptons of the first and second generation, respectively, the kinematics are the same. Note however that the bounds on the B_3 couplings are stronger for λ'_{1jk} than for λ'_{2jk} for example due to the non-observation of neutrinoless double beta decay.

Scenarios with $\lambda'_{3jk} \neq 0|_{\mathrm{GUT}}$

Some additional remarks are in order for a dominant λ'_{3jk} B_3 coupling. These couplings allow for resonant single $\tilde{\nu}_\tau$ production and, owing to the L–R mixing in the stau-sector, also both resonant $\tilde{\tau}_1$ and $\tilde{\tau}_2$ production ($j \neq 3$).

For $\tilde{\tau}_1$ production, we refer to the discussion of LSP decay modes in Section 8.2.1. Here the LSP couples directly to the B_3 operator and the inverse production process dominates the decay rate,

$$\bar{u}_j\, d_k \to \tilde{\tau}_1^- \to \bar{u}_j\, d_k\,. \tag{8.39}$$

Again, this process is kinematically not accessible for $j = 3$ and $m_{\tilde{\tau}_1} < m_t$. Instead, the stau decays into $Wb\bar{d}_k$, cf. Eq. (8.28). Note that $j = 3$ requires associated production, e. g. $g\, d_k \to \tilde{\tau}\, t$, due to the absence of top quarks inside the proton [175,196].

For $\tilde{\tau}_2$ and $\tilde{\nu}_\tau$ production, there are the following 2-body decay modes:

$$\bar{u}_j\, d_k \to \tilde{\tau}_2^- \to \left\{ \begin{array}{l} \bar{u}_j\, d_k \\ \tau^-\, \tilde{\chi}_1^0 \\ \tilde{\tau}_1^-\, h^0/Z^0 \end{array} \right. , \qquad \bar{d}_j\, d_k \to \tilde{\nu}_\tau \to \left\{ \begin{array}{l} \bar{d}_j\, d_k \\ \nu_\tau\, \tilde{\chi}_1^0 \\ \tilde{\tau}_1^-\, W \end{array} \right. . \tag{8.40}$$

The inverse production process contributes and leads to a jj final state. The decay into a lepton and a neutralino often dominates for small $\tan\beta$ ($\tan\beta \lesssim 10$). The neutralino decays further into the $\tilde{\tau}_1$ LSP which directly decays into two quarks:

$$\tilde{\chi}_1^0 \to \tau^\pm\, \tilde{\tau}_1^\mp, \qquad \tilde{\tau}_1^- \to \bar{u}_j\, d_k\,, \tag{8.41}$$

where we have included the two charge conjugated decays of the neutralino. The final states of these decay modes are $\tau^- \tau^\pm jj$, and there is the possibility of like-sign tau events. If the $\tilde{\chi}_1^0$ decay (8.37) is kinematically allowed, we can have an additional pair of electrons or muons in the final state.

The singly produced slepton can also decay into the $\tilde{\tau}_1$ LSP and a SM Z^0, h^0, or W boson, respectively (final states: $h^0/Z^0/W\, jj$). This decay mode is special for singly produced sleptons of the third generation because they are L-R mixed eigenstates. It can be the dominant decay mode of the $\tilde{\tau}_2$ and $\tilde{\nu}_\tau$, depending on the parameters.

The branching ratios for all B_3 conserving $\tilde{\tau}_2$ and $\tilde{\nu}_\tau$ 2-body decay modes are given in Tab. C.3 in Appendix C.2, for the SUSY parameter sets A and B.

8.3.2 Single smuon production: An explicit numerical example

In this section, we present explicit calculations of promising signal rates for resonant slepton production at the LHC in the B_3 mSUGRA model with a $\tilde{\tau}_1$ LSP, focussing on parameter sets A and B, cf. Eq. (8.12). First, we consider (exclusive) like-sign dimuon events, i. e. events with exactly two muons of the same charge in the final state. An analysis of SM and SUSY backgrounds for the like-sign dimuon signature is also given. Second, we present event rates for single smuon production leading to three or four muons in the final states, which are kinematically accessible within sets A and B.

Like-sign dimuon events

Following Refs. [181], we first concentrate on events with exclusive like-sign dimuons. Here events with more than two muons are rejected. In this sense, in $\tilde{\tau}_1$ LSP scenarios, only single smuon production leads to exclusive like-sign dimuon pairs, cf. Tab. 8.4. It has been shown in [181] that this selection criterion enhances the signal to background ratio considerably: Using a set of cuts, the SM background rate at the LHC, $\Gamma_B|_{\mathrm{SM}}$, can be reduced to

$$\Gamma_B|_{\mathrm{SM}} = 4.9 \pm 1.6 \text{ events}/10 \text{ fb}^{-1}. \tag{8.42}$$

At the same time the cut efficiency, i. e. the number of signal events which pass the cuts, lies roughly between 20% and 30%. Note that Refs. [181] assume a $\tilde{\chi}_1^0$ LSP. As we will argue below, similar cuts are also applicable in $\tilde{\tau}_1$ LSP scenarios. For the numbers presented in this section, however, no cuts are applied and full cross sections and event rates are given.

The total cross section for like-sign dimuon events is obtained from the resonant $\tilde{\mu}_L^+$ or $\tilde{\mu}_L^-$ production cross section multiplied by the respective branching ratios leading to like-sign dimuon final states. Both decays via the dominant λ'_{2jk} coupling and a generated λ_{233} coupling contribute. For a negatively charged smuon they are:

$$
\begin{aligned}
\bar{u}_j \, d_k \xrightarrow{\lambda'} \tilde{\mu}_L^- \to &\, \mu^- \, \tilde{\chi}_1^0 \\
&\hookrightarrow \tau^+ \, \tilde{\tau}_1^- \\
&\qquad \xrightarrow{\lambda'} \tau^- \mu^- \, u_j \, \bar{d}_k \,, \\
&\qquad \xrightarrow{\lambda} \nu_\tau \, \mu^- \,, \\
&\hookrightarrow \tau^- \, \tilde{\tau}_1^+ \\
&\qquad \xrightarrow{\lambda'} \tau^+ \mu^- \, u_j \, \bar{d}_k \,,
\end{aligned} \tag{8.43}
$$

plus the analogous decay chains where the neutralino decays first into an $\tilde{e}_R^\pm$-$e^\mp$ pair, cf. Eq. (8.37). The couplings depicted on the arrows indicate the employed B_3 coupling. The decay chain for a positively charged smuon follows from charge conjugation. However, one should keep in mind that the production cross sections for $\tilde{\mu}_L^+$ and $\tilde{\mu}_L^-$ differ at PP colliders, since charge conjugated quarks (and corresponding parton densities) are involved.

The cross sections for the exclusive like-sign dimuon final states are presented in Tab. 8.5 for Set A and in Tab. 8.6 for Set B. The smuon production cross sections, $\sigma_{\mathrm{prod.}}(\tilde{\mu}_L^\mp)$ (see also Tabs. C.1 and C.2), include NLO QCD and SUSY-QCD corrections [187], see Appendix C.1. For the numerical analysis, we only consider couplings λ'_{2jk} that involve partons of the first generation leading to large production cross sections at the LHC.

As already discussed, the $\tilde{\tau}_1$ LSP can either decay via λ' (4-body decay) or via λ (2-body decay). A list of the respective branching ratios is given in Appendix C.1, Tab. C.4, for

Set A		up-type mixing		down-type mixing	
$\lambda'_{2jk} = 0.002\vert_{\text{GUT}}$ $\sigma_{\text{prod.}}(\tilde{\mu}_L^{\mp})$		$\sigma_{\text{prod.}} \times \text{BR}_{\lambda'}$	$\sigma_{\text{prod.}} \times \text{BR}_{\lambda}$	$\sigma_{\text{prod.}} \times \text{BR}_{\lambda'}$	$\sigma_{\text{prod.}} \times \text{BR}_{\lambda}$
λ'_{211}	$\mu^-\mu^-$ 61.6	11.1	0.71	9.81	2.09
	$\mu^+\mu^+$ 108	19.4	1.25	17.2	3.66
λ'_{221}	$\mu^-\mu^-$ 42.0	7.84	–	4.51	3.88
	$\mu^+\mu^+$ 16.2	3.03	–	1.74	1.50
λ'_{212}	$\mu^-\mu^-$ 18.6	3.46	–	1.99	1.71
	$\mu^+\mu^+$ 86.0	16.1	–	9.23	7.94
λ'_{213}	$\mu^-\mu^-$ 8.80	1.67	–	1.32	0.40
	$\mu^+\mu^+$ 49.8	9.43	–	7.43	2.24

Table 8.5.: Cross sections for exclusive like-sign dimuon ($\mu^-\mu^-$ or $\mu^+\mu^+$) final states at the LHC within Set A. In the left column, we present the single-smuon production cross sections, $\sigma_{\text{prod.}}(\tilde{\mu}_L^{\mp})$, see also Tabs. C.1 and C.2. In the right column, we have folded in the relevant decay branching ratios, in order to obtain like-sign dimuons. All cross sections are given in fb. Where they exist, we have assumed always a cascade of 2-body decays. We consider in turn quark mixing in the up- and down-sector, when determining the dominant $\tilde{\tau}_1$ decay mode. The $\tilde{\tau}_1$ LSP can either decay via λ' (4-body decay) or via λ (2-body decay), cf. Tab. 8.3, which leads to different like-sign dimuon cross sections, $\sigma_{\text{prod.}} \times \text{BR}_{\lambda'}$ and $\sigma_{\text{prod.}} \times \text{BR}_{\lambda}$, respectively. The λ'_{2jk} couplings are in accordance with neutrino mass bounds [166,197]. In case of up-type mixing, larger values of λ'_{2jk} for the four considered couplings are allowed by the neutrino mass bounds. The cross sections scale with $|\lambda'|^2$ and the corresponding rescaling can easily be performed.

sets A and B and for several λ'_{2jk} couplings. Here we show the resulting cross section times branching ratio, $\sigma_{\text{prod.}} \times \text{BR}_{\lambda'}$ and $\sigma_{\text{prod.}} \times \text{BR}_{\lambda}$, for like-sign dimuon events involving $\tilde{\tau}_1$ decays via λ' and λ, respectively, as described in Eq. (8.43).

The total number of exclusive like-sign dimuon events is given by the integrated luminosity multiplied by the total cross section. In Set A with up-type (down-type) quark mixing, we obtain per $10\,\text{fb}^{-1}$,

$$N(\mu^-\mu^- + \mu^+\mu^+)/10\,\text{fb}^{-1} = \left[\sigma_{\text{prod.}}(\tilde{\mu}_L^-) + \sigma_{\text{prod.}}(\tilde{\mu}_L^+)\right] \times \left[\text{BR}_{\lambda'} + \text{BR}_{\lambda}\right] \times 10$$

$$\approx \begin{cases} 325 \;(330) \\ 110 \;(115) \\ 195 \;(210) \\ 110 \;(115) \end{cases} /10\,\text{fb}^{-1} \quad \text{for} \quad \begin{cases} \lambda'_{211} \\ \lambda'_{221} \\ \lambda'_{212} \\ \lambda'_{213} \end{cases} = 0.002\vert_{\text{GUT}}. \qquad (8.44)$$

Note that for up-type mixing, some larger couplings may be considered. From the neutrino mass bounds, also $\lambda'_{211,221,212,213} = 0.01\vert_{\text{GUT}}$ (and even larger) are allowed. The cross sections are proportional to $|\lambda'|^2$ and thus a five times larger coupling implies cross

Set B			up-type mixing		down-type mixing	
$\lambda'_{2jk} = 0.01\vert_{\text{GUT}}$		$\sigma_{\text{prod.}}(\tilde{\mu}_L^{\mp})$	$\sigma_{\text{prod.}} \times \text{BR}_{\lambda'}$	$\sigma_{\text{prod.}} \times \text{BR}_{\lambda}$	$\sigma_{\text{prod.}} \times \text{BR}_{\lambda'}$	$\sigma_{\text{prod.}} \times \text{BR}_{\lambda}$
λ'_{211}	$\mu^- \mu^-$	476	1.04	101	0.21	102
	$\mu^+ \mu^+$	885	1.93	188	0.39	189
λ'_{221}	$\mu^- \mu^-$	309	62.8	–	–	66.2
	$\mu^+ \mu^+$	105	21.4	–	–	22.5
λ'_{212}	$\mu^- \mu^-$	123	25.1	–	–	26.3
	$\mu^+ \mu^+$	681	139	–	–	146
λ'_{213}	$\mu^- \mu^-$	54.6	11.2	–	0.02	11.7
	$\mu^+ \mu^+$	370	75.6	–	0.16	79.4

Table 8.6.: Same as Tab. 8.5 but for single slepton production within Set B. The neutrino mass bounds are less restrictive in the case of Set B and $\lambda'_{2jk} = 0.01\vert_{\text{GUT}}$ are considered for both up- and down-type quark mixing. All cross sections are given in fb.

sections and event numbers multiplied by a factor of 25 compared to those of Tab. 8.5.

For Set B, $\lambda'_{2jk} = 0.01\vert_{\text{GUT}}$ is allowed for both up- and down-type mixing. The numbers of like-sign dimuon events are for up-type (down-type) quark mixing,

$$
N(\mu^- \mu^- + \mu^+ \mu^+)/10\,\text{fb}^{-1} \approx \begin{cases} 2920\,(2920) \\ 840\quad(890) \\ 1640\,(1720) \\ 870\quad(910) \end{cases} /10\,\text{fb}^{-1} \quad \text{for} \quad \begin{cases} \lambda'_{211} \\ \lambda'_{221} \\ \lambda'_{212} \\ \lambda'_{213} \end{cases} = 0.01\vert_{\text{GUT}}. \quad (8.45)
$$

As can be seen in Eqs. (8.44) and (8.45), for each non-zero λ' coupling the total event numbers for up- and down-mixing are of the same order. But as Tabs. 8.5 and 8.6 show, the parts contributing to the event rate can be quite different. In case of up-type mixing and $j \neq k$, the 4-body decays via λ' dominate and the contributions of the 2-body decay are negligible [since the size of the necessary λ coupling is proportional to $(\mathbf{Y}_D)_{jk}$]. In contrast, for down-type mixing all four considered couplings can generate a relatively large λ_{233}, cf. Fig. 8.2(a), and the 2-body decay modes contribute considerably. In Set B, where $\tan\beta$ is large and where thus the fraction of 2-body decays is especially high (see discussion of Fig. 8.5(a)), reliable event numbers are only obtained if the generation of λ_{233} is included in the theoretical framework. Moreover, a measurement of the ratio of 2-body to 4-body $\tilde{\tau}_1$ decays can reveal information about where the quark mixing takes place.

For $j = k$, the generation of a λ coupling is also possible in case of up-type mixing. In Set A, the generated λ_{233} is not large enough to allow for large 2-body decay rates. However in Set B, due to the large $\tan\beta$ value, the 2-body decays dominate over the 4-body decays. Thus, the different $\tilde{\tau}_1$ decay modes contain also information about $\tan\beta$.

We present in Tabs. 8.5 and 8.6 also the total hadronic cross sections for single smuon production, $\sigma_{\mathrm{prod.}}(\tilde{\mu}_L^{\mp})$. Within one parameter set, the cross sections vary strongly for different λ'_{2jk}. This is of course related to corresponding required parton density functions. The largest cross section is obtained for $\lambda'_{211} \neq 0$, i.e. for the processes $\bar{u}\,d \rightarrow \tilde{\mu}_L^-$ and $u\,\bar{d} \rightarrow \tilde{\mu}_L^+$. Smaller cross sections are obtained for $\lambda'_{212} \neq 0$ (involving an up quark and a strange quark) and the smallest cross section for $\lambda'_{221} \neq 0$ (charm quark and down quark) and $\lambda'_{213} \neq 0$ (up quark together with bottom quark).

Since the LHC is a proton-proton collider, there is an asymmetry between the $\tilde{\mu}_L^+$ and $\tilde{\mu}_L^-$ production cross sections. If experimentally a distinction between $\mu^+\mu^+$ and $\mu^-\mu^-$ event rates is found, the ratio can be used to constrain the indices of the non-zero λ'_{2jk} coupling. For example, a non-vanishing coupling λ'_{211} leads to a ratio of $N(\mu^+\mu^+) : N(\mu^-\mu^-) \sim 2 : 1$ in sets A and B, whereas for non-vanishing λ'_{221} the ratio is $1 : 2.5$ in Set A and $1 : 3$ in Set B. The highest event rates are obtained for processes that involve the valence quarks u and d. The charge conjugated processes, involving $\bar{u}$ or $\bar{d}$, are suppressed in comparison. Thus, a larger fraction of $\mu^+\mu^+$ events goes along with $j = 1$ (where the production process is $u\,\bar{d}_k \rightarrow \tilde{\mu}_L^+$) and a larger fraction of $\mu^-\mu^-$ events is related to $k = 1$ and $j \neq 1$ (production process $\bar{u}_j\,d \rightarrow \tilde{\mu}_L^-$).

Discussion of background and cuts for like-sign dimuon final states

In this section, we discuss the background for like-sign dimuon events from the SM and from SUSY particle pair production via gauge interactions. We follow Refs. [181] closely. There, single smuon production via λ'_{211} was investigated assuming a $\tilde{\chi}_1^0$ LSP. A detailed signal over background analysis was performed based on like-sign dimuon events. We argue that a similar or even the same set of cuts might be used to suppress the background in our case and we compare background and signal rates to determine the discovery potential of our analysis.

The main SM background sources are $t\bar{t}$ production, $b\bar{b}$ production, single top production, and gauge boson pair production, i.e. WW, WZ and ZZ production. In Refs. [181], the dominant signature from single smuon production including like-sign dimuon events is

$$\tilde{\mu}_L^- \rightarrow \mu^- \tilde{\chi}_1^0 \rightarrow \mu^- (\mu^- u \bar{d}). \tag{8.46}$$

The two muons of the signal (8.46) are isolated because they stem from different decays of SUSY particles. In addition, the muons carry large momenta since they originate from the decay of (heavy) SUSY particles. The following cuts were proposed to improve the signal over SM background ratio at the LHC:

- A cut on the muon rapidity $|\eta| < 2.0$, thus requiring all the leptons in the central region of the detector,

- a cut on the transverse momentum on each muon: $p_T|_\mu \geq 40$ GeV,

- an isolation cut on each of the muons,

- a cut on the transverse mass of each of the muons, 60 GeV $< M_T < 85$ GeV,

- a veto on the presence of a muon with the opposite charge as the like-sign dimuons,

- a cut on the missing transverse energy, $\not{E}_T \leq 20\,$GeV .

These cuts reduce the SM background to 4.9 ± 1.6 events per 10 fb^{-1} at the LHC , cf. Eq. (8.42). Among the above cuts, the isolation and p_T cut lead to the strongest suppression of the SM background.

We now investigate the case of a $\tilde{\tau}_1$ LSP. If the 4-body decays of the $\tilde{\tau}_1$ LSP, Eq. (8.25), dominate, the leading signature of resonant single smuon production including like-sign dimuon events can be written as

$$\tilde{\mu}_L^- \rightarrow \mu^- \tilde{\chi}_1^0 \rightarrow \mu^- \tau^\mp \tilde{\tau}^\pm \rightarrow \mu^- \tau^\mp (\tau^\pm \mu^- u \bar{d}). \tag{8.47}$$

As above, the muons originate from the decay of heavy particles ($\tilde{\tau}_1$ and $\tilde{\mu}_L$), are in general well isolated, and carry large momenta. Thus, for both signals Eq. (8.46) and Eq. (8.47), the same cuts should allow to discriminate between the signal and the SM background. Furthermore, the additional pair of taus in Eq. (8.47) allows to require one or two (isolated!) taus. This might additionally improve the signal to background ratio.

If the $\tilde{\tau}_1$ LSP predominantly decays via 2-body decay modes, Eq. (8.26), the situation is a bit different. The like-sign dimuon signature is now

$$\tilde{\mu}_L^- \rightarrow \mu^- \tilde{\chi}_1^0 \rightarrow \mu^- \tau^+ \tilde{\tau}^- \rightarrow \mu^- \tau^+ (\mu^- \nu_\tau). \tag{8.48}$$

We again have two isolated muons with large momenta and the same isolation and $p_T|_\mu$ cuts as before should be useful to suppress the SM background. But the neutrino of the $\tilde{\tau}_1$ decay leads to high missing transverse energy $\not{E}_T$ in the signal and an upper bound on $\not{E}_T$ is not appropriate anymore. Alternatively we propose a cut that requires a minimum missing energy, e.g. $\not{E}_T \geq 60$ GeV. This would also reduce the SM background where the main source of $\not{E}_T$ are low-energetic neutrinos from W boson decays. Furthermore, we can again require an additional tau in the final state. Finally, one can exploit the fact that the 2-body decays lead to a pure leptonic final state and a jet veto can be applied.

In Refs. [181], the SUSY background on like-sign dimuon events is suppressed by vetoing all events with more than two jets of $p_T|_{\text{jet}} > 50$ GeV. This cut will also work if the 4-body decay mode of the $\tilde{\tau}_1$ LSP dominates. The 2-body decay modes lead to purely leptonic final states and even no high-p_T jet may be required.

We conclude that for $\tilde{\tau}_1$ LSP scenarios, the background for like-sign dimuon events can be suppressed similarly as it has been proposed for $\tilde{\chi}_1^0$ LSP scenarios in [181].

We thus compare our signal, as given in Eq. (8.44) and Eq. (8.45) for sets A and B respectively, to the background, assuming that cuts as discussed above reduce the SM background to less than 5 events per 10 fb^{-1}, cf.Eq. (8.42). For the signal efficiency, we assume 20%, i.e. 20% of signal events pass the cuts. We neglect systematic errors, at this stage of the analysis.

For Set A a more than 5σ excess over the SM background can be obtained for an integrated luminosity of 10 fb^{-1} for all couplings given in Eq. (8.44). For Set B, a cut efficiency of 20% for the signal corresponds to an excess between $100\,\sigma$ and $300\,\sigma$ for the number of like-sign muon events over the SM background! Therefore, within Set B, couplings can be tested at the LHC down to $\lambda'_{2jk}|_{\mathrm{GUT}} \sim \mathcal{O}(10^{-3})$. But a detailed Monte-Carlo based signal over background analysis remains to be done.

Final states with three and four muons

To round off our studies, we also consider final states with more than two muons. For example, for parameter sets A and B, the $\tilde{\chi}_1^0$ cannot only decay into a $\tilde{\tau}_1$-τ pair but also into a $\tilde{\mu}_R$-μ or $\tilde{e}_R$-e pair. These are kinematically accessible and have non-negligible branching ratios (Set A: 7.0%, Set B: 2.2%; see Tab. C.3). As we have shown in Tab. 8.4, these decays lead to three or even four muons of mixed signs in the final state. Each of the muons stems from the decay of a different SUSY particle. Especially the four-muon final state cannot be found at a high rate in $\tilde{\chi}_1^0$ LSP scenarios and its observation could be a hint for a $\tilde{\tau}_1$ LSP. Therefore, we analyze the three- and four-muon final states in this section. All necessary branching ratios and production cross sections are given in Appendix C.1.

The four–muon events may be classified into $\mu^- \mu^- \mu^- \mu^+$, $\mu^- \mu^- \mu^+ \mu^+$, and $\mu^- \mu^+ \mu^+ \mu^+$ signatures and we introduce the notations $\sigma(---+)$, $\sigma(--++)$, and $\sigma(++ +-)$, for the respective cross sections. The four-muon final states require a long decay chain and many different decays contribute at various stages. For smuon production, summing up all contributions, the cross sections can be written in the following compact form

$$
\begin{aligned}
\sigma_{\tilde{\mu}}(---+) &= \sigma_{\mathrm{prod.}}(\tilde{\mu}_L^-) \times \mathrm{BR}(\tilde{\mu}_L^- \to \tilde{\chi}_1^0 \mu^-) \times \mathrm{BR}(\tilde{\chi}_1^0 \to \tilde{\mu}_R^+ \mu^-) \times P_{\tilde{\tau}_1}(1\mu)\,, \\
\sigma_{\tilde{\mu}}(++ +-) &= \sigma_{\tilde{\mu}}(---+) \times \sigma_{\mathrm{prod.}}(\tilde{\mu}_L^+)/\sigma_{\mathrm{prod.}}(\tilde{\mu}_L^-)\,, \\
\sigma_{\tilde{\mu}}(--++) &= \sigma_{\tilde{\mu}}(---+) + \sigma_{\tilde{\mu}}(++ +-)\,,
\end{aligned}
\tag{8.49}
$$

where $P_{\tilde{\tau}_1}(1\mu) = \mathrm{BR}(\tilde{\tau}_1^- \to \mu^- \ldots) + \mathrm{BR}(\tilde{\tau}_1^+ \to \mu^- \ldots)$ denotes the probability of a negatively charged final state muon in a $\tilde{\tau}_1$ decay. The difference between $\sigma_{\tilde{\mu}}(---+)$ and $\sigma_{\tilde{\mu}}(++ +-)$ stems from the different partons and parton densities involved in the production cross sections.

Smuon production can also lead to exactly three final state charged muons, $\mu^- \mu^- \mu^+$ or $\mu^+ \mu^+ \mu^-$. The corresponding cross sections now involve the probability $P_{\tilde{\tau}_1}(0\mu)$ for a $\tilde{\tau}_1$ decay without a final state muon,

$$
\begin{aligned}
\sigma_{\tilde{\mu}}(--+) &= \sigma_{\text{prod.}}(\tilde{\mu}_L^-) \times \text{BR}(\tilde{\mu}_L^- \to \tilde{\chi}_1^0 \mu^-) \times \text{BR}(\tilde{\chi}_1^0 \to \tilde{\mu}_R^+ \mu^-) \times 2P_{\tilde{\tau}_1}(0\mu), \\
\sigma_{\tilde{\mu}}(++-) &= \sigma_{\tilde{\mu}}(--+) \times \sigma_{\text{prod.}}(\tilde{\mu}_L^+)/\sigma_{\text{prod.}}(\tilde{\mu}_L^-).
\end{aligned}
\tag{8.50}
$$

There are 16 different decay chains of the $\tilde{\mu}_L^-$ leading to a $\mu^- \mu^- \mu^+$ final state. The factor of two in Eq. (8.50) is a consequence of summing over all these decay chains.

The same final-state signatures (exactly three muons) can be obtained via $\tilde{\nu}_\mu$ production. The decay chain is similar to that of a produced smuon. The missing muon from the slepton decay is here replaced by demanding a muon in the final $\tilde{\tau}_1$ decay,

$$
\begin{aligned}
\sigma_{\tilde{\nu}}(--+) &= \left[\sigma_{\text{prod.}}(\tilde{\nu}_\mu) + \sigma_{\text{prod.}}(\tilde{\nu}_\mu^*)\right] \times \text{BR}(\tilde{\nu}_\mu \to \tilde{\chi}_1^0 \nu_\mu) \times \text{BR}(\tilde{\chi}_1^0 \to \tilde{\mu}_R^+ \mu^-) \times P_{\tilde{\tau}_1}(1\mu), \\
\sigma_{\tilde{\nu}}(++-) &= \sigma_{\tilde{\nu}}(--+).
\end{aligned}
\tag{8.51}
$$

The total cross sections for (exactly) three final state muons are then given by

$$
\sigma(\mp \mp \pm) = \sigma_{\tilde{\mu}}(\mp \mp \pm) + \sigma_{\tilde{\nu}}(\mp \mp \pm).
\tag{8.52}
$$

Table 8.7 gives an overview over the numerical results. The same λ' couplings as in the previous Tabs. 8.5 and 8.6, respectively, are considered. The generation of λ_{233} has been taken into account for the $\tilde{\tau}_1$ decays and the cross sections give total numbers, including both 4- and 2-body $\tilde{\tau}_1$ decays.

We find that the sum of three– and four-muon events is in the same order of magnitude as the results for purely like-sign dimuons. For Set A, where $\text{BR}(\tilde{\chi}_1^0 \to \tilde{\mu}_R \mu) = 7\%$, the event numbers are even larger. In Set B, with $\text{BR}(\tilde{\chi}_1^0 \to \tilde{\mu}_R \mu) = 2\%$, the total contributions are smaller by a factor of about three. Depending on the experimental goals, these channels thus give important contributions and should be included in an analysis. On the other hand, these events also suggest to use three or four final state muons as a signal for slepton production since the background is expected to be very low.

	$\sigma(--+)$	$\sigma(++-)$	$\sigma(--++)$	$\sigma(+++-)$	$\sigma(---+)$	$\sum\sigma(--\dots)$	$\sum\sigma(++\dots)$
Set A							
$\lambda'_{211}=0.002\vert_{\mathrm{GUT}}$	9.38 (9.39)	12.9 (13.0)	5.32 (5.26)	3.39 (3.35)	1.93 (1.91)	16.6 (16.6)	21.7 (21.6)
$\lambda'_{221}=0.002\vert_{\mathrm{GUT}}$	5.77 (5.77)	3.84 (3.74)	1.89 (1.77)	0.53 (0.49)	1.36 (1.27)	9.02 (8.81)	6.26 (6.00)
$\lambda'_{212}=0.002\vert_{\mathrm{GUT}}$	4.02 (3.93)	9.05 (9.24)	3.39 (3.17)	2.79 (2.61)	0.60 (0.56)	8.01 (7.66)	15.2 (15.0)
$\lambda'_{213}=0.002\vert_{\mathrm{GUT}}$	2.04 (2.02)	5.14 (5.19)	1.85 (1.80)	1.57 (1.53)	0.28 (0.27)	4.17 (4.09)	8.56 (8.52)
Set B							
$\lambda'_{211}=0.01\vert_{\mathrm{GUT}}$	20.8 (20.8)	29.1 (29.1)	13.4 (13.4)	8.73 (8.73)	4.69 (4.69)	38.9 (38.9)	51.3 (51.3)
$\lambda'_{221}=0.01\vert_{\mathrm{GUT}}$	11.9 (12.0)	7.77 (7.59)	4.08 (3.88)	1.04 (0.98)	3.05 (2.89)	19.1 (18.7)	12.9 (12.4)
$\lambda'_{212}=0.01\vert_{\mathrm{GUT}}$	8.14 (7.98)	19.5 (19.9)	7.93 (7.53)	6.72 (6.39)	1.21 (1.15)	17.3 (16.7)	34.2 (33.8)
$\lambda'_{213}=0.01\vert_{\mathrm{GUT}}$	3.94 (3.85)	10.4 (10.6)	4.20 (4.00)	3.66 (3.48)	0.54 (0.51)	8.68 (8.36)	18.3 (18.1)

Table 8.7.: Cross sections for signals with three or four final state muons within parameter Set A for $\lambda'_{2jk}=0.002$ at Λ_{GUT} and for Set B for $\lambda'_{2jk}=0.01$ at Λ_{GUT} assuming down-type (up-type) quark mixing. Given are the cross sections as defined in Eqs. (8.49)-(8.52) and the sums for two negatively or positively charged muons, $\sum\sigma(--\dots)$ or $\sum\sigma(++\dots)$, respectively. All cross sections are given in femtobarn [fb].

Chapter 9
Conclusions

With the LHC almost ready to start operation, we will soon enter a new era in particle physics. It will be possible to test the Standard Model and the large variety of its extension candidates at energy ranges which were not accessible at particle accelerators before. If supersymmetry is playing a vital role as the extension the Standard Model, there is a good chance that we detect first SUSY signals at the LHC. A precise knowledge of SUSY particle production cross sections and detailed investigations of decay signatures are indispensable for a conclusive discrimination between Standard Model and supersymmetric physics. The work presented here covers topics from both fields of research.

We have studied the hadronic production of pairs of colored SUSY particles, squarks and gluinos, in the framework of the MSSM. If SUSY is realized, colored SUSY particles have large production cross sections at hadron colliders since they are produced via the strong interaction. Pair production of squarks and gluinos is therefore among the most promising SUSY discovery channels at the LHC.

We considered top-squark pair $(\tilde{t}_a \tilde{t}_a^*)$, gluino–squark pair $(\tilde{g}\tilde{q}_a)$, and same-sign squark-squark pair $(\tilde{q}_a \tilde{q}_a)$ production processes and calculated the EW cross section contributions up to $\mathcal{O}(\alpha_s^2 \alpha)$. At this order of perturbation theory, numerous interferences between QCD-mediated and EW-mediated diagrams come into play. Virtual corrections arise from the interference contributions of tree-level QCD amplitudes and mixed EW–QCD one-loop diagrams, as well as from the interference of tree-level EW and pure-QCD one-loop amplitudes. Bremsstrahlung corrections comprise real photon, real gluon and real quark radiation processes. We also included the tree-level EW and EW–QCD interference contributions of $\mathcal{O}(\alpha^2)$ and $\mathcal{O}(\alpha_s \alpha)$ and photon-induced subprocesses of $\mathcal{O}(\alpha_s \alpha)$, if present.

Particular care was taken to obtain IR-finite results. Both photonic and gluonic singularities had to be addressed. We regularized the IR singularities by means of infinitesimal photon, gluon and quark masses, respectively. Real particle radiation processes have been calculated using the phase-space slicing method, isolating the soft and collinear singularities by imposing cuts on the photon and gluon energies and on the separation angles. The universal quark mass logarithms from initial-state collinear singularities have been ab-

sorbed into the quark parton distribution functions by appropriate redefinitions at $\mathcal{O}(\alpha)$ and $\mathcal{O}(\alpha_s)$, respectively. For a consistent treatment, a set of PDFs that includes both NLO QED and NLO QCD effects (MRST 2004 QED) has been used in the calculation of hadronic observables.

Pair production of lighter top-squarks, $\tilde{t}_1 \tilde{t}_1^*$, is of particular interest since these are candidates for the lightest colored SUSY particle in many mSUGRA models and thus highest hadronic cross sections are expected. The $\mathcal{O}(\alpha_s^2 \alpha)$ corrections from $q\bar{q}$ and gg initial states reduce the LO predictions by typically a few percent. The γg fusion process was found to yield contributions of comparable size but opposite sign. In the SPS1a' scenario, the summed EW contributions to the integrated hadronic cross section are below 1%. But they reach the (negative) $10\% - 20\%$ level in differential distributions and are thus significant in the high-p_T and high-$M_{\rm inv}$ regions. The situation is similar in other SUSY scenarios. Outside singular parameter configurations associated with thresholds, the dependence of the EW contributions on the MSSM parameters is rather smooth and moderate.

We also investigated the pair production of the heavier top-squarks, $\tilde{t}_2 \tilde{t}_2^*$. The production cross section is suppressed by the large mass of the final-state particles and the EW contributions are small in absolute size. However the relative NLO EW corrections depend strongly on the top-squark mixing angle and are enhanced for the typically more left-handed $\tilde{t}_2$ eigenstates. As a result, the EW contributions alter the integrated LO cross section by about -15% (in the SPS1a' scenario) and grow even larger in differential distributions.

The sensitivity of the EW contributions to the chirality of the produced particles becomes strongest in case of light-flavor squarks in the final state, when the L–R mixing of the squark gauge eigenstates can be neglected. We performed a detailed numerical analysis of the EW contribution to each case of producing a left- or right-handed, up- or down-type squark in association with a gluino. The EW contributions to $\tilde{g}\tilde{q}_L$ production become sizable in distributions, in particular where the virtual $\mathcal{O}(\alpha_s^2 \alpha)$ and real photon corrections dominate. In case of right-handed squarks in the final state, the impact of EW corrections is negligible. We also investigated the dependence on the masses of the final-state squark and gluino. Whereas these parameters are crucial for the absolute size of the cross section, the relative EW contribution to inclusive gluino–squark production depends only weekly on the masses and ranges at the percent level.

The calculation of EW contributions to the production of pairs of light-flavor squarks is technically the most challenging one. In contrast to the production of third-generation squarks or gluinos, these processes allow for both QCD- and EW-mediated processes that give non-zero interferences already at tree-level. The resulting interference contributions at $\mathcal{O}(\alpha_s^2 \alpha)$ require renormalization at both $\mathcal{O}(\alpha)$ and $\mathcal{O}(\alpha_s)$ and suffer from soft and collinear singularities related to real photon, gluon, and quark radiation processes. Moreover, owing to the chirality and flavor dependence of EW contributions, various classes of diagonal,

non-diagonal and mixed-flavor squark pairs have to be addressed separately. We presented a first investigation of the EW contributions to diagonal same-sign $\tilde{q}_a\tilde{q}_a$ production and gave numerical results for $\tilde{u}_a\tilde{u}_a$ final states.

Previous studies on the production of colored SUSY particles were concentrated on higher-order corrections of QCD origin. The work described in this thesis represents an important step towards a complete one-loop description of all squark and gluino pair production processes at the LHC. Studying the processes of $\tilde{t}_a\tilde{t}_a^*$, $\tilde{g}\tilde{q}_a$, and $\tilde{q}_a\tilde{q}_a$ production, we gained a wide experience in computing EW contributions up to the one-loop level. The investigation of the yet-missing EW contributions to non-diagonal squark–squark and squark–anti-squark production or to processes with bottom-squarks in the final state provides an interesting range of applications to further exploit our methods.

In Chapter 8, we presented the first detailed study on the phenomenology of $\mathcal{R}$-parity violating B$_3$ mSUGRA models with a $\tilde{\tau}_1$ LSP, including an analysis of the distinct $\tilde{\tau}_1$ LSP decay signatures at colliders. Allowing for $\mathcal{R}$-parity violation, the LSP is unstable and can be charged in accordance with cosmological observations. The relatively heavy SUSY particles are expected to decay rapidly via long cascade decay chains to the LSP. The nature of the LSP and its possible decay modes are thus crucial for the identification of SUSY signatures at collider experiments.

We assume only one non-vanishing B$_3$ coupling λ'_{ijk} at the GUT scale. Concerning the possible $\tilde{\tau}_1$ LSP decay modes, we would expect either a 4-body or 2-body decay of the $\tilde{\tau}_1$ LSP depending on whether the dominant B$_3$ operator couples directly to the $\tilde{\tau}_1$ LSP or not. However, because of the CKM mixing of different quark flavors, the RGEs of B$_3$ couplings are highly coupled and further B$_3$ couplings are generated at the weak scale that allow for additional $\tilde{\tau}_1$ LSP decays.

We have numerically investigated the generation of λ_{i33} couplings via dominant λ'_{ijk} couplings for $i \neq 3$ (i.e. the $\tilde{\tau}_1$ does not directly couple to the dominant B$_3$ operator). The generated couplings are typically smaller by at least two orders of magnitude but lead to 2-body LSP decays which have larger phase space and do not involve heavy propagators. A careful analysis of the parameter dependence of the $\tilde{\tau}_1$ LSP decay modes revealed that in large regions of the parameter space the 2-body decay dominates over the 4-body decay.

As an application of our studies, we discussed the resulting signatures of single slepton production at the LHC and provided numerical results for single smuon production within two representative $\tilde{\tau}_1$ LSP scenarios. From the experimental point of view, the final states with like-sign dileptons or more than two charged leptons are of special interest. For the given example sets of parameters, we found cross sections for exclusive like-sign dimuon events of the order of 100 fb. Additional three- and four-muon events can occur with the same rate. This is a novel slepton discovery mechanism and of particular interest also for the experiments at the LHC.

Appendix A

Notations and definitions

In this appendix, we briefly summarize the notations and conventions used in this thesis. In particular, we give the definition for the metric tensor $g_{\mu\nu}$ in Section A.1. Dirac and Pauli matrices are introduced in Section A.2. Details on spinor calculus and properties of Weyl spinors are listed in Section A.3. Finally, we define Dirac and Majorana spinors in Section A.4. All results and input parameters presented in this work are given in natural units, i. e. $\hbar = c = 1$.

A.1 Metric conventions

A general covariant (contravariant) four-vector is denoted by x_μ (x^μ), with

$$
\begin{aligned}
x_\mu &= (x_0, x_1, x_2, x_3) = (x_0, -\vec{x}), \\
x^\mu &= (x^0, x^1, x^2, x^3) = (x_0, +\vec{x}).
\end{aligned}
\tag{A.1}
$$

The indices can be lowered and raised with the help of the metric tensor $g_{\mu\nu}$,

$$
x_\mu = g_{\mu\nu} x^\nu, \quad x^\mu = g^{\mu\nu} x_\nu,
\tag{A.2}
$$

Here, we use the "$g_{00} = +1$" convention, i. e.

$$
g_{\mu\nu} = g^{\mu\nu} = \mathrm{diag}(1, -1, -1, -1).
\tag{A.3}
$$

Repeated indices can be suppressed and the scalar product of two four-vectors x, y is given by $xy \equiv x_\mu y^\mu = x^\mu y_\mu = x_0 y_0 - \vec{x}\vec{y}$, yielding for a particle with four-momentum $p_\mu = (E, \vec{p})$ and mass m the on-shell relation

$$
p^2 = E^2 - \vec{p}^2 = m^2.
\tag{A.4}
$$

The co- and contravariant four-gradients ∂_μ and ∂^μ, respectively, are defined by

$$\partial_\mu \equiv \frac{\partial}{\partial x^\mu} = \left(\frac{\partial}{\partial t}, \vec{\nabla}\right), \quad \partial^\mu \equiv \frac{\partial}{\partial x_\mu} = \left(\frac{\partial}{\partial t}, -\vec{\nabla}\right). \tag{A.5}$$

A.2 Dirac and Pauli matrices

The Dirac matrices γ_μ are defined by the Clifford algebra in D dimensions[28],

$$\{\gamma_\mu, \gamma_\nu\} = 2g_{\mu\nu}\mathbb{1}_D, \tag{A.6}$$

where $\mathbb{1}_D$ is the D dimensional unit matrix and the indices μ, ν run from 0 to $D-1$. γ_0 is hermitian and γ_i are anti-hermitian. Under hermitian conjugation the gamma matrices behave as $\gamma_\mu^\dagger = \gamma_0\gamma_\mu\gamma_0$.

Contraction of indices in D dimensions yields for products of two or more Dirac matrices

$$\begin{aligned}
\gamma_\alpha\gamma^\alpha &= D\,\mathbb{1}_D, \\
\gamma_\alpha\gamma_\mu\gamma^\alpha &= (2-D)\gamma_\mu, \\
\gamma_\alpha\gamma_\mu\gamma_\nu\gamma^\alpha &= 4g_{\mu\nu}\,\mathbb{1}_D - (4-D)\gamma_\mu\gamma_\nu, \\
\gamma_\alpha\gamma_\mu\gamma_\nu\gamma_\rho\gamma^\alpha &= -2\gamma_\rho\gamma_\nu\gamma_\mu + (4-D)\gamma_\mu\gamma_\nu\gamma_\rho.
\end{aligned} \tag{A.7}$$

The computation of traces (Tr) of Dirac matrices is done by making use of Eq. (A.6) and the condition $\mathrm{Tr}(\mathbb{1}_D) = 4$, yielding

$$\begin{aligned}
\mathrm{Tr}(\gamma_\mu\gamma_\nu) &= 4g_{\mu\nu}, \\
\mathrm{Tr}(\gamma_\mu\gamma_\alpha\gamma_\nu\gamma_\beta) &= 4\left(g_{\mu\alpha}g_{\nu\beta} - g_{\mu\nu}g_{\alpha\beta} + g_{\mu\beta}g_{\alpha\nu}\right),
\end{aligned} \tag{A.8}$$

and traces of an odd number of Dirac matrices vanish.

In four dimensions, we define a matrix $\gamma_5 = \gamma^5 = i\gamma^0\gamma^1\gamma^2\gamma^3$, with properties

$$\{\gamma_\mu, \gamma_5\} = 0, \quad \gamma_5^2 = \mathbb{1}_4, \quad \gamma_5^\dagger = \gamma_5. \tag{A.9}$$

Traces involving the γ_5 matrix are given in four dimensions by

$$\begin{aligned}
\mathrm{Tr}(\gamma_5) &= 0, \quad \mathrm{Tr}(\gamma_5\gamma_\mu) = 0, \\
\mathrm{Tr}(\gamma_5\gamma_\mu\gamma_\nu\gamma_\rho\gamma_\sigma) &= 4i\epsilon_{\mu\nu\rho\sigma},
\end{aligned} \tag{A.10}$$

where $\epsilon_{\mu\nu\rho\sigma}$ is the totally antisymmetric Levi-Civita tensor with $\epsilon^{0123} = -\epsilon_{0123} = +1$. The

---

[28]In the approach of dimensional regularization, the Dirac matrices are defined as D-dimensional objects with $D < 4$. Most parts of the calculations are however performed in dimensional reduction where the Dirac matrices remain four-dimensional. In this case $D = 4$ has to be considered in the equations given below.

generalization of γ_5 to D dimensions as required for dimensional regularization, is more involved. However, a consistent treatment is possible, see [119–121] and the discussions in [124]. Following [121], we treat γ_5 in the "naive" scheme and consider the anticommuting and trace relations Eqs. (A.9) and (A.10) to hold also in D dimensions.

An explicit representation of the Dirac matrices is given by the Weyl representation in terms of the Pauli matrices σ^i,

$$\gamma^0 = \begin{pmatrix} 0 & \mathbb{1}_2 \\ \mathbb{1}_2 & 0 \end{pmatrix}, \quad \gamma^i = \begin{pmatrix} 0 & \sigma^i \\ -\sigma^i & 0 \end{pmatrix}, \quad \gamma_5 = \begin{pmatrix} -\mathbb{1}_2 & 0 \\ 0 & \mathbb{1}_2 \end{pmatrix}, \tag{A.11}$$

with

$$\sigma^1 = \begin{pmatrix} 0 & 1 \\ 1 & 0 \end{pmatrix}, \quad \sigma^2 = \begin{pmatrix} 0 & -i \\ i & 0 \end{pmatrix}, \quad \sigma^3 = \begin{pmatrix} 1 & 0 \\ 0 & -1 \end{pmatrix}. \tag{A.12}$$

A.3 Weyl spinors

Weyl spinors ψ_α and their conjugates $\overline{\psi}^{\dot\alpha}$ are two-component objects which transform under a Lorentz transformation as

$$\psi_\alpha \to M_\alpha{}^\beta \psi_\beta, \quad \overline{\psi}^{\dot\alpha} \to \left((M^{-1})^\dagger\right)^{\dot\alpha}{}_{\dot\beta} \overline{\psi}^{\dot\beta}, \tag{A.13}$$

where $M = M(\Lambda)$ is the 2-dimension matrix representation of a Lorentz transformation Λ. The distinct spinor indices $\alpha, \beta = 1, 2$ and $\dot\alpha, \dot\beta = 1, 2$ can be lowered and raised using the antisymmetric ϵ tensor,

$$\psi_\alpha = \epsilon_{\alpha\beta} \psi^\beta, \quad \psi^\alpha = \epsilon^{\alpha\beta} \psi_\beta,$$
$$\overline{\psi}_{\dot\alpha} = \epsilon_{\dot\alpha\dot\beta} \overline{\psi}^{\dot\beta}, \quad \overline{\psi}^{\dot\alpha} = \epsilon^{\dot\alpha\dot\beta} \overline{\psi}_{\dot\beta}, \tag{A.14}$$

with the following definitions, yielding $\epsilon_{\alpha\beta}\epsilon^{\beta\gamma} = \delta_\alpha^\gamma$,

$$\epsilon_{\alpha\beta} = \epsilon_{\dot\alpha\dot\beta} = \begin{pmatrix} 0 & -1 \\ 1 & 0 \end{pmatrix} \quad \text{and} \quad \epsilon^{\alpha\beta} = \epsilon^{\dot\alpha\dot\beta} = \begin{pmatrix} 0 & 1 \\ -1 & 0 \end{pmatrix}. \tag{A.15}$$

The spinors ψ and $\overline{\psi}$ are related by hermitian conjugation, i.e.

$$\overline{\psi}_{\dot\alpha} \equiv (\psi_\alpha)^\dagger = (\psi^\dagger)_{\dot\alpha}, \quad \text{and} \quad \psi^\alpha = (\overline{\psi}^{\dot\alpha})^\dagger. \tag{A.16}$$

In the notation of the scalar product of two Weyl spinors ξ, χ repeated spinor indices can

be suppressed. We use the convention of implicit ${}^\alpha_{\alpha}$ and ${}_{\dot\alpha}^{\dot\alpha}$ indices, i.e.

$$\begin{aligned}
\xi\chi &= \xi^\alpha\chi_\alpha = \chi^\alpha\xi_\alpha = \chi\xi, \\
\overline{\xi}\overline{\chi} &= \overline{\xi}_{\dot\alpha}\overline{\chi}^{\dot\alpha} = \overline{\chi}_{\dot\alpha}\overline{\xi}^{\dot\alpha} = \overline{\chi}\overline{\xi} = (\xi\chi)^\dagger = (\chi\xi)^\dagger,
\end{aligned} \tag{A.17}$$

while $\xi^\alpha\chi_\alpha = -\xi_\alpha\chi^\alpha$ and $\overline{\xi}_{\dot\alpha}\overline{\chi}^{\dot\alpha} = -\overline{\xi}^{\dot\alpha}\overline{\chi}_{\dot\alpha}$.

Similarly, repeated spinor indices are omitted in Lorentz invariant vectors as

$$\xi\sigma^\mu\overline{\chi} = \xi^\alpha(\sigma^\mu)_{\alpha\dot\beta}\,\overline{\chi}^{\dot\beta}, \qquad \overline{\xi}\overline{\sigma}^\mu\chi = \overline{\xi}_{\dot\alpha}(\overline{\sigma}^\mu)^{\dot\alpha\beta}\,\chi_\beta, \tag{A.18}$$

in terms of the elements of the Pauli matrices, Eq. (A.12), and

$$(\sigma^\mu)_{\alpha\dot\beta} = (\mathbb{1}_2, \sigma^i)_{\alpha\dot\beta} \quad \text{and} \quad (\overline{\sigma}^\mu)^{\dot\alpha\beta} = (\mathbb{1}_2, -\sigma^i)^{\dot\alpha\beta}. \tag{A.19}$$

Antisymmetrized products of the Pauli matrices are given by

$$(\sigma^{\mu\nu})_\alpha{}^\beta \equiv \frac{i}{2}(\sigma^\mu\overline{\sigma}^\nu - \sigma^\nu\overline{\sigma}^\mu)_\alpha{}^\beta \quad \text{and} \quad (\overline{\sigma}^{\mu\nu})^{\dot\alpha}{}_{\dot\beta} \equiv \frac{i}{2}(\overline{\sigma}^\mu\sigma^\nu - \overline{\sigma}^\nu\sigma^\mu)^{\dot\alpha}{}_{\dot\beta}. \tag{A.20}$$

A.4 Dirac and Majorana spinors

A four-component Dirac spinor field Ψ is made up of two mass-degenerate two-component Weyl spinors ξ_α and χ_α as follows,

$$\Psi = \begin{pmatrix} \xi_\alpha \\ \overline{\chi}^{\dot\alpha} \end{pmatrix}, \tag{A.21}$$

with two distinct spinor indices $\alpha = 1, 2$ and $\dot\alpha = 1, 2$. The Dirac-adjoint spinor $\overline{\Psi}$ is given by

$$\overline{\Psi} \equiv \Psi^\dagger\gamma^0 = (\chi^\alpha\ \overline{\xi}_{\dot\alpha}), \tag{A.22}$$

and the charge conjugated field Ψ^c is obtained by application of the charge conjugation matrix C onto the transposed spinor,

$$\Psi^c \equiv C\overline{\Psi}^T = \begin{pmatrix} \chi_\alpha \\ \overline{\xi}^{\dot\alpha} \end{pmatrix}, \tag{A.23}$$

where the charge conjugation matrix C satisfies $C^{-1}\gamma^\mu C = -(\gamma^\mu)^T$.

In terms of γ_5, we define chiral projection operators $P_{L/R} = \frac{1}{2}(1 \mp \gamma_5)$ that allow to

project out the left- and right-handed state of a Dirac field, respectively,

$$\Psi_L \equiv P_L \Psi = \begin{pmatrix} \xi_\alpha \\ 0 \end{pmatrix}, \quad \text{and} \quad \Psi_R \equiv P_R \Psi = \begin{pmatrix} 0 \\ \overline{\chi}_{\dot\alpha} \end{pmatrix}. \tag{A.24}$$

In this sense, we call ξ_α a left-handed Weyl spinor and $\overline{\chi}_{\dot\alpha}$ a right-handed Weyl spinor.

If the two Weyl spinors are identical $\xi = \chi$, it is

$$\Psi = \begin{pmatrix} \xi_\alpha \\ \overline{\xi}^{\dot\alpha} \end{pmatrix}, \quad \overline{\Psi} = (\xi^\alpha \ \overline{\xi}_{\dot\alpha}), \qquad \text{i.e.} \quad \Psi = \Psi^c. \tag{A.25}$$

A spinor defined by Eq. (A.25) is named Majorana spinor.

An extensive dictionary of how to relate results obtained in terms of four-component spinors and results from the two-component Weyl spinor formalism is given in [198]. Here, we just cite the translation rules for two Dirac spinors $\Psi_i = \begin{pmatrix} \xi_i \\ \overline{\chi}_i \end{pmatrix}$, $i = 1, 2$ (spinor indices are suppressed)

$$\begin{aligned} \overline{\Psi}_i P_L \Psi_j &= \chi_i \xi_j, & \overline{\Psi}_i P_R \Psi_j &= \overline{\xi}_i \overline{\chi}_j, \\ \overline{\Psi}_i \gamma^\mu P_L \Psi_j &= \overline{\xi}_i \overline{\sigma}^\mu \xi_j, & \overline{\Psi}_i \gamma^\mu P_R \Psi_j &= \chi_i \sigma^\mu \overline{\chi}_j. \end{aligned} \tag{A.26}$$

A.5 Grassmann numbers

Grassmann numbers θ_α are anticommuting fermionic objects,

$$\{\theta_\alpha, \theta_\beta\} = \{\overline{\theta}_{\dot\alpha}, \overline{\theta}_{\dot\beta}\} = \{\theta_\alpha, \overline{\theta}_{\dot\beta}\} = 0. \tag{A.27}$$

In particular, the square of a Grassmann number vanishes, $\theta_\alpha \theta_\alpha = 0$. The product of two Grassmann numbers is defined with the help of the ϵ-tensor, Eq. (A.15),

$$\theta\theta \equiv \theta^\alpha \theta_\alpha = \theta^\alpha \epsilon_{\alpha\beta} \theta^\beta = \epsilon^{\alpha\beta} \theta_\beta \theta_\alpha, \tag{A.28}$$

yielding with Eq. (A.27),

$$\begin{aligned} \theta^\alpha \theta^\beta &= -\frac{1}{2}\epsilon^{\alpha\beta}(\theta\theta), & \theta_\alpha \theta_\beta &= +\frac{1}{2}\epsilon_{\alpha\beta}(\theta\theta), \\ \text{and} \quad \overline{\theta}^{\dot\alpha} \overline{\theta}^{\dot\beta} &= +\frac{1}{2}\epsilon^{\dot\alpha\dot\beta}(\overline{\theta}\,\overline{\theta}), & \overline{\theta}_{\dot\alpha} \overline{\theta}_{\dot\beta} &= -\frac{1}{2}\epsilon_{\dot\alpha\dot\beta}(\overline{\theta}\,\overline{\theta}). \end{aligned} \tag{A.29}$$

Every product of more than two Grassmann numbers is zero,

$$\theta^\alpha \theta^\beta \theta^\gamma = 0, \qquad \text{since} \quad \alpha, \beta, \gamma \in \{1, 2\}. \tag{A.30}$$

Integration over Grassmann variables is defined as follows,

$$\int d\theta_\alpha = 0, \qquad \int d\theta_\alpha\,\theta_\beta = \delta_{\alpha\beta},$$
$$\int d^2\theta = 0, \qquad \int d^2\theta\,\theta^\alpha = 0, \qquad \int d^2\theta\,\theta^\alpha\theta^\beta = -\frac{1}{2}\epsilon^{\alpha\beta}, \qquad \int d^2\theta\,(\theta\theta) = 1, \tag{A.31}$$

where θ and $\overline{\theta}$ are considered to be independent,

$$\int d\theta\,d\overline{\theta} = \overline{\theta}\theta = 1, \qquad \int d^4\theta\,(\theta\theta)(\overline{\theta}\,\overline{\theta}) = 1. \tag{A.32}$$

Spinorial derivatives are defined by

$$\frac{\partial\theta^\beta}{\partial\theta^\alpha} \equiv \partial_\alpha\theta^\beta = \delta_\alpha{}^\beta, \qquad \frac{\partial\overline{\theta}_{\dot\beta}}{\partial\overline{\theta}_{\dot\alpha}} \equiv \overline{\partial}^{\dot\alpha}\overline{\theta}_{\dot\beta} = \delta^{\dot\alpha}{}_{\dot\beta}, \qquad \frac{\partial\overline{\theta}_{\dot\beta}}{\partial\theta^\alpha} = \frac{\partial\theta^\beta}{\partial\overline{\theta}_{\dot\alpha}} = 0, \tag{A.33}$$

with the conventions

$$\partial_\alpha = -\epsilon_{\alpha\beta}\partial^\beta, \quad \partial^\alpha = -\epsilon^{\alpha\beta}\partial_\beta, \quad \overline{\partial}_{\dot\alpha} = -\epsilon_{\dot\alpha\dot\beta}\overline{\partial}^{\dot\beta}, \quad \overline{\partial}^{\dot\alpha} = -\epsilon^{\dot\alpha\dot\beta}\overline{\partial}_{\dot\beta}, \tag{A.34}$$

to ensure that e. g. $\delta_\alpha{}^\beta = \partial_\alpha\theta^\beta = \partial^\beta\theta_\alpha$.

Appendix B

Input parameters for numerical cross section computations

We summarize the SM and MSSM input parameters as used for the numerical studies of colored SUSY particle production processes at the LHC presented in Chapters 5–7.

B.1   Standard Model parameters

The Standard Model input parameters are chosen in correspondence with [157,158]. In particular, we choose as input the fine structure constant α (α-scheme), with the value $\alpha = 1/137.036$, corresponding to the classical electron charge $e = \sqrt{4\pi\alpha}$. The strong coupling constant α_s has been defined in the $\overline{\text{MS}}$ scheme using the two-loop renormalization group equations with five light flavors and $\alpha_s(m_Z) = 0.119$. The masses of the SM gauge bosons are

$$m_Z = 91.1876\,\text{GeV}, \quad m_W = 80.42477\,\text{GeV}, \tag{B.1}$$

while we use for the third-generation fermions the on-shell values

$$m_\tau = 1.777\,\text{GeV}, \quad m_t = 170.9\,\text{GeV}, \quad m_b = 4.7\,\text{GeV}, \tag{B.2}$$

which corresponds to

$$m_b^{\overline{\text{MS}}}(m_b) = 4.2\,\text{GeV}, \quad m_b^{\overline{\text{DR}}}(1\ \text{TeV}) = 2.936\,\text{GeV}\,. \tag{B.3}$$

All other fermion masses are set to zero unless where they are used for regularization.

B.2   MSSM parameters

For the numerical evaluation of our cross section computations, we refer to mSUGRA scenarios with conserved $\mathcal{R}$-parity and real parameters. As discussed in Section 2.3.3, the

213

low-energy spectrum is determined by only five universal GUT-scale parameters (M_0, $M_{1/2}$, A_0, $\tan\beta$, $\mathrm{sgn}(\mu)$), cf. Eq. (2.55), which act as boundary equations for the renormalization group running of the soft-breaking parameters. In the numerical application, we use the program `Softsusy 2.0.18` [75] to evolve the GUT-scale parameters down to the (SUSY) scale Q_{SUSY}. We choose as a common SUSY scale for all scenarios

$$Q_{\mathrm{SUSY}} = 1 \text{ TeV}, \tag{B.4}$$

in reference to the SPA convention [158].

At Q_{SUSY}, the full SUSY particle spectrum can then be obtained from the running ($\overline{\mathrm{DR}}$) soft-breaking parameters and SM inputs according the tree-level relations given in Section 2.3.4. However in the renormalization scheme we are using, the input parameters are the on-shell masses of the two up-type squark mass eigenstates and the lighter of the down-type squark mass eigenstates within each generation i, as well as the on-shell stop mixing angle, cf. Eq. (2.104),

$$\left(m^2_{\tilde{u}_{1i}}\right)^{\mathrm{OS}}, \quad \left(m^2_{\tilde{u}_{2i}}\right)^{\mathrm{OS}}, \quad \left(m^2_{\tilde{d}_{1i}}\right)^{\mathrm{OS}}, \quad \left(\theta_{\tilde{t}}\right)^{\mathrm{OS}}, \quad \left(A_b\right)^{\overline{\mathrm{DR}}}. \tag{B.5}$$

Hence, a translation of the squark masses and the mixing angle as obtained from `Softsusy` into the OS scheme is needed. This can be achieved by exploiting the one-loop relation between masses and angles renormalized in different schemes:

$$\left(m^2_{\tilde{q}}\right)^{\overline{\mathrm{DR}}} + \left(\delta m^2_{\tilde{q}}\right)^{\overline{\mathrm{DR}}} = \left(m^2_{\tilde{q}}\right)^{\mathrm{OS}} + \left(\delta m^2_{\tilde{q}}\right)^{\mathrm{OS}}, \tag{B.6a}$$

$$\left(\theta_{\tilde{q}}\right)^{\overline{\mathrm{DR}}} + \left(\delta\theta_{\tilde{q}}\right)^{\overline{\mathrm{DR}}} = \left(\theta_{\tilde{q}}\right)^{\mathrm{OS}} + \left(\delta\theta_{\tilde{q}}\right)^{\mathrm{OS}}, \tag{B.6b}$$

where $m^2_{\tilde{q}}$ is the squared mass of the squark $\tilde{q}$, $\delta m^2_{\tilde{q}}$ is the corresponding one-loop counterterm and $\theta_{\tilde{q}}$ and $\delta\theta_{\tilde{q}}$ are the mixing angle between the two gauge eigenstates $\tilde{q}_{L,R}$ and its counterterm, respectively. The UV divergences cancel along Eq. (B.6) as the $\overline{\mathrm{DR}}$ and OS counterterms differ by UV-finite parts only.

Note that for a consistent translation between the schemes care has to be taken to start from parameters which are pure $\overline{\mathrm{DR}}$ quantities. For the squark masses this implies that both the soft-breaking parameters and the SM particle masses which enter the squark mass matrices are needed in the $\overline{\mathrm{DR}}$ scheme.

Owing to the $SU(2)_L$ invariance, the masses of the remaining down-type squarks are dependent parameters, cf. Eq. (2.102), and beyond tree-level they do not longer correspond to the physical OS masses. This has to be taken into account in the case of $\tilde{g}\tilde{d}_L$ production, where the left-handed down-squarks are external particles and considered to be on their mass shell. At the one-loop level, the OS mass of the left-handed down-squark $\left(m^2_{\tilde{d}_L}\right)^{\mathrm{OS}}$ is

obtained from the dependent mass $\left(m_{\tilde{d}_L}^2\right)^{\text{dep.}}$ as follows,

$$\left(m_{\tilde{d}_L}^2\right)^{\text{OS}} = \left(m_{\tilde{d}_L}^2\right)^{\text{dep.}} + \delta m_{\tilde{d}_L}^2 - \text{Re}\Sigma_{\tilde{d}_L}\left(m_{\tilde{d}_L}^2\right), \tag{B.7}$$

where $\delta m_{\tilde{d}_L}^2$ is the (dependent) mass counterterm defined in Eq. (4.38) and $\Sigma_{\tilde{d}_L}$ is the self-energy of the squark $\tilde{d}_L$.

Sleptons, Higgs bosons, and gauginos do not enter in the LO diagrams and the difference between $\overline{\text{DR}}$ and OS masses is a higher-order effect which can be neglected.

In summary, our MSSM input parameters in the squark sector are defined by Eqs. (B.5) and (B.7), while all other SUSY particle masses are calculated from the low-energy $\overline{\text{DR}}$ soft-breaking parameters obtained by `Softsusy`, via the tree-level relations given in Section 2.3.4[29]. The procedure of obtaining our low-energy input parameters is visualized in Fig. B.1.

For completeness, we give here the tree-level relations between the soft-breaking parameters and mass eigenstates of a given sfermion $\tilde{f}_i$ of generation i. Comparing the expressions Eqs. (2.92) and (2.100) for the sfermion mass matrix $\mathcal{M}_{\tilde{f}_i}^2$, one finds in terms of a general parameterization of the sfermion mixing matrix U^{f_i} the following conditions for the left-handed softbreaking parameters $m_{\tilde{F}_{Li}}^2 = m_{\tilde{Q}_i}^2, m_{\tilde{L}_i}^2$,

$$\left(\mathcal{M}_{\tilde{f}_i}^2\right)_{11} = m_{f_i}^2 + A_i^{LL} = \left(U_{11}^{f_i}\right)^2 m_{\tilde{f}_{1i}}^2 + \left(U_{21}^{f_i}\right)^2 m_{\tilde{f}_{2i}}^2,$$
$$\rightarrow \quad m_{\tilde{F}_{Li}}^2 = \left(U_{11}^{f_i}\right)^2 m_{\tilde{f}_{1i}}^2 + \left(U_{21}^{f_i}\right)^2 m_{\tilde{f}_{2i}}^2 - m_{f_i}^2 + \left(I_{f_i}^3 - e_{f_i}\sin^2\theta_W\right)m_Z^2\cos 2\beta, \tag{B.8}$$

for the right-handed soft-breaking parameters , $m_{\tilde{F}_{Ri}}^2 = m_{\tilde{U}_i}^2, m_{\tilde{D}_i}^2, m_{\tilde{E}_i}^2$,

$$\left(\mathcal{M}_{\tilde{f}_i}^2\right)_{22} = m_{f_i}^2 + C_i^{RR} = \left(U_{12}^{f_i}\right)^2 m_{\tilde{f}_{1i}}^2 + \left(U_{22}^{f_i}\right)^2 m_{\tilde{f}_{2i}}^2,$$
$$\rightarrow \quad m_{\tilde{F}_{Ri}}^2 = \left(U_{12}^{f_i}\right)^2 m_{\tilde{f}_{1i}}^2 + \left(U_{22}^{f_i}\right)^2 m_{\tilde{f}_{2i}}^2 - m_{f_i}^2 - e_{f_i}\sin^2\theta_W\, m_Z^2\cos 2\beta, \tag{B.9}$$

and for the trilinear couplings A_{f_i},

$$\left(\mathcal{M}_{\tilde{f}_i}^2\right)_{12} = m_{f_i}^2\, B_i^{LR} = U_{12}^{f_i} U_{12}^{f_i} m_{\tilde{f}_{1i}}^2 + U_{21}^{f_i} U_{22}^{f_i} m_{\tilde{f}_{2i}}^2,$$
$$\rightarrow \quad A_{f_i} = \frac{1}{m_{f_i}}\left(U_{12}^{f_i} U_{12}^{f_i} m_{\tilde{f}_{1i}}^2 + U_{21}^{f_i} U_{22}^{f_i} m_{\tilde{f}_{2i}}^2\right) + \mu\kappa. \tag{B.10}$$

Here, e_{f_i} and $I_{f_i}^3$ denote the electrical charge and the eigenvalue of the third component of the weak isospin of sfermion $\tilde{f}_i$, respectively. $\kappa = \cot\beta$ for up-type squarks and charged sleptons, while for right-handed squarks it is $\kappa = \tan\beta$.

---

[29]Note that in the Higgs sector, we use the public program `FeynHiggs` [81] or a two-loop approximation [82] included in [83] to compute the masses.

1. define mSUGRA parameters at GUT scale:
$$\rightarrow \quad M_0, \ M_{1/2}, \ \tan\beta, \ A_0, \ \text{sgn}(\mu)$$

$$\downarrow$$

2. evolve soft-breaking parameters via RGEs down to Q_{SUSY} (using `Softsusy`)
$$\rightarrow \quad \overline{\text{DR}} \text{ soft-breaking and OS SM parameters}$$

$$\downarrow$$

3. translate squark masses and mixing angles into OS scheme (at Q_{SUSY}):

  3.1 calculate one-loop counterterms for gauge bosons, quarks and squarks

  3.2 translate SM parameters into $\overline{\text{DR}}$,
     extract $\overline{\text{DR}}$ squark masses from pure-$\overline{\text{DR}}$ squark mixing matrices

  3.3 translate $\overline{\text{DR}}$ squark masses and stop mixing angle into OS scheme
$$\rightarrow \quad \left(m_{\tilde{u}_{1i}}^2\right)^{\text{OS}}, \ \left(m_{\tilde{u}_{2i}}^2\right)^{\text{OS}}, \ \left(m_{\tilde{d}_{1i}}^2\right)^{\text{OS}}, \ \left(\theta_{\tilde{t}}\right)^{\text{OS}}.$$

  3.4 recalculate OS soft-breaking parameters $(m_{\tilde{Q}_i}^2, \ m_{\tilde{U}_i}^2, \ m_{\tilde{D}_i}^2, \ A_t)$ from the
     OS squark mixing matrix according to Eqs. (B.8) – (B.10)
     (e.g. needed as further inputs for `FormCalc`)

$$\downarrow$$

4. calculate physical mass for the dependent squark (at Q_{SUSY})
according to Eq. (B.7)

Figure B.1.: Definition of low-energy input parameters as used for the numerical evaluations of production cross sections for colored SUSY particles.
A common scale $Q_{\text{SUSY}} = 1$ TeV has been chosen in all calculations.

B.3   SPS benchmark points

The "Snowmass Points and Slopes" (SPS) are a set of benchmark points in the MSSM parameter space which were suggested by [162] in order to unify the various conventions used in theoretical computations and experiments and to set a basis for future studies of SUSY phenomenology. Ten characteristic mSUGRA, GMSB, and AMSB scenarios have been proposed. Here, we only consider the five mSUGRA-like scenarios, characterized by the five universal GUT-scale parameters M_0, $M_{1/2}$, A_0, $\tan\beta$, $\text{sgn}(\mu)$. For convenience, we give the low-energy values $\tan\beta(Q_{\text{SUSY}})$ for $Q_{\text{SUSY}} = 1$ TeV below.

The *SPS1a' benchmark scenario* has been introduced by the Supersymmetry Parameter Analysis (SPA) convention and project [158],

$$M_0 = 70 \text{ GeV}, \qquad M_{1/2} = 250 \text{ GeV}, \qquad A_0 = -300 \text{ GeV},$$
$$\tan\beta(Q_{\text{SUSY}}) = 10, \qquad \text{sgn}(\mu) > 0. \tag{B.11}$$

Being a "typical" mSUGRA scenario, the SPS1a' point is a very popular benchmark and often referred to in the literature. It is close to the SPS1a scenario defined in [162] with slight modification of the GUT-scale parameters M_0 and A_0 in order to be compatible with all high-energy mass bounds, with low-energy precision data, and with the observed cold dark matter density.

The *SPS2 benchmark scenario* is chosen to lie in the "focus point" region, where the lightest neutralino has a sizable higgsino component and thus its annihilation cross section is large enough to agree with WMAP constraints on the cold dark matter density.

$$M_0 = 1450 \text{ GeV}, \qquad M_{1/2} = 300 \text{ GeV}, \qquad A_0 = 0 \text{ GeV},$$
$$\tan\beta(Q_{\text{SUSY}}) = 9.66, \qquad \text{sgn}(\mu) > 0. \tag{B.12}$$

For our studies, the distinguishing feature of the SPS2 scenario is the high value of M_0 which results in heavy masses for squarks and sleptons. In particular, the squarks are heavier than the gluino.

The *SPS3 benchmark scenario* is defined close to the "coannihilation region", where a low relic abundance can be explained by the fact that the LSP and the next-to-lightest SUSY particle are nearly degenerated in mass and coannihilate rapidly.

$$M_0 = 90 \text{ GeV}, \qquad M_{1/2} = 400 \text{ GeV}, \qquad A_0 = 0 \text{ GeV},$$
$$\tan\beta(Q_{\text{SUSY}}) = 9.66, \qquad \text{sgn}(\mu) > 0. \tag{B.13}$$

The most interesting aspect for collider phenomenology in general is the small slepton-neutralino mass difference in the SPS3 scenario. In the context of production processes of colored SUSY particles, however, this particular configuration is of small importance only.

The *SPS4 benchmark scenario* is characterized by a large value of $\tan\beta$,

$$M_0 = 400 \text{ GeV}, \qquad M_{1/2} = 300 \text{ GeV}, \qquad A_0 = 0 \text{ GeV},$$
$$\tan\beta(Q_{\text{SUSY}}) = 49.4, \qquad \text{sgn}(\mu) > 0. \tag{B.14}$$

As a consequence, the couplings in the Higgs sector to down-type quarks and charged leptons are enhanced and large production cross sections for the heavy Higgs bosons are predicted. Interesting for our purposes, the large value of $\tan\beta$ induces an important L–R mixing of the stop gauge eigenstates. Furthermore, the gluino turns out to be lighter than the squarks of the first two generations.

The *SPS5 benchmark scenario* is defined by a large, negative value of the trilinear coupling A_0. Due to this, a relatively low value of $\tan\beta$ can be chosen and does not contradict

scenario		SUSY particle masses [GeV] and mixing angle [°]									
		$\tilde{u}_L$	$\tilde{u}_R$	$\tilde{d}_L$	$\tilde{d}_R$	$\tilde{t}_1$	$\tilde{t}_2$	$\tilde{b}_1$	$\tilde{b}_2$	$\tilde{g}$	θ_t
SPS1a'	$\overline{\text{DR}}$	523.3	506.0	529.0	501.7	328.2	555.3	468.0	504.7	–	34.8
	OS	560.7	543.4	566.4	539.4	359.5	581.9	500.0	538.1	609.0	33.9
SPS2	$\overline{\text{DR}}$	1539	1536	1541	1535	983.3	1300	1289	1523	–	6.9
	OS	1559	1554	1561	1553	992.4	1331	1301	1540	784.9	7.6
SPS3	$\overline{\text{DR}}$	819.7	790.3	823.3	781.8	621.4	813.9	755.5	783.7	–	30.9
	OS	860.8	830.7	864.2	822.6	649.7	843.3	787.9	819.7	938.1	28.4
SPS4	$\overline{\text{DR}}$	730.4	731.1	734.5	708.4	524.1	675.8	581.9	663.3	–	33.0
	OS	766.1	748.6	770.1	744.1	545.0	686.7	583.1	658.2	735.9	35.2
SPS5	$\overline{\text{DR}}$	637.9	616.8	642.2	611.0	186.3	623.7	524.8	610.7	–	31.1
	OS	676.8	655.5	680.8	649.9	224.9	647.6	552.4	647.7	723.7	30.1

Table B.1.: $\overline{\text{DR}}$ and OS masses of squarks and gluinos within the different SPS mSUGRA scenarios. The translation from the $\overline{\text{DR}}$ to the OS scheme has been performed at the scale $Q_{\text{SUSY}} = 1$ TeV. For the left-handed down-squark and the lighter bottom-squark the physical masses according to Eq. (B.7) are given in the respective second rows.

constraints from direct Higgs searches at LEP [199],

$$M_0 = 150 \text{ GeV}, \qquad M_{1/2} = 300 \text{ GeV}, \qquad A_0 = -1000 \text{ GeV},$$
$$\tan\beta(Q_{\text{SUSY}}) = 4.82, \qquad \text{sgn}(\mu) > 0. \tag{B.15}$$

The SPS5 scenario provides a very light top-squark $\tilde{t}_1$ and thus high $\tilde{t}_1\tilde{t}_1^*$ production cross sections are expected. Light-flavor squarks and gluinos have intermediate masses.

An interesting aspect in the philosophy behind the SPS conventions is that the low-energy SUSY particle masses and MSSM parameters should be regarded as the actual benchmarks [162,200]. As a consequence, results from different projects are independent of the numerical program which has been used to evolve the GUT-scale parameters down to lower scales and to calculate the spectrum. Thus specifying a benchmark scenario in terms of the GUT-scale parameters is understood to be an abbreviation only of the low-energy phenomenology. Here, we proceed as described above, using `Softsusy` for the evolution of the soft-breaking parameters and subsequently translate the squark masses into the OS scheme. As an overview, we collect the $\overline{\text{DR}}$ and OS masses of the squarks and the stop mixing angle in the various scenarios in Table B.1. We also quote the OS mass of the gluino for completeness.

Appendix C

Slepton production and decay in specific B₃ mSUGRA models

C.1 Cross sections and branching ratios

In this Appendix we give the necessary cross sections and branching ratios to calculate rates of all possible decay signatures for single slepton production at the LHC, within the B₃ mSUGRA sets A and B with a $\tilde{\tau}_1$ LSP defined in Eq. (8.12).

In Tables C.1 and C.2, all hadronic production cross sections of resonant single sleptons within parameter Set A and Set B, respectively, are given. We consider here $\lambda'_{ijk} = 0.01|_{\mathrm{GUT}}$, but the cross section scales with $|\lambda'_{ijk}|^2$. The running of λ'_{ijk} is taken into account according to Eq. (8.17a), leading to the following values at the SUSY scale Q_{SUSY}, cf. Eq. (8.20):

$$
\begin{aligned}
\text{Set A:} \quad & \lambda'_{2jk} = 0.0282, \quad \lambda'_{23k} = 0.0258, \quad \lambda'_{2j3} = 0.0281, \quad \lambda'_{233} = 0.0255, \\
& \lambda'_{3jk} = 0.0282, \quad \lambda'_{33k} = 0.0257, \quad \lambda'_{3j3} = 0.0280, \quad \lambda'_{333} = 0.0254;
\end{aligned}
\tag{C.1a}
$$

$$
\begin{aligned}
\text{Set B:} \quad & \lambda'_{2jk} = 0.0274, \quad \lambda'_{23k} = 0.0249, \quad \lambda'_{2j3} = 0.0269, \quad \lambda'_{233} = 0.0238, \\
& \lambda'_{3jk} = 0.0271, \quad \lambda'_{33k} = 0.0247, \quad \lambda'_{3j3} = 0.0266, \quad \lambda'_{333} = 0.0236,
\end{aligned}
\tag{C.1b}
$$

where $j, k = 1, 2$ and $Q_{\mathrm{SUSY}} = 893$ GeV for Set A and $Q_{\mathrm{SUSY}} = 1209$ GeV for Set B.

The production cross sections include NLO SUSY-QCD corrections [187]. The latter depend on the trilinear soft-breaking squark-squark-slepton coupling, $\mathbf{h}_{D^k}$. In B₃ mSUGRA models, additional $\mathcal{R}$-parity violating soft-breaking terms compared to those in the MSSM Eq. (2.51) are allowed [166],

$$
\begin{aligned}
\mathcal{L}_{\mathrm{soft},\mathcal{R}} = \\
& - \left[(\mathbf{h}_{U^i})_{jk}\, \tilde{u}^*_{Ri}\, \tilde{u}^*_{Rj}\, \tilde{d}^*_{Rk} + (\mathbf{h}_{D^k})_{ij}\, \tilde{\ell}_{Li}\, \tilde{q}_{Lj}\, \tilde{d}^*_{Rk} + (\mathbf{h}_{E^k})_{ij}\, \tilde{\ell}_{Li}\, \tilde{\ell}_{Lj}\, \tilde{e}^*_{Rk} - \tilde{\kappa}_i\, \tilde{\ell}_{Li}\, h_u \right] + h.c. \\
& - \left[\tilde{\ell}^\dagger_{Li} \left(\mathbf{m}^2_{\tilde{L}_i h_d} \right) h_d + h^\dagger_d \left(\mathbf{m}^2_{h_d \tilde{L}_i} \right) \tilde{\ell}_{Li} \right],
\end{aligned}
\tag{C.2}
$$

Set A	$\sigma_{\mathrm{prod.}}$ [fb]				$\sigma_{\mathrm{prod.}}$ [fb]					
	$\tilde{e}_L^+/\tilde{\mu}_L^+$	$\tilde{e}_L^-/\tilde{\mu}_L^-$	$\tilde{\nu}_{e/\mu}^*$	$\tilde{\nu}_{e/\mu}$	$\tilde{\tau}_2^+$	$\tilde{\tau}_2^-$	$\tilde{\tau}_1^+$	$\tilde{\tau}_1^-$	$\tilde{\nu}_\tau^*$	$\tilde{\nu}_\tau$
$\lambda'_{i11} = 0.01\vert_{\mathrm{GUT}}$	2700	1540	1860	1860	2620	1500	434	272	190	190
$\lambda'_{i22} = 0.01\vert_{\mathrm{GUT}}$	268	268	410	410	2600	2600	64.5	64.5	421	421
$\lambda'_{i12} = 0.01\vert_{\mathrm{GUT}}$	2150	464	1430	602	2090	451	360	103	1460	616
$\lambda'_{i21} = 0.01\vert_{\mathrm{GUT}}$	405	1050	602	1430	393	1020	91.9	197	616	1460
$\lambda'_{i13} = 0.01\vert_{\mathrm{GUT}}$	1240	220	788	292	1210	214	216	51.3	806	299
$\lambda'_{i23} = 0.01\vert_{\mathrm{GUT}}$	119	119	191	191	116	116	30.0	30.0	196	196
$\lambda'_{i31} = 0.01\vert_{\mathrm{GUT}}$	–	–	247	666	–	–	–	–	253	681
$\lambda'_{i32} = 0.01\vert_{\mathrm{GUT}}$	–	–	161	161	–	–	–	–	166	166
$\lambda'_{i33} = 0.01\vert_{\mathrm{GUT}}$	–	–	69.3	69.3	–	–	–	–	71.1	71.1

Table C.1.: Complete list of hadronic cross sections for resonant single slepton/sneutrino production via $\lambda'_{ijk} = 0.01\vert_{\mathrm{GUT}}$ at the LHC ($\sqrt{S} = 14$ TeV) within the parameter Set A. The cross sections include QCD and SUSY-QCD corrections at NLO [187]. For λ'_{i3k}, sleptons cannot be produced because of the vanishing top-quark density in the proton.

where the couplings $\mathbf{h}_{U^i}$, $\mathbf{h}_{D^k}$, $\mathbf{h}_{E^k}$ are the analogues to the trilinear couplings $\mathbf{a}_U$, $\mathbf{a}_D$, $\mathbf{a}_E$ in Eq. (2.51), the bilinear coupling $\tilde{\kappa}_i$ corresponds to κ_i, and the terms in the last row provide additional terms to the slepton-Higgs mass matrix. In complete analogy to the $\mathcal{R}$-parity conserving case, we apply mSUGRA unification assumptions to the trilinear couplings and consider the universal boundary conditions at the GUT scale, cf.Eq. (2.54),

$$(\mathbf{h}_{D^k})_{ij} = A_0\,\lambda'_{ijk}, \quad (\mathbf{h}_{U^i})_{jk} = A_0\,\lambda''_{ijk}, \quad (\mathbf{h}_{E^k})_{ij} = A_0\,\lambda_{ijk}. \tag{C.3}$$

Numerically, it is $(\mathbf{h}_{D^k})_{ij} = -23.4$ GeV (-21.2 GeV) for $\lambda'_{ijk} = 0.01\vert_{\mathrm{GUT}}$ within Set A (Set B) at the respective SUSY scale. We incorporated the running of $\mathbf{h}_{D^k}$ by using the one-loop contributions from gauge interactions [166].

Second, for the calculation of the rate for a given signature of resonant single slepton production, the branching ratios for the slepton decay and for the subsequent decay chains down to the $\tilde{\tau}_1$ LSP are needed. For all dominant λ'_{ijk} couplings these branching ratios are universal within parameter Set A and Set B, respectively, and are given in Tab. C.3 for the numerical boundary condition $\lambda'_{ijk} = 0.01\vert_{\mathrm{GUT}}$.

Finally, we show in Table C.4 all branching ratios of $\tilde{\tau}_1$ LSP decays for different couplings λ'_{2jk} at the GUT scale. Branching ratios within scenarios with $\lambda'_{1jk} \neq 0$ are analogous and can be obtained from the tables by replacing μ by e in the final-state signatures.

In the case of a non-vanishing λ'_{3jk}, the $\tilde{\tau}_1$ LSP directly couples to the dominant $L_3 Q_j \bar{D}_k$ operator and decays predominantly via the inverse production process, see also the discussion in Sect. 8.2.1. For the special case of $\lambda'_{33k} \neq 0$ and $m_{\tilde{\tau}_1} < m_t$, however, the $\tilde{\tau}_1$ decays

Set B	$\sigma_{\text{prod.}}$ [fb]				$\sigma_{\text{prod.}}$ [fb]					
	$\tilde{e}_L^+/\tilde{\mu}_L^+$	$\tilde{e}_L^-/\tilde{\mu}_L^-$	$\tilde{\nu}_{e/\mu}^*$	$\tilde{\nu}_{e/\mu}$	$\tilde{\tau}_2^+$	$\tilde{\tau}_2^-$	$\tilde{\tau}_1^+$	$\tilde{\tau}_1^-$	$\tilde{\nu}_\tau^*$	$\tilde{\nu}_\tau$
$\lambda'_{i11} = 0.01\|_{\text{GUT}}$	885	476	559	559	949	515	1168	750	657	657
$\lambda'_{i22} = 0.01\|_{\text{GUT}}$	67.3	67.3	102	102	74.7	74.7	192	192	124	124
$\lambda'_{i12} = 0.01\|_{\text{GUT}}$	681	123	414	155	735	136	976	301	490	187
$\lambda'_{i21} = 0.01\|_{\text{GUT}}$	105	309	155	414	117	337	269	548	187	490
$\lambda'_{i13} = 0.01\|_{\text{GUT}}$	370	54.6	214	70.2	401	60.6	572	146	255	85.4
$\lambda'_{i23} = 0.01\|_{\text{GUT}}$	28.2	28.2	44.4	44.4	31.4	31.4	87.2	87.2	54.3	54.3
$\lambda'_{i31} = 0.01\|_{\text{GUT}}$	–	–	60.4	184	–	–	–	–	73.5	219
$\lambda'_{i32} = 0.01\|_{\text{GUT}}$	–	–	38.2	38.2	–	–	–	–	46.7	46.7
$\lambda'_{i33} = 0.01\|_{\text{GUT}}$	–	–	14.8	14.8	–	–	–	–	18.2	18.2

Table C.2.: Same as Tab. C.1 but for parameter Set B.

into a W boson and two jets, cf. Eq. (8.28). The corresponding matrix element and partial width are calculated in Appendix C.2.

C.2 The B₃ slepton decay $\tilde{\ell}_i^- \to W^- \bar{b} d_k$

A non-vanishing $L_i Q_3 \bar{D}_k$ operator allows for the decay of a left-handed charged slepton $\tilde{\ell}_{Li}$ into a top quark t and a down-type quark d_k of generation k,

$$\tilde{\ell}_{Li}^- \to \bar{t} d_k \,. \tag{C.4}$$

However, this decay mode is kinematically only allowed if $m_{\tilde{\ell}_{Li}} > m_t + m_{d_k}$. For $m_{\tilde{\ell}_{Li}} < m_t + m_{d_k}$, the slepton decays via a virtual top quark or a virtual sneutrino,

$$\tilde{\ell}_{Li}^- \to W^- \bar{b} d_k. \tag{C.5}$$

This 3-body decay has not been considered in the literature yet and is not implemented in the R-parity violating version of `Herwig`, either. We complete the picture by calculating the 3-body decay (C.5) in the following.

The relevant parts of the supersymmetric Lagrangian are [13,201]

$$\begin{aligned}
\mathcal{L}_{L_i Q_3 \bar{D}_k} &= -\lambda'_{i3k} \left(\tilde{\nu}_i \, \bar{d}_k \, P_L \, b - U_{1a}^{\tilde{\ell}_i} \, \tilde{\ell}_{ai} \, \bar{d}_k \, P_L \, t \right) + h.c., \\
\mathcal{L}_{btW} &= -\frac{g}{\sqrt{2}} \left(W_\mu^+ \, \bar{t} \, \gamma^\mu \, P_L \, b + W_\mu^- \, \bar{b} \, \gamma^\mu \, P_L \, t \right), \\
\mathcal{L}_{\tilde{\ell}_i \tilde{\nu}_i W} &= -\frac{ig}{\sqrt{2}} \left(U_{1a}^{\tilde{\ell}_i} \, W_\mu^+ \, \tilde{\nu}_i^* \overleftrightarrow{\partial}^\mu \tilde{\ell}_{ai} + U_{1a}^{\tilde{\ell}_i} \, W_\mu^- \, \tilde{\ell}_{ai}^* \overleftrightarrow{\partial}^\mu \tilde{\nu}_i \right),
\end{aligned} \tag{C.6}$$

	BRs [%]			
	$\lambda'_{2jk} = 0.01\vert_{\text{GUT}}$		$\lambda'_{3jk} = 0.01\vert_{\text{GUT}}$	
	Set A	Set B	Set A	Set B
$\tilde{\mu}_L^- \to \tilde{\chi}_1^0 \, \mu^-$	91.1	91.3	100	100
$\tilde{\mu}_L^- \to \bar{u}_j \, d_k$	8.9	8.7	–	–
$\tilde{\nu}_\mu \to \tilde{\chi}_1^0 \, \nu_\mu$	91.7	91.5	100	100
$\tilde{\nu}_\mu \to \bar{d}_j \, d_k$	8.3	8.4	–	–
$\tilde{\chi}_1^0 \to \tilde{\tau}_1^\pm \, \tau^\mp$	36.0	45.7	36.0	45.7
$\tilde{\chi}_1^0 \to \tilde{\mu}_R^\pm \, \mu^\mp$	7.0	2.2	7.0	2.2
$\tilde{\chi}_1^0 \to \tilde{e}_R^\pm \, e^\mp$	7.0	2.1	7.0	2.1
$\tilde{\mu}_R^- \to \tilde{\tau}_1^+ \, \mu^- \, \tau^-$	54.3	64.1	54.3	64.1
$\tilde{\mu}_R^- \to \tilde{\tau}_1^- \, \mu^- \, \tau^+$	45.7	35.9	45.7	35.9
$\tilde{\tau}_2^- \to \tilde{\chi}_1^0 \, \tau^-$	58.4	14.7	55.5	14.5
$\tilde{\tau}_2^- \to \tilde{\tau}_1^- \, h^0$	22.5	41.8	21.4	41.2
$\tilde{\tau}_2^- \to \tilde{\tau}_1^- \, Z^0$	19.1	43.5	18.1	42.9
$\tilde{\tau}_2^- \to \bar{u}_j \, d_k$	–	–	5.0	1.3
$\tilde{\nu}_\tau \to \tilde{\chi}_1^0 \, \nu_\tau$	62.2	13.6	58.8	13.4
$\tilde{\nu}_\tau \to \tilde{\tau}_1^- \, W^+$	37.8	86.4	35.8	85.2
$\tilde{\nu}_\tau \to \bar{d}_j \, d_k$	–	–	5.4	1.4

Table C.3.: Table of branching ratios, BRs, that are relevant for single slepton production and decays within the B$_3$ mSUGRA scenarios Set A and Set B. Two different non-zero B$_3$ couplings are considered, $\lambda'_{2jk} = 0.01\vert_{\text{GUT}}$ for columns 2 and 3 and $\lambda'_{3jk} = 0.01\vert_{\text{GUT}}$ for columns 4 and 5. The branching ratios for $\lambda'_{1jk} \neq 0$ can be obtained from those for $\lambda'_{2jk} \neq 0$ by interchanging muon and electron flavor in the first four decay channels. The branching ratios for $\tilde{e}_L$ ($\tilde{\nu}_e$, $\tilde{e}_R$) in scenarios with $\lambda'_{ijk} \neq 0$, $i \neq 1$ are equal to those of $\tilde{\mu}_L$ ($\tilde{\nu}_\mu$, $\tilde{\mu}_R$) with $\lambda'_{3jk} \neq 0$. The branching ratios for $\tilde{\tau}_1$ LSP decays are listed separately in Tab. C.4.

where $U^{\tilde{\ell}_i}$ is the slepton mixing matrix, a denoting the mass eigenstate of the charged slepton. The derivate operator in the last line is defined as $A \overleftrightarrow{\partial}^\mu B \equiv A(\partial^\mu B) - (\partial^\mu A)B$.

From Eq. (C.6), the squared matrix elements (summed over final state polarizations and colors) can be derived,

$$\overline{\sum} \left| \mathcal{M}_t \big(\tilde{\ell}_{ai}^- \to W^- \bar{b} d_k \big) \right|^2 = \frac{3\lambda'^2_{i3k} \big(U_{1a}^{\tilde{\ell}_i} \big)^2 g^2}{\big[(W+b)^2 - m_t^2 \big]^2 + m_t^2 \, \Gamma_t^2}$$

$$\times \left\{ (d_k \cdot b) \left[m_b^2 - m_W^2 + 4(W \cdot b) + \frac{4(W \cdot b)^2}{m_W^2} \right] + 2(W \cdot d_k) \left[m_b^2 + 2(W \cdot b) - m_b^2 \, \frac{(W \cdot b)}{m_W^2} \right] \right\},$$

$$\text{(C.7)}$$

		BR$_2$				BR$_4$							
		$\tilde{\tau}_1^- \xrightarrow{\lambda} \nu_\mu \tau^-$ [$= \tilde{\tau}_1^- \xrightarrow{\lambda} \nu_\tau \mu^-$]		$\tilde{\tau}_1^- \xrightarrow{\lambda} \bar{\nu}_\mu \tau^-$		$\tilde{\tau}_1^- \xrightarrow{\lambda'} \tau^- \mu^- u_j \bar{d}_k$		$\tilde{\tau}_1^- \xrightarrow{\lambda'} \tau^- \mu^+ \bar{u}_j d_k$		$\tilde{\tau}_1^- \xrightarrow{\lambda'} \tau^- \nu_\mu d_j \bar{d}_k$		$\tilde{\tau}_1^- \xrightarrow{\lambda'} \tau^- \bar{\nu}_\mu \bar{d}_j d_k$	
Set A	λ'_{211}	7.9%	(2.7%)	0.2%	(0.1%)	11.8%	(13.3%)	25.3%	(28.5%)	15.2%	(17.1%)	31.6%	(35.6%)
	λ'_{212}	21.5%	(−)	0.5%	(−)	7.9%	(14.2%)	17.1%	(29.3%)	10.2%	(18.1%)	21.3%	(38.4%)
	λ'_{213}	10.5%	(−)	0.2%	(−)	11.1%	(14.1%)	23.8%	(30.2%)	14.3%	(18.1%)	29.6%	(37.6%)
	λ'_{221}	21.5%	(−)	0.5%	(−)	7.9%	(14.2%)	17.1%	(29.3%)	10.2%	(18.1%)	21.3%	(38.4%)
	λ'_{222}	46.8%	(46.8%)	1.1%	(1.1%)	0.7%	(0.8%)	1.6%	(1.6%)	1.0%	(1.0%)	2.0%	(2.0%)
	λ'_{223}	48.2%	(−)	1.1%	(−)	0.4%	(14.2%)	0.8%	(29.3%)	0.5%	(18.2%)	1.0%	(38.4%)
	λ'_{231}	17.9%	(−)	0.4%	(−)	−	(−)	−	(−)	20.7%	(32.1%)	43.0%	(67.9%)
	λ'_{232}	48.8%	(−)	1.1%	(−)	−	(−)	−	(−)	0.4%	(32.5%)	0.8%	(67.5%)
	λ'_{233}	49.4%	(49.4%)	1.1%	(1.1%)	−	(−)	−	(−)	−	(−)	−	(−)
Set B	λ'_{211}	49.0%	(48.6%)	1.7%	(1.7%)	−	(0.1%)	0.1%	(0.4%)	−	(0.1%)	0.1%	(0.5%)
	λ'_{212}	49.1%	(−)	1.7%	(−)	−	(5.6%)	−	(41.1%)	−	(6.3%)	−	(46.9%)
	λ'_{213}	49.0%	(−)	1.7%	(−)	−	(5.7%)	0.1%	(41.0%)	−	(6.4%)	0.1%	(46.9%)
	λ'_{221}	49.1%	(−)	1.7%	(−)	−	(5.6%)	−	(41.0%)	−	(6.3%)	−	(47.0%)
	λ'_{222}	49.1%	(49.1%)	1.7%	(1.7%)	−	(−)	−	(−)	−	(−)	−	(−)
	λ'_{223}	49.1%	(−)	1.7%	(−)	−	(5.7%)	−	(41.0%)	−	(6.4%)	−	(47.0%)
	λ'_{231}	49.1%	(−)	1.7%	(−)	−	(−)	−	(−)	−	(12.0%)	0.1%	(88.0%)
	λ'_{232}	49.1%	(−)	1.7%	(−)	−	(−)	−	(−)	−	(12.0%)	−	(88.0%)
	λ'_{233}	49.1%	(49.1%)	1.7%	(1.7%)	−	(−)	−	(−)	−	(−)	−	(−)

Table C.4.: Branching ratios of the $\tilde{\tau}_1$ LSP in sets A and B for different non-zero λ'_{2jk} couplings at the GUT scale. The branching ratios are calculated within the mSUGRA parameter Set A for the SUSY breaking scale $Q_{\text{susy}} = 893$ GeV and in Set B for the SUSY breaking scale $Q_{\text{susy}} = 1209$ GeV. We assume down-type (up-type) quark mixing. Branching ratios for non-vanishing λ'_{1jk} are analogous, with μ replaced by e.
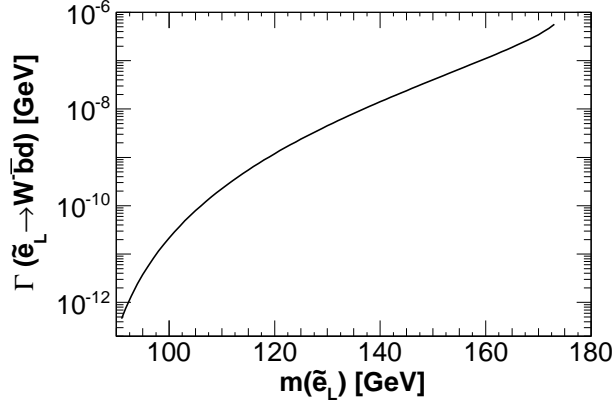
Figure C.1.: Partial width in GeV for the 3-body decay $\tilde{e}_L \to W^- \bar{b} d$ as a function of the selectron mass $m_{\tilde{e}_L}$. We take $\lambda'_{131} = 0.01$ and $U^{\tilde{e}}_{11} = 1$ and $m_{\tilde{\nu}} = 400$ GeV in Eq. (C.7).

$$\overline{\sum} \left| \mathcal{M}_{\tilde{\nu}} \left(\tilde{\ell}^-_{ai} \to W^- \bar{b} d_k \right) \right|^2 = \frac{3 \lambda'^2_{i3k} \left(U^{\ell_i}_{1a} \right)^2 g^2}{\left[(d_k + b)^2 - m^2_{\tilde{\nu}_i} \right]^2}$$
$$\times \left\{ -4(d_k \cdot b) \left[m^2_b + m^2_{d_k} + 2(d_k \cdot b) - \frac{[(W \cdot b) + (W \cdot d_k)]^2}{m^2_W} \right] \right\},$$

$$\overline{\sum} 2\mathrm{Re}\left\{ \left(\mathcal{M}_t \right)^* \mathcal{M}_{\tilde{\nu}} \right\} = \frac{3 \lambda'^2_{i3k} \left(U^{\ell_i}_{1a} \right)^2 g^2}{\left[(W + b)^2 - m^2_t \right] \left[(d_k + b)^2 - m^2_{\tilde{\nu}_i} \right]}$$
$$\times \left\{ 4m^2_{d_k} \left(m^2_b + (W \cdot b) \right) - 4m^2_b (W \cdot d) \left(1 + \frac{(W \cdot d) + (W \cdot b)}{m^2_W} \right) \right.$$
$$\left. - 4(d_k \cdot b) \left[m^2_b + (W \cdot d) + 2(d_k \cdot b) - (W \cdot b) \left(1 + 2 \frac{(W \cdot d) + (W \cdot b)}{m^2_W} \right) \right] \right\}.$$
$$\tag{C.8}$$

We denote the particle four-momenta by the particle letter, and m_t, m_b, and m_W, are the top, bottom and W mass, respectively. Γ_t is the total width of the top quark.

From the summed squared matrix elements we obtain easily the partial width for the 3-body decay (C.5), see e. g. [201]. We show in Fig. C.1 the partial width $\Gamma(\tilde{e}_L \to W^- \bar{b} d)$ as a function of the left-handed selectron mass $m_{\tilde{e}_L}$. Here we consider $\lambda'_{131} = 0.01$ and $U^{\tilde{e}}_{11} = 1$ and $m_{\tilde{\nu}} = 400$ GeV, in Eq. (C.7). The amplitude Eq. (C.7) gives the dominant contribution, the decay via a virtual sneutrino and the interference contribution are suppressed by the typically heavy sneutrino mass.

In comparison to the 3-body decay (C.5), the possible 4-body decays via λ'_{i3k} are negligible. For example for the parameter Set B with non-vanishing λ'_{331}, the branching ratio of the 3-body $\tilde{\tau}_1$ LSP decay (C.5) is larger by five orders of magnitude than the branching ratio of the 4-body $\tilde{\tau}_1$ LSP decays.

Bibliography

[1] S. L. Glashow, *Partial Symmetries of Weak Interactions*, Nucl. Phys. **22** (1961) 579–588.

S. Weinberg, *A Model of Leptons*, Phys. Rev. Lett. **19** (1967) 1264–1266.

A. Salam, *Weak and Electromagnetic Interactions*. Originally printed in *Svartholm: Elementary Particle Theory, Proceedings Of The Nobel Symposium Held 1968 At Lerum, Sweden*, Stockholm 1968, 367-377.

[2] S. L. Glashow, J. Iliopoulos, and L. Maiani, *Weak Interactions with Lepton-Hadron Symmetry*, Phys. Rev. **D2** (1970) 1285–1292.

[3] H. Fritzsch, M. Gell-Mann, and H. Leutwyler, *Advantages of the Color Octet Gluon Picture*, Phys. Lett. **B47** (1973) 365–368.

[4] D. J. Gross and F. Wilczek, *Asymptotically Free Gauge Theories. 1*, Phys. Rev. **D8** (1973) 3633–3652.

D. J. Gross and F. Wilczek, *Asymptotically Free Gauge Theories. 2*, Phys. Rev. **D9** (1974) 980–993.

H. D. Politzer, *Reliable Perturbative Results for Strong Interactions?*, Phys. Rev. Lett. **30** (1973) 1346–1349.

[5] **Particle Data Group** Collaboration, C. Amsler *et. al.*, *Review of Particle Physics*, Phys. Lett. **B667** (2008) 1. [http://pdg.lbl.gov].

[6] J. Wess and B. Zumino, *A Lagrangian Model Invariant Under Supergauge Transformations*, Phys. Lett. **B49** (1974) 52.

D. V. Volkov and V. P. Akulov, *Is the Neutrino a Goldstone Particle?*, Phys. Lett. **B46** (1973) 109–110.

[7] J. Wess and B. Zumino, *Supergauge Transformations in Four Dimensions*, Nucl. Phys. **B70** (1974) 39–50.

[8] E. Witten, *Dynamical Breaking of Supersymmetry*, Nucl. Phys. **B188** (1981) 513.

R. K. Kaul and P. Majumdar, *Cancellation of Quadratically Divergent Mass Corrections in Globally Supersymmetric Spontaneously Broken Gauge Theories*, Nucl. Phys. **B199** (1982) 36.

[9] L. E. Ibáñez and G. G. Ross, *Low-Energy Predictions in Supersymmetric Grand Unified Theories*, Phys. Lett. **B105** (1981) 439.

S. Dimopoulos, S. Raby, and F. Wilczek, *Supersymmetry and the Scale of Unification*, Phys. Rev. **D24** (1981) 1681–1683.

[10] J. R. Ellis, J. S. Hagelin, D. V. Nanopoulos, K. A. Olive, and M. Srednicki, *Supersymmetric Relics from the Big Bang*, Nucl. Phys. **B238** (1984) 453–476.

[11] **WMAP** Collaboration, J. Dunkley *et. al.*, *Five-Year Wilkinson Microwave Anisotropy Probe (WMAP) Observations: Likelihoods and Parameters from the WMAP Data*, [arXiv:0803.0586].

[12] H. P. Nilles, *Supersymmetry, Supergravity and Particle Physics*, Phys. Rept. **110** (1984) 1–162.

[13] H. E. Haber and G. L. Kane, *The Search for Supersymmetry: Probing Physics Beyond the Standard Model*, Phys. Rept. **117** (1985) 75–263.

[14] R. Barbieri, *Looking Beyond the Standard Model: The Supersymmetric Option*, Riv. Nuovo Cim. **11N4** (1988) 1–45.

[15] S. Heinemeyer, W. Hollik, D. Stöckinger, A. M. Weber, and G. Weiglein, *Precise Prediction for M(W) in the MSSM*, JHEP **08** (2006) 052 [hep-ph/0604147].
J. R. Ellis, S. Heinemeyer, K. A. Olive, A. M. Weber, and G. Weiglein, *The Supersymmetric Parameter Space in Light of B-Physics Observables and Electroweak Precision Data*, JHEP **08** (2007) 083 [arXiv:0706.0652].
S. Heinemeyer, W. Hollik, A. M. Weber, and G. Weiglein, *Z Pole Observables in the MSSM*, JHEP **04** (2008) 039 [arXiv:0710.2972].

[16] O. Buchmüller *et. al.*, *Predictions for Supersymmetric Particle Masses in the CMSSM using Indirect Experimental and Cosmological Constraints*, JHEP **09** (2008) 117 [arXiv:0808.4128].

[17] S. Heinemeyer, W. Hollik, and G. Weiglein, *Electroweak Precision Observables in the Minimal Supersymmetric Standard Model*, Phys. Rept. **425** (2006) 265–368 [hep-ph/0412214].

[18] **Muon G-2** Collaboration, G. W. Bennett *et. al.*, *Final Report of the Muon E821 Anomalous Magnetic Moment Measurement at BNL*, Phys. Rev. **D73** (2006) 072003 [hep-ex/0602035].
J. P. Miller, E. de Rafael, and B. L. Roberts, *Muon g-2: Review of Theory and Experiment*, Rept. Prog. Phys. **70** (2007) 795 [hep-ph/0703049].
D. Stöckinger, $(g-2)_\mu$ *and Supersymmetry: Status and Prospects*, [arXiv:0710.2429].

[19] P. R. Harrison and C. H. Llewellyn Smith, *Hadroproduction of Supersymmetric Particles*, Nucl. Phys. **B213** (1983) 223.
G. L. Kane and J. P. Leveille, *Experimental Constraints on Gluino Masses and Supersymmetric Theories*, Phys. Lett. **B112** (1982) 227.
E. Reya and D. P. Roy, *Supersymmetric Particle Production at $P\bar{P}$ Collider Energies*, Phys. Rev. **D32** (1985) 645.
S. Dawson, E. Eichten, and C. Quigg, *Search for Supersymmetric Particles in Hadron - Hadron Collisions*, Phys. Rev. **D31** (1985) 1581.
H. Baer and X. Tata, *Component Formulae for Hadronproduction of Left-handed and Right-handed Squarks*, Phys. Lett. **B160** (1985) 159.

[20] W. Beenakker, R. Höpker, M. Spira, and P. M. Zerwas, *Squark and Gluino Production at Hadron Colliders*, Nucl. Phys. **B492** (1997) 51–103 [`hep-ph/9610490`].

[21] W. Beenakker, M. Krämer, T. Plehn, M. Spira, and P. M. Zerwas, *Stop Production at Hadron Colliders*, Nucl. Phys. **B515** (1998) 3–14 [`hep-ph/9710451`].

[22] A. Kulesza and L. Motyka, *Threshold Resummation for Squark-Antisquark and Gluino-Pair Production at the LHC*, Phys. Rev. Lett. **102** (2009) 111802 [`arXiv:0807.2405`].

A. Kulesza and L. Motyka, *Soft Gluon Resummation for the Production of Gluino-Gluino and Squark-Antisquark Pairs at the LHC*, [`arXiv:0905.4749`].

[23] U. Langenfeld and S.-O. Moch, *Higher-Order Soft Corrections to Squark Hadro-Production*, [`arXiv:0901.0802`].

[24] W. Hollik, M. Kollar, and M. K. Trenkel, *Hadronic Production of Top-Squark Pairs with Electroweak NLO Contributions*, JHEP **02** (2008) 018 [`arXiv:0712.0287`].

[25] W. Hollik, E. Mirabella, and M. K. Trenkel, *Electroweak Contributions to Squark–Gluino Production at the LHC*, JHEP **02** (2009) 002 [`arXiv:0810.1044`].

[26] W. Hollik and E. Mirabella, *Squark Anti-Squark Pair Production at the LHC: The Electroweak Contribution*, JHEP **12** (2008) 087 [`arXiv:0806.1433`].

[27] E. Mirabella, *NLO Electroweak Corrections to Gluino Pair Production at Hadron Colliders*, [`in preparation`].

[28] N. Sakai and T. Yanagida, *Proton Decay in a Class of Supersymmetric Grand Unified Models*, Nucl. Phys. **B197** (1982) 533.

[29] S. Weinberg, *Supersymmetry at Ordinary Energies. 1. Masses and Conservation Laws*, Phys. Rev. **D26** (1982) 287.

[30] A. Y. Smirnov and F. Vissani, *Upper Bound on all Products of R-parity Violating Couplings λ' and λ'' from Proton Decay*, Phys. Lett. **B380** (1996) 317–323 [`hep-ph/9601387`].

G. Bhattacharyya and P. B. Pal, *Upper Bounds on all R-parity Violating $\lambda\lambda''$ Combinations from Proton Stability*, Phys. Rev. **D59** (1999) 097701 [`hep-ph/9809493`].

[31] R. Barbier *et. al.*, *R-parity Violating Supersymmetry*, Phys. Rept. **420** (2005) 1–202 [`hep-ph/0406039`].

[32] **Super-Kamiokande** Collaboration, M. Shiozawa *et. al.*, *Search for Proton Decay via $p \to e^+\pi^0$ in a Large Water Cherenkov Detector*, Phys. Rev. Lett. **81** (1998) 3319–3323 [`hep-ex/9806014`].

[33] G. R. Farrar and P. Fayet, *Phenomenology of the Production, Decay, and Detection of New Hadronic States Associated with Supersymmetry*, Phys. Lett. **B76** (1978) 575–579.

[34] H. K. Dreiner, C. Luhn, and M. Thormeier, *What is the Discrete Gauge Symmetry of the MSSM?*, Phys. Rev. **D73** (2006) 075007 [`hep-ph/0512163`].

[35] L. E. Ibáñez and G. G. Ross, *Discrete Gauge Symmetry Anomalies*, Phys. Lett. **B260** (1991) 291–295.

L. E. Ibáñez and G. G. Ross, *Discrete Gauge Symmetries and the Origin of Baryon and Lepton Number Conservation in Supersymmetric Versions of the Standard Model*, Nucl. Phys. **B368** (1992) 3–37.

[36] Y. Grossman and H. E. Haber, *(S)neutrino Properties in R-parity Violating Supersymmetry. I: CP-Conserving Phenomena*, Phys. Rev. **D59** (1999) 093008 [`hep-ph/9810536`].

[37] H. K. Dreiner, C. Luhn, H. Murayama, and M. Thormeier, *Baryon Triality and Neutrino Masses from an Anomalous Flavor U(1)*, Nucl. Phys. **B774** (2007) 127–167 [`hep-ph/0610026`].

[38] M. C. Gonzalez-Garcia and M. Maltoni, *Phenomenology with Massive Neutrinos*, Phys. Rept. **460** (2008) 1–129 [`arXiv:0704.1800`].

M. Maltoni, T. Schwetz, M. A. Tortola, and J. W. F. Valle, *Status of Global Fits to Neutrino Oscillations*, New J. Phys. **6** (2004) 122 [`hep-ph/0405172`].

[39] F. del Aguila, J. A. Aguilar-Saavedra, and R. Pittau, *Neutrino Physics at Large Colliders*, J. Phys. Conf. Ser. **53** (2006) 506–527 [`hep-ph/0606198`].

[40] P. W. Higgs, *Broken Symmetries, Massless Particles and Gauge Fields*, Phys. Lett. **12** (1964) 132–133.

P. W. Higgs, *Broken Symmetries and the Masses of Gauge Bosons*, Phys. Rev. Lett. **13** (1964) 508–509.

P. W. Higgs, *Spontaneous Symmetry Breakdown Without Massless Bosons*, Phys. Rev. **145** (1966) 1156–1163.

F. Englert and R. Brout, *Broken Symmetry and the Mass of Gauge Vector Mesons*, Phys. Rev. Lett. **13** (1964) 321–322.

T. W. B. Kibble, *Symmetry Breaking in Non-Abelian Gauge Theories*, Phys. Rev. **155** (1967) 1554–1561.

[41] N. Cabibbo, *Unitary Symmetry and Leptonic Decays*, Phys. Rev. Lett. **10** (1963) 531–533.

M. Kobayashi and T. Maskawa, *CP Violation in the Renormalizable Theory of Weak Interaction*, Prog. Theor. Phys. **49** (1973) 652–657.

[42] T. Hambye and K. Riesselmann, *Matching Conditions and Higgs Mass Upper Bounds Revisited*, Phys. Rev. **D55** (1997) 7255–7262 [`hep-ph/9610272`].

[43] **LEP Working Group for Higgs boson searches** Collaboration, R. Barate *et. al.*, *Search for the Standard Model Higgs Boson at LEP*, Phys. Lett. **B565** (2003) 61–75 [`hep-ex/0306033`]. [`http://lepewwg.web.cern.ch/LEPEWWG`].

[44] A. Djouadi, *The Anatomy of Electro-Weak Symmetry Breaking. I: The Higgs Boson in the Standard Model*, Phys. Rept. **457** (2008) 1–216 [`hep-ph/0503172`].

[45] G. 't Hooft, *Renormalization of Massless Yang-Mills Fields*, Nucl. Phys. **B33** (1971) 173–199.

G. 't Hooft, *Renormalizable Lagrangians for Massive Yang-Mills Fields*, Nucl. Phys. **B35** (1971) 167–188.

[46] C. Bouchiat, J. Iliopoulos, and P. Meyer, *An Anomaly Free Version of Weinberg's Model*, Phys. Lett. **B38** (1972) 519–523.

D. J. Gross and R. Jackiw, *Effect of Anomalies on Quasirenormalizable Theories*, Phys. Rev. **D6** (1972) 477–493.

[47] S. L. Adler and W. A. Bardeen, *Absence of Higher Order Corrections in the Anomalous Axial Vector Divergence Equation*, Phys. Rev. **182** (1969) 1517–1536.

R. Jackiw and K. Johnson, *Anomalies of the Axial Vector Current*, Phys. Rev. **182** (1969) 1459–1469.

[48] W. Hollik, *The Electroweak Standard Model*, in *Proceedings of the 1999 Summer School in Particle Physics, ICTP Series in Theoretical Physics, Vol. 16* (G. Senjanović and A. Smirnov, eds.), Singapore, World Scientific, 2000, pp. 1–52.

[49] H. Georgi and S. L. Glashow, *Unity of All Elementary Particle Forces*, Phys. Rev. Lett. **32** (1974) 438–441.

[50] H. Fritzsch and P. Minkowski, *Unified Interactions of Leptons and Hadrons*, Ann. Phys. **93** (1975) 193–266.

[51] S. P. Martin, *A Supersymmetry Primer*, [`hep-ph/9709356`].

[52] I. J. R. Aitchison, *Supersymmetry in Particle Physics: An Elementary Introduction*, 2007. SLAC-R-865.

D. Bailin and A. Love, *Supersymmetric Gauge Field Theory and String Theory.* Taylor and Francis Group, 1994.

[53] S. R. Coleman and J. Mandula, *All Possible Symmetries of the S Matrix*, Phys. Rev. **159** (1967) 1251–1256.

[54] R. Haag, J. T. Łopuszański, and M. Sohnius, *All Possible Generators of Supersymmetries of the S Matrix*, Nucl. Phys. **B88** (1975) 257.

[55] D. Z. Freedman, P. van Nieuwenhuizen, and S. Ferrara, *Progress Toward a Theory of Supergravity*, Phys. Rev. **D13** (1976) 3214–3218.

S. Deser and B. Zumino, *Consistent Supergravity*, Phys. Lett. **B62** (1976) 335.

[56] M. F. Sohnius, *Introducing Supersymmetry*, Phys. Rept. **128** (1985) 39–204.

[57] L. O'Raifeartaigh, *Spontaneous Symmetry Breaking for Chiral Scalar Superfields*, Nucl. Phys. **B96** (1975) 331.

[58] P. Fayet and J. Iliopoulos, *Spontaneously Broken Supergauge Symmetries and Goldstone Spinors*, Phys. Lett. **B51** (1974) 461–464.

[59] L. Girardello and M. T. Grisaru, *Soft Breaking of Supersymmetry*, Nucl. Phys. **B194** (1982) 65.

[60] H. P. Nilles, *Dynamically Broken Supergravity and the Hierachy Problem*, Phys. Lett. **B115** (1982) 193.

H. P. Nilles, *Supergravity Generates Hierarchies*, Nucl. Phys. **B217** (1983) 366.

[61] A. H. Chamseddine, R. L. Arnowitt, and P. Nath, *Locally Supersymmetric Grand Unification*, Phys. Rev. Lett. **49** (1982) 970.

R. Barbieri, S. Ferrara, and C. A. Savoy, *Gauge Models with Spontaneously Broken Local Supersymmetry*, Phys. Lett. **B119** (1982) 343.

[62] M. Dine and A. E. Nelson, *Dynamical Supersymmetry Breaking at Low Energies*, Phys. Rev. **D48** (1993) 1277–1287 [`hep-ph/9303230`].

M. Dine, A. E. Nelson, and Y. Shirman, *Low-Energy Dynamical Supersymmetry Breaking Simplified*, Phys. Rev. **D51** (1995) 1362–1370 [`hep-ph/9408384`].

M. Dine, A. E. Nelson, Y. Nir, and Y. Shirman, *New Tools for Low-Energy Dynamical Supersymmetry Breaking*, Phys. Rev. **D53** (1996) 2658–2669 [`hep-ph/9507378`].

[63] G. F. Giudice and R. Rattazzi, *Theories with Gauge-Mediated Supersymmetry Breaking*, Phys. Rept. **322** (1999) 419–499 [`hep-ph/9801271`].

[64] L. Randall and R. Sundrum, *Out of This World Supersymmetry Breaking*, Nucl. Phys. **B557** (1999) 79–118 [`hep-th/9810155`].

G. F. Giudice, M. A. Luty, H. Murayama, and R. Rattazzi, *Gaugino Mass Without Singlets*, JHEP **12** (1998) 027 [`hep-ph/9810442`].

[65] T. Gherghetta, G. F. Giudice, and J. D. Wells, *Phenomenological Consequences of Supersymmetry with Anomaly-Induced Masses*, Nucl. Phys. **B559** (1999) 27–47 [`hep-ph/9904378`].

S. Ambrosanio, G. D. Kribs, and S. P. Martin, *Signals for Gauge-Mediated Supersymmetry Breaking Models at the CERN LEP2 Collider*, Phys. Rev. **D56** (1997) 1761–1777 [`hep-ph/9703211`].

[66] M. Dine, *Supersymmetry Breaking at Low Energies*, [`arXiv:0901.1713`].

[67] S. Dimopoulos, S. Raby, and F. Wilczek, *Proton Decay in Supersymmetric Models*, Phys. Lett. **B112** (1982) 133.

[68] H. K. Dreiner and S. Grab, *All Possible Lightest Supersymmetric Particles in R-parity Violating mSUGRA*, [`arXiv:0811.0200`].

[69] T. Fritzsche, *Berechnung von Observablen zur Supersymmetrischen Teilchenerzeugnung an Hochenergie-Collidern unter Einschluss Höherer Ordnungen*. Cuvillier Verlag Göttingen, 2005.

[70] J. Rosiek, *Complete Set of Feynman Rules for the Minimal Supersymmetric Extension of the Standard Model*, Phys. Rev. **D41** (1990) 3464.

J. Rosiek, *Complete Set of Feynman Rules for the MSSM – ERRATUM*, [`hep-ph/9511250`].

[71] I. Simonsen, *A Review of Minimal Supersymmetric Electroweak Theory*, [`hep-ph/9506369`].

[72] J. F. Gunion and H. E. Haber, *Higgs Bosons in Supersymmetric Models. 1*, Nucl. Phys. **B272** (1986) 1.

[73] A. Denner, H. Eck, O. Hahn, and J. Küblbeck, *Feynman Rules for Fermion Number Violating Interactions*, Nucl. Phys. **B387** (1992) 467–484.

[74] S. Dimopoulos and D. W. Sutter, *The Supersymmetric Flavor Problem*, Nucl. Phys. **B452** (1995) 496–512 [`hep-ph/9504415`].

[75] B. C. Allanach, *SOFTSUSY: A C++ Program for Calculating Supersymmetric Spectra*, Comput. Phys. Commun. **143** (2002) 305–331 [`hep-ph/0104145`].

[76] L. E. Ibáñez and G. G. Ross, $SU(2)_L \times U(1)$ *Symmetry Breaking as a Radiative Effect of Supersymmetry Breaking in GUTs*, Phys. Lett. **B110** (1982) 215–220.

[77] **ALEPH** Collaboration, S. Schael *et. al.*, *Search for Neutral MSSM Higgs Bosons at LEP*, Eur. Phys. J. **C47** (2006) 547–587 [`hep-ex/0602042`].

[78] **Tevatron electroweak working group** Collaboration. [`http://tevewwg.fnal.gov/higgs/`].

[79] S. Heinemeyer, W. Hollik, H. Rzehak, and G. Weiglein, *High-Precision Predictions for the MSSM Higgs Sector at* $\mathcal{O}(\alpha_b\alpha_s)$, Eur. Phys. J. **C39** (2005) 465–481 [`hep-ph/0411114`].

[80] G. Degrassi, S. Heinemeyer, W. Hollik, P. Slavich, and G. Weiglein, *Towards High-Precision Predictions for the MSSM Higgs Sector*, Eur. Phys. J. **C28** (2003) 133–143 [`hep-ph/0212020`].

[81] S. Heinemeyer, W. Hollik, and G. Weiglein, *FeynHiggs: A Program for the Calculation of the Masses of the Neutral CP-even Higgs Bosons in the MSSM*, Comput. Phys. Commun. **124** (2000) 76–89 [`hep-ph/9812320`].

T. Hahn *et. al.*, *Higher-Order Corrected Higgs Bosons in FeynHiggs 2.5*, Pramana **69** (2007) 861–870 [`hep-ph/0611373`].

M. Frank *et. al.*, *The Higgs Boson Masses and Mixings of the Complex MSSM in the Feynman-Diagrammatic Approach*, JHEP **02** (2007) 047 [`hep-ph/0611326`].

[82] S. Heinemeyer, W. Hollik, and G. Weiglein, *The Mass of the Lightest MSSM Higgs Boson: A Compact Analytical Expression at the Two-Loop Level*, Phys. Lett. **B455** (1999) 179–191 [`hep-ph/9903404`].

[83] T. Hahn and M. Perez-Victoria, *Automatized One-Loop Calculations in Four and D Dimensions*, Comput. Phys. Commun. **118** (1999) 153–165 [`hep-ph/9807565`].

T. Hahn and M. Rauch, *News from FormCalc and LoopTools*, Nucl. Phys. Proc. Suppl. **157** (2006) 236–240 [`hep-ph/0601248`].

[84] S. Antusch and M. Spinrath, *New GUT Predictions for Quark and Lepton Mass Ratios Confronted with Phenomenology*, [`arXiv:0902.4644`].

[85] **ATLAS** Collaboration, U. De Sanctis, *Supersymmetry Searches with ATLAS Detector at LHC*, Nuovo Cim. **121B** (2006) 761–770.

CMS Collaboration, A. Tricomi, *SUSY Searches in Early CMS Data*, J. Phys. Conf. Ser. **110** (2008) 062026.

[86] A. Djouadi, J. Kalinowski, P. Ohmann, and P. M. Zerwas, *Heavy SUSY Higgs Bosons at* e^+e^- *Linear Colliders*, Z. Phys. **C74** (1997) 93–111 [`hep-ph/9605339`].

[87] J. R. Ellis and S. Rudaz, *Search for Supersymmetry in Toponium Decays*, Phys. Lett. **B128** (1983) 248.

[88] **ATLAS** Collaboration, *Detector and Physics Performance Technical Design Report*, CERN/LHCC/ **99-15** (1999).
[http://atlasinfo.cern.ch/Atlas/GROUPS/PHYSICS/TDR/access.html].

[89] **CMS** Collaboration, G. L. Bayatian *et. al.*, *CMS Technical Design Report, Volume II: Physics Performance*, J. Phys. **G34** (2007) 995–1579.

[90] L. Randall and D. Tucker-Smith, *Dijet Searches for Supersymmetry at the LHC*, Phys. Rev. Lett. **101** (2008) 221803 [arXiv:0806.1049].

[91] **D0** Collaboration, V. M. Abazov *et. al.*, *Search for Squarks and Gluinos in Events with Jets and Missing Transverse Energy using 2.1 fb^{-1} of $P\bar{P}$ Collision Data at $\sqrt{s} = 1.96$ TeV*, Phys. Lett. **B660** (2008) 449–457 [arXiv:0712.3805].

[92] **CDF** Collaboration, T. Aaltonen *et. al.*, *Inclusive Search for Squark and Gluino Production in $P\bar{P}$ Collisions at $\sqrt{s} = 1.96$ TeV*, [arXiv:0811.2512].

[93] **CDF - Run II** Collaboration, M. D'Onofrio, *Inclusive Search for Squarks and Gluinos Production at CDF*, [arXiv:0710.5114].

[94] D. E. Kaplan and M. D. Schwartz, *Constraining Light Colored Particles with Event Shapes*, Phys. Rev. Lett. **101** (2008) 022002 [arXiv:0804.2477].

[95] A. Djouadi and Y. Mambrini, *Three-Body Decays of Top and Bottom Squarks*, Phys. Rev. **D63** (2001) 115005 [hep-ph/0011364].

[96] **ALEPH** Collaboration, A. Heister *et. al.*, *Search for Scalar Quarks in e^+e^- Collisions at $\sqrt{s}$ up to 209 GeV*, Phys. Lett. **B537** (2002) 5–20 [hep-ex/0204036].
DELPHI Collaboration, P. Abreu *et. al.*, *Search for Supersymmetric Partners of Top and Bottom Quarks at $\sqrt{s} = 189$ GeV*, Phys. Lett. **B496** (2000) 59–75 [hep-ex/0103034].
L3 Collaboration, M. Acciarri *et. al.*, *Searches for Scalar Quarks in e^+e^- Interactions at $\sqrt{s} = 189$ GeV*, Phys. Lett. **B471** (1999) 308–320 [hep-ex/9910020].
OPAL Collaboration, G. Abbiendi *et. al.*, *Search for Scalar Top and Scalar Bottom Quarks at LEP*, Phys. Lett. **B545** (2002) 272–284 [hep-ex/0209026].

[97] A. C. Kraan, *Stop and Sbottom Searches at LEP*, [hep-ex/0305051].

[98] **H1** Collaboration, A. Aktas *et. al.*, *Search for Bosonic Stop Decays in R-parity Violating Supersymmetry in e^+p Collisions at HERA*, Phys. Lett. **B599** (2004) 159–172 [hep-ex/0405070].
ZEUS Collaboration, S. Chekanov *et. al.*, *Search for Stop Production in R-parity Violating Supersymmetry at HERA*, Eur. Phys. J. **C50** (2007) 269–281 [hep-ex/0611018].

[99] **D0** Collaboration, V. M. Abazov *et. al.*, *Search for Scalar Top Quarks in the Acoplanar Charm Jets and Missing Transverse Energy Final State in $P\bar{P}$ Collisions at $\sqrt{s}=1.96$ TeV*, Phys. Lett. **B665** (2008) 1–8 [arXiv:0803.2263].

[100] **D0** Collaboration, V. M. Abazov *et. al.*, *Search for the Lightest Scalar Top Quark in Events with Two Leptons in $P\bar{P}$ Collisions at $\sqrt{s}=1.96$ TeV*, [arXiv:0811.0459].

[101] **CDF** Collaboration, T. Aaltonen, *Search for Direct Pair Production of Supersymmetric Top and Supersymmetric Bottom Quarks in $P\bar{P}$ Collisions at $\sqrt{s}$=1.96 TeV*, [`arXiv:0707.2567`].

[102] **SUGRA Working Group** Collaboration, S. Abel *et. al.*, *Report of the SUGRA Working Group for Run II of the Tevatron*, [`hep-ph/0003154`].

R. Demina, J. D. Lykken, K. T. Matchev, and A. Nomerotski, *Stop and Sbottom Searches in Run II of the Fermilab Tevatron*, Phys. Rev. **D62** (2000) 035011 [`hep-ph/9910275`].

[103] R. D. Field and R. P. Feynman, *Quark Elastic Scattering as a Source of High Transverse Momentum Mesons*, Phys. Rev. **D15** (1977) 2590–2616.

[104] R. K. Ellis, J. W. Stirling, and B. R. Webber, *QCD and Collider Physics*. Cambridge University Press, 1996.

[105] J. C. Collins, D. E. Soper, and G. Sterman, *Factorization of Hard Processes in QCD*, Adv. Ser. Direct. High Energy Phys. **5** (1988) 1–91 [`hep-ph/0409313`].

[106] G. Altarelli and G. Parisi, *Asymptotic Freedom in Parton Language*, Nucl. Phys. **B126** (1977) 298.

[107] A. D. Martin, R. G. Roberts, W. J. Stirling, and R. S. Thorne, *Parton Distributions Incorporating QED Contributions*, Eur. Phys. J. **C39** (2005) 155–161 [`hep-ph/0411040`].

[108] G. Bozzi, B. Fuks, and M. Klasen, *Non-Diagonal and Mixed Squark Production at Hadron Colliders*, Phys. Rev. **D72** (2005) 035016 [`hep-ph/0507073`].

[109] D. Berdine and D. Rainwater, *Mixed Top-Bottom Squark Production at the LHC*, Phys. Rev. **D72** (2005) 075003 [`hep-ph/0506261`].

[110] M. Glück, E. Reya, and A. Vogt, *Dynamical Parton Distributions of the Proton and Small x Physics*, Z. Phys. **C67** (1995) 433–448.

[111] W. Beenakker, R. Höpker, and M. Spira, *PROSPINO: A program for the PROduction of Supersymmetric Particles In Next-to-leading Order QCD*, [`hep-ph/9611232`].

[112] W. Hollik and M. Kollar, *NLO QED Contributions to Top-Pair Production at Hadron Collider*, Phys. Rev. **D77** (2008) 014008 [`arXiv:0708.1697`].

[113] S. Bornhauser, M. Drees, H. K. Dreiner, and J. S. Kim, *Electroweak Contributions to Squark Pair Production at the LHC*, Phys. Rev. **D76** (2007) 095020 [`arXiv:0709.2544`].

[114] G. Bozzi, B. Fuks, B. Herrmann, and M. Klasen, *Squark and Gaugino Hadroproduction and Decays in Non-Minimal Flavour Violating Supersymmetry*, Nucl. Phys. **B787** (2007) 1–54 [`arXiv:0704.1826`].

[115] J. Germer, W. Hollik, E. Mirabella, and M. K. Trenkel [`in preparation`].

[116] W. Hollik *et. al.*, *Renormalization of the Minimal Supersymmetric Standard Model*, Nucl. Phys. **B639** (2002) 3–65 [`hep-ph/0204350`].

W. Hollik *et. al.*, *Renormalization of the Minimal Supersymmetric Standard Model*, Nucl. Phys. Proc. Suppl. **116** (2003) 397–401 [`hep-ph/0210016`].

[117] W. Pauli and F. Villars, *On the Invariant Regularization in Relativistic Quantum Theory*, Rev. Mod. Phys. **21** (1949) 434–444.

[118] C. G. Bollini and J. J. Giambiagi, *Dimensional Renormalization: The Number of Dimensions as a Regularizing Parameter*, Nuovo Cim. **B12** (1972) 20–25.

J. F. Ashmore, *A Method of Gauge Invariant Regularization*, Lett. Nuovo Cim. **4** (1972) 289–290.

[119] G. 't Hooft and M. J. G. Veltman, *Regularization and Renormalization of Gauge Fields*, Nucl. Phys. **B44** (1972) 189–213.

[120] P. Breitenlohner and D. Maison, *Dimensional Renormalization and the Action Principle*, Commun. Math. Phys. **52** (1977) 11–38.

[121] F. Jegerlehner, *Facts of Life with γ_5*, Eur. Phys. J. **C18** (2001) 673–679 [`hep-th/0005255`].

[122] W. Siegel, *Supersymmetric Dimensional Regularization via Dimensional Reduction*, Phys. Lett. **B84** (1979) 193.

D. M. Capper, D. R. T. Jones, and P. van Nieuwenhuizen, *Regularization by Dimensional Reduction of Supersymmetric and Nonsupersymmetric Gauge Theories*, Nucl. Phys. **B167** (1980) 479.

[123] W. Siegel, *Inconsistency of Supersymmetric Dimensional Regularization*, Phys. Lett. **B94** (1980) 37.

[124] D. Stöckinger, *Regularization by Dimensional Reduction: Consistency, Quantum Action Principle, and Supersymmetry*, JHEP **03** (2005) 076 [`hep-ph/0503129`].

[125] W. A. Bardeen, A. J. Buras, D. W. Duke, and T. Muta, *Deep Inelastic Scattering Beyond the Leading Order in Asymptotically Free Gauge Theories*, Phys. Rev. **D18** (1978) 3998.

A. J. Buras, *Asymptotic Freedom in Deep Inelastic Processes in the Leading Order and Beyond*, Rev. Mod. Phys. **52** (1980) 199.

[126] W. J. Marciano and A. Sirlin, *Precise SU(5) Predictions for $\sin^2\theta_W$, m(W) and m(Z)*, Phys. Rev. Lett. **46** (1981) 163.

A. Sirlin, *Role of $\sin^2\theta_W(m_Z)$ at the Z^0 Peak*, Phys. Lett. **B232** (1989) 123.

G. Passarino and M. J. G. Veltman, *On the Definition of the Weak Mixing Angle*, Phys. Lett. **B237** (1990) 537.

[127] M. Böhm, H. Spiesberger, and W. Hollik, *On the One Loop Renormalization of the Electroweak Standard Model and Its Application to Leptonic Processes*, Fortsch. Phys. **34** (1986) 687–751.

[128] A. Denner, *Techniques for Calculation of Electroweak Radiative Corrections at the One Loop Level and Results for W Physics at LEP-200*, Fortschr. Phys. **41** (1993) 307–420 [`arXiv:0709.1075`].

[129] W. Hollik and H. Rzehak, *The Sfermion Mass Spectrum of the MSSM at the One-Loop Level*, Eur. Phys. J. **C32** (2003) 127–133 [`hep-ph/0305328`].

[130] A. Dabelstein, *The One Loop Renormalization of the MSSM Higgs Sector and its Application to the Neutral Scalar Higgs Masses*, Z. Phys. **C67** (1995) 495–512 [`hep-ph/9409375`].

[131] P. H. Chankowski, S. Pokorski, and J. Rosiek, *Supersymmetric Higgs Boson Decays with Radiative Corrections*, Nucl. Phys. **B423** (1994) 497–531.

[132] M. Frank, S. Heinemeyer, W. Hollik, and G. Weiglein, *FeynHiggs1.2: Hybrid MS-bar/On-Shell Renormalization for the CP-Even Higgs Boson Sector in the MSSM*, [`hep-ph/0202166`].

[133] A. Freitas and D. Stöckinger, *Gauge Dependence and Renormalization of tanβ in the MSSM*, Phys. Rev. **D66** (2002) 095014 [`hep-ph/0205281`].

[134] T. Fritzsche and W. Hollik, *Complete One-Loop Corrections to the Mass Spectrum of Charginos and Neutralinos in the MSSM*, Eur. Phys. J. **C24** (2002) 619–629 [`hep-ph/0203159`].
A. Freitas, A. von Manteuffel, and P. M. Zerwas, *Slepton Production at e^+e^- and e^-e^- Linear Colliders*, Eur. Phys. J. **C34** (2004) 487–512 [`hep-ph/0310182`].

[135] H. A. Rzehak, *Zwei-Schleifen-Beiträge im Supersymmetrischen Higgs-Sektor*. PhD thesis, Max Planck Institute for Physics and TU Munich, Munich, 2005.

[136] W. Beenakker, R. Höpker, M. Spira, and P. M. Zerwas, *Squark Production at the Tevatron*, Phys. Rev. Lett. **74** (1995) 2905–2908 [`hep-ph/9412272`].

[137] S. Berge, W. Hollik, W. M. Mösle, and D. Wackeroth, *SUSY QCD One-Loop Effects in (Un)Polarized Top-Pair Production at Hadron Colliders*, Phys. Rev. **D76** (2007) 034016 [`hep-ph/0703016`].

[138] T. Kinoshita, *Mass Singularities of Feynman Amplitudes*, J. Math. Phys. **3** (1962) 650–677.

[139] S. Dittmaier, *Separation of Soft and Collinear Singularities from One-Loop N-Point Integrals*, Nucl. Phys. **B675** (2003) 447–466 [`hep-ph/0308246`].

[140] T. D. Lee and M. Nauenberg, *Degenerate Systems and Mass Singularities*, Phys. Rev. **133** (1964) B1549–B1562.

[141] M. Böhm, A. Denner, and H. Joos, *Gauge Theories of the Strong and Electroweak Interaction*. B. G. Teubner Stuttgart - Leizig - Wiesbaden, 2001.

[142] B. W. Harris and J. F. Owens, *The Two Cutoff Phase Space Slicing Method*, Phys. Rev. **D65** (2002) 094032 [`hep-ph/0102128`].

[143] S. Catani and M. H. Seymour, *The Dipole Formalism for the Calculation of QCD Jet Cross Sections at Next-to-Leading Order*, Phys. Lett. **B378** (1996) 287–301 [`hep-ph/9602277`].
S. Catani and M. H. Seymour, *A General Algorithm for Calculating Jet Cross Sections in NLO QCD*, Nucl. Phys. **B485** (1997) 291–419 [`hep-ph/9605323`].

[144] S. Catani, S. Dittmaier, M. H. Seymour, and Z. Trocsanyi, *The Dipole Formalism for Next-to-Leading Order QCD Calculations with Massive Partons*, Nucl. Phys. **B627** (2002) 189–265 [`hep-ph/0201036`].

[145] S. Dittmaier, *A General Approach to Photon Radiation off Fermions*, Nucl. Phys. **B565** (2000) 69–122 [`hep-ph/9904440`].

[146] S. Dittmaier, A. Kabelschacht, and T. Kasprzik, *Polarized QED Splittings of Massive Fermions and Dipole Subtraction for Non-Collinear-Safe Observables*, [`arXiv:0802.1405`].

[147] G. 't Hooft and M. J. G. Veltman, *Scalar One Loop Integrals*, Nucl. Phys. **B153** (1979) 365–401.

[148] A. Bredenstein, S. Dittmaier, and M. Roth, *Four-Fermion Production at Gamma Gamma Colliders. II: Radiative Corrections in Double-Pole Approximation*, Eur. Phys. J. **C44** (2005) 27–49 [`hep-ph/0506005`].

[149] U. Baur, S. Keller, and D. Wackeroth, *Electroweak Radiative Corrections to W Boson Production in Hadronic Collisions*, Phys. Rev. **D59** (1999) 013002 [`hep-ph/9807417`].

[150] S. Dittmaier and M. Krämer, *Electroweak Radiative Corrections to W-Boson Production at Hadron Colliders*, Phys. Rev. **D65** (2002) 073007 [`hep-ph/0109062`].

[151] D. Wackeroth and W. Hollik, *Electroweak Radiative Corrections to Resonant Charged Gauge Boson Production*, Phys. Rev. **D55** (1997) 6788–6818 [`hep-ph/9606398`].

K. P. O. Diener, S. Dittmaier, and W. Hollik, *Electroweak Radiative Corrections to Deep-Inelastic Neutrino Scattering: Implications for NuTeV?*, Phys. Rev. **D69** (2004) 073005 [`hep-ph/0310364`].

[152] W. Hollik, T. Kasprzik, and B. A. Kniehl, *Electroweak Corrections to W-Boson Hadroproduction at Finite Transverse Momentum*, Nucl. Phys. **B790** (2008) 138–159 [`arXiv:0707.2553`].

[153] W. Hollik, M. Kollar, and M. K. Trenkel, *EW NLO Corrections to Pair Production of Top-Squarks at the LHC*, [`arXiv:0710.2472`].

W. Hollik, M. Kollar, E. Mirabella, and M. K. Trenkel, *Hadronic Production of Colored SUSY Particles with Electroweak NLO Contributions*, AIP Conf. Proc. **1078** (2009) 250–252 [`arXiv:0810.1138`].

[154] J. Küblbeck, M. Böhm, and A. Denner, *FeynArts: Computer Algebraic Generation of Feynman Graphs and Amplitudes*, Comput. Phys. Commun. **60** (1990) 165–180.

T. Hahn, *Generating Feynman Diagrams and Amplitudes with FeynArts 3*, Comput. Phys. Commun. **140** (2001) 418–431 [`hep-ph/0012260`].

T. Hahn and C. Schappacher, *The Implementation of the Minimal Supersymmetric Standard Model in FeynArts and FormCalc*, Comput. Phys. Commun. **143** (2002) 54–68 [`hep-ph/0105349`].

G. Passarino and M. J. G. Veltman, *One Loop Corrections for e^+e^- Annihilation Into $\mu^+\mu^-$ in the Weinberg Model*, Nucl. Phys. **B160** (1979) 151.

[155] W. Beenakker and A. Denner, *Infrared Divergent Scalar Box Integrals With Applications in the Electroweak Standard Model*, Nucl. Phys. **B338** (1990) 349–370.

A. Denner, U. Nierste, and R. Scharf, *A Compact Expression for the Scalar One Loop Four Point Function*, Nucl. Phys. **B367** (1991) 637–656.

[156] O. Brein and W. Hollik, *Distributions for MSSM Higgs Boson + Jet Production at Hadron Colliders*, Phys. Rev. **D76** (2007) 035002 [arXiv:0705.2744].

[157] **Tevatron Electroweak Working Group** Collaboration, *Combination of CDF and D0 Results on the Mass of the Top Quark*, 2009.
[http://www-cdf.fnal.gov/physics/new/top/top.html].

[158] J. A. Aguilar-Saavedra *et. al.*, *Supersymmetry Parameter Analysis: SPA Convention and Project*, Eur. Phys. J. **C46** (2006) 43–60 [hep-ph/0511344].

[159] U. Baur, *Weak Boson Emission in Hadron Collider Processes*, Phys. Rev. **D75** (2007) 013005 [hep-ph/0611241].

[160] M. Beccaria, M. Melles, F. M. Renard, S. Trimarchi, and C. Verzegnassi, *Sudakov Expansions at One Loop and Beyond for Charged Scalar and Fermion Pair Production in SUSY Models at Future Linear Colliders*, Int. J. Mod. Phys. **A18** (2003) 5069–5098 [hep-ph/0304110].

[161] A. Arhrib and W. Hollik, *Radiative Corrections to Scalar Fermion Pair Production in High Energy e^+e^- Collisions*, JHEP **04** (2004) 073 [hep-ph/0311149].

[162] B. C. Allanach *et. al.*, *The Snowmass Points and Slopes: Benchmarks for SUSY Searches*, Eur. Phys. J. **C25** (2002) 113–123 [hep-ph/0202233].
G. Weiglein, *The Snowmass Points and Slopes*.
[http://www.ippp.dur.ac.uk/~georg/sps/sps.html].

[163] F. E. Paige, *SUSY Signatures in ATLAS at LHC*, [hep-ph/0307342].

[164] A. Denner, *Lectures on Unstable Particles in Gauge Theories, I- IV*, Prepared for the Second Graduate School in Physics at Colliders, Torino, July 2003.
[http://people.web.psi.ch/denner/public/talks/torino03/].
S. Dittmaier, *Introduction to Standard Model and Precision Physics, I - IV*, Prepared for the Parma School of Theoretical Physics, Italy, September 5 - 15, 2006.
[http://www.fis.unipr.it/infn/snft/2006/ditt_lectures.html].

[165] H. K. Dreiner, S. Grab, and M. K. Trenkel, *$\tilde{\tau}$ LSP Phenomenology: Two versus Four-Body Decay Modes. Example: Resonant Single Slepton Production at the LHC*, Phys. Rev. **D79** (2009) 016002 [arXiv:0808.3079].

[166] B. C. Allanach, A. Dedes, and H. K. Dreiner, *R-parity Violating Minimal Supergravity Model*, Phys. Rev. **D69** (2004) 115002 [hep-ph/0309196].

[167] B. C. Allanach, M. A. Bernhardt, H. K. Dreiner, C. H. Kom, and P. Richardson, *Mass Spectrum in R-parity Violating mSUGRA and Benchmark Ppoints*, Phys. Rev. **D75** (2007) 035002 [hep-ph/0609263].

[168] H. K. Dreiner, *An Introduction to Explicit R-parity Violation*, [hep-ph/9707435].

[169] H. K. Dreiner and G. G. Ross, *R-parity Violation at Hadron Colliders*, Nucl. Phys. **B365** (1991) 597–613.

[170] **R-parity Working Group** Collaboration, B. Allanach *et. al.*, *Searching for R-parity Violation at Run II of the Tevatron*, [hep-ph/9906224].

[171] S. P. Martin and M. T. Vaughn, *Two Loop Renormalization Group Equations for Soft Supersymmetry Breaking Couplings*, Phys. Rev. **D50** (1994) 2282 [`hep-ph/9311340`].

[172] B. C. Allanach, A. Dedes, and H. K. Dreiner, *2-Loop Supersymmetric Renormalisation Group Equations Including R-parity Violation and Aspects of Unification*, Phys. Rev. **D60** (1999) 056002 [`hep-ph/9902251`].

[173] L. J. Hall and M. Suzuki, *Explicit R-parity Breaking in Supersymmetric Models*, Nucl. Phys. **B231** (1984) 419.

R. Hempfling, *Neutrino Masses and Mixing Angles in SUSY-GUT Theories with Explicit R-parity Breaking*, Nucl. Phys. **B478** (1996) 3–30 [`hep-ph/9511288`].

F. Borzumati, Y. Grossman, E. Nardi, and Y. Nir, *Neutrino Masses and Mixing in Supersymmetric Models Without R-parity*, Phys. Lett. **B384** (1996) 123–130 [`hep-ph/9606251`].

M. Hirsch, M. A. Diaz, W. Porod, J. C. Romao, and J. W. F. Valle, *Neutrino Masses and Mixings from Supersymmetry with Bilinear R-parity Violation: A Theory for Solar and Atmospheric Neutrino Oscillations*, Phys. Rev. **D62** (2000) 113008 [`hep-ph/0004115`].

B. C. Allanach and C. H. Kom, *Lepton Number Violating mSUGRA and Neutrino Masses*, JHEP **04** (2008) 081 [`arXiv:0712.0852`].

H. K. Dreiner, J. Soo Kim, and M. Thormeier, *A Simple Baryon Triality Model for Neutrino Masses*, [`arXiv:0711.4315`].

[174] A. G. Akeroyd, M. A. Diaz, J. Ferrandis, M. A. Garcia-Jareno, and J. W. F. Valle, *Charged Higgs Boson and Stau Phenomenology in the Simplest R-parity Breaking Model*, Nucl. Phys. **B529** (1998) 3–22 [`hep-ph/9707395`].

A. de Gouvea, A. Friedland, and H. Murayama, *Less Minimal Supersymmetric Standard Model*, Phys. Rev. **D59** (1999) 095008 [`hep-ph/9803481`].

A. G. Akeroyd, C. Liu, and J.-H. Song, *Stau LSP and Comparison with $H^{\pm}$ Phenomenology*, Phys. Rev. **D65** (2002) 015008 [`hep-ph/0107218`].

A. Bartl, M. Hirsch, T. Kernreiter, W. Porod, and J. W. F. Valle, *Testing the Mechanism of R-parity Breaking with Slepton LSP Decays*, JHEP **11** (2003) 005 [`hep-ph/0306071`].

B. C. Allanach *et. al.*, *R-parity Violating Minimal Supergravity at the LHC*, [`arXiv:0710.2034`].

[175] M. A. Bernhardt, H. K. Dreiner, S. Grab, and P. Richardson, *Single Slepton Production in Association with a Single Top Quark at the Tevatron and LHC*, Phys. Rev. **D78** (2008) 015016 [`arXiv:0802.1482`].

[176] C. H. Kom. PhD thesis, Cambridge.

[177] M. Chemtob, *Phenomenological Constraints on Broken R-parity Symmetry in Supersymmetry Models*, Prog. Part. Nucl. Phys. **54** (2005) 71–191 [`hep-ph/0406029`].

[178] H. K. Dreiner, M. Krämer, and B. O'Leary, *Bounds on R-parity Violation from Leptonic and Semi-Leptonic Meson Decays*, Phys. Rev. **D75** (2007) 114016 [`hep-ph/0612278`].

[179] B. C. Allanach, A. Dedes, and H. K. Dreiner, *Bounds on R-parity Violating Couplings at the Weak Scale and at the GUT Scale*, Phys. Rev. **D60** (1999) 075014 [`hep-ph/9906209`].

[180] K. Agashe and M. Graesser, *R-parity Violation in Flavor Changing Neutral Current Processes and Top Quark Decays*, Phys. Rev. **D54** (1996) 4445–4452 [`hep-ph/9510439`].

[181] H. K. Dreiner, P. Richardson, and M. H. Seymour, *Resonant Slepton Production at the LHC*, [`hep-ph/0001224`].
H. K. Dreiner, P. Richardson, and M. H. Seymour, *Resonant Slepton Production in Hadron Hadron Collisions*, Phys. Rev. **D63** (2001) 055008 [`hep-ph/0007228`].

[182] H. K. Dreiner, P. Richardson, and M. H. Seymour, *Resonant Slepton Production*, [`hep-ph/9903419`].
G. Moreau, E. Perez, and G. Polesello, *Resonant Sneutrino Production in Supersymmetry with R-parity Violation at the LHC*, Nucl. Phys. **B604** (2001) 3–31 [`hep-ph/0003012`].
F. Deliot, G. Moreau, and C. Royon, *Single Superpartner Production at Tevatron Run II*, Eur. Phys. J. **C19** (2001) 155–181 [`hep-ph/0007288`].

[183] S. Dimopoulos and L. J. Hall, *Lepton and Baryon Number Violating Collider Signatures from Supersymmetry*, Phys. Lett. **B207** (1988) 210.
S. Dimopoulos, R. Esmailzadeh, L. J. Hall, and G. D. Starkman, *Cross-Sections for Lepton and Baryon Number Violating Processes from Supersymmetry at $P\bar{P}$ Colliders*, Phys. Rev. **D41** (1990) 2099.

[184] B. C. Allanach, M. Guchait, and K. Sridhar, *Resonant Slepton Production at the LHC in Models with an Ultralight Gravitino*, Phys. Lett. **B586** (2004) 373–381 [`hep-ph/0311254`].

[185] **D0** Collaboration, V. M. Abazov *et. al.*, *Search for the Production of Single Sleptons Through R-parity Violation in $P\bar{P}$ Collisions at $\sqrt{s}$= 1.8 TeV*, Phys. Rev. Lett. **89** (2002) 261801 [`hep-ex/0207100`].
D0 Collaboration, V. M. Abazov *et. al.*, *Search for Resonant Second Generation Slepton Production at the Tevatron*, Phys. Rev. Lett. **97** (2006) 111801 [`hep-ex/0605010`].

[186] D. Choudhury, S. Majhi, and V. Ravindran, *QCD Corrections to Resonant Slepton Production in Hadron Colliders*, Nucl. Phys. **B660** (2003) 343–361 [`hep-ph/0207247`].
L. L. Yang, C. S. Li, J. J. Liu, and Q. Li, *Soft Gluon Resummation Effects in Single Slepton Production at Hadron Colliders*, Phys. Rev. **D72** (2005) 074026 [`hep-ph/0507331`].

[187] H. K. Dreiner, S. Grab, M. Krämer, and M. K. Trenkel, *Supersymmetric NLO QCD Corrections to Resonant Slepton Production and Signals at the Tevatron and the LHC*, Phys. Rev. **D75** (2007) 035003 [`hep-ph/0611195`].

[188] Y.-Q. Chen, T. Han, and Z.-G. Si, *QCD Corrections to Single Slepton Production at Hadron Colliders*, JHEP **05** (2007) 068 [`hep-ph/0612076`].

[189] M. Drees and S. P. Martin, *Implications of SUSY Model Building*, [`hep-ph/9504324`].

[190] V. D. Barger, G. F. Giudice, and T. Han, *Some New Aspects of Supersymmetry R-parity Violating Interactions*, Phys. Rev. **D40** (1989) 2987.

[191] B. de Carlos and P. L. White, *R-parity Violation Effects through Soft Supersymmetry Breaking Terms and the Renormalisation Group*, Phys. Rev. **D54** (1996) 3427–3446 [`hep-ph/9602381`].

[192] W. H. Press *et. al.*, eds., *Numerical Recipes in C++*. Cambridge University Press, 2002, Second Edition.

[193] B. C. Allanach and M. A. Bernhardt, *Including R-parity Violation in the Numerical Computation of the Spectrum of the Minimal Supersymmetric Standard Model: SOFTSUSY3.0*, [`arXiv:0903.1805`].

[194] F. E. Paige, S. D. Protopopescu, H. Baer, and X. Tata, *ISAJET 7.69: A Monte Carlo Event Generator for PP, $\bar{P}P$, and e^+e^- reactions*, [`hep-ph/0312045`].

[195] G. Corcella *et. al.*, *HERWIG 6: An Event Generator for Hadron Emission Reactions with Interfering Gluons (Including Supersymmetric Processes)*, JHEP **01** (2001) 010 [`hep-ph/0011363`].
G. Corcella *et. al.*, *HERWIG 6.5 Release Note*, [`hep-ph/0210213`].
S. Moretti, K. Odagiri, P. Richardson, M. H. Seymour, and B. R. Webber, *Implementation of Supersymmetric Processes in the HERWIG Event Generator*, JHEP **04** (2002) 028 [`hep-ph/0204123`].

[196] F. Borzumati, J.-L. Kneur, and N. Polonsky, *Higgs-Strahlung and R-parity Violating Slepton-Strahlung at Hadron Colliders*, Phys. Rev. **D60** (1999) 115011 [`hep-ph/9905443`].
E. Accomando *et. al.*, *Workshop on CP Studies and Non-Standard Higgs Physics*, [`hep-ph/0608079`].
A. Belyaev, M.-H. Genest, C. Leroy, and R. R. Mehdiyev, *Signals from R-parity Violating Top Quark Decays at LHC*, JHEP **09** (2004) 012 [`hep-ph/0401065`].

[197] B. C. Allanach and M. A. Bernhardt. [`unpublished`].

[198] H. K. Dreiner, H. E. Haber, and S. P. Martin, *Two-Component Spinor Techniques and Feynman Rules for Quantum Field Theory and Supersymmetry*, [`arXiv:0812.1594`].

[199] A. Djouadi, M. Drees, and J. L. Kneur, *Constraints on the Minimal Supergravity Model and Prospects for SUSY Particle Production at Future Linear e^+e^- Colliders*, JHEP **08** (2001) 055 [`hep-ph/0107316`].

[200] N. Ghodbane and H.-U. Martyn, *Compilation of SUSY Particle Spectra from Snowmass 2001 Benchmark Models*, [`hep-ph/0201233`].

[201] P. Richardson, *Simulations of R-parity Violating SUSY Models*, [`hep-ph/0101105`].

Acknowledgments

First of all, I would like to thank my supervisor Prof. Wolfgang Hollik for his guidance and continuous support and encouragement during all phases of this thesis.

I thank Prof. Herbert Dreiner and Sebastian Grab for the fruitful and inspiring collaboration over the last years. Sebastians enthusiasm in starting off so many discussions always impressed me.

I also would like to thank Prof. Tilman Plehn for taking care of his "MPI kids".

I am most grateful to my colleagues Edoardo Mirabella, Jan Germer, and Monika Kollar, it was a great pleasure to work with them. I am particularly indebted to Edoardo for all the constructive discussions and for answering my countless questions.

Sincere thanks are also given to all my colleagues in the theory group of the Max-Planck-Institute for Physics and in particular to my numerous office mates Christoph Reißer, Stefan Kallweit, Marina Billoni, Ananda Landwehr, and Jochen Baumann for creating a most enjoyable working atmosphere and for all the lively discussions. I also thank the community of PhD students at the MPI for the great support during my time as PhD representative.

Last but not least, I would like to express my deepest gratitude to Daniel and to my family for their undestroyable optimism and unconditional encouragement during the entire time.